Scintillation on Global Navigation Satellite Signals and its Mitigation

Arslan Ahmed

School of Electrical and Electronic Engineering

Newcastle University

This dissertation is submitted for the degree of

Doctor of Philosophy

Newcastle University

November 2015

I would like to dedicate this thesis to my loving parents, brother and sister

Declaration

I hereby declare that except where specific reference is made to the work of others, the contents of this dissertation are original and have not been submitted in whole or in part for consideration for any other degree or qualification in this, or any other university. This dissertation is my own work and contains nothing which is the outcome of work done in collaboration with others, except as specified in the text and acknowledgements.

Arslan Ahmed

November 2015

Acknowledgements

In the name of Allah, the most Beneficent and the most Merciful.

I would like to thank the following people for their technical advice, funding support, and assistance during my Ph.D without whom this thesis would not have been possible.

First and foremost, I would like to thank my supervisors: Dr Hal Strangeways, Dr Rajesh Tiwari and Professor Said Boussakta. Please let me express my deep sense of gratitude and appreciation to all of you for the knowledge, guidance and the support you have given me. I will never forget the enjoyable time spent doing research with all of you and these unforgettable days will influence the rest of my life.

I would also like to acknowledge the School of Electrical and Electronic Engineering for providing the necessary resources and research environment for me to conduct my PhD work. I would like to express my sincere gratitude to Professor Gui Yun Tian and Mr. Jeff Neasham for being part of the internal examiner committee for accessing my research work for going through the PhD progression stages. All the friends and office mates, who made my stay in Newcastle not only enjoyable but also productive one.

I would also like to acknowledge the financial support provided by the Higher Education Commission (HEC) of Pakistan and the Sukkur Institute of Business Administration, Pakistan.

Love from my parents, brother and sister is invaluable. Thank you for always being so encouraging over the years. Although I saw your faces only several times in the past few years but smiles from each of you are kept in my mind. I look forward to being with you more often after my graduation.

My sincere thanks to all of you.

Abstract

The scintillation effects on the Global Positioning system (GPS) or other GNSS (global navigation satellite system) receivers have been investigated by many researchers and several mitigation strategies have been proposed in this regard but the problem is not yet fully solved. This thesis covers the investigation of scintillation effects on GPS receivers and developing a mitigation approach which can play an important role in mitigating the effects of scintillation on these and other GNSS receivers.

Firstly, a new GPS signal acquisition method known as the repetitive block acquisition (RBA) is presented which can be used to speed up the GPS signal acquisition in case fast acquisition is required. This acquisition method is implemented using coarse-acquisition (C/A) codes and tested by collecting real GPS data. The RBA method can also be used for other codes as well. It is rather difficult to show that how scintillation affects the acquisition process in a GPS receiver because mostly it results in tracking loop loss of lock due to cycle slip. However, during strong amplitude scintillation which is usually most important at low or near-equatorial latitudes, deep power fades resulting from amplitude scintillation result in the selection of long data records which leads to slow acquisition due to long acquisition times. It is shown in this thesis that, by using the RBA method, the acquisition time can be reduced to a fairly low level by reducing the number of computations involved in acquisition compared to other well-known methods such as the parallel FFT-based method and zero padding method (ZP).

Secondly, the scintillation effects on the GPS tracking loop have also been investigated in this thesis and, based on this investigation, a new improved analogous phase scintillation index, $\sigma_{\phi a}^{\mathrm{w}}$, has been designed to more accurately represent the phase scintillation intensity at European high latitudes. This is then also validated using the real GPS data from Trondheim, Norway (63.41^o N, 10.4^o E). The $\sigma_{\phi a}^{\mathrm{w}}$ uses dual frequency ($L1$ & $L2$) based

time and spatial variations of total electron contents (TEC) at 1 Hz for estimating the phase scintillation values. For deriving the $\sigma_{\phi a}^{\mathrm{w}}$, the low frequency TEC fluctuations due to Doppler shift of the satellite/receiver motion and also due to the slowly varying background ionosphere need to be removed in order to consider only the high frequency TEC fluctuations which are responsible for scintillation due to the fast moving electron density irregularities which is done by using the wavelet transform. The $\sigma_{\phi a}^{\mathrm{w}}$ is really an improved version of $\sigma_{\phi a}$ where, rather than using time-invariant digital high pass filters (HPF), which according to several researchers are in-appropriate for filtering the non-stationary raw GPS signals affected by the ionospheric scintillation, a wavelet-based filtering technique is used. Although, the wavelet transform has been used previously in detrending raw amplitude and phase observations at 50 Hz for estimating the scintillation indices (amplitude and phase), due to the high sample data rate it may not be desirable to use this transform due to its very high computational cost. Since, $\sigma_{\phi a}^{\mathrm{w}}$ uses TEC data at 1 Hz so this problem has been overcome. The performance of the new improved index ($\sigma_{\phi a}^{\mathrm{w}}$) is investigated and is also compared with the previously proposed $\sigma_{\phi a}$ and σ_{ϕ} indices using one whole year of data from a GPS receiver at Trondheim, Norway (63.41^o N, 10.4^o E).

The raw TEC observations and the $\sigma_{\phi a}^{\mathrm{w}}$ index are then used in estimating the tracking phase jitter using two different methods. The phase jitter helps in defining the tracking thresholds for the tracking loops in a receiver which is useful in updating the tracking loop parameters during scintillation conditions as required in robust GPS/GNSS receiver designs because the phase jitter decides how wide the tracking (and thus the noise) bandwidth should be allowed in the tracking loop for the tracking to remain efficient. It is shown that if the phase jitter is estimated using the new proposed methods, generally a better estimate can be obtained compared to the previously proposed phase jitter estimation methods which employs $\sigma_{\phi a}$ and σ_{ϕ} indices. These new phase jitter estimation methods can further be used in GPS/GNSS receivers for updating the tracking loop parameters during scintillation conditions and hence can serve as a good alternative for mitigating the effects of scintillation on GPS/GNSS receivers.

Table of contents

List of figures

List of tables

Nomenclature

Acronyms / Abbreviations

C/A	Coarse Acquisition
C/N_o	Carrier-to-noise ratio
S/N_o	signal-to-noise ratio
ADC	Analog-to-Digital converter
DFT	Discrete Fourier transform
DIX	Disturbance Ionospheric Index
DOP	Dilution of precision
FFT	Fast Fourier transform
GISTM	GNSS ionospheruc scintillation monitors
GNSS	Global navigation satellite system
HPF	High pass filter
IF	Intermediate frequency
IFFT	Inverse fast Fourier transform
IGS	International GPS Geodynamics Service
IPP	Ionospheric Pierce Point

IWT	Inverse wavelet transform
IZP	Improved zero padding
LPF	Low pass filter
MEO	Mediumn earth orbit
MLT	Magnetic local time
NBP	Narrow-band power
NUDET	Nuclear detonation detection
PDF	Probability density function
PRN	Pseud-random number
RBA	Repetitive block acquisition
RINEX	Receiver Independent Exchange Format
RoT	Rate of change of TEC
SA	Selective availability
SoL	Safety of life
SPLN	St. Petersburg-Leeds-Newcastle
STEC	Slant total electron content
TEC	Total electron content
USRP	Universal software radio peripheral
UT	Universal time
WBP	Wide-band power
WDC	World Data Centre
ZP	Zero padding

Chapter 1

Introduction and Background

Satellite-based navigation is one of the most important tools for navigation having a wide range of applications which includes aviation and marine navigation in addition to life saving applications; thus the expectation of its availability, reliability and accuracy is very important. There are currently two global navigation satellite systems that are fully functional and operational; the first one is the U.S-based GPS (Global Positioning System) and the second one is the Russian GLONASS (Global Navigation Satellite System).

The development of GLONASS dates back to 1976 under the Soviet rule, however the launching of the GLONASS constellation satellites began in October 1982 with the launch of the first three satellites namely Kosmos-1413, Kosmos-1414, and Kosmos-1415 [1]. The constellation was completed in 1995 with the optimal status of 24 fully operational GLONASS satellites for Global coverage. GLONASS uses frequency division multiple access (FDMA) as a modulation technique for signal transmission at L1 (1.602 GHz) and L2 (1.246 GHz) frequency bands to provide navigation services to civilian and military users. A third frequency band G3 [1] was also later added in GLONASS which can be used for safety-of-life and military purposes.

The history of GPS, on the other hand, goes back to 1973 with the formation of the NAVSTAR GPS development programme initiated by the U.S Department of Defense under the supervision of Bradford Parkinson who is also known as the father of GPS [2]. With the launch of the Block-I experimental satellites beginning in 1978, the GPS system was declared fully operational by the U.S Air force in April 1995 with the total of 24

constellation satellites. The GPS uses several frequency bands to provide different kinds of services to both civilian and military users. These frequency bands are:

- L1 (1575.42 MHz) – Coarse-acquisition (C/A) code for civilian use and encrypted P(Y) code for militaryuse.
- L2 (1227.60 MHz) – P(Y) code, military codes and the additional improved L2C code for civilian use.
- L3 (1381.05 MHz) – Used for nuclear detonation (NUDET) detection.
- L4 (1379.913 MHz) – Being studied for additional ionospheric correction.
- L5 (1176.45 MHz) – For civilian safety-of-life (SoL) purpose.

The GPS and GLONASS signals are sent from more than 20,000 km above the Earth's surface and therefore encounter several phenomena that degardes the performance of these systems such as the atmospheric attenuation, satellite and receiver geometry, correlation loss, polarization loss, tropospheric delay, ionospheric scintillation etc. Most of these errors don't have a significant impact and can be dealt with during the positioning solution. However, ionospheric scintillation effects can be severe, particularly at high and near equatorial latitudes. Ionospheric scintillation is the rapid random fluctuations in amplitude and/or phase of the received transionospheric radio waves resulting from propagating through electron density irregularities such as those embedded in the plasma bubbles. These irregularities are small scale electron density fluctuations in the ionosphere which can result from geomagnetic storms and increased solar activity. Scintillation effects are different at different latitudes. Strong amplitude scintillation is more common at low geomagnetic latitudes due to plasma bubbles rising through the propagation path. However, it can also be observed at high latitudes but with less severity and lesser effects on the GPS/GNSS signals while the mid latitude regions usually have no significant phase and amplitude scintillation effects on the GPS/GNSS receivers. High latitude regions are more likely to be disturbed by the phase scintillation which occurs due to auroral phenomena in

auroral oval regions. Many researchers have used different methods to mitigate the effects of scintillation on GNSS/GPS receivers. In this regard, new techniques for scintillation mitigation are also proposed but they are still not able to solve this problem completely.

This PhD work is focussed on the study of ionospheric scintillation and their effects on GPS/GNSS receivers and also to propose strategies for scintillation mitigation. In this regard, a new TEC-based phase scintillation index $\sigma_{\phi a}^{\mathrm{w}}$ is designed which uses 1 Hz total electron content (TEC) data from a dual frequency GPS receiver to predict the phase scintillation at high latitude regions. The proposed index uses time and spatial variations of TEC for the prediction of phase scintillations and the performance comparison with the standard scintillation index, σ_{ϕ}, and the previously proposed analogous phase scintillation index, $\sigma_{\phi a}$, proves it to be a better indicator of the phase scintillation activity at high latitudes. On the application side towards scintillation mitigation, the raw TEC observations and the $\sigma_{\phi a}^{\mathrm{w}}$ index are used to calculate the tracking phase jitter using two different phase jitter estimation methods which can be used in configurable tracking loop designs of geodetic receivers and also in software-based GPS receivers for updating the tracking loop parameters and has the advantage of low computational cost.

1.1 Thesis Objectives

The main aim of this research is to study the effects of scintillation on GNSS/GPS receivers and develop mitigation strategies in order to improve their performance in reliability, availability and accuracy during moderate to strong ionospheric scintillation. This includes several objectives which are mentioned below:

1. To study ionospheric scintillation and the theory behind it.
2. To investigate the effects of ionospheric scintillation on GNSS/GPS receivers.
3. To design improved methods for quantifying the scintillation values.
4. To develop strategies which can be used to mitigate the effects of scintillation on GNSS/GPS receivers.

1.2 Thesis Contributions

Based on the aims and objectives above, the thesis contributions are summarized as follows:

1. The thesis presents a comprehensive study of the ionospheric scintillation and its morphology. In this regard, the statistics of occurrences of scintillation from European high latitudes are presented.

2. The effects of scintillation on the GPS receiver are analyzed by employing different acquisition and tracking loop models during both the scintillation and non-scintillation conditions.

3. A new method of quantifying the phase scintillation values is presented in this thesis which uses dual frequency total electron content (TEC) observations at 1 Hz rather than using 50 Hz raw phase observations as used in many standard scintillation monitoring receivers. The newly presented phase scintillation index is then validated by using the data from a high latitude region.

4. Due to the ability of the newly presented scintillation index in predicting more accurate phase scintillation values as compared to the previously used methods, the index is used to estimate the tracking phase jitter which can be further used to mitigate the effects of scintillation on GPS/GNSS receivers due to its low implementation cost.

1.3 Thesis outline

The whole thesis is divided into the following main chapters:

Chapter 2:

In this chapter, a detail overview of the GPS system is presented. The chapter starts with a brief introduction on satellite based navigation and then discusses the signal structure of the GPS system. A complete overview of a GPS receiver is also presented in this chapter along with the hardware and software aspects involved in signal acquisition, tracking

and position estimation. The discussion then proceeds on to the factors that affects the performance of the GPS receiver such as the multipath, satellite geometry, satellite and receiver clock errors, tropospheric delay and ionospheric delay.

Chapter 3:

The complete morphology of the ionosphere is discussed in this chapter. This chapter outlines the basic knowledge about the ionosphere, ionospheric layers and the phenomena that lead to the formation of ionospheric layers. This discussion is then further widened by presenting the concept of total electron content (TEC), ionosphere irregularities and the ionospheric scintillation.

Chapter 4:

This chapter discusses the scintillation effects on the receiver performance. The chapter can be divided into two parts. The first part covers the acquisition strategies that can be used to speed up the GPS signal acquisition in case the signal is affected by the noise or scintillation. In the second part, a complete theoretical and mathematical background of the PLL tracking loop is presented and it is also shown that how the amplitude and phase scintillation affects the receiver performance and what are the conditions beyond which the tracking loop loses lock during scintillation. The strategies to mitigate the loss of lock due to scintillation in the tracking loops are also discussed in this chapter.

Chapter 5:

This chapter details the concept of TEC fluctuations and the relationship between the TEC and the scintillation producing ionospheric irregularities. Some previous work on TEC-based indices is also highlighted in this chapter. In this regard, a new analogous phase index, $\sigma_{\phi a}$, is presented and its performance is validated using the GPS data from European high latitudes. The performance of this new analogous phase index is also compared with the standard phase scintillation index, σ_{ϕ}.

Chapter 6:

In this chapter, a new improved TEC-based phase scintillation index, $\sigma_{\phi a}^{\mathrm{w}}$, is presented using a wavelet transform based filtering approach. The chapter starts with a detailed overview of the wavelet transform, its mathematical description, applications and using wavelets as a filtering technique. A detailed analysis of some improper filtering effects in deriving the phase scintillation indices using high latitude data is explained and it is also discussed why the wavelet-based filtering approach is a better method for dealing with high latitude raw GPS signals. This chapter details the deficiencies in the previously proposed analogous phase index and also the standard phase scintillation index and then discussed the advantages of using the $\sigma_{\phi a}^{\mathrm{w}}$ index over the $\sigma_{\phi a}$ and σ_{ϕ} indices. The performance of the new $\sigma_{\phi a}^{\mathrm{w}}$ index is compared with the $\sigma_{\phi a}$ and σ_{ϕ} indices under different geomagnetic conditions to validate its performance as a potential alternative to these indices for representing the phase scintillation acitvity.

Chapter 7:

This chapter discusses the possible applications of the research work presented in this thesis which involves estimation of the tracking phase jitter. Since tracking jitter is the key component in a receiver used to determine the loss of lock time during scintillation and is also used for updating the tracking loop paramters, two different methods for estimating the phase jitter are presented in this chapter. One method uses $\sigma_{\phi a}^{\mathrm{w}}$, whereas, the other method uses the raw TEC observation at 1 Hz from which the phase jitter is derived.

Chapter 8:

This chapter concludes the work presented in this thesis and discusses the future trends of the work in order to mitigate the scintillation effects on the GPS/GNSS and the possible applications of the proposed work for further developments.

1.4 List of Publications

1.4.1 Journals

1. **A. Ahmed**, R. Tiwari, H. J. Strangeways, S. Dlay and M. G. Johnsen, "Wavelet-based analogous phase scintillation index for high latitudes," *Space Weather*, 2015. [Online]. Available: http://dx.doi.org/10.1002/2015SW001183

2. R. Tiwari a, H.J. Strangeways, S. Tiwari and **A. Ahmed**, "Investigation of ionospheric irregularities and scintillation using TEC at high latitude," in *Advances in Space Research*, vol. 52, no. 6, pp. 1111 – 1124, 2013. [Online]. Available: http://www.sciencedirect.com/science/article/pii/S0273117713003517

3. **A. Ahmed**, R. Tiwari, H. J. Strangeways, S. Boussakta and S. Dlay, "On determining the tracking phase jitter using dual frequency-based TEC observations for scintillation mitigation on GPS tracking loops," (*to be submitted*)

1.4.2 Conferences

1. R. Tiwari, **A. Ahmed**, H. J. Strangeways, S. Dlay and K. S. Jacobsen, "Auroral Monitoring Index using a Network of GNSS Receivers," in *Proceedings of the 28th International Technical Meeting of The Satellite Division of the Institute of Navigation*, Florida, September 2015 (in press).

2. **A. Ahmed**, R. Tiwari, H. J. Strangeways, and S. Boussakta, "Software-based receiver approach for acquiring GPS signals using block repetition method," in *IEEE 7th ESA Workshop on Satellite Navigation Technologies and European Workshop on GNSS Signals and Signal Processing (NAVITEC)*, pp. 1 - 7, Dec 2014. [Online]. Available: http://ieeexplore.ieee.org/xpl/articleDetails.jsp?arnumber=7045144

3. **A. Ahmed**, R. Tiwari, H. J. Strangeways, and S. Boussakta, "GPS Tracking Loop Performance using Wavelet Denoising," in *7th ESA Workshop on Satellite Navigation Technologies and European Workshop on GNSS Signals and Signal Process-*

ing (NAVITEC), Dec 2014. [Online]. Available: http://eprint.ncl.ac.uk/file_store/production/209080/54B02592-4B8C-4C27-A440-380A0EE24AC3.pdf

4. **A. Ahmed**, R. Tiwari, H. J. Strangeways, and S. Boussakta, "Software-based Receiver Approach for Acquiring Scintillated Signals," in *The International Beacon Satellite Symposium BSS2013*, Bath, UK, July 2013.

5. R. Tiwari, S. Tiwari, H. J. Strangeways and **A. Ahmed**, "Investigation of Ionospheric Irregularities and Scintillation using relative TEC at High Latitudes," in *39th COSPAR Scientic Assembly*, Mysore, India, 2012.

6. **A. Ahmed**, R. Tiwari, H. J. Strangeways, and S. Boussakta, "Reconfigurable Software based GPS Receiver," in *Royal Institute of Navigation (RIN) News Navigator Seminar*, Harwell, Oxfordshire, June 2014.

7. **A. Ahmed**, R. Tiwari, H. J. Strangeways, and S. Boussakta, "Effect of Geomagnetic Storm of March 2012 on GPS Receivers at European High latitude," in *Festival of Radio Science*, Durham University, Durham, UK, April 2012.

Chapter 2

GPS and the Satellite-based Navigation

2.1 Introduction

The GPS is a satellite based navigation system, one of the 4 different systems currently deployed, known generically as the Global Navigation Satellite System (GNSS). The GPS uses five frequency bands to provide navigation services to a wide range of communities, i.e., $L1$ signal at 1575.42 MHz (used for civilian and mililatry purposes), $L2$ and L2C signals at 1227.60 MHz (used for more precise civilian and military navigation purposes), $L3$ signal at 1381.05 MHz (used for nuclear detonation (NUDET) detection), $L4$ signal at 1379.913 MHz (being studied for additional ionospheric corrections) and $L5$ signal at 1176.45 MHz (proposed for use as a civilian safety-of-life (SoL) purpose). There are a total of 24 or more satellites in the active constellation placed in 6 orbital planes where each orbit contains 4 or more satellites with an inclination angle of 55^o to the equator. The orbital radius of each satellite from the centre of the Earth is 26,560 km and each satellite completes its orbit in 11 hours, 57 min and 57.26 sec [3].

Two frequency bands, $L1$ and $L2$, are widely used for navigation to cover the civilian and military customers. The $L1$ signal transmits the C/A code and P-code whereas the $L2$ signal transmits the P-code encrypted by the Y-code and is sometime refer as the $P(Y)$-code and a new L2C signal as well [3]. The P-code is a 266 days (38 weeks) long pseudorandom noise (PRN) code sequence divided into 37 portions and each satellite uses a different portion of the code having a chip rate of 10.23 MHz [4]. The C/A code on the

other hand consists of 1023 chips with a period of 1 ms and a chipping rate of 1.023 MHz. Each satellite is assigned a unique C/A code for its identification. The navigation on the $L1$ C/A coded signal is available to all users free of cost, however the range measurements are less precise than those from the P-code. The GPS signals are also modulated by the 50 bps (50 Hz) data stream known as the navigation message which includes the Almanac Data, Ephemeris Data, Ionospheric Delay Data, Timing Data and the Satellite Health Message (SHM). The almanac data contains the orbital information of the satellites to allow the receiver to determine which satellites are visible at a given location and is valid for several months. The Ephemeris data is similar to the almanac data but allows more accurate determination of the satellite position and is valid for only a few hours. The ionospheric delay data includes coefficients to estimate the ionospheric effects on the GPS signals. The Timing data contains the transmission time of the GPS signal and the Satellite Health Message contains the information about the current health of the satellite.

2.2 GPS Segments

In terms of functionalities, the complete GPS system is divided into three main segments, i. e., space segment, control segment and the user segment whose graphical representation is shown in Fig. 2.1. Together, these three segments control the complete GPS system and provide the navigatoin services to its users.

2.2.1 Space Segment

The Space segment consists of all the satellites in the GPS constellation. There are 24 satellites in the active constellation placed in the medium Earth orbit (MEO) and each satellite orbits the Earth twice a day. The first block of satellites in the GPS constellation were known as the Block I satellites which were then replaced by the more recent ones (Block IIA, Block IIR, Block IIR(M), Block IIF) in order to improve the GPS availability. The most recent Block of satellites are known as the GPS III which are in the production stage and will be launched in 2016 [2].

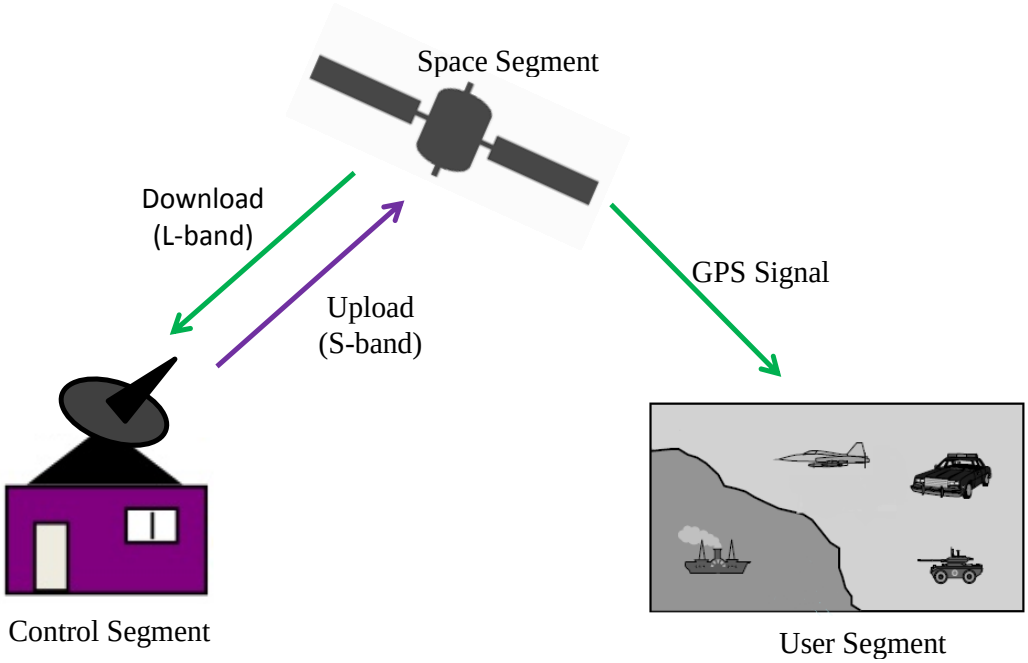

Figure 2.1: GPS Segments

2.2.2 Control Segment

The Control segment of the GPS system consists of a Master control station (MCS), monitor stations (MS) and the ground antennas which receives information from the satellites on the L-band and sends the information to the satellites using S-band [5]. The control segment keeps information about the locations of the GPS satellites in the orbit, monitor the satellites health and also send commands using the S-band for updating the navigation message. As of today, there is currently an active MCS located in Schriever Air Force Base (AFB) Colorado, USA whereas an alternate MCS is located in Vandenberg AFB California, USA. There are 12 ground antennas and 16 MS at different locations around the world controlled by the MCS [2]. Six of the MS are controlled by the Air Force whereas 10 are controlled by the Geospatial-Intelligence Agency (NGA). Some of the MS and ground antennas are also connected to the Air Force Satellite Control Network (AFSCN) remote tracking stations for increasing the visibility and tracking of the GPS system. The locations of the stations in the control segment around the world are shown in Fig. 2.2.

2.2.3 User Segment

The user segment consists of the user equipment used for navigation in which the GPS receiver is one of the major components. The user segment consists of all the the military and the civilian users around the world.

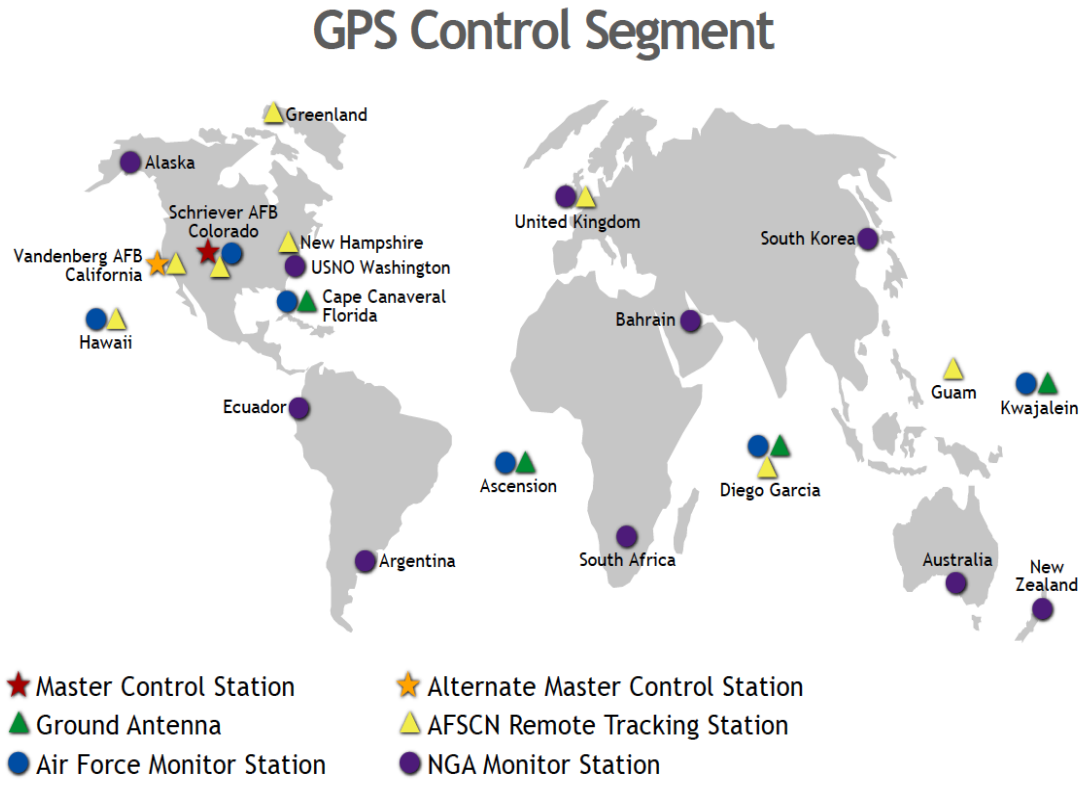

Figure 2.2: Control segment of the GPS [2].

2.3 GPS Signal Structure

The mathematical form of the GPS signal at the $L1$ and $L2$ frequencies can be given as

$$S_{L1} = A_I C(t) D(t) \cos(2\pi f_1 t + \phi) + A_Q P(t) D(t) \sin(2\pi f_1 t + \phi) \tag{2.1}$$

$$S_{L2} = A_Q P(t) D(t) \sin(2\pi f_2 t + \phi) \tag{2.2}$$

where,

- S_{L1} = signal at $L1$ frequency
- S_{L2} = signal at $L2$ frequency
- A_I = in-phase carrier power
- A_Q = quadrature carrier power
- $C(t) = C/A$ code
- $P(t) = P(Y)$ code
- $f_1 = L1$ carrier frequency
- $f_2 = L2$ carrier frequency
- ϕ = phase shift
- $D(t)$ = navigation data at 50 Hz

The GPS signal at the $L1$ frequency consists of in-phase and quadrature components. The in-phase component is bi-phase modulated by the C/A code and the navigation data message. The quadrature component, on the other hand, is bi-phase modulated by the $P(Y)$-code and the navigation data message. The $L2$ signal, on the other hand, in (2.2), is only modulated by the $P(Y)$-code and the 50 Hz navigation data message. However, a new $L2C$ signal is also added recently whose description can be found in [2]. The structure of the C/A code and the $P(Y)$-codes at the $L1$ frequency are shown in Fig. 2.3 and Fig. 2.4 respectively.

In all GPS signals, the navigation data message contains the key information which is used for estimating the position in a receiver. A single bit of the navigation data message is 20 ms (50 Hz) long. The complete navigation message contains 25 frames having 1500 bits which takes 750 s for transmission. A single frame is composed of 5 subframes where each subframe contains 10 words and each word is 30 bits long. It takes approximately 30 s to transmit a single frame of the navigation message. The subframes 1, 2 and 3 contains the clock correction data and the ephemeris data used to determine the velocity and position of the satellites which is then used in the positioning solution. Subframe 4 contains the

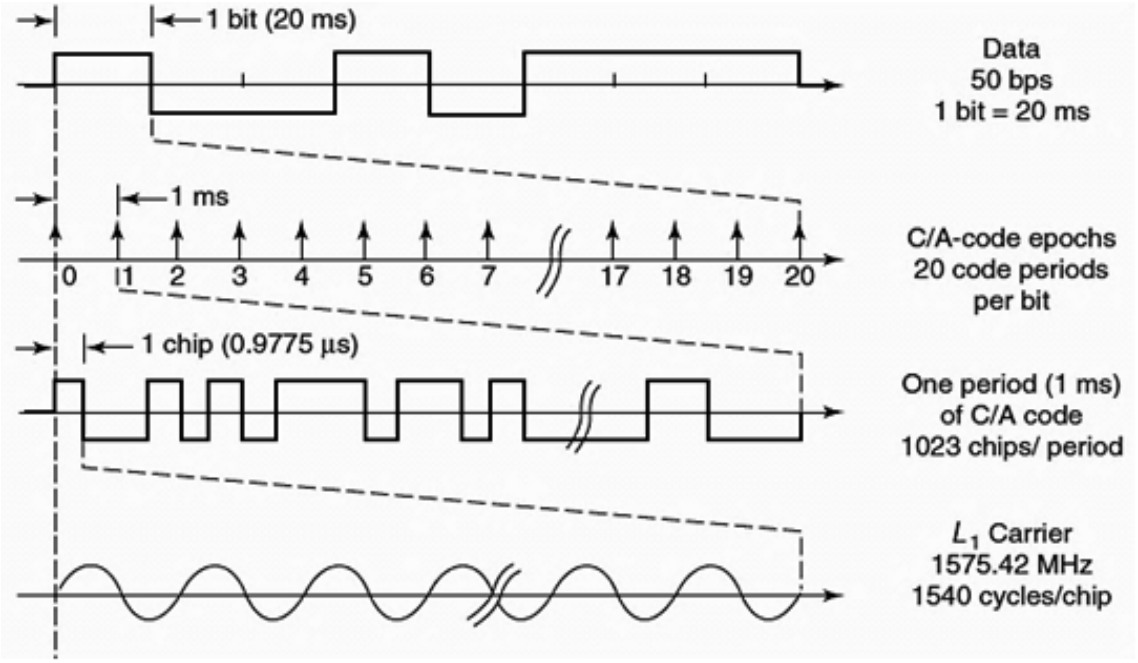

Figure 2.3: Structure of the C/A code at $L1$ frequency [4].

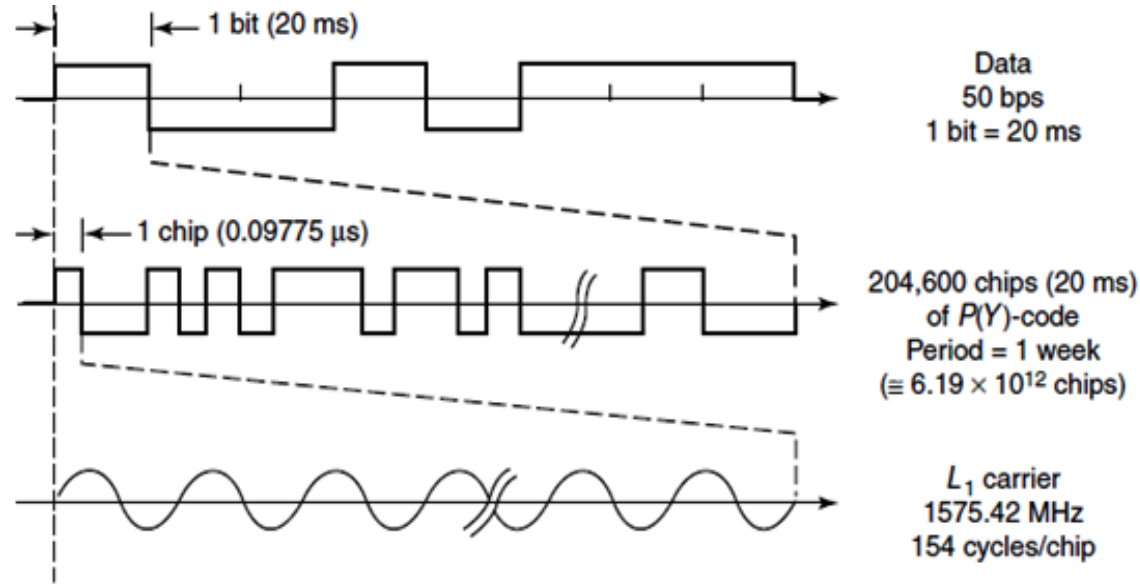

Figure 2.4: Structure of the $P(Y)$-code at $L1$ frequency[4].

ionospheric correction terms and coefficients to convert the GPS time to UTC time and also some free space to accomodate future applications [6]. Subframe 5 contains the alamanac data of PRN's 1 to 24. The structure of the navigation message is shown in Fig. 2.5.

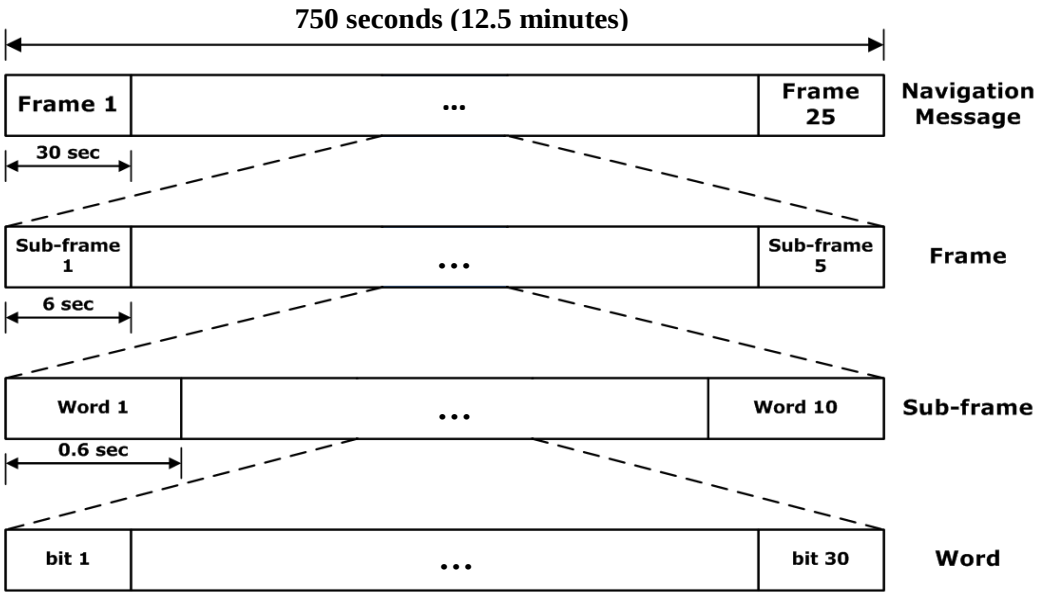

Figure 2.5: Structure of the GPS navigation data message.

2.4 GPS Receiver Structure

A simple block diagram of a GPS receiver is shown in Fig. 2.6. The GPS signals received by the antenna are passed through the front end device to downconvert the signal and then digitized using the analog-to-digital converter (ADC). These three components together make up the hardware part of the GPS receiver. The rest of the components can be implemented both in harware or software.

Once the signal is downconverted and digitized, it is then processed by the acquisition block to find the visible satellites. The tracking section finds the correct beginning of the PRN code of the acquired satellites and locks onto the carrier frequency to extract the navigation information. The navigation data demodulation process reads each and every

bit of the navigation message to recover the Ephemeris data. The last block estimates the user position. A complete explanation of these blocks is given below.

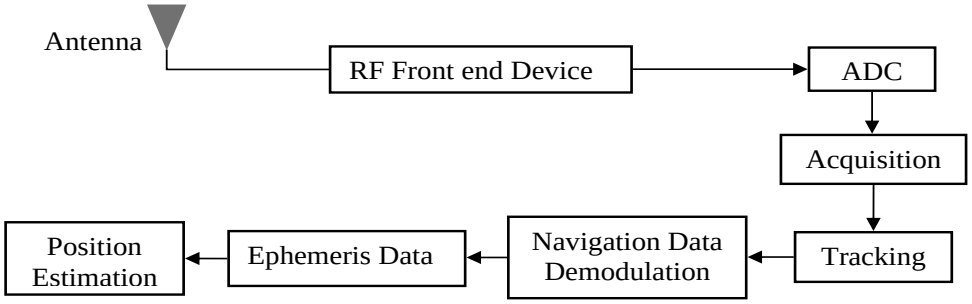

Figure 2.6: Block diagram of a typical GPS/GNSS receiver.

2.4.1 Front End Device

The Front end device is the first component after the antenna used to downconvert and digitize the received signal. The front end device consists of a chain of amplifiers and filters [7] to maintain the signal gain and allow the signals within a particular bandwidth to pass. It also uses an intermediate frequency (IF) converter which serves as a mixer to downconvert the received signal to a lower frequency so that it can be digitized by the analog-to-digital converter (ADC). A typical design of a GPS front end is shown in Fig. 2.7.

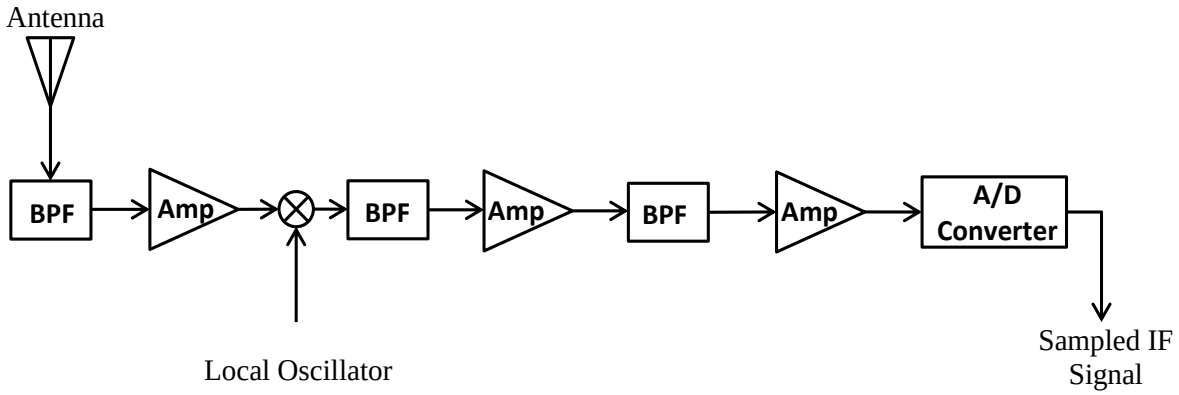

Figure 2.7: RF Front-end device.

An important factor to consider while downconverting the signal to the sampled IF signal is the sampling frequency. According to the Nyquist criteria, if the bandwidth of the input signal is Δf then the sampling frequency should be greater than $2\Delta f$. In practical applications, usually $2.5\Delta f$ is used to filter out the out-of-band signals.

2.4.2 Acquisition

Once the the signal is received in a sampled form by the front end device, the acquisition process is started to find the beginning of the PRN codes of the satellites to despread the spectrum of the received signal by correlating it with the locally generated PRN code sequence of each and every satellite present. The despreaded signal becomes continuous from which the carrier frequency can be found. An example of how despreading is done is shown in Fig. 2.8. The despreaded signal and the carrier frequency are the two parameters passed to the tracking program for further processing.

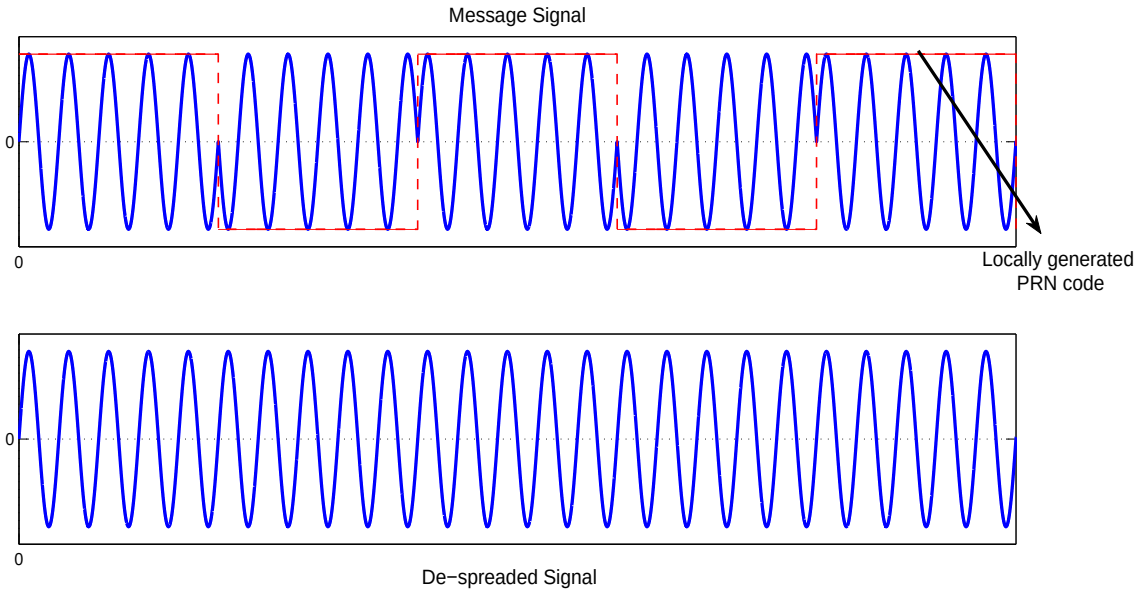

Figure 2.8: Signal de-spreading uisng locally generated PRN code.

Two factors must be considered during the acquisiton process [8]. The first is the data length used for acquisition and the second is the frequency steps in acqusition.

Data Length for Acquisition

The data length for acquisition must be selected very carefully as a long data set slows down the acquisition process although it improves the input signal-to-noise ratio (S/N_o). Conversely, a short data length may speed up the acquisition process but at the expense of reduced input S/N_o. In the case of the C/A code, a minimum of 1 ms of data can be used for acquisition [8] however longer data sets can also be used but care must be taken because the incoming signal is also bi-phase modulated by the navigation message (20 ms long) and if there is a data transition due to navigation data bit (which occurs every 20 ms), then the output will no longer be a continuous wave and the acquisition process will be degraded.

Frequency Steps in Acqusition

The frequency steps in acqusition are associated with the Doppler search space. In the case of GPS signals, the maximum Doppler search space is ± 10 kHz [8] in case of a high speed aircraft. If 1 ms of data is used for acquisition, then the frequency steps to cover the Doppler search space will be 1 kHz apart which is the reciprocal of the data length. Similarly, if 10 ms of data is used, then the frequency steps will be 100 Hz apart. For fast data acquisition, choosing the minimum permissable data length will give the best results.

2.4.3 Tracking

Acquisition provides a rough estimate of the carrier frequency and beginning of the PRN code of a particular satellite. To refine these results and extract the navigation information from the GPS signal, tracking is performed to completely remove the PRN code and to track the carrier frequency. Two loops are used for tracking; the code tracking loop and the carrier tracking loop. These two loops work simultaneously to provide code and carrier tracking in order to extract the navigation information from the received signal.

Code Tracking Loop

The code tracking loop is simple to implement compared to the carrier tracking loop as a rough estimate of the beginning of the C/A code is already known from the acquisition program. This information is then used to perform more fine and accurate correlation by generating the early, prompt and delayed versions of the acquired PRN code [7]. For this purpose, the prompt code is considered to be a perfect replica of the received signal whereas the early and late codes are the shifted versions to the left and right respectively by some samples. If a single chip of a PRN code consists of 4 samples then the correlation between the received signal and the locally generated PRN code will gradually slide down to zero, if 4 samples apart. The main idea behind the early and late gate approach also known as the DLL (Delay Locked Loop) is to find the movement of the PRN code from its maximum correlation value towards left or right due to Doppler shift. This can be best described by a correlation triangle in Fig. 2.9 where the maximum correlation between the received signal and the local PRN code is at zero position and gradually decreases to no correlation when outsampled at 4 and -4. In order to keep track of the received PRN code, the maximum correlation must be maintained to perfectly align the locally generated PRN code with the incoming signal.

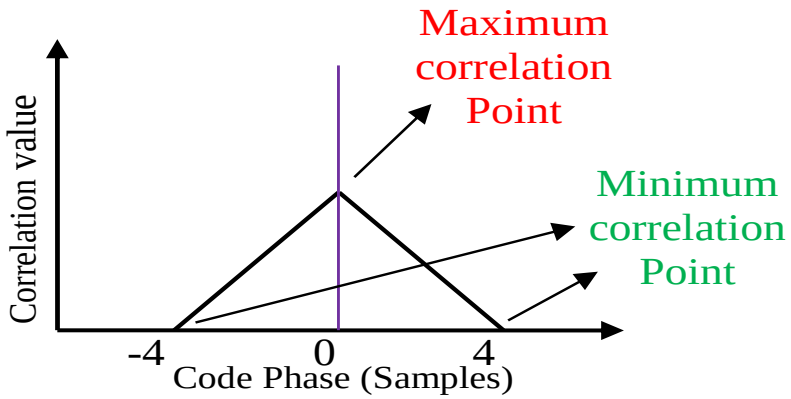

Figure 2.9: Correlation triangle.

A simple block diagram of a code tracking loop using an early and late gate approach [9] is shown in Fig. 2.10. The sampled IF signal from the acquisition program is first

converted into the in-phase (I) and quadrature (Q) components using the carrier frequency from the numerically controlled oscillator (NCO) which is initially set to the carrier frequency passed from the acquisition program, and will keep on updating itself using the frequency from the carrier tracking loop discussed in next section. Once the signal is decomposed into I and Q components, it is then multiplied with the prompt (P), early (E) and late (L) versions of the locally generated PRN code using a shift introduced by a shift register. The shift used for the early and late codes is nominally ± 0.5 chips. After the integration and the dump process, the in-phase (I_E, I_P, I_L) and the quadrature (Q_L, Q_P, Q_E) correlation outputs are then passed to the code loop discriminator to find the power difference between the early-prompt and late-prompt correlation results. The output from the discriminator is then passed to the shift register after passing through the code NCO and code generator to decide whether to introduce a shift in the generated local PRN code or not.

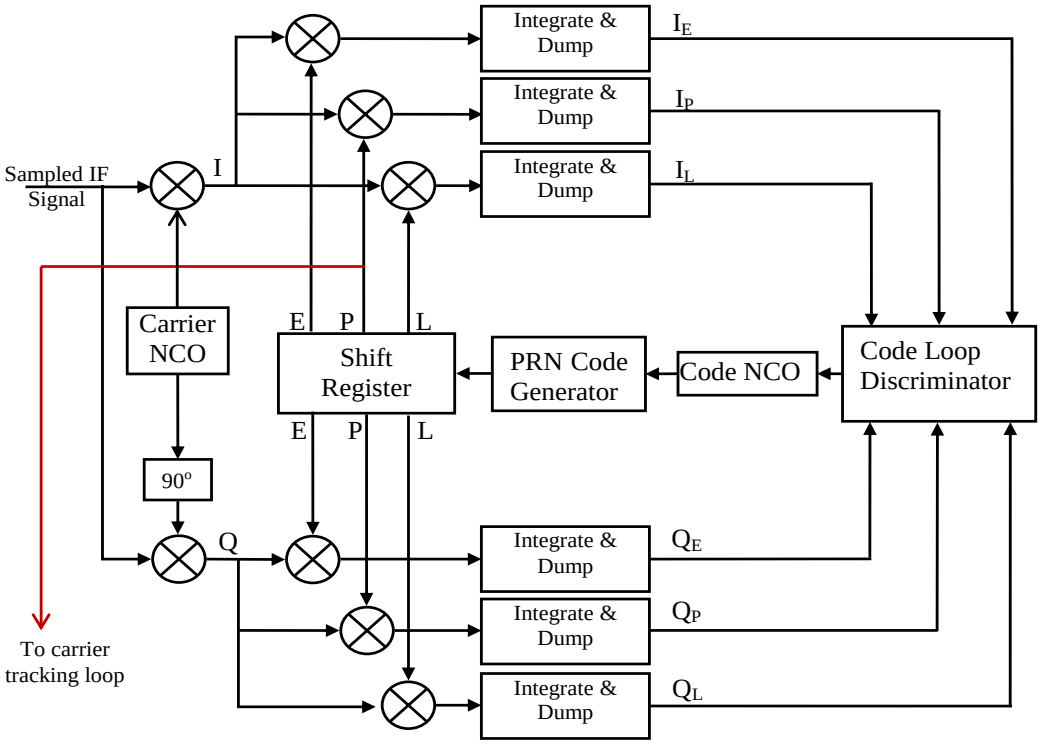

Figure 2.10: Code tracking loop.

If C_p, C_E and C_L are the correlations of the prompt, early and late codes respectively and if the locally generated prompt code is perfectly aligned with the input signal, then the

ratio C_L/C_E must be equal to one. However, in case the ratio is more than 1 or less than 1, it means that a shift must be introduced in the prompt code based on some threshold. The late-early correlation power ratio is the simplest algorithm that can be used for the discriminator output. There are several other discriminators which are also used for the decision making process. Some of them are listed in Table 2.1.

Table 2.1: Code loop discriminators

Discriminators	Description
$(I_E^2+Q_E^2)-(I_L^2+Q_L^2)$	Early minus Late power
$\frac{(I_E^2+Q_E^2)-(I_L^2+Q_L^2)}{(I_E^2+Q_E^2)+(I_L^2+Q_L^2)}$	Normalized Early minus Late Power
$I_P(I_E-I_L)+Q_P(Q_E-Q_L)$	It is more like a dot product and uses all the outputs from the discriminator for decision making

Carrier Tracking Loop

Once the PRN code is stripped off from the input signal, the carrier tracking loop receives a signal phase modulated only by the navigation data bits. In the carrier tracking loop, the sampled IF signal is first decomposed into the in-phase and quadrature components using the carrier frequency from the NCO which is initially set to the frequency derived from the acquisition stage. This is the frequency which needs to be adjusted to follow the input signal frequency. These signals are then multiplied with the prompt replica code received from the code tracking loop to remove the PRN code from the received signal which is then integrated over a certain time period and passed to the atan discriminator to calculate the phase error. A simple form of an atan discriminator is given by (2.3). The main advantage of using the atan discriminator is its insensitivity to 180^o phase shifts caused by the navigation data which occurs every 20 ms in the GPS signals. The purpose of the tracking is to keep the I component as large as possible while keeping the Q component close to zero as the I component is the one which is used to recover the navigation data. Once the navigation data is demodulated, the ephemeris data is then recovered to find the

positioning solution. A simple block diagram implementation of the Costas phase locked loop (PLL) [10] is shown in Fig. 2.11.

$$\text{atan} = \tan^{-1}\left(\frac{Q_p}{I_p}\right) \tag{2.3}$$

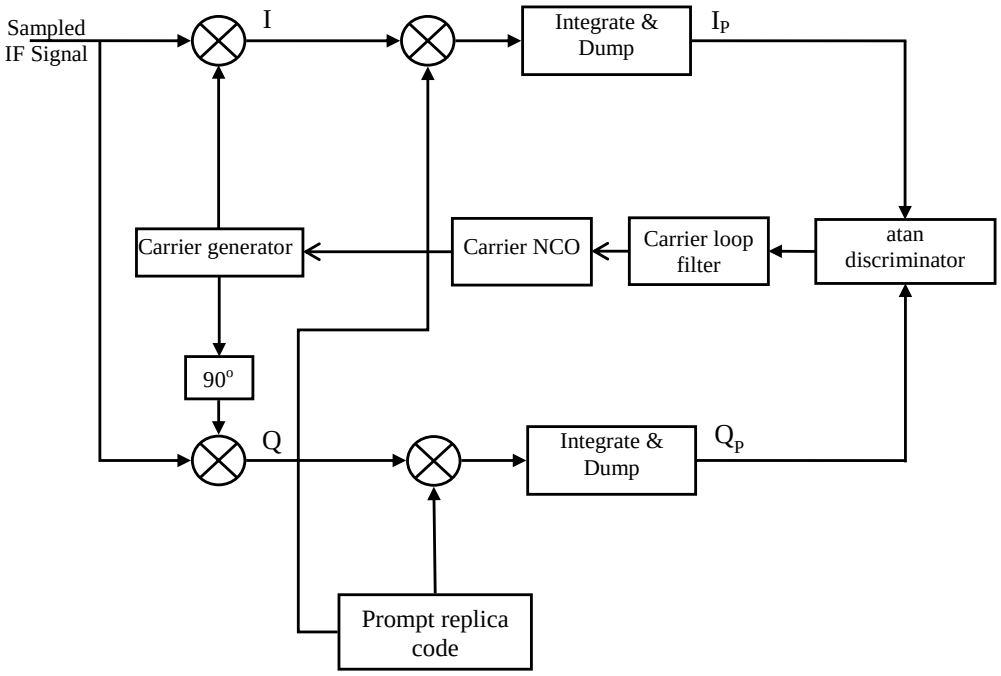

Figure 2.11: Costas carrier tracking loop.

2.4.4 Position Estimation

The position of the user can be estimated by either the pseudorange or the carrier phase [11, 12]. The pseudorange is a measure of the distance between the satellite and the receiver which contains some errors. The distance between the satellite and the receiver can be found by computing the time difference between the transmitted and the received signal. If t_{si} is the true time of transmission and t_r is the true time of reception at the receiver, the distance between the satellite and the receiver [13] can be found as

$$\rho_T = c(t_r - t_{si}) \tag{2.4}$$

where ρ_T is the true range and c is the speed of light in vacuum. It is very difficult to find the true range between the satellite and the receiver due to the several factors which introduce errors in the received signal such as the ionospheric delay, tropospheric delay, user clock error, satellite clock error etc. Thus the equation for the measured pseudorange [11, 12] will be different from the true range and can be given as

$$\rho = \rho_T + c(b - B + e + E + T + I + v_\rho) \tag{2.5}$$

where b is the receiver clock error, B is the satellite clock error, e and E are the time delay within the receiver and satellite, T is the tropospheric delay, I is the ionospheric range delay and v_ρ is the receiver noise error. A more accurate method to determine the range is through the carrier phase measurements which are potentially more accurate than the pseudorange mesurements. Mathematically, the observed carrier phase [12] can be given as

$$\phi = \frac{\rho_T}{\lambda} + \frac{c}{\lambda}(b - B + e + E + T - I + v_\phi) + m \tag{2.6}$$

where m is the phase ambiguity and v_ϕ is the phase noise. GPS uses trilateration to find the distance between the satellite and the receiver [13] where a minimum of four satellites are needed for the positioning solution. In effect, three satellies are required to find the x, y and z co-ordinates and the fourth one to determine the receiver clock error.

2.5 Sources of Errors in Position Solution

There are several factors which affects the positioning solution in a GPS/GNSS receiver [14]. Some of them are listed below.

2.5.1 Ionospheric Delay

The ionosphere is the region of the earth's atmosphere which extends from approximately 50 km to 1000 km above the earth surface. The ionospheric delay refers to the amount of delay introduced by the ionosphere to the signal passing through it. The ionosphere

changes the signal propagation group velocity which introduces range delay errors. As mentioned earlier, the subframe 4 of the navigation message contains the ionosphere delay terms which can be used in single frequency GPS receivers to reduce the positioning errors through correction of all the pseudoranges. However, in case of dual frequency receivers which can acquire both the $L1$ and $L2$ frequencies, the time delay, t_1, introduced by the ionosphere at the $L1$ carrier frequency [15] can be found as

$$t_1 = \frac{f_2^2}{f_1^2 - f_2^2}\delta(t) \tag{2.7}$$

where f_1 and f_2 are the $L1$ and $L2$ carrier frequencies and δt is the time delay between the two frequencies.

2.5.2 Tropospheric Delay

The troposphere is the bottom-most layer of the earth's surface that extends up to 50 km and consists of dry gases and water vapors. The troposphere is a non-dispersive medium for the GPS frequencies and therefore the delay introduced in both the pseudorange and carrier phase measurements is identical. The troposphere can introduce up to 2.5 m range errors at zenith and 28 m if the satellite elevation angle is below 10^o [16, 17]. The tropospheric delay (t_p) can be estimated by using the formula in (2.8) [16].

$$t_p = \frac{2.47}{\sin E + 0.0121} \quad \text{meters} \tag{2.8}$$

where E is the elevation angle.

2.5.3 Multipath

Multipath occurs when there are obstacles between the satellite and the receiver (tall buildings, trees etc) and multiple copies of the signal arrived at the receiver from different directions in addition to the direct line-of-sight path. These indirect copies of the signal may add-up destructively to degrade the receiver performance. The mulipath can introduce errors up to 10 m or more and can also result in decreased receiver sensitivity [10]. As an extra measure to reduce the multipath error, most high precision GPS receivers use

choke ring antennas which have the capability to reject the multipath signal based on its polarization. Another important method which can also reduce the multipath is the use of a dual polarized antenna which can receive both the right-hand and left-hand circularly polarized signals.

2.5.4 Satellite and Receiver Clock Errors

The satellite clocks are usually very precise and the navigation message also contains the satellite clock terms which can be used to fix the errors due to the satellite clock. The receiver clocks, on the other hand, are not as precise as the satellite clocks and therefore can introduce major errors. In order to cope with the receiver clock errors, usually it is estimated as an extra unknown term in the positioning solution in addition to the x,y and z co-ordinates and therefore a minimum of four satellites are needed for the positioning solution as mentioned in section 2.4.4.

2.5.5 Satellite Geometry/Shading

Poor relative geometrical locations of the satellite can also increase the range error. A better positioning solution can be achieved when the satellites involved in the positioning calculation are position well apart from each other. The range error due to satellite geometry is also known as the Dilution of Precision (DOP) [14]. A high value of DOP implies a poor satellite geometry which leads to more error in the positioning solution whereas a small DOP value refers to a better satellite geometry and therefore a better positioning solution.

2.5.6 Intentional degradation of the satellite signal

GPS signals used to be intentionally degraded by the U.S. Department of Defence through Selective Availability (SA). This was introduced in the C/A code available to the civilian users but, subsequently, the decision to implement this was reverted and the SA was terminated on May 1, 2000.

2.6 Signal Power Levels

The satellite geometry is one of several factors that directly affect the received signal power. The GPS satellites are 26,560 km away from the centre of the earth and placed in circular orbit. The radius of the earth is 6,357 km around the poles and 6,378 km around the equator. If we normalize and consider 6,368 km as the average radius of the earth, then the radius of the satellite orbit will become 20,192 km at zenith and the distance between the user P and the satellite will be 25,785 km ($\sqrt{26560^2 - 6368^2}$) at the horizon as shown in Fig. 2.12. This distance is different at different positions as shown in Fig. 2.12 and so is the received power. From [18], the difference between the power levels of the received signal at the horizon and at the zenith is

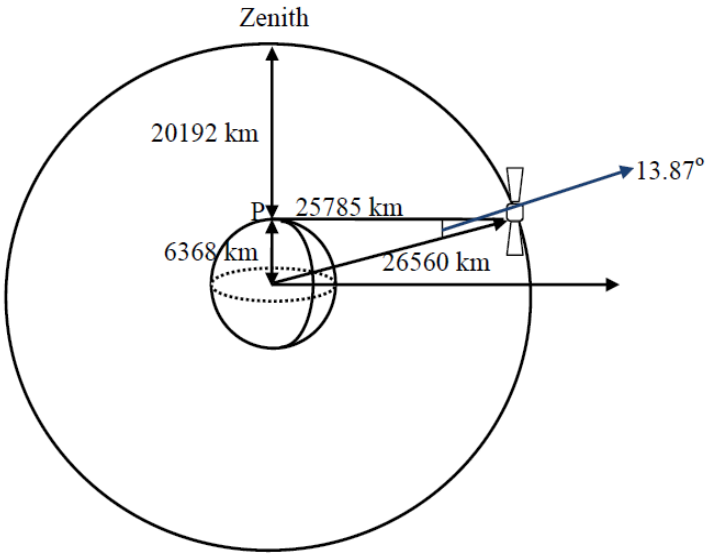

Figure 2.12: Maximum and minimumm distance between the satellite and the user [3].

$$\Delta P = 10\log\left(\frac{25785^2}{20192^2}\right) \approx 2.1\ dB \tag{2.9}$$

The difference in power loss due to satellite-earth geometry can be compensated by designing a transmitting antenna pattern so that all satellites can generate the same power level whether their distance to the surface is closest or furthest away. The strength of the signal at the receiver depends on several factors such as the power of the transmitting antenna, its beamwidth, the distance between the satellite and the receiver, the effective

area of the receiving antenna and any atmospheric losses. According to [18], the input power to the transmitting antenna is 14.3 dBW. The area A on the surface of the earth covered by the beamwidth of the transmitting antenna by an angle θ can be found as

$$A = \int_0^{\theta} 2\pi(r\sin\theta)r\, d\theta = 2\pi r^2(1-\cos\theta) \tag{2.10}$$

where θ is the satellite angle to cover the radius of the earth which is 13.87^o in an ideal case as shown in Fig. 2.12. However, it is mentioned in [18], that this angle is 21.3^o for the $L1$ signals and 23.4^o for the $L2$ signals. The gain of the antenna can be found by dividing the surface area of the sphere by (2.10) using the solid angle of 21.3^o.

$$Gain = \frac{4\pi r^2}{2\pi r^2(1-\cos\theta)} = 29.27 \approx 14.7 \text{ dBW} \tag{2.11}$$

The effective transmitted power of the satellite antenna based on the above calulation is found to be 29 dbW (14.7 dBW+ 14.3 dBW), but the transmitted power of the antenmna is listed as 26.8 dBW in [2, 18] which could be due to the transmitter power loss, cable losses or antenna efficiency. According to the Friis transmission formula, the received power can be found as

$$P_r = \frac{P_t\, A_{eff}}{4\pi R^2} \tag{2.12}$$

where R is the distance between the satellite and the user and $A_{eff} = \lambda^2/4\pi$ for a unity gain wire antenna. In case of GPS $L1$ signals, the wavelength of the received signal is 0.19 m. Using 25,785 km as the maximum distance between the satellite and the user and using 26.8 dBW as the transmitting antenna power, the received power using (2.12) will be approximately -158 dBW. This is the minimum received signal power when the satellite is furthest from the user location on the surface of the earth. This can be further reduced by 2 dB due to atmospheric loss. The received signal power is also a function of the elevation angle and is maximum when the elevation angle is 40 degrees as shown in Fig. 2.13.

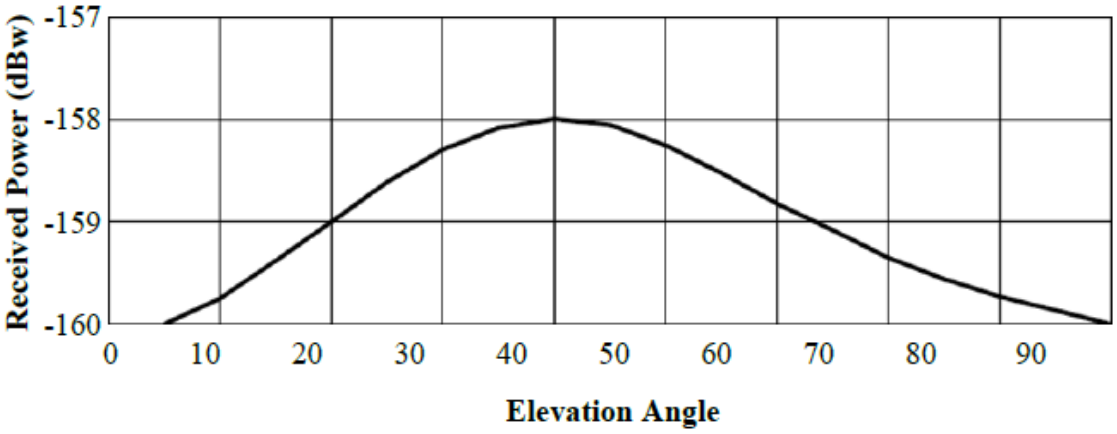

Figure 2.13: Signal power dependence on elevation [2].

The -160 dBw (-130 dBm) is the minimum received signal power at the user location including the atmospheric losses. At the input of the receiver, the thermal noise power N_i can be given as

$$N_i = kTB \tag{2.13}$$

where k is the Boltzmann's constant ($1.38 \times 10^{-23}\ J/K$), B is the bandwidth of the receiver and T is the temperature of the receiving antenna which is $290^o\ K$ under normal operating conditions. Using the above values in (2.13), the thermal noise power per MHz is

$$N_i = -174 \text{ dBm/Hz} \quad \text{or} \quad -114 \text{ dBm/MHz} \tag{2.14}$$

In the case of C/A codes with a null-to-null bandwidth of 2.046 MHz, the N_i is -111 dBm. Since the minimum received signal power is -130 dBm, it means that the GPS C/A coded signal will be 19dB (-130+111) below the noise floor or in other words the nominal value of the carrier-to-noise ratio (C/N_o) will be 44 dB (-130 + 174) under normal conditions. This nominal value of the C/N_o is used in chapter 4 in analyzing the detection performance of the different acquisition methods.

2.7 Chapter Summary

GPS based navigation is widely used worldwide due to its reliability and avaalability. There are several components involved which together makes it possible to provide the navigation services to both the civilian and military users. These components not only involve satellites at the transmitting end but also involved a number of different configuration receivers which are used to provide navigation services with minimum errors involved in the positioning solution. However, the performance of the receiver is affected by several phenomena such as the satellite geometry, acquisition and tracking models used in the receiver, position estimation algorithms, the Earth's atmosphere, satellite/receiver clock errors and multipath. In the positioning solution, these factors must be considered as they can degrade the positioning solution.

Chapter 3

Ionosphere and Scintillation

3.1 Introduction

The Earth atmosphere is filled with gases that surrounds the Earth and is therefore divided into several regions namely the troposphere, stratosphere, mesosphere, thermosphere and exosphere as shown in Fig. 3.1. The upper part of the mesosphere, the thermosphere and the lower part of the exosphere is also the extent of the ionosphere (further divided into D, E and F layers) which extends from approximately 75 km to more than 1000 km as shown in Fig. 3.1 and is formed due to ionization by solar fluxes. The name ionosphere was adopted from this well known phenomenon of ionization [19] which affects the radio waves, propagating through the ionosphere due to the presence of free electrons and electrically charged atoms and molecules.

The bottom layer, i.e., troposphere has an upper bound of 12 km and is composed of nitrogen and oxygen with percentages of 78% and 21% respectively. The remaining 1% of the troposphere is composed of other gases. Most of the weather takes place in the troposphere as it contains all the water vapors and moisture present in the earth's atmosphere. The second layer, i.e., the stratosphere extends from 12 to 50 km and also contains the ozone layer which stretches from 15 to 35 km [19]. The area between the stratosphere and the mesosphere is known as the stratopause. The mesosphere, which extends from 50 km to approximately 85 km, is also known as the middle atmosphere where the temperature decreases with increasing altitude. The area that joins the mesosphere and

the thermosphere is known as the mesopause. The fourth region of the earth atmosphere, i.e., the thermosphere, which starts from approximately 85 km and extends up to more than 600 km, is the layer which is completely free of water vapors and clouds and moslty contains the electrically charged atoms and molecules and also the free electrons which affects the radio wave propagation. The aurora borealis and the aurora australis, when they occur, are also seen in the thermosphere at high latitudes. The last region, i.e., the exosphere, also the outermost layer of the earth's atmosphere, is mostly composed of some heavier molecules such as nitrogen, oxygen and carbon dioxide and some extremely low density gases such as helium and hydrogen [19]. Some scientists do not consider the exosphere as part of the earth's atmosphere as it is almost a vacuum and most of the low orbiting communcation satellites are also located in the exosphere.

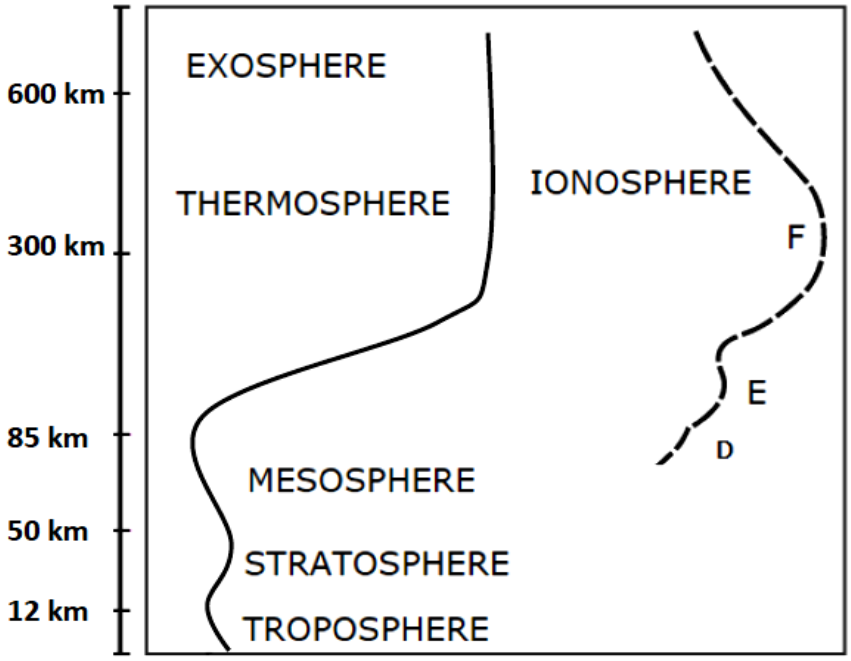

Figure 3.1: Earth's atmospheric regions.

3.2 The Ionosphere

The ionosphere which is usually conisdered as the third region from the bottom in the earth's atmosphere is mainly composed of free electrons and electrically charged atoms and molecules that affect the radio wave propagation. The height of the ionosphere starts at about 75 km and goes up to 1000 km although there are no well defined boundaries for the ionosphere as it may expand beyond 1000 km depending on the solar activity, the time of the day and seasons.

The ionosphere is an ionized medium due to the ionization process in which one or more electrons from atoms or molecules are stripped-off from their outermost shell due to high energy collision from the cosmic rays or solar radiation and become positively charged. Another phenomenon, i.e., the recombination process, also takes place in the ionosphere where the free electrons are then re-captured by positive ions. The ionization process is the main cause of signal degradation (attenuation, refraction, delay etc.) of radio waves passing through the ionosphere [20, 21]. The ionosphere is further divided into D (60-90 km), E (90-140 km) and F (200-500 km) layers as shown in Fig. 3.1. The amount of ionization in each layer varies according to the local time, being higher during the day than at night due to the increased solar activity which further divides the F layer into the F1 and F2 layers during the day. The ionization process in the D and the E layers is extremely low during the night time which results in the disappearance of the D layer while the E layer becomes weakened at night.

3.2.1 D Layer

The D layer whichc extends from 60 km to 90 km is highly dependent on the solar activity for its existence and normally affects communcation in the low or medium frequency bands and almost disappears at night.

3.2.2 E Layer

The E layer, which is directly above the D layer exists at an altitude from about 90 km to 140 km and can obliquely reflect radio waves having frequencies up to 10 MHz. The E

layer is also known as the Kennelly–Heaviside layer as it was predicted by the American engineer Arthur Edwin Kennelly and the British physicist Oliver Heaviside in 1902 and its existence was experimentally confirmed by Edward V. Appleton and Miles Barnett in 1924 [19, 22]. Sometimes, the abnormal behaviour of the E layer gives rise to a phenomenon known as the sporadic-E layer also denoted by E_s [19]. The sporadic-E layer arises when the normal level of ionization is temporarily considerably enhanced in the E layer during the peak period of the sunspot cycle and can reflect frequencies up to 200 MHz [23] but the phenomenon lasts for only a few minutes or hours. At mid-latitudes, the sporadic-E layer usually occurs during the summer, mainly in the months of May to June, whereas in the equatorial latitudes, it is mostly observed during the daytime. At high latitudes and in the polar regions, the sporadic E layer phenomenon can take place in the morning hours.

3.2.3 F Layer

The F layer which extends from about 150 km to more than 500 km, also known as the Appleton-Barnett layer, is the part of the ionosphere where the free electron density is the greatest. This layer is further divided into the F1 and F2 layers during the daytime due to increased solar activity.

3.3 Measuring the Ionosphere

There are several methods [23–26] used to measure electron density at different heights in the ionosphere such as the incoherent scatter radars, vertical sounders, in-situ measurements etc. However, the ionosonde is the most widely used method.

The ionosonde is a special radar system also known as the ionospheric sounder or chirpsounde as it utilizes the refractive properties of the ionosphere for measuring the height of each layer in the ionosphere. The technology was developed by Gregory Breit and Merle A. Tuve which was then used as a method for measuring the ionosphere in the late $1920's$ by many researchers. The ionosonde consist of a high frequency (HF) radar which usually covers the frequency range of $1-40$ MHz and a tracking receiver to track the transmitted frequency [25]. The radar send short pulses of varying frequencies

(low to high) vertically towards the ionosphere and then measure the time delay between the the transmission and the reception time to determine the height of each layer (D, E, F) in the ionosphere. A pulse will penetrate a particular layer when its transmission frequency reaches the maximum plasma frequency of that layer also known as the critical frequency. The vertical incidence critical frequencies of the ionospheric layers for the ordinary propagation modes are denoted by $f_oE, f_oF1, f_oF2, f_oEs$ [20]. The ordinary and extra-ordinary modes are determined by the $+/-$ signs in the denominator in (3.2) (below) for the refractive index of the ionosphere and correspond to the two circular/elliptical wave polarisations.

The data from the ionosondes is represented in the form of ionograms which shows the approximate height of each layer against the critical frequency. An example of how the data looks in the ionogram is shown in Fig. 3.2. In this figure the terms h'E, h'F1 and h'F2 shows the approximate heights whereas the terms foE, foF1 and foF1 shows the critical frequencies of the E, F1 and F2 layers respectively for the ordinary modes.

3.4 Variations in the Ionospheric Layers

The variations in the ionospheric layers and overall ionosphere depends on the number of free electrons present at any given time and their height distribution which usually follows seasonal, latitudinal and diurnal variations which are mainly but not exclusively determined by the solar flux and its variation. The details about these variations are discussed below.

3.4.1 Daily variations

The free electron concentration and the frequencies that are reflected by each layer are usually at a peak around noon and then gradually decrease resulting in loss of the E and F1 layers. The daily variations in the ionospheric E and F layers are graphically shown in Fig. 3.3.

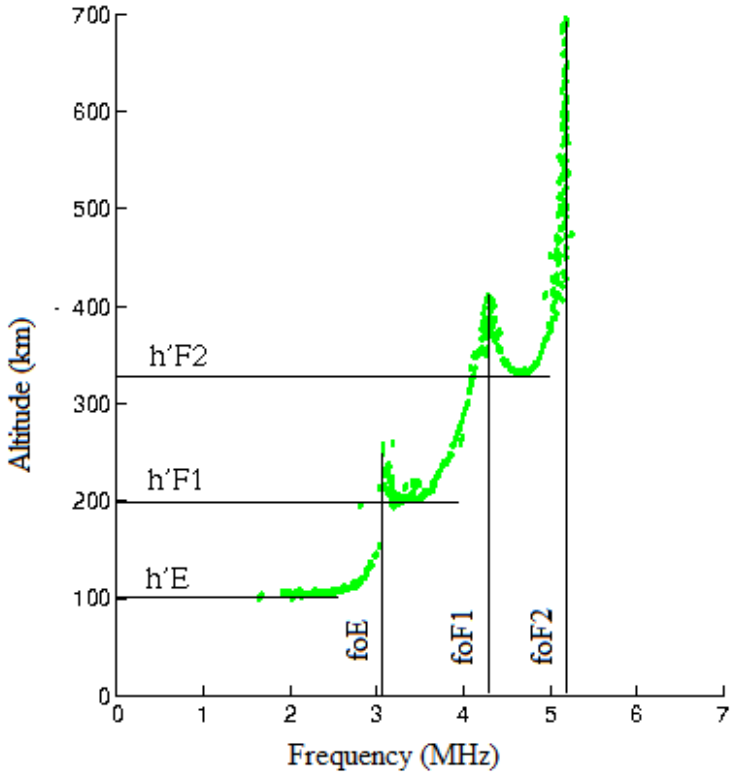

Figure 3.2: An ionogram representing the ionosonde data [27].

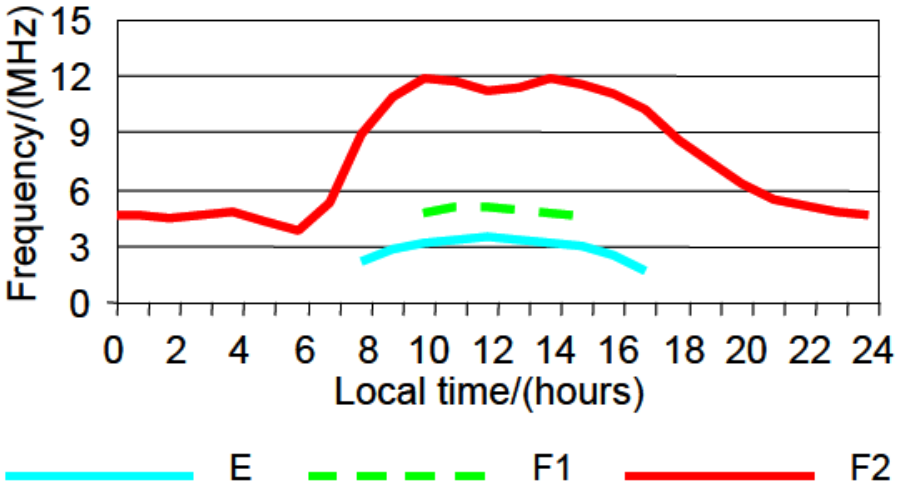

Figure 3.3: Daily variations in the maximum frequency reflected at vertical incidence from the ionospheric layers [25].

3.4.2 Seasonal variations

The summertime increase in the ionospheric layers is greater than winter specially from March to September due to the production of more free electrons during the daytime [25]. This phenomenon is true during the solar minimum period but during the solar maximum period, the reverse phenomenon takes place and the electron concentration is greater in the winter than summer also known as the winter anomaly [19].

3.4.3 Latitudinal Variations

The latitudinal variations also result in the increase or decrease in the height of the ionospheric layers and the frequencies that reflect from each layer. The maximum frequencies reflected by each ionospheric layer decrease with increasing latitude as the day gradually moves towards the night. This is due to the production of less free electrons which results in the D and the E layers becoming invisible. The latitudinal variations in the E and the F layers are shown in Fig. 3.4. There is an equatorial anomaly region as well where the daytime F region peak frequencies occur at around $\pm 20^o$ from the magnetic equator rather than at equator [25].

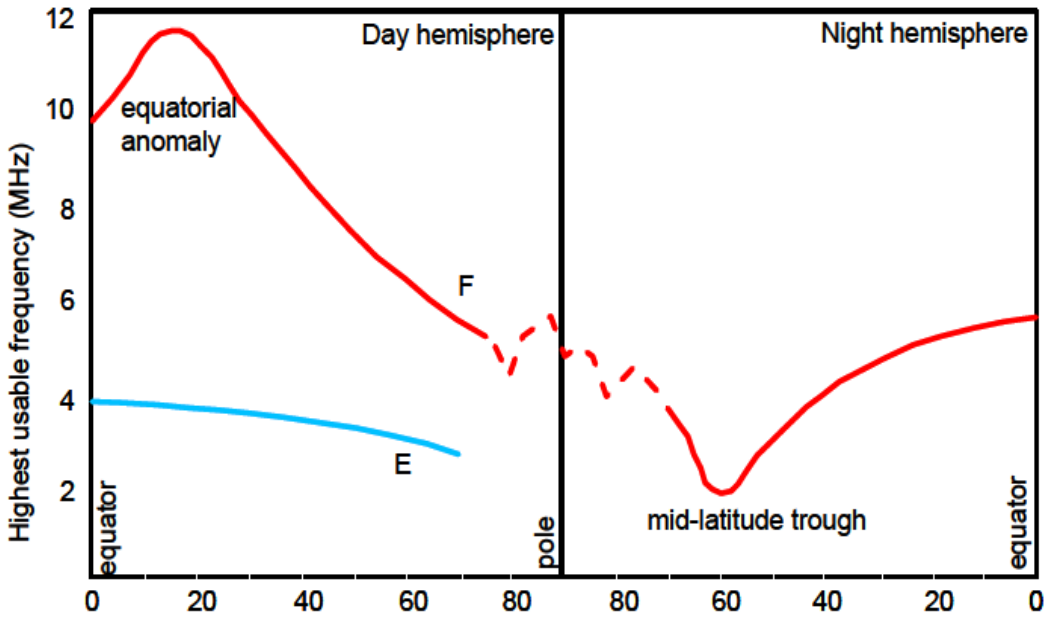

Figure 3.4: Latitudinal variations in the Ionospheric layers [25].

3.4.4 Variations based on Solar activity

The density of free electrons in the ionosphere normally follows on average the solar cycle which lasts about 11 years. A relationship between the solar activity based on the sunspot number and the variations in the frequencies that can be reflected by the E and the F layers over Canberra, Australia (35.3075^o S, 149.1244^o E) from 1988 to 2005 is shown in Fig. 3.5. It can be seen that there is no major change in the E and the F1 layer frequencies, the main variation being between the day and night time activity. However, the F2 layer shows a great variation of maximum reflection frequencies (foF1 and foF2) with respect to increasing and decreasing solar activity.

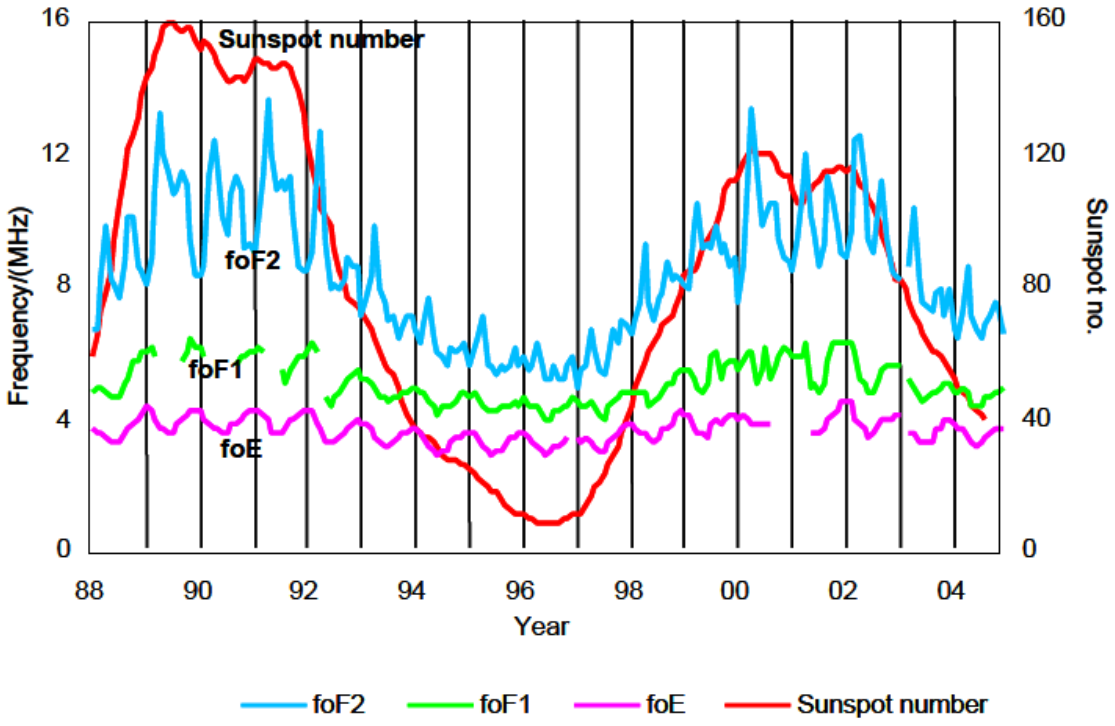

Figure 3.5: Variations in the ionospheric layers based on the solar activity [25].

3.5 Ionospheric Delay and the Total Electron Content

The navigation satellites (such as GPS) are placed in the medium earth orbit (MEO) having an approximate altitude of 20,000 km from the earth's surface. The signals from these satellites may suffer refraction and diffraction while propagating through the ionosphere.

Most of the navigation satellites uses the frequency bands which are high enough to penetrate the ionosphere. However, the signals while passing through the ionosphere incur delays depending on the electron density along the path from the satellite to the receiver which can be approximated using the total electron content (TEC).

The ionospheric TEC can be defined as the total number of free electrons present per square metre cross-section along a signal path between, for example, a satellite transmitter and a ground receiver. The amount of delay incurred from day to day depends on the changes in the Earth's atmosphere and sun-spot activity and is increased when the ionosphere has a higher electron concentration. The delay is also frequency dependent due to the dispersive nature of the ionosphere where the delay is greatest at the lower frequencies compared to the higher frequencies [28]. There are several models which are used to correct the range errors introduced by the ionosphere. Some of the most commonly used models are: Klobuchar Model [29]; the NeQuick Model [30] developed by the Aeronomy and Radiopropogation Laboratory of the Abdus Salam International Centre for the Theoretical Physics in Italy and the University of Graz, Austria; the International Reference Ionosphere (IRI) model [31] developed by the joint working group of the Committee on Space Research (COSPAR) and the International Union of Radio Science (URSI); GAIM (Global Assimilative Ionospheric Model) [32] originally developed in 1999 sponsored by the U.S Department of Defence; and Multi-Instrument Data Analysis System (MIDAS) Model [33] developed by the University of Bath in 2001.

3.6 Wave Propagation through the Ionosphere

The ionosphere is a dense medium of free moving electrons [24, 34, 35] which not only affects the signal properties but also results in refraction. The amount of refraction introduced by the ionosphere can be found through the change in the refractive index. The refractive index of a medium can be defined as the measure of the amount of refraction introduced by a medium to a signal passing through it. An example of the refraction introduced in the signal when it enters from one medium to another is shown in Fig. 3.6.

According to Snell's law, the refractive index (n) of a medium can be found through the angle of incidence and the angle of refraction using (3.1):

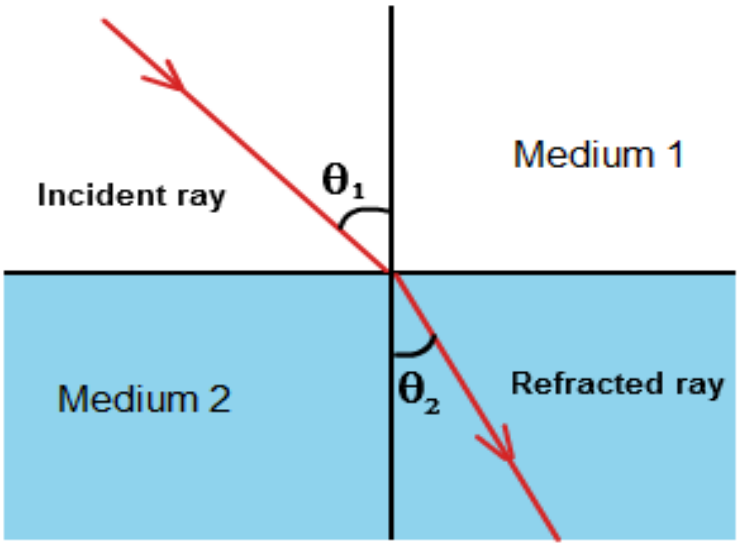

Figure 3.6: Snell's law to define the wave propagation in two different mediums.

$$\frac{\sin\theta_1}{\sin\theta_2} = \frac{v_1}{v_2} = \frac{n_1}{n_2} \tag{3.1}$$

where θ_1 is the angle of incidence in Medium 1, θ_2 is the angle of refraction in Medium 2, n_1 is the refractive index of Medium 1, n_2 is the refractive index of Medium 2, v_1 is the velocity of the light in Medium 1 and v_2 is the velocity of light in Medium 2. In the case of ionosphere, the refractive index is variable which depends mainly on the vertical variation of the electron density profile. From [36], the refractive index of the ionosphere can be given as

$$n_{ion}^2 = 1 - \frac{X}{1 - \frac{Y^2\sin^2\theta}{2(1-X)} \pm \frac{1}{2(1-X)}\cdot\sqrt{Y^4\sin^4\theta + Y^2\cos^2\theta(1-X)^2}} \tag{3.2}$$

where,

$$X = f_p^2/f^2, \qquad Y = f_H/f$$

$$f_p^2 = \frac{N_e e^2}{4\pi^2 \varepsilon_0 m_e}, \qquad f_H = \frac{B \mid e \mid}{2\pi m_e}$$

where f_p is the plasma frequency , f is the wave frequency, B is the magnitude of the magnetic field vector, θ is the angle between the wave and the magnetic field vector B, ε_0 is the permittivity of free space, e is the charge of an electron, m_e is the mass of an electron and N_e is the electron density. There are several approximations of (3.2), one such approximation adopted from [37] is given in (3.3) where the phase refractive index of the ionosphere can be represented in the form of increasing function of the wave frequency, f, using

$$n_{ion} = 1 - \frac{C_X}{2} N_e f^{-2} \pm \frac{C_X C_Y}{2} N_e B \cos\theta f^{-3} - \frac{C_X}{8} N_e^2 f^{-4} \tag{3.3}$$

where

$$C_X = \frac{e^2}{4\pi^2 \varepsilon_0 m_e}, \qquad C_Y = \frac{\mu_0 e}{2\pi m_e}$$

The last two terms in (3.3) are orders of magnitude smaller than the second term in (3.3) therefore neglecting the last two terms, (3.3) can be reduced to

$$n_{ion} = 1 - \frac{C_X}{2} N_e f^{-2} \tag{3.4}$$

Equation (3.4) can be used to determine the phase refractive index of the ionosphere. The group refractive index can be obtained by differentiating (3.4) (see [37] for further explanation). Equation (3.4) can be further simplified by putting in the constant values:

$$n_{ion} = 1 - 40.31 \frac{N_e}{f^2} \tag{3.5}$$

From [38], the ionospheric delay between the satellite and the receiver can be estimated by taking the difference between the measured range $s = \int_{rx}^{sat} n_{ion} ds$ and the geometric range s_0. The s_0 can be obtained by assuming that there is no ionosphere so that the

refractive index is one along the whole path. Taking the difference between the measured and the geometric range, the ionospheric delay can be given as

$$\rho = \int_{rx}^{sat} n_{ion} ds - \int_{rx}^{sat} ds_0 \tag{3.6}$$

where the integral $\int_{rx}^{sat}$ represents the satellite to receiver path. Using (3.5) into (3.6), the range delay can be given as

$$\rho = -\frac{40.31}{f^2} \int_{rx}^{sat} N_e ds + \int_{rx}^{sat} ds - \int_{rx}^{sat} ds_0 \tag{3.7}$$

where $\int_{rx}^{sat} ds - \int_{rx}^{sat} ds_0$ represents the difference between the measured and the geometric range and is also deonted as the curvature effect [37]. If it is assumed that the integrals in (3.7) are evaluated along the geometric path s_0, then the curvature effect can be neglected and (3.7) will become

$$\rho = -\frac{40.31}{f^2} \int N_e ds_0 \tag{3.8}$$

where $\int N_e ds_0$ represents the TEC between the satellite and the receiver path measured in TECU (1 TECU $= 10^{16}$ $electrons/m^2$). Assuming a slant path between the satellite and the receiver, (3.8) can be transformed to

$$\rho = -\frac{40.31}{f^2} \text{STEC} \qquad \text{metres} \tag{3.9}$$

where STEC is the slant TEC. Using (3.9), the ionospheric delay can be estimated using the phase measurements. For pseudorange measurements, the negative sign will change to positive as the free electrons reduce the group velocity but increase the phase velocity [37]. A complete derivation of the delay using the pseudorange measurements can be found in [37].

3.7 Ionospheric Scintillations

The ionosphere is not only a refractive medium but is also a highly ionized medium where plasma instabilities can give rise to a phenomenon known as the electron density irregulari-

ties. These irregularities casuses amplitude and phase fluctuations in the transionospheric signals which can degrade the signal quality and may result in loss of information content [39–41]. The amplitude and phase fluctuations due to these time varying electron density irregularities are known as the ionospheric scintillations. The fluctuations in the phase/amplitude are also termed phase/amplitude scintillation respectively. The amplitude scintillation is denoted by the S_4 index whereas the phase scintillation is quantified by the σ_ϕ index.

The scintillation effects are different at different latitudes and occur predominantly in the auroral regions and polar caps and between +20 and -20 degrees geomagnetic latitude particularly around the equatorial anomaly regions [42–44]. At high latitudes, phase scintillation is more dominant compared to the amplitude scintillation due to the auroral phenomena [45, 46] whereas at low latitudes, the amplitude scintillation has more severe affects on the transionospheric signals due to the instabilities in the ionosphere F-layer [42, 47, 48].

The equatorial scintillations are both longitudinal and seasonal dependent and are high during the equinox (between April to September) in the Pacific regions while low in the American, African and Indian regions during these months [46]. By contrast, the reverse happens from the mid of September to the end of March. The instabilities in the F-region during the evening hours give rise to the equatorial spread-F phenomenon [35, 47, 48] where the recombination in the E and the F1 layers is faster than the topside F-layer which results in the formation of the low density plasma bubbles which move towards the upside denser region and due to the increase in the vertical plasma velocity results in the formation of the irregularity regions of the order of 300 m or less in size which cause the scintillation at L-band frequencies. These low density bubbles form the irregularity patches which can travel up to 2000 km along the magnetic field lines towards the north and the south and can accumulate to produce stronger scintillation effects in the equatroial anomaly regions ($\pm 20^o$) than at the equator. The scintillation at L-band frequencies can also occur during the daylight hours which can be due to the presence of a sporadic-E layer but this effect is less common compared to the spread-F phenomenon.

At high latitudes, the scintillation is produced due to the irregularities which are asociated with the polar cap patches and auroral phenomena which is at peak during a geomagnetic storm or increased solar acitivity [45, 46, 49]. Compared to the equatorial scintillations, the auroral and polar scintillations can occur at any time of the day having a duration of a few hours or several days.

3.7.1 Measuring Ionospheric Scintillation using a GNSS/GPS Receiver

At low latitudes ($\pm 20^o$ geomagnetic latitude), amplitude scintillations are more dominant and the GNSS/GPS signal passing through the ionosphere may suffer small angle scattering due to the equatorial spread-F. The scattered signal at the receiver may add destructively to produce deep power fades. If the power fades are frequent and of sufficient time duration, the GNSS/GPS signal may fall below the lock threshold and be considered absent at the receiver [50–52]. The minimmum received power of a GPS $L1$ C/A coded signal is -130 dBm. The atmospheric attenuation path loss accounts for less than 2 dB in the worst case [53]. The polarization mismatch loss is 3.4 dB [53]. Imperfect correlation may lead to a 1 dB loss. Troposphere errors are often small and can be mitigated using the already existing models such as Hopfield model. All the above mentioned factors add up to a maximum of 5 to 6 dB loss based on the satellite elevation angle and have no significant effects on the GPS receiver performance because the signals are still much higher than their minimum power level of -130 dBm [53]. However, the loss due to the ionospheric scintillation can be a big problem as the amplitude scintillation can introduce up to 20 dB fading at L-band frequencies. The fading due to ionospheric scintillation depends both on the geographic location and time of the day and follows the maxima and minima of the solar cycle. Worldwide fading variations at L-band frequencies are well shown in Fig. 3.7 for the solar maxima and minimum periods [54, 55]. Two regions are vulnerable to the L-band fading. i.e., high latitutde (auroral and polar zones) and low latitude regions ($\pm 20^o$ geomagnetic latitude). Low-latitude scintillation poses greater impact on the GPS signals where fading of up to 20 dB [54] may occur after sunset during the peak period of the solar cycle (left in Fig. 3.7) whereas it is less than 5 dB during the solar minimum period (right in Fig. 3.7). At high latitudes, fading is not significant and can only reach up to a

maximum of 5 dB during the peak period of the solar cycle and is almost negligible during the solar minimum period.

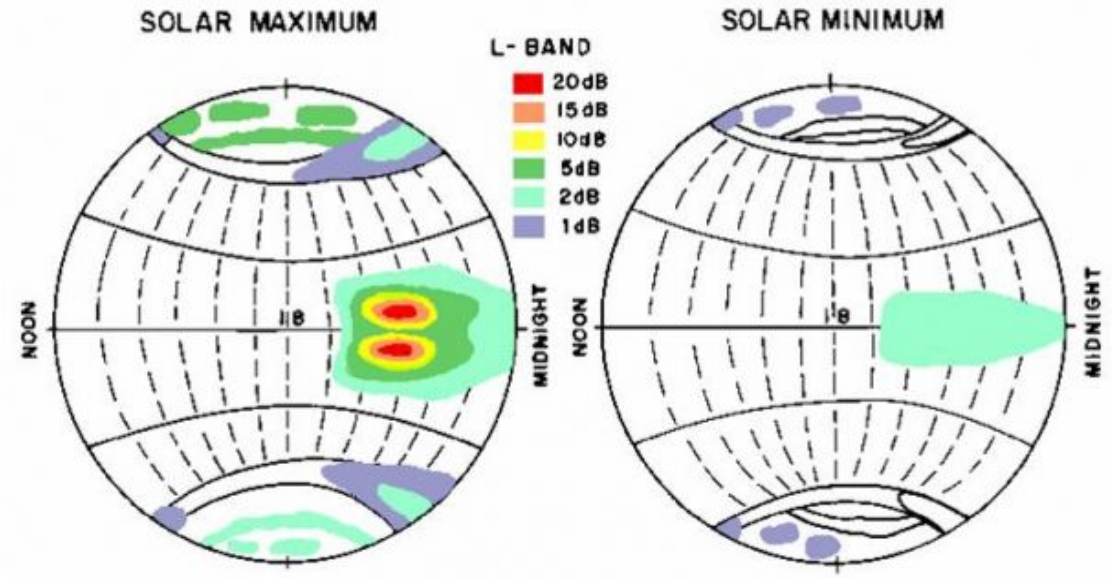

Figure 3.7: L-band fading due to scinitillation at high and low latitude regions during solar maximum and minimum [55].

A simplified mathematical form of a GNSS signal modulated by a PRN code sequence $c(t)$ without scintillation can be given as

$$s(t) = A\ d(t)c(t)\cos(\omega t + \phi) + n(t) \tag{3.10}$$

where A is the signal amplitude, $d(t)$ is the navigation information, ω is the carrier fequency and $n(t)$ is the noise. If there are amplitude and phase fluctuations in the signal due to scintillation, (3.10) can be re-written as

$$s(t) = A.\delta A d(t)c(t)\cos(\omega t + \phi + \delta\phi) + n(t) \tag{3.11}$$

where δA is the amplitude fading due to amplitude scintillation and $\delta\phi$ are the phase fluctuations due to phase scintillation. The probability density function (PDF) of the phase scintillations can be modelled as a zero mean Gaussian PDF [56]:

$$p(\delta\phi) = \frac{1}{\sqrt{2\pi}\sigma_\phi} e^{-\delta\phi^2/2\sigma_\phi^2} \tag{3.12}$$

where σ_ϕ is the phase scintillation index which is the square root of the standard deviation of the $\delta\phi$ over a certain time interval, generally 60 s. The fading due to amplitude scintillation, on the other hand, can be modeled as a Nakagami-m distribution [57]:

$$p(\delta I) = \frac{m^m \delta I^{m-1}}{\Gamma(m)\ \langle\delta I\rangle^m} e^{-m\delta I/\langle\delta I\rangle}, \quad \delta I \geq 0 \tag{3.13}$$

where $\delta I = \delta A^2$ is the intensity of the scintillated signal, $\Gamma(.)$ is the Gamma function and m is the strength of the scintillation activity given as

$$m = \frac{[E(\delta I)]^2}{E[\delta I^2] - (E[\delta I])^2} = \frac{1}{S_{4T}^2} \tag{3.14}$$

where $E[]$ is the expectation value and S_{4T} is the ampltiude scinitillation index and should be less than $\sqrt{2}$ according to the properties of the Nakagami-m distribution. From (3.14), the S_{4T} index can be defined as the normalized standard deviation of the signal intensity given by

$$S_{4T} = \frac{\sqrt{E[\delta I^2] - (E[\delta I])^2}}{E(\delta I)} \tag{3.15}$$

It should be noted that the S_{4T} index contain the effects of ambient noise.The amplitude scintillation due to the ambient noise [40] can be given as

$$S_{4N_o} = \sqrt{\frac{100}{S/N_o}\left[1 + \frac{500}{19S/N_o}\right]} \tag{3.16}$$

The overall S_4 also known as the corrected ampltiude scintillation index can be obtained by subtracting (3.16) from (3.15):

$$S_4 = \sqrt{\frac{E[\delta I^2] - (E[\delta I])^2}{[E(\delta I)]^2} - \frac{100}{S/N_o}\left[1 + \frac{500}{19S/N_o}\right]} \tag{3.17}$$

From (3.17), it is clear that the estimation of the S_4 index requires the computation of the scintillation intensity (δI) and the S/N_o. Both of these parameters can be calculated by using the in-phase and the quadrature components of the tracked signal, once the signal is locked by the tracking loop. From [40], the signal intensity, δI, can be given as

$$\delta I = \frac{(NBP - WBP)}{(NBP - WBP)_{LPF}} \tag{3.18}$$

where NBP is the narrow band power, WBP is the wide band power and LPF is the low pass filtered signal. The NBP and the WBP can be given as

$$NBP = \left(\sum_{k=1}^{N} i_k\right)^2 + \left(\sum_{k=1}^{N} q_k\right)^2 \tag{3.19}$$

$$WBP = \sum_{k=1}^{N} \left(i_k^2 + q_k^2\right) \tag{3.20}$$

where i and q are the in-phase and quadrature components respectively of the received signal and N is the summing length which usually equals to the length of the navigation data bit. In the case of GPS $L1$ C/A coded signals, N is taken as 20 ms and the standard deviation of the signal intensity is computed over one minute for estimating the S_4 index. The WBP can also be used to find the C/N_o which can then be converted to S/N_o. The C/N_o can be found as

$$C/N_o = 10\log\left[\left(\frac{\text{WBP}}{N} - 1\right) \times 50\right] \tag{3.21}$$

3.7.2 Scintillation Models

There are several methods which are used to model the ionospheric scintillation activity such as the Wide Band ionospheric scintillation model (WBMOD) [58] and the Global

Ionospheric Propagation Model (GIM) [59]. These models consists of an ionospheric model, which provides the model of the background ionosphere and the embedded ionospheric irregularities, and a propagation model to determine the effects of the scintillation on the transmitted signals. The WBMOD is the most widely used scintillation model developed by the researchers at the Northwest Research Associates, Inc. (NWRA) and incorporates a worlwide climatology of the scintillation producing ionospheric irregularities. The WBMOD provides the amplitude and phase scintillation indices at a given time and location, spectral index of phase (p), spectral strength of phase (T) and also the occurence statistics.

The deterministic and random phase screen models are also widely used to demonstrate the effects of ionospheric irregularities on the transionospheric signals [60]. These models are based on the Fresnel-Kirchoff diffraction theory and assume that the irregularities are concentrated in a thin layer (phase screen) whose height is equivalent to the peak height of the F2 layer (i.e., 350 to 400 km). In the deterministic phase screen model, the irrgularities are considered as discrete lenses alighned along the earth's magentic field lines. The phase purturbations produced by k such lenses [61] can be given as

$$\Phi(x) = \sum_{i=1}^{k} \Phi_{oi}\, exp\left[\frac{-(x-x_{0i})^2}{l_i^2}\right] \tag{3.22}$$

where Φ_{oi} is the peak phase variations, l_i is the size of the irregularities, x_{0i} is the centre of the irregularities and x is the horizontal position normal to the earth's magnetic field lines. The peak phase variations, Φ_{oi}, in (3.22) includes both the diffraction and the refraction effects and can be calculated through the rate of change of TEC (ΔTEC) which could be both positive (enhancements in TEC) or negative (depletion in TEC).

$$\Phi_{oi} = 40.3 \times 2\pi \frac{\Delta TEC}{cf} \qquad \text{radians} \tag{3.23}$$

where f is the wave frequency. The peak phase variations in (3.23) will occur due to the maximum TEC variations. A more realistic model to determine the effects of scintillation producing ionospheric irregularities on the signals passing through the ionosphere is the power law phase screen model. This model assumes that the emergent phase perturbations

in the received signal, resulting from passing through the phase screen, are random with a Gaussian distribution whose amplitude and phase power spectra [62] can be given as

$$\Phi_I(q) = \Phi_\phi(q)\sin^2\left(\frac{q^2 r_F^2}{8\pi}\right) \tag{3.24}$$

$$\Phi_P(q) = \Phi_\phi(q)\cos^2\left(\frac{q^2 r_F^2}{8\pi}\right) \tag{3.25}$$

where q is the horizontal wave number across the phase screen, ϕ represents the phase deviations and $r_F = \sqrt{2\lambda r}$ is the Fresnel radius where r is the distance between the phase screen and the observer and it is assumed that this is a much smaller distance than that between the satellite and the ionosphere. The $\Phi_\phi(q)$ in (3.24) and (3.25) is the power spectrum of the phase screen and from [62] can be given as

$$\Phi_\phi(q) = \frac{C_s}{(q^2 + q_0^2)^{-p/2}} \tag{3.26}$$

where C_s determines the strength of the scintillation activity, $q_0 = 2\pi/l_0$ where l_0 is the outer scale size of the irregularities and p is the spectral index.

3.8 Chapter Summary

The earth's atmosphere is a major factor which affects the performance of the satellite-based navigation systems (GPS/GNSS). The earth's atmosphere consists of several layers such as the stratosphere, troposphere ionosphere and exosphere. Most of these layers do not have a significant impact on the satellite-based navigation as the pre-developed models used in the positioning solution are used to minimize the errors within the pre-defined limit. However, the ionospheric scintillation introduces amplitude and/or phase fluctuations in the transionospheric signals due to the time varying electron density irregularties and therefore can result in reduced S/N_o or loss of lock at the receiver. In this chapter, a complete morphology of ionospheric scintillation and its effects on transionospheric signals has been discussed and it has also been discussed that how the effects of the scintillation producing ionospheric irregularities can be modelled.

Chapter 4

Scintillation Effects on GNSS/GPS Receivers

4.1 Introduction

Ionospheric scintillation (amplitude and phase) is the main cause of degraded receiver performance specifically affecting the signal acquisition and tracking due to rapid random fluctuations in the amplitude and/or phase of the received signal. The amplitude scintillation can results in deep and frequent power fades of a few milliseconds up to several hours which may cause the signal level to drop below the lock threshold and hence it can be considered absent at the receiver. The other possible implication of amplitude scintillation can be a reduced detection performance in terms of the probability of detection (P_d). There are several acquisition methods [63, 64] which are used to increase the detection performance of a GPS/GNSS receiver by using a combination of coherent and non-coherent integrations [65]. The phase scintillation, on the other hand, is mainly responsible for loss of lock in the tracking loop due to cycle slip [50]. To avoid loss of lock, several tracking loop designs such as the phase locked loop (PLL), frequency locked loop (FLL), FLL-assisted PLL etc. are used for robust GNSS/GPS signal tracking as discussed in [66–68].

In this chapter, the amplitude and phase scintillation effects on the GPS receiver acquisition and tracking are analyzed and discussed. At acquisition stage, a new acquisition method known as the Repetitive Block Acquisition (RBA) [69] is proposed whose per-

formance is compared with the conventional FFT-based circular correlation method and the zero padding method. At the tracking stage, the scintillation effects on GPS tracking loops in terms of loss of lock are discussed by estimating the tracking error variance of 2nd and 3rd order PLL's and a mathematical derivation is given for estimating the tracking thresholds beyond which loss of lock occurs. A case study is also carried out by implementing the PLL and FLL-assisted PLL tracking loop designs using the simulated GPS signals containing scintillation effects to determine how the loss of lock occured and how it affects the carrier phase information and navigation data. Furthermore, a wavelet-based denoising technique is also used in the PLL and FLL-assisted PLL tracking loop designs to come up with a more robust design for these loops to reduce the carrier phase error of a tracking loop.

4.2 Acquisition Methodologies

Several methods are used for acquisition in a GPS receiver such as the serial search method, the parallel FFT–based circular correlation, data folding method and the Zero Padding (ZP) method [63, 64, 70]. However, the FFT-based circular correlation method is the most commonly used acquisition method due to its high detection performance whereas the ZP method is considered to be the fastest method for acquiring weak signals [63, 70]. In the next sections, these two methods are discussed in detail and the performance is compared with the newly designed RBA method.

4.2.1 Parallel FFT-based Circular Correlation Method

The FFT-based circular correlation method [63] uses a two dimentional search strategy to find the frequency and code phase of the received signal. Here frequency means the acquired frequency of the received signal and code phase means the starting point of the PRN code of an acquired satellite in the received signal. The mathematical form of the GPS $L1$ C/A coded signal can be given as

$$s(t) = A\, d_\tau(t)\, c_\tau(t) \times \cos(2\pi(f_{L1} + f_d)t + \theta) + n(t) \tag{4.1}$$

where A is the signal amplitude, $d_\tau(t)$ is the navigation data bit at 50 Hz, $c_\tau(t)$ is the C/A code, τ is the unknown code phase shift, f_{L1} is the $L1$ carrier frequency of the received signal, f_d is the unknown Doppler shift, θ is the phase of the received signal and $n(t)$ is the noise in the received signal. The received signal is first downconverted to an IF signal by mixing with the local oscillator signal and then passed through the ADC to produce the sampled version of the signal given by

$$s_{IF}[n] = A\, d_\tau[n]\, c_\tau[n] \times \cos(2\pi(f_{IF} + f_d)nT_s + \Delta\theta) + n_{IF}[n] \tag{4.2}$$

where f_{IF} is the frequency of the downconverted signal, T_s is the sampling interval, $n =$ 0, 1, 2, ..., $N$are the signal samples, $n_{IF}[n]$ are the noise samples and $\Delta\theta$ is the phase difference between the incoming signal and the reference oscillator signal after the IF stage. The IF signal is then passed to the acquisition algorithm for correlating with the locally generated C/A coded signal. We used the FFT-based circular correlation method for performing the correlation [63]. A simple block diagram of the FFT-based circular correlation method is shown in Fig. 4.1.

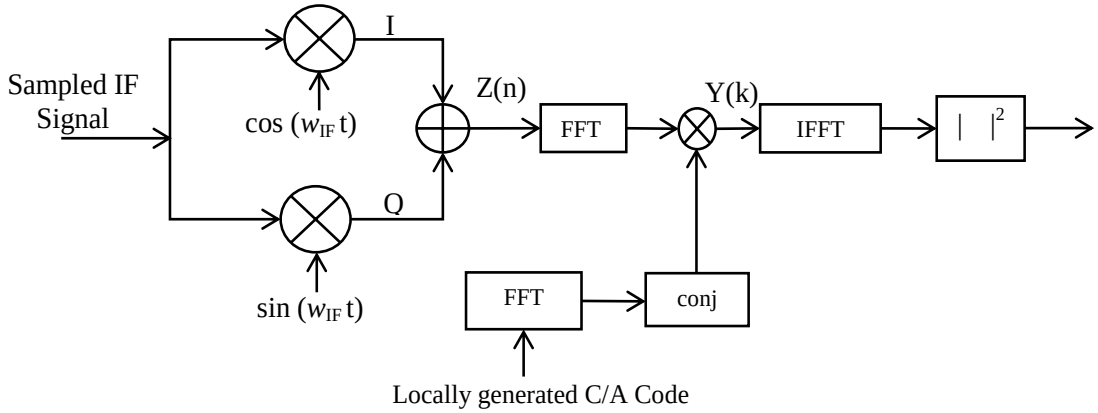

Figure 4.1: Block diagram of the FFT-based circular correlation method.

In order to perform correlation, the downconverted IF signal is first multiplied with the reference sine and cosine signals for carrier removal to produce the in-phase and quadrature components given as

$$s_I = Ad_\tau[n]c_\tau[n]\cos(2\pi f_d nT_s + \phi) + n_I[n] \tag{4.3}$$

$$s_Q = Ad_\tau[n]c_\tau[n]\sin(2\pi f_d nT_s + \phi) + n_Q[n] \tag{4.4}$$

where ϕ is the phase offset and $n_I[n]$ and $n_Q[n]$ are the in-phase and quadrature noise terms and are treated as Gaussian white noise in the acquisition program with zero-mean and variance σ^2 ($n_I[n], n_Q[n] \sim N(0, \sigma^2)$). The in-phase and quadrature signals are then combined together to produce a complex signal ($z(n)$) which is then converted to the frequency domain by taking the FFT. For circular correlation, the FFT of the incoming complex signal ($z(n)$) is then multiplied with the conjugate FFT of the locally generated C/A coded signal. The mathematical form of the C/A coded signal can be given as

$$c_{\hat{\tau}} = c_{\hat{\tau}}[n] = \sum_{k=-\infty}^{+\infty} q_{k,N_c} \prod(nT_s - kt_c) \tag{4.5}$$

where q_k is the locally generated PRN code sequence with N_c chips, $\prod$ is the rectangular function, t_c is the chip duration and $\hat{\tau}$ is the actual start time of the PRN code. The result of the multiplication between the FFT of the complex incoming signal and the conjugate FFT of the local C/A code is then converted to a time domain signal by performing the inverse FFT (IFFT) and then the absolute is taken to complete the correlation process. If a peak is found crossing a certain threshold, the signal is said to be present and the index of the peak value will mark the beginning of the C/A code in the incoming signal. The same process must be repeated for all the visible satellites to complete the acquisition process.

The FFT-based method explained above was used to acquire real GPS signals using the experimental setup shown in Fig. 4.2. The received signals were downconverted at an IF of 1.25 MHz and sampled at 5 MHz (1 ms = 5000 code phase samples) using the universal software radio peripheral (USRP2) N210 RF front end device [71] connected to a roof-mounted choke ring antenna. In Fig. 4.2, a NovAtel GISTM (GNSS Ionospheric Scintillation and TEC Monitor) GSV4004B series dual frequency receiver was also used to confirm the presence of the acquired satellites. A similar setup is also used to log the ISMR data containing the S_4 and σ_ϕ at a 1 min rate and raw TEC data at 1 Hz at Trondheim receiver station which is used in Chapters 5 and 6. The data for the acquisition was collected on 21 August 2013 from 13:00 to 15:00 local time at the School of Electrical

and Electronic Engineering at Newcastle University, UK (54.97^o N, 1.61^o W). Acquisition was performed using non-coherent integration on 2 ms of data with a Doppler search space of $\pm$10 kHz. The acquisition result for one of the PRN$'$s found, i. e., PRN 16 is shown in Fig. 4.3. A unique peak can clearly be seen with a code phase of 434. The Doppler offset was found to be 500 Hz and therefore the acquired frequency was 1.2505 MHz.

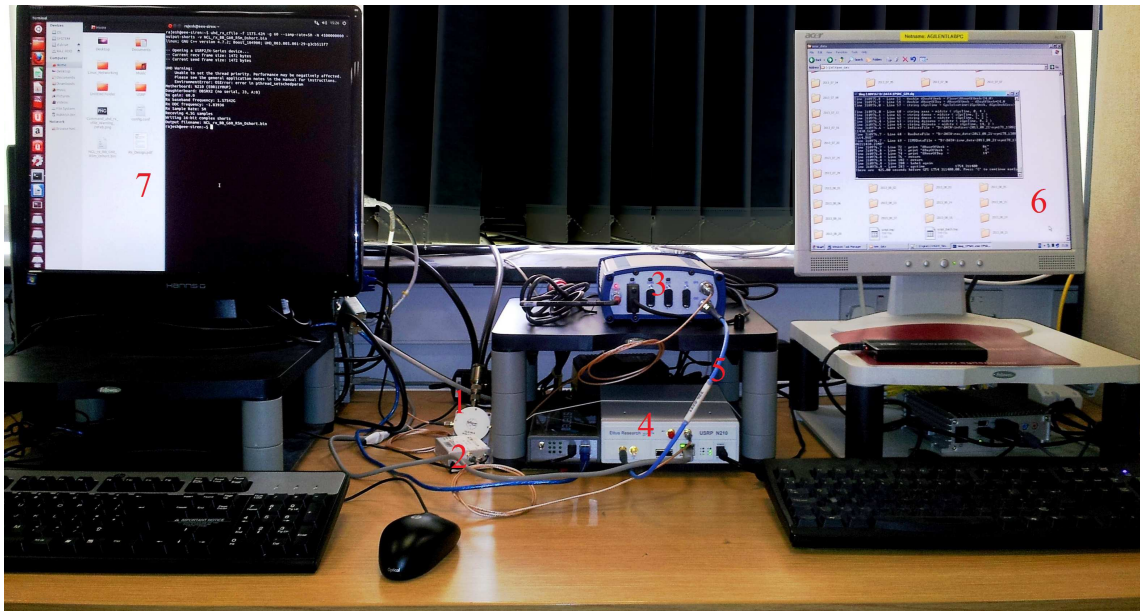

Figure 4.2: Experimental setup for capturing GPS data. In this experimental setup components are numbered as: (1) amplifier to boost the signal strength connected to the roof mounted antenna; (2) splitter to split the signal between the Novatel receiver and the USRP2 N210; (3) Novatel GPS receiver; (4) USRP2 N210 RF front end device; (5) oscillator output from (3) to (4); (6) positioning solution using Novatel receiver; (7) storing raw GPS data from USRP2 in a binary file to be used by the acquisition program [69].

4.2.2 Zero Padding Method

The zero padding (ZP) method [70, 72] works the same way as the FFT-based circular correlation method. However, instead of using the complete N selected samples for acquisition, the received signal and the local C/A code samples are divided into M small blocks of equal lengths and then correlation is performed between the corresponding blocks circularly. The overall method can be defined as follows:

1. Divide the N samples of the incoming signal into M blocks of equal lengths and combine the every two adjacent blocks to extend the block lengths. Name the

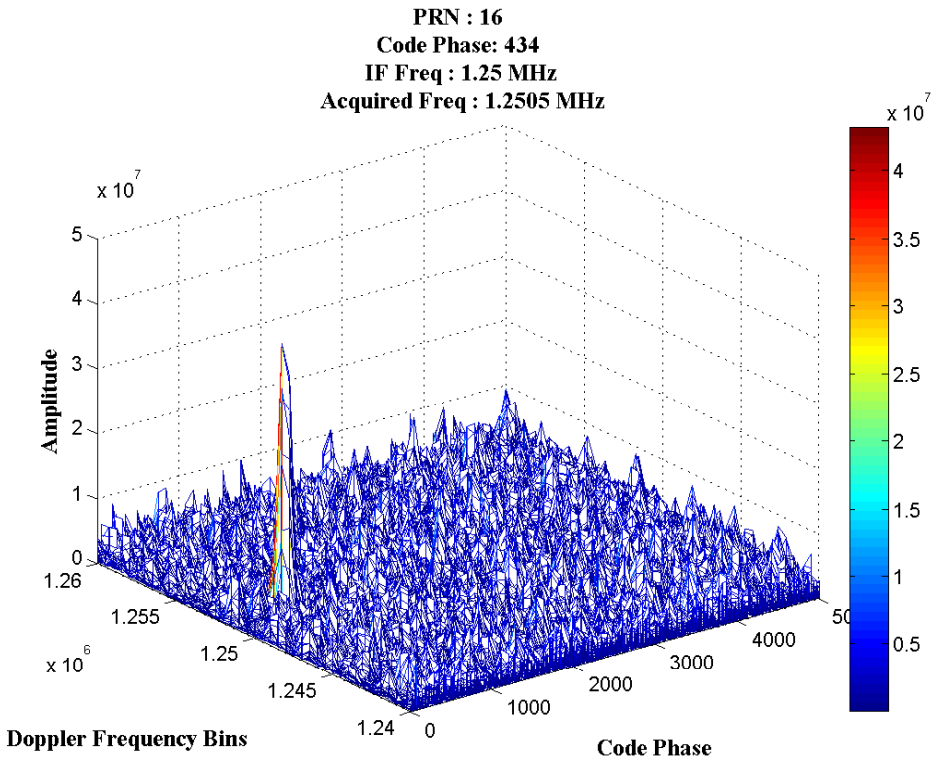

Figure 4.3: Acquisition using the FFT-based circular correlation method for PRN 16.

extended blocks as b_m where $m = 1,2,3,...,M$ represents the block numbers. The length of each block can be denoted by l.

2. Generate N samples of the local C/A code and divide them into M equally spaced blocks having the same length as the incoming signal blocks. Now pad each block with equal number of zeros to double the block lengths and name them as c_n where $m = 1,2,3,...,M$.

3. Circular correlate b_m and c_m in an ordered way such that the correlation will be first performed between the blocks b_1 and c_1 and save only the first $l/2$ correlation results discarding the rest. The same will be repeated for the rest $M-1$ blocks. Using the corresponding output point from each blocks one can perform the M-point FFT to find the frequency. The total FFT's must be performed M$\times$M times.

4. The above procedure will be repeated $M-1$ more times using the following block arrangements; $m = 1,2,3,...,M$, the n is arranged as $n = 2,3,...,M,1$; $n = 3,4,...,M,1,2$; $n = M,1,2...,M-1$;

5. Searching for the maximum peak will give the code phase of the signal and the frequency can be found using the FFT.

For performing the acquisition on the GPS signals using the ZP method, we used the same data set as collected using the experimental setup shown in Fig. 4.2. Following steps 1 to 5, the acquisition results for PRN 16 are shown in Fig. 4.4. It should be noted that rather than presenting the results of each block separately, we combine all the correlation results obtained in step 5 to show the position of the correct code phase and then found the frequency using the FFT. The peak was found at the code phase index of 434 which is the same as founded in the case of the FFT-based method and the frequency was found to be 1.2505 MHz.

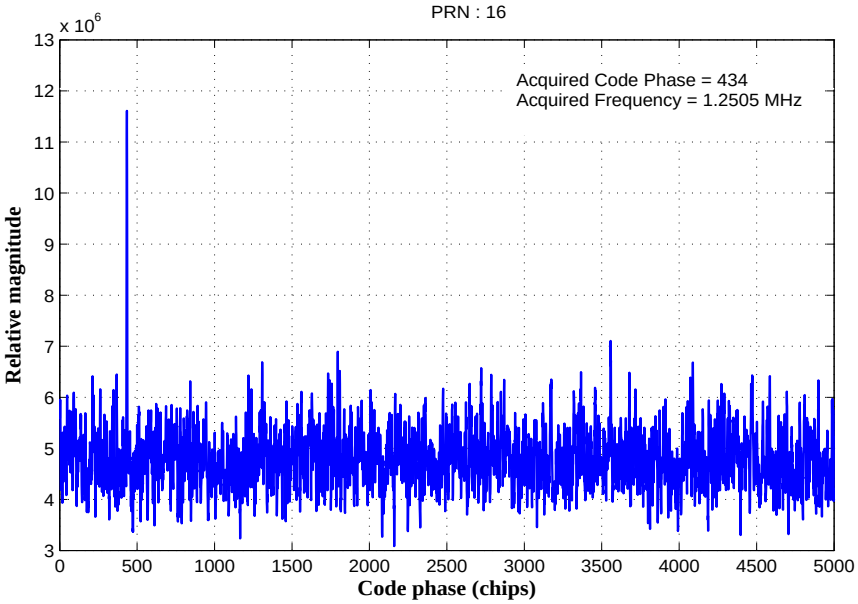

Figure 4.4: Acquisition results using the ZP method for PRN 16.

4.2.3 Acquisition using the Block Repetition Method

As discussed previously, the received GPS signals can be affected by several phenomena such as the ionospheric delay, satellite and receiver clock errors, multipath errors, satellite geometry and the ionospheric scintillation. At acquisition level, the effect is usually seen in the form of signal fading which can reduce the input S/N_o of a signal and hence can lead to reduced detection performance in terms of the probability of detection. To overcome this problem and to increase the detection performance, one strategy is to increase the coherent integration time in the acquisition process. However, this also increases the acquisition time. Due to long coherent integration times, the FFT-based method is the most commonly used acquisition method due to its high detection performance [63]. The ZP method, on the other hand, is a faster one but at the expense of reduced detection performance [63]. In order to improve the detection performance and speed up the acquisition process overall, a new Repetitive Block Acquisition (RBA) method is here proposed [69]. The RBA method uses a parallel overlapping block structure rather than padding zeros as in the case of the ZP method. In the RBA method, after dividing the incoming signal and the local PRN code into M equally spaced blocks, every two neighbouring blocks are combined together and then correlation is performed. A simple block diagram of the overlapping block formation using the RBA method is shown in Fig. 4.5. The symbols $s_1, s_2, ..., s_M$ represent the extended signal blocks whereas $c_1, c_2, ..., c_M$ represents the local C/A code blocks formed using the RBA method.

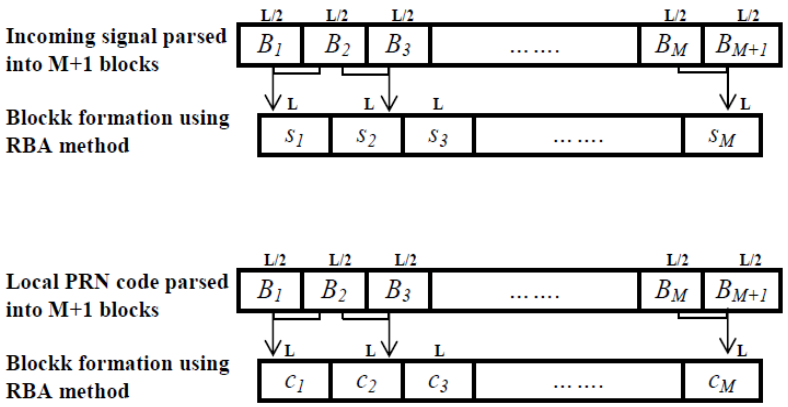

Figure 4.5: Block formation using the RBA method [69].

The block diagram of the RBA method is shown in Fig. 4.6 and the complete algorithm is defined below.

1. Choose N samples of the received GPS signal and divide them into $M+1$ blocks each having length $L/2$.

2. Starting from the first block, combine every two adjoining blocks to generate M new blocks of length L and then perform FFT on all the blocks.

3. Generate N samples of the local C/A code and form M new blocks of length L by following the same procedure as in step 2 and perform the FFT and conjugation.

4. Multiply the FFT results of all the corresponding blocks of step 2 and step 3 and perform IFFT. Keep the first $L/2$ correlation results from each block and discard the rest of the $L/2$ results and perform non-coherent integration.

5. Check for the maximum peak against a predetermined threshold (γ). If the peak is above the threshold, acquisition can be declared.

6. If no peak is found, shift C/A code blocks to the left by one step and repeat steps 4 and 5. This process must be repeated M times overall if no peak is found in the first $M-1$ searches .

7. For unsuccessful acquisition, the old data block is shifted out and the new data block is shifted in to start the acquisition process from step 1.

The acquisition results using the RBA method for PRN 16 are shown in Fig. 4.7. The code phase (434) and the acquired frequency (1.2505 MHz) were both found to be the same as found in the case of the FFT-based and ZP methods which shows that the RBA method provides the correct acquisition results. In the next sections, the detection performance and the computational complexity involved in each method is analyzed and discussed and it is shown that how the detection performance can be improved in case the signal is weakened by the fading which can occur due to both the increased levels of noise or amplitude scintillation.

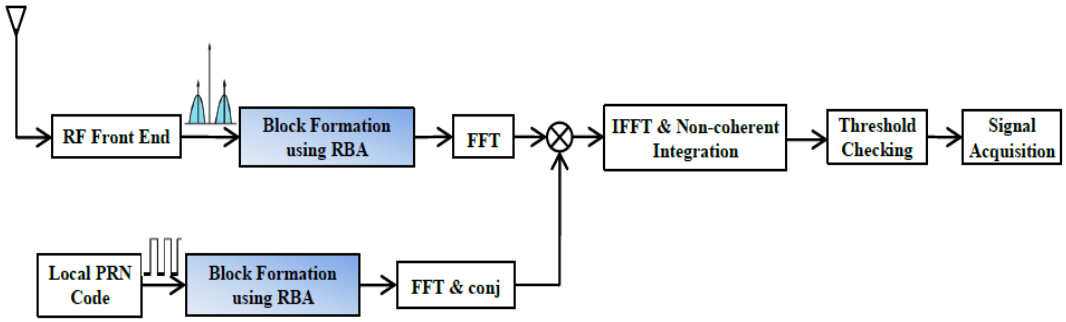

Figure 4.6: Block diagram of signal acquisition process using the RBA method.

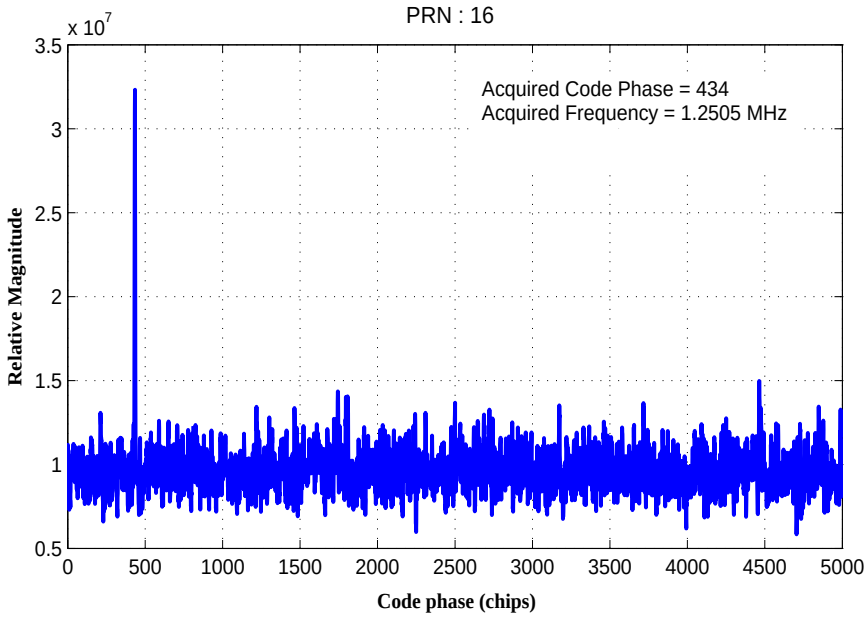

Figure 4.7: Acquisition results using the RBA method for PRN 16.

4.3 Detection Performance and the Probability of Detection

The correlation between the in-phase and quadrature components of the incoming signal and the locally generated C/A coded signal can be given as

$$I = \tilde{A} d_{\tau}[n] R(\tilde{\theta}) sinc((f_d - \hat{f}_d) T_I) \cos(\theta_i) + n_{I_i} \tag{4.6}$$

$$Q = \tilde{A} d_\tau[n] R(\tilde{\theta}) sinc((f_d - \hat{f}_d)T_I)\sin(\theta_i) + n_{Q_i} \tag{4.7}$$

where $R[\tilde{\theta}]$ is the autocorrelation function, $\tilde{\theta} = \tau - \hat{\tau}$ is used to represent the correlation loss due to error in estimating the code delay, $f_d - \hat{f}_d$ is the error in estimating the Doppler offset in the transmission frequency, T_I is the coherent integration time and θ_i is the average phase error over the correlation interval. Assuming that the navigation data bit, $d_\tau[n]$, is constant during the coherent integration time as the C/A is 1 ms long whereas navigation message is 20 ms long and setting up a hypothesis test with hypothesis H_1 that the signal is present and hypothesis H_0 that the signal is absent. Under hypothesis H_1, the envelope of the signal $E = \sqrt{I^2 + Q^2}$ after power detection will be Rician with a probability density function (PDF) [73] given as

$$p_{H_1}(E) = \frac{E}{\sigma^2_{H_1}}.exp\left(-\frac{E^2 + \tilde{A}^2}{2\sigma^2_{H1}}\right) I_o\left(\frac{E\tilde{A}}{\sigma^2_{H_1}}\right) \tag{4.8}$$

where $\tilde{A} = \sigma_{H_1}\sqrt{2T_I C/N_0}$ is the signal amplitude after the correlator integrator, $\sigma^2_{H_1}$ is the noise variance and $I_o\left(E\tilde{A}/\sigma^2_{H_1}\right)$ is the zero order modified Bessel function of the first kind and can be given as

$$I_n(x) = \sum_{c=0}^{\infty} \frac{(x/2)^{2c+n}}{c!\Gamma(c+n+1)} \tag{4.9}$$

where $\Gamma(c+n+1) = (c+n)!$. The probability that the envelope, E, will exceed a predetermined threshold, γ, can be given as

$$P_d = \int_\gamma^\infty p_{H_1}(E)dE \;=\; \int_\gamma^\infty \frac{E}{\sigma^2_{H_1}}.exp\left(-\frac{E^2 + \tilde{A}^2}{2\sigma^2_{H1}}\right) I_o\left(\frac{E\tilde{A}}{\sigma^2_{H_1}}\right) \tag{4.10}$$

where P_d is the probability of detection. According to [73], if we neglect the terms $> \tilde{A}^3$, assume $E\tilde{A}/\sigma_n^2 >> 1$, $\tilde{A} >> |E - \tilde{A}|$ and applying series approximation, the detection probability can be given as

$$P_d = \frac{1}{2}\left[1 - erf\left(\frac{\gamma - \tilde{A}}{\sqrt{2}\,\sigma_{H_1}}\right)\right] + \left\{\frac{exp\left[-(\gamma-\tilde{A})^2/2\sigma_{H_1}^2\right]}{2\sqrt{2\pi}\left(\tilde{A}/\sigma_{H_1}\right)}\right\} \times \left\{1 - \frac{\gamma-\tilde{A}}{4\tilde{A}} + \frac{1+\left[(\gamma-\tilde{A})^2/\sigma_{H_1}^2\right]}{8\tilde{A}^2/\sigma_{H_1}^2}\right\} \quad (4.11)$$

From [73], using $\tilde{A}^2/\sigma_{H_1}^2$ as the post detection signal-to-noise ratio, $(S/N)_f$, (4.11) can be used to find the probability of detection as a function of the $(S/N)_f$. Equation (4.11) also shows that the P_d is a function of the signal characteristics and can be affected by the scintillation if there are strong amplitude fluctuations in the signal. From hypothesis testing, under hypothesis H_0, the $\tilde{A}^2$ will be 0 and the envelope, E, of the signal will follow a Rayleigh distribution with PDF [73] given as

$$p_{H_0}(E) = \frac{E}{\sigma_{H_0}^2} e^{-(\gamma^2/2\sigma_{H_0}^2)} \quad (4.12)$$

where $\sigma_{H_0}^2$ is the noise variance under hypothesis H_0. The probability that the envelope of the noise alone will cross the threshold γ, also known as the probability of false alarm (P_{fa}) can be given as

$$P_{fa} = \int_{\gamma}^{\infty} p_{H_0}(E)dE = e^{-(\gamma^2/2\sigma_{H_0}^2)} \quad (4.13)$$

In (4.13) settting a suitable value of the P_{fa}, the detection threshold, γ, can be found as

$$\gamma = \sqrt{-2\sigma_{H_0}^2 ln(P_{fa})} \quad (4.14)$$

From (4.13), it can be seen that the P_{fa} is not a function of the signal amplitude and therefore will not be affected by the scintillation. Suppose, the received signal is affected by the scintillation and $\tilde{A}$ is the purturbed signal amplitude then the relationship between the purturbed and unpurturbed signal amplitude can be given as $A_N = \tilde{A}/A$, where A is the actual unpurturbed signal amplitude and A_N is the normalized amplitude. In the presence of scintillation, the detection probability in (4.11) will be dependent on the amplitude,

$\tilde{A}$, and the PDF of the signal envelope as a function of the signal amplitude [74] under hypothesis, H_1, will be given by

$$p_{H_1}(E) = p_{H_1,\tilde{A}}(E \mid \tilde{A}) p_{\tilde{A}}(A) dA \tag{4.15}$$

where $p_{\tilde{A}}(A)$ represents the degradation in the detection probability due to amplitude scintillation and from [74] can be modelled as a Nakagami-m distribution

$$p_{\tilde{A}}(A) = \frac{2m^m . A^{2m-1}}{\Gamma(m)\langle A^2 \rangle} e^{-mA^2/\langle A^2 \rangle} \tag{4.16}$$

where $m = 1/S_4^2$. The P_d in the presence of amplitude scintillation [74] can be given as

$$P_d = \int_0^\infty p_{H_1,\tilde{A}}(E \mid \tilde{A}) p_{\tilde{A}}(A) dA \tag{4.17}$$

Using the above assumptions and by setting $P_{fa} = 0.01$, the P_d is plotted as a function of S_4 for different C/N_o values as shown in Fig. 4.8. As discussed in chapter 3, the amplitude scintillation can introduce up to 20 dB fading in the received signal. This will affect the input S/N_o of the signal and will lead to poor detection performance. This can also be seen in Fig. 4.8 where the increasing S_4 value is leading to a reduced detection probability.

4.4 Improving the Detection Performance

The coherent and non-coherent integrations are the two approaches which can be used to increase the detection probability at the acquisition stage. As discussed in section 2.6, the noise floor of the received signal is - 114 dBm/MHz using a front end having a noise figure of 2 dB. The bandwidth of the C/A code receiver is approximately 2 MHz. Based on this bandwidth, the noise floor of the received signal will be -111 dBm. Since the miminum received signal strength of the received GPS $L1$ signal is -130 dBm, then the S/N_o of the received signal will be -19 dB (-130+111). However, if we are using 1 ms signal for acquisition with the frequency steps of 1 kHz then the noise floor will be - 144 dBm and the S/N_o of the received signal will be 14 dB (-130 + 144). It is reported by [8] that an

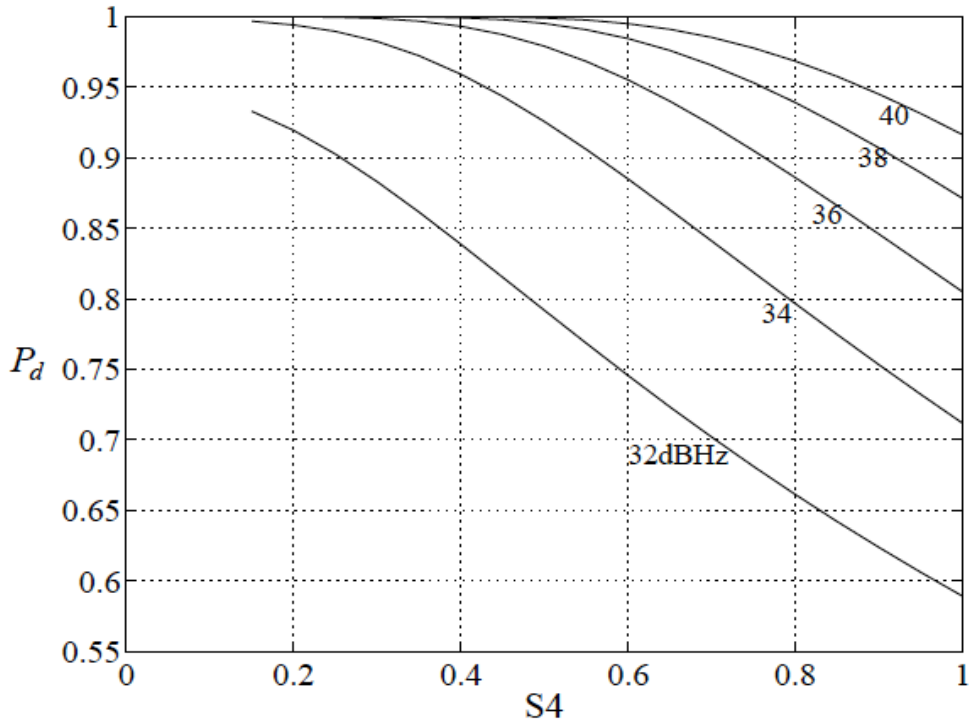

Figure 4.8: P_d plotted against the S_4 for different C/N_o values [74].

input S/N_o of 14 dB is a reasonable value for achieving 90% detection probability. The coherent integration gain, $G_c(n)$, of n ms of data over 1 ms is

$$G_c(n) = 10log(n) \tag{4.18}$$

For acquisition, a maximum of 19 ms of data can be processed coherently because there will be a navigation data bit transition every 20 ms in the case of GPS signals. For weak signals, a long data record is needed and the coherent processing becomes impractical if the signal is very weak. In that case, the input S/N_o can be increased by accomplishing the acquisition using a combination of coherent and non-coherent integrations.The non-coherent integration gain [8], $G_i(n)$, can be obtained by subtracting the non-coherent intergration loss, $L(n)$, from the coherent intergration gain, $G_c(n)$, given as

$$G_i(n) = G_c(n) - L(n) \tag{4.19}$$

where n is the non-coherent integration number and $L(n)$ is the non-coherent integration loss and can be given as

$$L(n) = 10log\left[\frac{1+\sqrt{9.2n/D_c(1)}}{1+\sqrt{9.2/D_c(1)}}\right] \tag{4.20}$$

where $D_c(1)$ is the ideal detectability factor given as

$$D_c(1) = [\ erf^{-1}(1-2P_{fa}) - \ erf^{-1}(1-2P_d)\ ]^2 \tag{4.21}$$

where erf^{-1} is the inverse of the error function erf ($erf = \frac{2}{\sqrt{\pi}}\int_0^z e^{-t^2}dt$). Equation (4.19) shows that non-coherent integration gain is a function of the P_d. If we set a suitable value for the P_{fa}, then increasing the non-coherent intgeration length will lead to an increased detection probability. A plot of the S/N_o gain and loss versus the non-coherent integration length, n, is shown in Fig. 4.9. From this figure, it can be seen that by performing 1000 non-coherent integrations for a given coherent data length, 20 dB extra gain can be achieved. Suppose, the received signal is at -151 dBm and acquisition is performed using the 10 ms coherent length. The input S/N_o of the signal will be 0 dB. In order to achieve 90% detection probability, 14 dB more gain is required which can be achieved by using 100 non-coherent integrations or 1 s of data. A similar approach was also used by [75] to show that an overall 26 dB gain can be achieved by processing 4 s of data. From Fig. 4.9, we observed that a 16.2 dB gain can be achieved by performing 200 non-coherent integrations for a given coherent length. The remaining 800 integrations only add up to a 3.8 dB gain, so it is impractical to perform 400% more operations for the extra 3.8 dB gain. In the next section, the detection performance of the FFT-based, ZP and RBA methods is analyzed using the non-coherent integration for the improved detection performance.

4.5 Performance Comparison between the FFT-based, RBA and ZP methods

In this section, the detection probability of the RBA, ZP and the FFT-based methods is analyzed using the simulated GPS L1 C/A coded signals generated using the Spirent

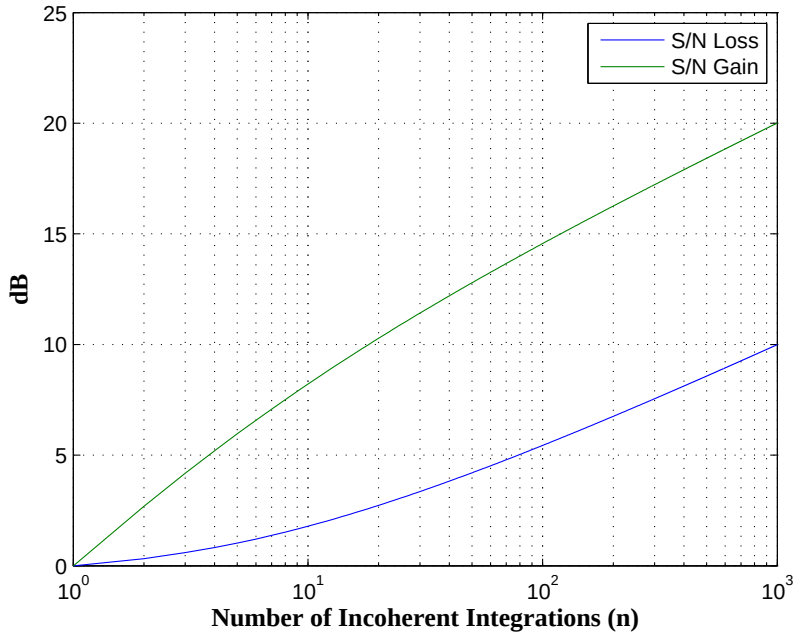

Figure 4.9: Non-coherent integration loss and gain.

GSS8000 multi-GNSS constellation simulator. The GPS signals from the Spirent simulator were collected and downconverted at an intermediate frequency, f_{IF}, of 1.25 MHz and sampled at 5 MHz using the USRP2 (universal software radio peripheral) N210 front end device. The experimental test-bed for generating the GPS signals is shown in Fig. 4.10. Since the C/A code is 1 ms long, then, based on the sampling frequency of 5 MHz there will be 5000 code phase samples in 1 ms. For this analysis, a controlled environment was used in which the S/N_o of the received signal was degraded by adding white Gaussian noise. A study of the hardware computational load in terms of the number of FFT multiplications and additions has also been carried out to show the computational complexity involved in each method. The acquisition was performed by selecting the short and long coherent lengths (code phase lengths).

The detection probabilities of the RBA, ZP and FFT-based methods are shown in Fig. 4.11. For calculating the detection probability, (4.11) was used and the P_{fa} was chosen as 10^{-7}. It can be seen in Fig. 4.11 that the RBA method has achieved better detection probability than the ZP method when compared for code phase lengths of 20,000, 40,000, 60,000, 150,000 and 200,000. On average, the RBA method achieved 25% to 30% better

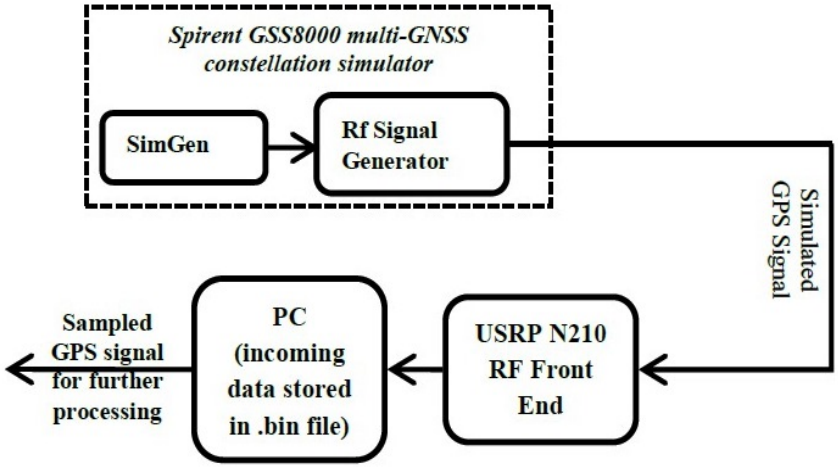

Figure 4.10: Experimental test bed for simulating the GPS signals using the Spirent simulator.

performance than the ZP method. On the other hand, the detection probability of the RBA method was found to be less than the FFT-based circular correlation method when compared using the same code phase lengths. This can be due to performing correlation by dividing the large data sets into small blocks in the case of the RBA method which affects the correlation properties of the C/A codes. However, if we compare the detection probability of the FFT-based method with 60,000 code phase length to the RBA method with 200,000 code phase length, both of them share the same detection performance in terms of P_d. This shows that, in the case of the RBA method, to achieve the same detection performance as the FFT-based method, the integration time must be increased by more than a factor 3. However, if we compare the computational load of the two methods in Fig. 4.12, it was found that RBA method with 200,000 code phase lengths was taking only 1.88416×10^8 computations compared to the 5.2147×10^8 computations using 60,000 code phase length in the case of the FFT-based method. This shows that to achieve better detection proabaility with less computational time, the RBA is better than both the FFT-based method and the ZP methods.

The acquisition speed in the case of the FFT-based, RBA and ZP methods depends on the number of FFT and IFFT operations involved in a correlation process. An N-point FFT contains $(N/2)log_2N$ complex multiplications and $Nlog_2N$ complex additions. This

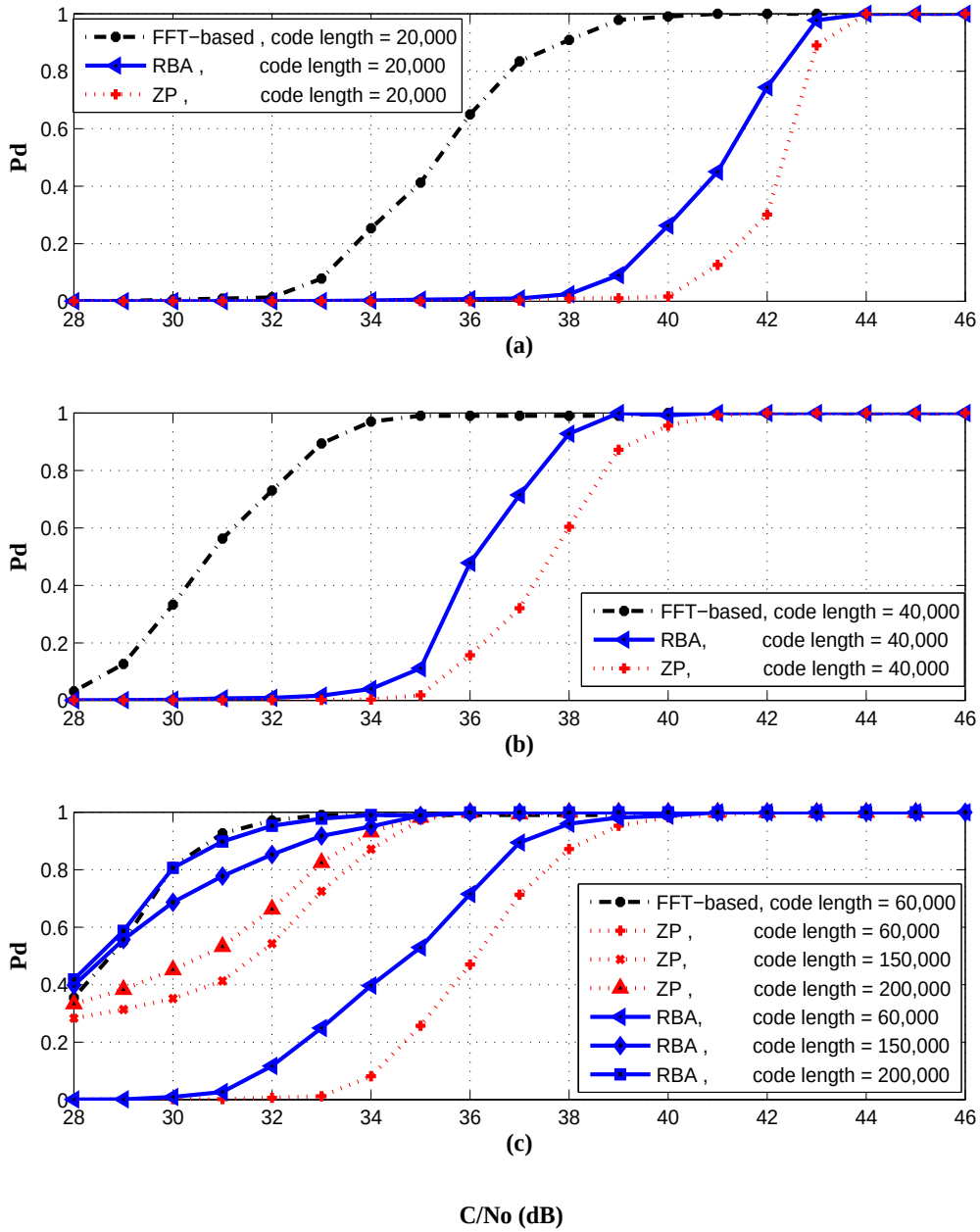

Figure 4.11: Probability of detection for the FFT-based, RBA and ZP methods for different code phase length: (a) 20,000 code phase length. (b) 40,000 code phase length. (c) multiple code phase lengths.

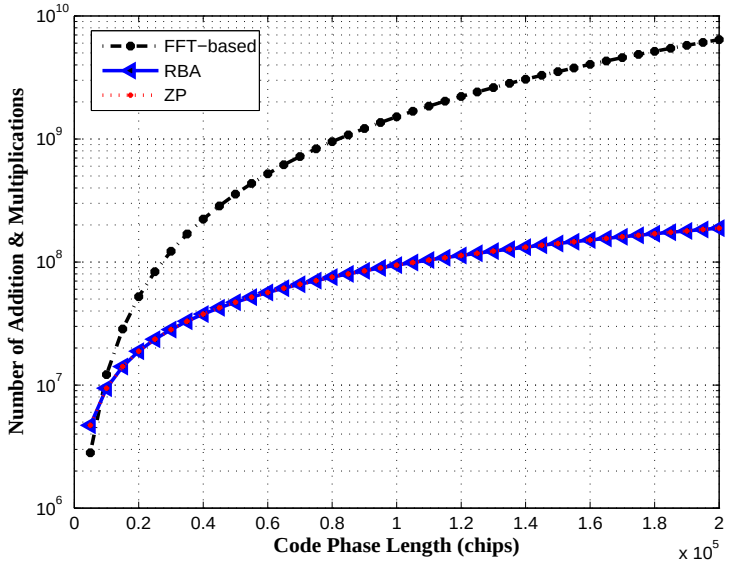

Figure 4.12: Number of Additions and Multplications for the FFT-based, RBA and ZP methods

criteria was used to find the combined number of additions and multiplications involved in each method in Fig. 4.12.

4.6 Scintillation Activity and the Receiver Performance

To monitor the scintillation activity, several GPS receiver stations are established at different high latitude regions as part of the the EPSRC (Engineering and Physical Science Research Council) funded project through the grant $EP/H004637/1$. The location of these receiver stations is shown in Fig. 4.13. The receivers used for monitoring the scintillation activity are the Novatel GISTM GSV-4004B series which can log scintillation indices (S_4, σ_ϕ) at a 60 s rate. The amplitude and phase scintillation activity at Trondheim, Norwy (63.42^o N, 10.4^o E) on 24 April, 2014 is shown in Fig. 4.14. The Kp plot for the day is shown in the lower panel of Fig. 4.14 which shows that during 00:00 to 09:00 UT and between 21:00 to 24:00 UT, there was a strong geomagnetic storm with Kp reaching as high as 7 during 00:00 to 03:00 UT. This resulted in strong phase scintillation on most of the PRN's visible during this time whereas no significant amplitude scintillation activity was observed. It should be noted that the amplitude scintillation is more dominant at the

equatorial regions compared to the high latitude regions. However, since we do not have suitable data available from equatorial latitudes, we are using the high latitude data to observe the scintillation effects on receiver tracking loop loss of lock performance.

The scintillation acitivity for one of the PRN′s, i. e., PRN 19, is shown in Fig. 4.15 where the amplitude and phase scintillation is plotted in the top panel, loss of lock in the middle panel and the C/N_o is plotted in the lower panel of Fig. 4.15. Strong phase scintillation was observed between 01:00 to 03:00 UT which resulted in frequent loss of lock at the $L2$ frequency. However the $L1$ signal did not observe any loss of lock during this time which shows that for this case the higher frequency was more vulnerable to scintillation. On the other hand, no significant decrease in the C/N_o was observed on both frequencies. The small variations were due to the effect of the changing elevation angle. This shows that the cycle slips due to phase scintillation are the main cause of loss of lock compared to the amplitude scintillation which mostly results in decreased signal power due to deep and frequent power fades [65, 75]. In the next sections, the scintillation effects on the carrier phase tracking loops are analyzed and discussed.

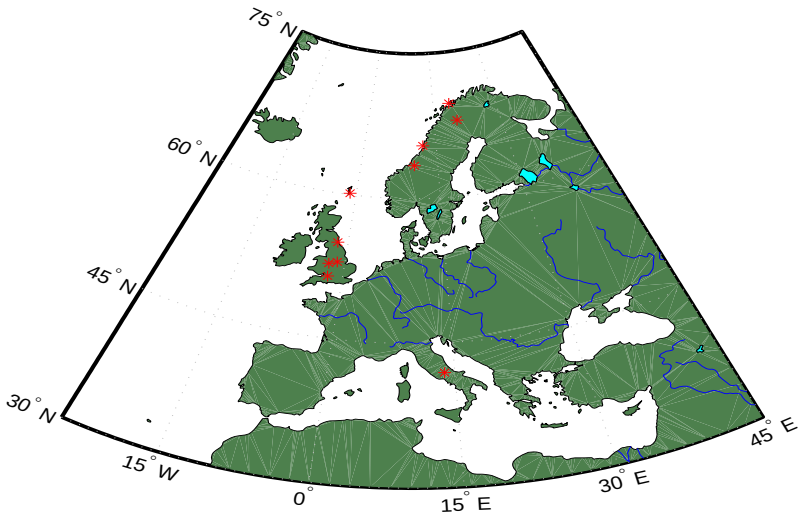

Figure 4.13: GNSS receiver stations for recording the scintillation activity.

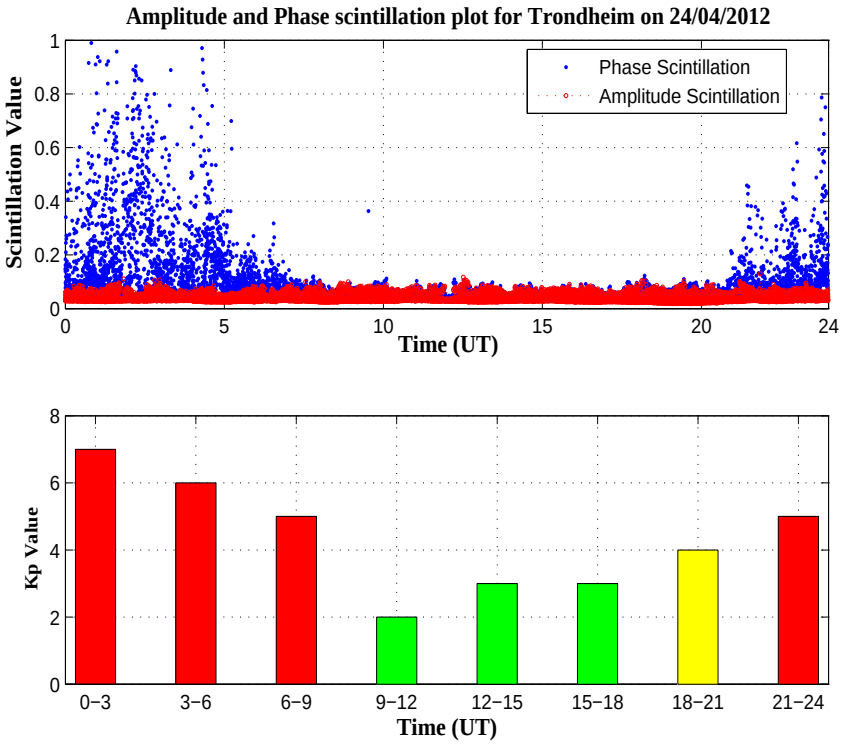

Figure 4.14: Amplitude and phase scintillation activity at Trondheim, Norway on 24 April, 2012.

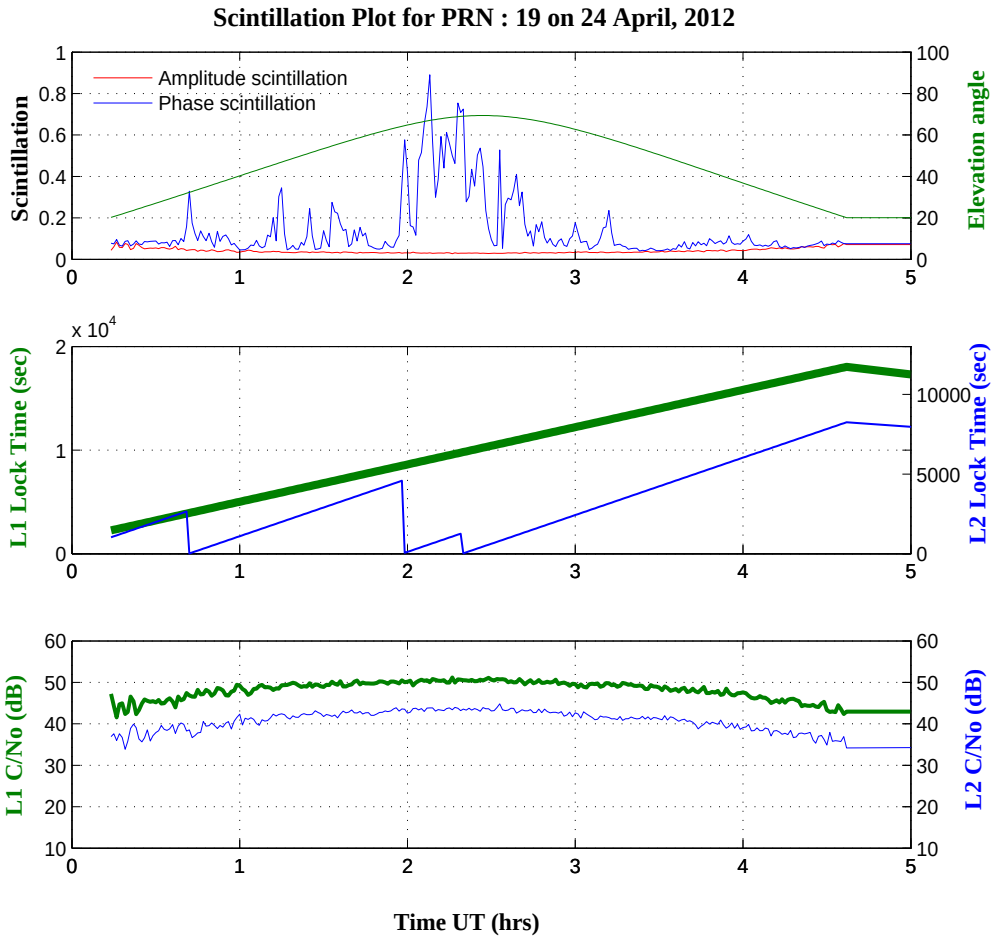

Figure 4.15: Scintillation plot of PRN 19 at Trondheim, Norway on 24 April, 2012.

4.7 Scintillation Effects on Carrier Tracking Loops

The main purpose of the tracking loop in a GNSS/GPS receiver is to lock and track the incoming signal. The phase lock loop (PLL) is the most commonly used method for tracking the GNSS/GPS signals. The PLL finds the difference between the phase of the incoming signal and the local reference signal and then use it to adjust the frequency of the local oscillator to match frequency of the incoming signal. A block diagram of a conventional PLL design taken from [76] is shown in Fig. 4.16 where $\Phi_i(s)$ is the input signal in the s-domain which can be obtained using the Laplace transform, $\Phi_f(s)$ is the output signal, $N(s) = k_1$ is the gain of the voltage conrolled oscillator (VCO), $\varepsilon(s)$ is the phase error between $\Phi_i(s)$ and $\Phi_f(s)$, $\sum$ is the phase comparator, k_o is the amplifier gain and $F(s)$ is the transfer function of the loop filter. Adopted from [9], the s-domain representation of the second and third order PLL's are shown in Fig. 4.17 and Fig. 4.18 respectively. In these figures, a_{PLL} and b_{PLL} are the filter coefficients and ω_n is the natural frequency (the frequency at which the loop frequency will oscillate until not disturbed by outside effects). In a conventional GPS receiver, a second order PLL is used which employs a first order loop filter. The transfer function of the loop filter to make a second order PLL can be given as

$$F(s) = \frac{s\tau_2 + 1}{s\tau_1} \tag{4.22}$$

From Fig. 4.16, the transfer function of the PLL tracking loop can be found as

$$H(s) = \frac{\Phi_f(s)}{\Phi_i(s)} = \frac{k_o k_1 F(s)}{s + k_o k_1 F(s)} \tag{4.23}$$

Using (4.22) in (4.23):

$$H(s) = \frac{k_o k_1 \frac{s\tau_2+1}{s\tau_1}}{s + k_o k_1 \left(\frac{s\tau_2+1}{s\tau_1}\right)} \tag{4.24}$$

and simplifying (4.24) will give

$$H(s) = \frac{2\zeta\omega_n s + \omega_n^2}{s^2 + 2\zeta\omega_n s + \omega_n^2} \tag{4.25}$$

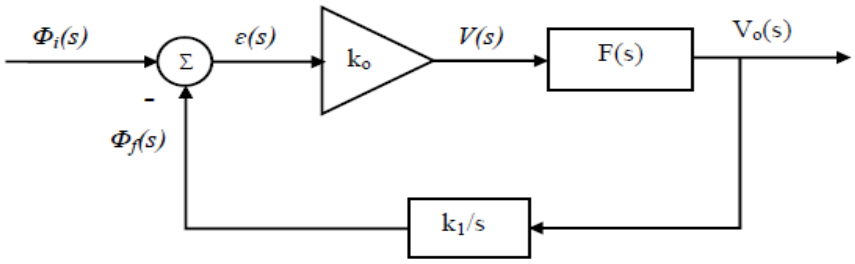

Figure 4.16: S-domain representation of a Phase lock loop.

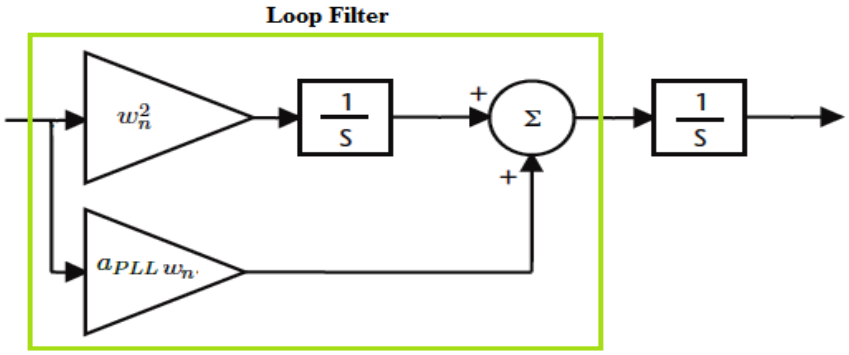

Figure 4.17: 2nd order PLL design.

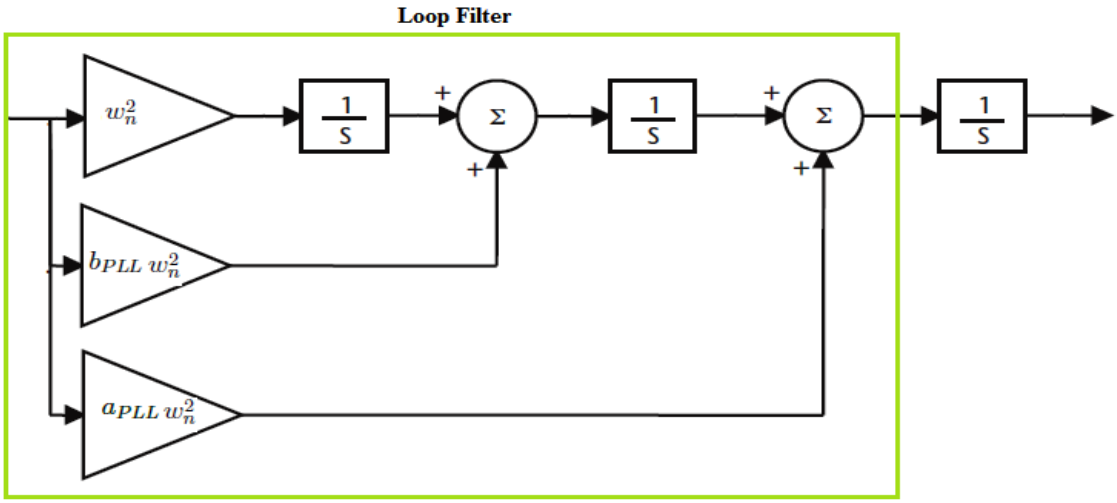

Figure 4.18: 3rd order PLL design.

where ζ is the damping ratio and from [76], the ω_n and ζ can be given as

$$\omega_n = \sqrt{\frac{k_o k_1}{\tau_1}} \tag{4.26}$$

$$\zeta = \frac{\omega_n \tau_2}{2} \tag{4.27}$$

Equation (4.25) is an analog representation of the transfer function of a PLL for continuous time systems. In order to convert it into a discrete time system for digitized data, the z-transform can be used. To convert the s-domain into a z-domain, the bilinear transform given in (4.28) can be used

$$s = \frac{2}{t_s}\frac{1-z^{-1}}{1+z^{-1}} \tag{4.28}$$

where t_s is the sampling time. Using the bilinear transform and simplifying, the loop transfer function, $F(s)$, in z-domain can be given as

$$F(z) = C_1 + \frac{C_2}{1-z^{-1}} \tag{4.29}$$

where C_1 and C_2 are the filter coefficients given as

$$C_1 = \frac{2\tau_2 - t_s}{\tau_1}, \qquad C_2 = \frac{t_s}{\tau_1}$$

Similarly, the transfer function $N(s) = k_1/s$ of the VCO in z-domain, using the bilinear transform, can be given as

$$N(z) = \frac{k_1 z^{-1}}{1-z^{-1}} \tag{4.30}$$

The transfer function of the PLL in z-domain is

$$H(s) = \frac{k_o k_1 F(z) N(z)}{1 + k_o k_1 F(z) N(z)} \tag{4.31}$$

Substituting $N(z)$ and $F(z)$ in (4.31) gives

$$H(z) = \frac{k_o k_1 (C_1 + C_2) z^{-1} - k_o k_1 C_1 z^{-2}}{1 + [k_o k_1 (C_1 + C_2) - 2] z^{-1} + (1 - k_o k_1 C_1) z^{-2}} \tag{4.32}$$

In (4.32), to find the filter coefficients C_1 and C_2, certain parameters needs to be estimated beforehand such as ω_n , ζ and the gain of the loop filter ($k_o k_1$). From [76], ω_n for a 2nd order PLL can be found as

$$B_n = \int_0^\infty |\, H(w) \,|^2 \, df = \frac{\omega_n}{2} \left(\zeta + \frac{1}{4\zeta} \right) \tag{4.33}$$

$$\omega_n = \frac{4\zeta B_n}{4\zeta^2 + 1} \tag{4.34}$$

where B_n is the noise bandwidth (see Appendix B for derivation). The damping factor, ζ, is usually taken as 0.707 as it is close to the optimum value as mentioned by [76] and we have also used the same in tracking the signals. The loop gain ($k_o k_1$) can be set to an arbitrary value but from [76] we have used $4\pi \times 100$ in this thesis, however other values can also be used depending on the application. From the PLL block diagram in Fig. 4.17, the overall transfer function after the phase comparator for a second order PLL can be given as

$$G_2(s) = k_o k_1 F(s) N(s) = k_o k_1 \left(\frac{s\tau_2 + 1}{s\tau_1} \right) \left(\frac{1}{s} \right) \tag{4.35}$$

Putting the values of τ_1 and τ_2 in (4.35), it will be reduced to

$$G_2(s) = \frac{\omega_n^2 + a_{PLL} \omega_n s}{s^2} \tag{4.36}$$

Using a Costas PLL implementation, the overall tacking loop design is shown in Fig. 4.19. The parameters I_p and Q_P are the in-phase and quadrature correlation results respectively derived using the prompt replica code. The reason for choosing the Costas discriminator is its insensitivity to 180^o phase shift. The equations for the I_p and Q_p correlations can be given as

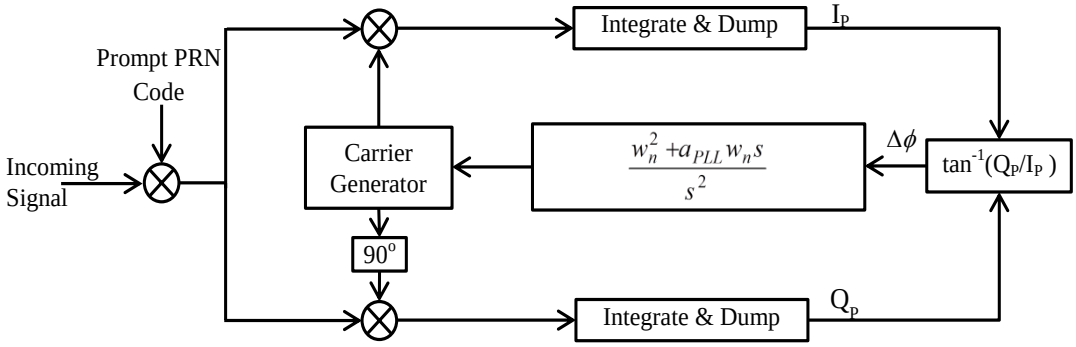

Figure 4.19: Carrier tracking using a 2nd order Costas PLL.

$$I_p = ANR(\theta)sinc((f_d - \hat{f}_d)T_I)\cos(\theta_i) + n_I \tag{4.37}$$

$$Q_p = ANR(\theta)sinc((f_d - \hat{f}_d)T_I)\sin(\theta_i) + n_Q \tag{4.38}$$

where N is the total number of samples, T_I is the predetection integration time and n_I and n_Q are the noise terms in the in-phase and quadrature components respectively. From the PLL block diagram in Fig. 4.18, the transfer function after the phase comparator for a third order PLL can be given as

$$G_3(s) = \frac{\omega_n^3 + a_{PLL}\omega_n^2 s + b_{PLL}\omega_n s^2}{s^3} \tag{4.39}$$

The 3rd order PLL tracking loop implementation design using a Costass PLL is shown in Fig. 4.20. In the next section, the amplitude and phase scintillation effects on the 2nd and 3rd order PLL are discussed based on the explanation given above for the 2nd and 3rd order PLL's.

4.7.1 Phase Scintillation Effects

The phase tracking error variance is an important parameter which is not only used to determine the performance of a GNSS/GPS receiver during the scintillation and non-

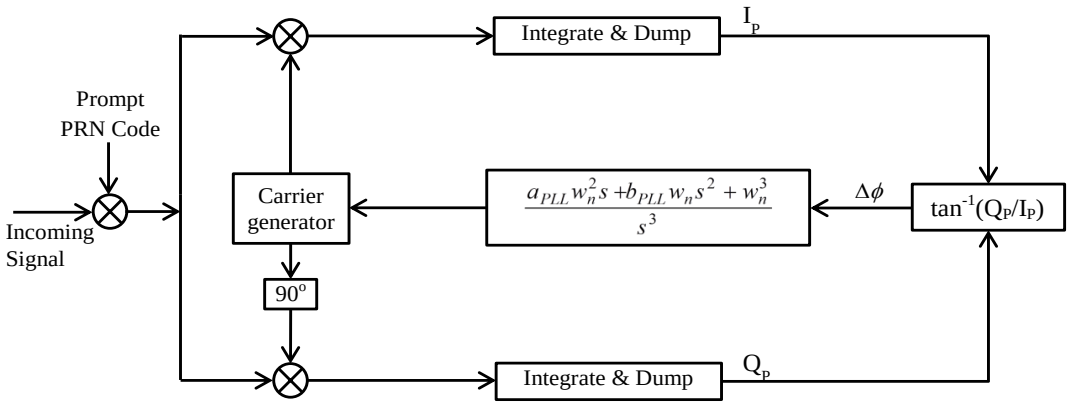

Figure 4.20: Carrier tracking using a 3rd order Costas PLL.

scintillation conditions but is also used to update the tracking loop parameters for robust signal tracking [77–79] and further used to define the tracking thresholds for updating the tracking loop paramters in the receiver beyond which loss of lock occurs. The phase tracking error variance at the output of a PLL [80] can be given as

$$\sigma_{\phi\varepsilon}^2 = \sigma_{\phi s}^2 + \sigma_{\phi T}^2 + \sigma_{\phi,osc}^2 \tag{4.40}$$

where $\sigma_{\phi s}$, $\sigma_{\phi T}$, $\sigma_{\phi,osc}$ are the tracking error variances from the phase scintillation, thermal noise and the oscillator noise respectively. From [80], the $\sigma_{\phi,osc}$ is assumed to be 0.1 rad. Assuming that the amplitude scintillation is almost negligible, the error variance due to thermal noise component [80] can be given as

$$\sigma_{\phi T}^2 = \frac{B_n}{C/N_o}\left(1 + \frac{1}{2T_I C/N_o}\right) \tag{4.41}$$

where T_I is the integration time. The tracking error variance due to phase scintillation [80] can be given as

$$\sigma_{\phi s}^2 = \int_{\infty}^{-\infty} \mid 1 - H(f) \mid^2 S_{\phi}(f) df \tag{4.42}$$

where $\mid 1 - H(f) \mid^2$ is the closed loop transfer function of the PLL given as

$$\mid 1 - H(f) \mid^2 = \frac{f^{2k}}{f^{2k} + f_n^{2k}} \tag{4.43}$$

where f is the signal frequency, f_n is the natural frequency and k is the loop order. In (4.42), the term $S_\phi(f)$ is the power spectral density (PSD) of the phase scintillation given as

$$S_\phi(f) = \frac{T}{(f_0^2 + f^2)^{p/2}} \qquad (\text{radians}^2/\text{Hz}) \tag{4.44}$$

where f_o is the outer scale cut-off, T is the spectral strength at 1 Hz and p is the slope of the PSD. Using (4.43) and (4.44) in (4.42) and integrating, the error variance due to phase scintillation can be given as

$$\sigma_{\phi s}^2 = \frac{\pi T}{k f_n^{p-1} \sin\left(\frac{(2k+1-p)\pi}{2k}\right)}, \quad 1 < p < 2k \tag{4.45}$$

Using (4.41) and (4.45) in (4.40) and neglecting the oscillator noise, as we are considering the software-based models for PLL, the total phase tracking error variance in the presence of phase scintillation and thermal noise is

$$\sigma_{\phi\varepsilon}^2 = \frac{\pi T}{k f_n^{p-1} \sin\left(\frac{(2k+1-p)\pi}{2k}\right)} + \frac{B_n}{C/N_o}\left(1 + \frac{1}{2T_I C/N_o}\right) \tag{4.46}$$

In Fig. 4.21, the phase tracking error due to thermal noise and phase scintillation ($\sigma_{\phi s}$) is plotted as a function of the spectral strength (T) using varying noise bandwidths (B_n) for the 2nd and 3rd order PLL's. Following parameter values were used for the two tracking loops in Fig. 4.21 to generate this figure: $T_I = 0.02$, $C/N_o = 42$ dBHz, $p = 2.5$. Fig. 4.21 shows, that as T increases, the tracking error also increases. The tracking error in Fig. 4.21 is higher for small noise bandwidths due to the fact that although narrower tracking loop (and hence also noise) bandwidths can be used to reduce the noise entering the receiver tracking loops in order to improve the S/N_o, they cannot accomodate the large random phase fluctuations due to scintillation when there is a high probability that the receiver will most likely lose lock due to tracking loop treating these phase fluctuations as noise and hence can lead to large errors when this exceeds the narrower receiver bandwidth. The error contribution due to thermal noise was almost negligible and was less than 0.01 radians due to the high C/N_o value used and therefore was not of any great concern. The

reason for using the high C/N_o is due the fact that we were only interested in seeing the effects of phase scintillation on the tracking loops.

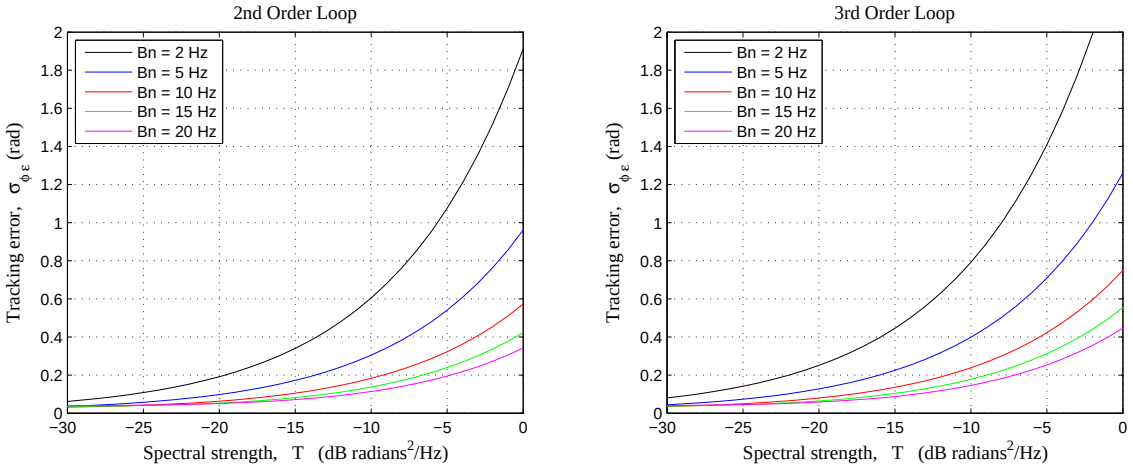

Figure 4.21: Tracking error ($\sigma_{\phi\varepsilon}$) in the presence of phase scintillation and thermal noise for the 2nd and 3rd order PLL's.

In order to evaluate the performance of a receiver regarding the loss of lock state, a threshold for the spectral strength (T) must be defined based on the noise bandwidth and the spectral index (p). From [61], the linear phase tracking error threshold for the Costas loop can be given as

$$\sigma^2_{\phi\varepsilon}\,|_{Th} = \left(\frac{\pi}{12}\right)^2 \quad radians^2 \tag{4.47}$$

Equation (4.47) suggest that the phase tracking error, $\sigma_{\phi\varepsilon}\,|_{Th}$, should not exceed $\pi/12$ otherwise the receiver is likely to loose lock. Comparing (4.46) and (4.47), the threshold spectral strength is found as

$$T\,|_{Th} = \frac{1}{\pi}\left(\sigma^2_{\phi\varepsilon}\,|_{Th} - \sigma^2_{\phi T}\right).k f_n^{p-1} \sin\left(\frac{(2k+1-p)\pi}{2k}\right) \tag{4.48}$$

The threshold spectral strength (T) is plotted in Fig. 4.22 as a function of the noise bandwidth, Bn, and the spectral index, p, for a second and third order PLL. The same parameter values were used for this graph as used to generate Fig. 4.21. In Fig. 4.22, it can be seen that the loop performance is more dependent on the noise bandwidth compared to the spectral index (p). It was also found that $T\,|_{Th}$ was higher for the 2nd order loop compared to the 3rd which shows that, during phase scintillation, the 2nd order loop will

give more robust performance compared to the 3rd order loop due to accommodating a high threshold spectral strength. It was also reported by [61] that for minimum phase error, the 2nd order loop is better than the 3rd order loop.

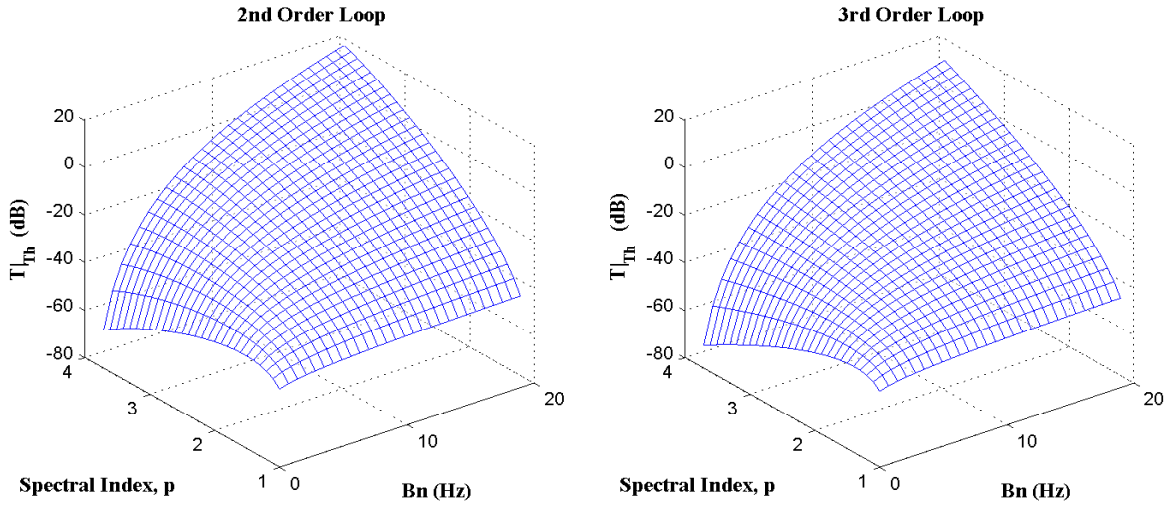

Figure 4.22: Threshold spectral strength ($T\,|_{Th}$) as a function of the noise bandwidth and spectral index for the 2nd and 3rd order PLL's.

4.7.2 Amplitude Scintillation Effects

In the previous section, the effects of the phase scintillation and thermal noise on the carrier tracking loops were observed. In this section, the tracking error variance equations for the Costas tracking loop will be derived as a function of the amplitude scintillation, S_4. Since the joint statistics of the amplitude and phase scintillations are unknown, so both of these components are usually dealt with separately and therefore amplitude scintillation effects are translated to the thermal noise due to the amplitude fluctuations degrading the C/N_o of the received signal. Neglecting the oscillator noise, the tracking error from phase and amplitude scintillation is

$$\sigma^2_{\phi\varepsilon} = \sigma^2_{\phi s} + \sigma^2_{\phi T} \tag{4.49}$$

In the case that there are amplitude fluctuations due to scintillation, the thermal noise tracking error variance will be a function of the purturbed signal amplitude, $\tilde{A}$, and from [61] can be given as

$$\sigma^2_{\phi T}(\tilde{A}) = 2T_I B_n(\tilde{A})\sigma^2(\tilde{A}) \tag{4.50}$$

where $\sigma^2(\tilde{A})$ is the noise variance of the Costas discriminator [61] and can be given as

$$\sigma^2(\tilde{A}) = \frac{N_o}{T_I \tilde{A^2}}\left(1 + \frac{N_o}{T_I \tilde{A^2}}\right) \tag{4.51}$$

Using (4.51) in (4.50), the tracking error variance in the presence of amplitude fluctuations can be give as

$$\sigma^2_{\phi T}(\tilde{A}) = 2T_I B_n(\tilde{A}) \times \frac{N_o}{T_I \tilde{A^2}}\left(1 + \frac{N_o}{T_I \tilde{A^2}}\right) \tag{4.52}$$

Normalising the signal amplitude with $\tilde{A_N} = \tilde{A}/A$ where A is the unpurturbed signal amplitude and using the definition $C/N_o = A^2/2N_o$, (4.52) can be transformed to

$$\sigma^2_{\phi T}(\tilde{A}) = \frac{B_n(\tilde{A})}{C/N_o}\left(\frac{1}{\tilde{A_N}^2} + \frac{1}{2T_I C/N_o \tilde{A_N}^4}\right) \tag{4.53}$$

where $B_n(\tilde{A})$ is the noise bandwidth as a function of the perturbed signal amplitude and is

1. Second order loop:

$$B_n(\tilde{A}) = \frac{\omega_n}{2}\left(\frac{\tilde{A_N}^2}{g_N}\zeta + \frac{1}{4\zeta}\right) \tag{4.54}$$

2. Third order loop:

$$B_n(\tilde{A}) = \left(\frac{\tilde{A_N}^2}{g_N}\right)\frac{\omega_n}{1.2} \tag{4.55}$$

where $g_N = g/A$ is the normalised gain factor of the tracking loop [61] and for an ideal case, $g_N = \tilde{A_N}^2$. The overall tracking error variance in the presence of amplitude scintillation can be given as

$$\sigma_{\phi T}^2 = \int_0^\infty \sigma_{\phi T}^2(\tilde{A_N}) f_{\tilde{A_N}}(A_N) dA_N \tag{4.56}$$

Using (4.53) in (4.56)

$$\sigma_{\phi T}^2 = \frac{B_n(\tilde{A})}{C/N_o}\left[\int_0^\infty \frac{1}{\tilde{A_N}^2} f_{\tilde{A_N}}(A_N) dA_N + \frac{1}{2T_I C/N_o}\int_0^\infty \frac{1}{\tilde{A_N}^4} f_{\tilde{A_N}}(A_N) dA_N\right] \tag{4.57}$$

where $f_{\tilde{A_N}}(A_N)$ is the PDF of the signal amplitude and is assumed to follow a Nakagami-m distribution given by

$$f_{\tilde{A_N}}(A_N) = \frac{2m^m A_N^{2m-1}}{\Gamma(m)}.\exp(-mA_N^2) dA_N \tag{4.58}$$

Using (4.58) in (4.57) and integrating (see Appendix A for complete derivation), the final form of (4.57) gives

$$\sigma_{\phi T}^2 = \frac{\bar{B_n}}{C/N_o}\left[\frac{1}{1-S_4^2} + \frac{1}{2T_I C/N_o(1-3S_4^2+2S_4^4)}\right], \qquad \text{radians}^2 \tag{4.59}$$

where $\bar{B_n}$ is the loop design bandwidth and can be adopted from (4.54) and (4.55). Equation (4.59) is only valid for $S_4 < 1/\sqrt{2}$. If we use $g_N = \tilde{A_N}^2$, the outcome of (4.59) will be same regardless of the loop order as only the noise bandwidth, $\bar{B_n}$, needs to be selected in (4.59). The tracking error variance as a function of the amplitude scintillation is plotted in Fig. 4.23 for different C/N_o values. It can be seen that for $S_4 < 0.7$, the effect of amplitude scintillation is very low and not of great concern. However, as the S_4 approaches 0.7 there is a sudden increase in the error variance which points out to the fact that the strong amplitude scintillation may cause some problems and signals with low C/N_o are more likely to be affected by the scintillation.

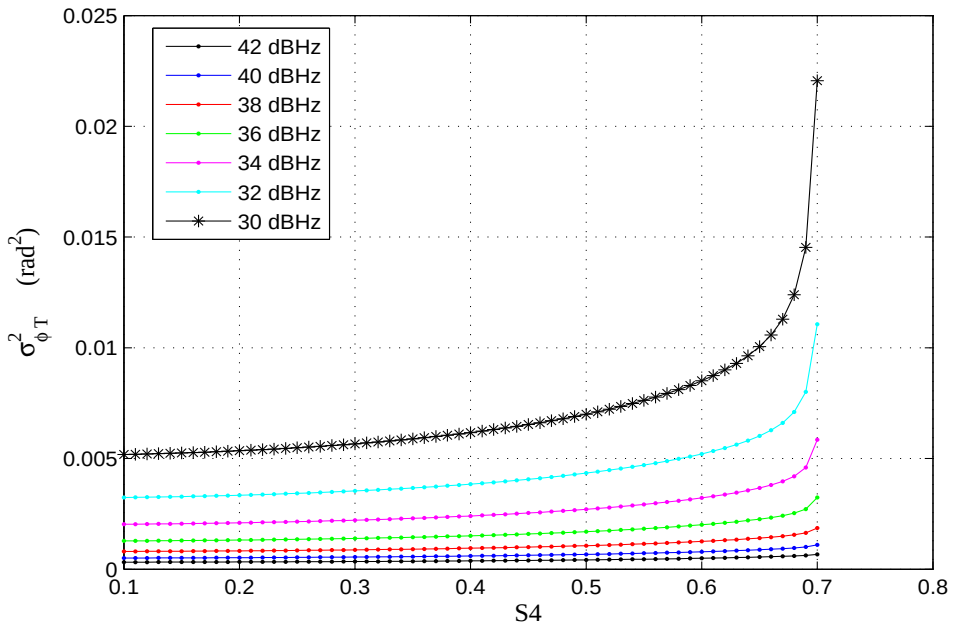

Figure 4.23: Thermal noise tracking error variance in the presence of amplitude scintillation.

4.8 Mean Cycle Slip Time & the Probability of Loss of Lock

From [81], the mean cycle slip time for the 1^{st} order PLL can be given as

$$T_{slip} = \frac{\pi^2}{2\bar{B}_n}\rho_e I_o^2(\rho_e) \tag{4.60}$$

where $\rho = 1/\sigma^2_{\phi T}$. The function $I_o(.)$ is the modified Bessel function of the first kind and zero order. From [81], the mean cycle slip time for the higher order loops can be given as

$$T_{slip} = \frac{\pi}{4\bar{\bar{B}}_n}e^{2\alpha\rho} \tag{4.61}$$

where α represents the S/N_o loss and $\alpha = 0.891$ for the 2nd order loop and $\alpha = 0.794$ for the 3rd order loop [81]. In Fig. 4.24, the mean cycle slip time of the 2nd and 3rd order loops is plotted as a function of the tracking error variance for different noise bandwidths. It can be seen that the 3rd order loop is more vulnerable to cycle slips and therefore can loose lock more quickly than the 2nd order loop for large tracking error variances.

Another observation that can be deduced from Fig. 4.24 is that the 2nd order loop has more tolerance towards tracking error variance in terms of the mean time to loose lock and therefore can perform better during scintillation conditions than the 3rd order loop. Using the thermal noise error variance definition in the presence of amplitude scintillation from (4.59), the mean cycle slip time can be given as

$$T_{slip}(\text{scintillation}) = \frac{\pi}{4\bar{B}_n}\exp\left[2\alpha.\frac{C/N_o}{\bar{B}_n}.\left(\frac{2T_IC/N_o(1-S_4^2)(1-3S_4^2+2S_4^2)}{2T_IC/N_o(1-3S_4^2+2S_4^2)+(1-S_4^2)}\right)\right] \tag{4.62}$$

In [61], it is mentioned that if we consider the slipping process as a Poisson distribution, the probability of cycle slip can be given as

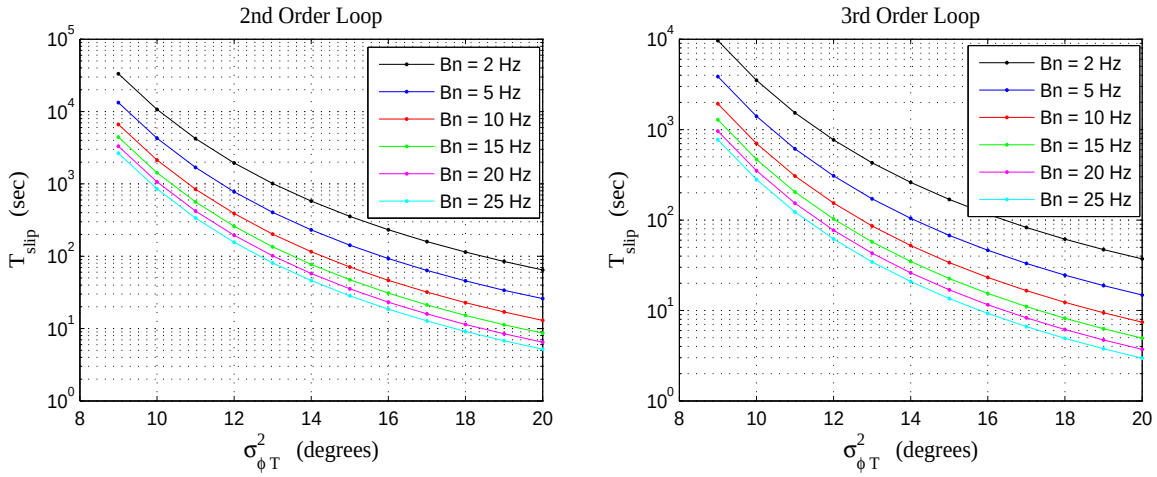

Figure 4.24: Mean cycle slip time as a function of the thermal noise tracking error variance for a 2nd and 3rd order tracking loop.

$$P_{slip} = 1 - \exp(-\tau/T_{slip}) \tag{4.63}$$

where τ is the time in seconds and is used to define the duration of the fade in the signal. Since fading affects the C/N_o of the received signal, the relationship between the unfaded C/N_o and the faded C/N_o is $(C/N_o)_{faded} = F \times C/N_o$ where F is the fade depth. In Fig. 4.25, the P_{slip} is plotted as a function of the fade duration, τ, for different fade depths

for the 2nd and 3rd order tracking loops. Fig. 4.25 shows that, during scintillation, the probability of loss of lock for a 3rd order loop is approximately 10 to 15 % higher than the 2nd order loop which further confirms the fact that the 2nd order loops can provide more robust tracking during scintillation conditions than the 3rd order loop. In the next section, a case study is carried out by implementing these tracking loop designs in Matlab and then tracking the GPS signals to observe how scintillation affects the tracking loop performance.

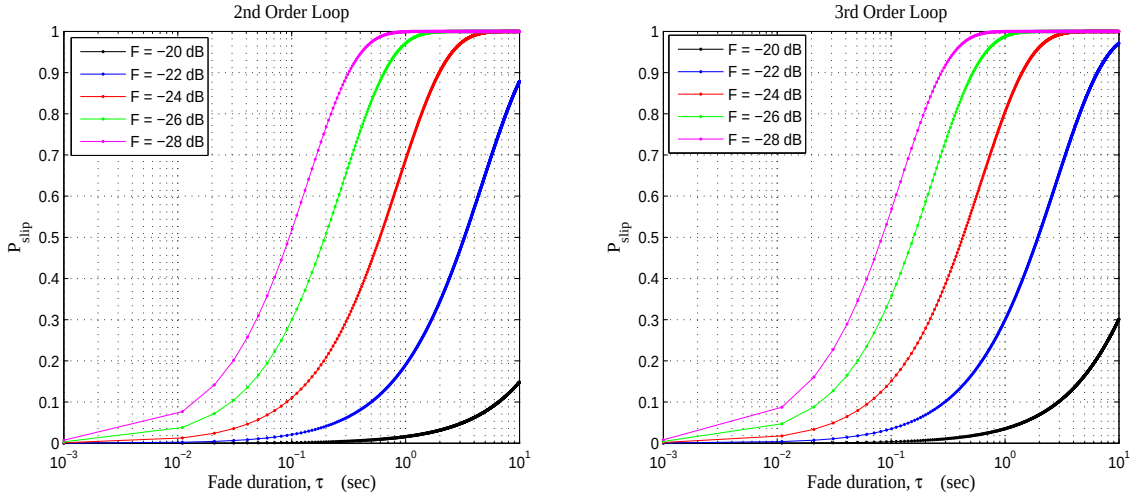

Figure 4.25: Probability of cycle slip in the presence of amplitude scintillation

4.9 Case Study for comparing the tracking loop performance

In order to observe how the scintillation affects the peformance of a GPS receiver, a case study was carried out by using simulated scintillated GPS $L1$ C/A coded signals. For this case study, we used the stand alone PLL and FLL-assisted PLL tracking loop designs by implementing them in Matlab R2011a. The reason for choosing the FLL-assisted PLL in addition to the PLL is due to its robust GPS signal tracking compared to the conventional tracking loops which can help improve the tracking performance as mentioned by many researchers [68, 82]. Apart from these two tracking loop designs, a new method of wavelet

denoising is also used in tracking the GPS signals and the performance is then compared with the PLL and the FLL-assisted PLL.

The 2nd and 3rd order PLL designs are adopted from Fig. 4.19 and Fig. 4.20 whereas the FLL-assisted PLL tracking loop design is explained below.

4.9.1 FLL-aasissted PLL

The PLL uses a phase discriminator to find the difference between the phase of the incoming signal and the local refence signal and uses this in the NCO to find the frequency of the incoming signal. The frequency locked loop (FLL), on the other hand, uses a frequency discriminator to follow the frequency of the incoming signal. The FLL can be implemented using the same tracking loop designs as used for the PLL. The only difference is that the phase discriminator will be replaced by a frequency discriminator. One type of frequency discriminator that can be used to implement an FLL is the maximum likelihood estimator [68] given as

$$\Delta f = \frac{1}{2\pi T_I} \tan^{-1}\left(\frac{cross}{dot}\right) \tag{4.64}$$

where

$$cross = I_{p-1}Q_p - I_pQ_{p-1}$$

$$dot = I_{p-1}I_p - Q_pQ_{p-1}$$

The subscripts p and $p-1$ denote the in-phase and quadrature correlation results at the current and previous integration times. The FLL-assisted PLL loop design works on the principle of simultaneously estimating the frequency and phase errors using the frequency and phase discriminators respectively. These parameters are then passed through the two separate loop filters and the outputs combined together to generate a local replica of the incoming signal. The performance of the FLL-assisted PLL tracking loop is better than the conventional PLL or FLL due to following both the frequency and phase of the incoming signal. If there are rapid phase fluctuations due to phase scintillation or deep power fades due to amplitude scintillations, the PLL or FLL loses lock rapidly compared

to the FLL-assisted PLL tracking loop which can switch to a pure FLL or PLL under scintillation conditions and can thus provide robust signal tracking [82]. A block diagram of the FLL-assisted PLL tracking loop design using a 2nd order FLL and a 3rd order PLL adopted from [68] is shown in Fig. 4.26. The $\Delta\phi$ and Δf represents the phase and the frequency error from the phase and frequency discriminators respectively. These errors are then passed through the two separate loop filters and combined together to generate the local replica of the incoming signal through the carrier generator. The output of the FLL-assisted PLL can be written as

$$y(s) = \frac{w_n^3 + a_{PLL} w_n^2 s + b_{PLL} w_n s^2}{s^3} . \Delta\phi + \frac{w_n^2 + a_{FLL} w_n s}{s^2} . \Delta f \tag{4.65}$$

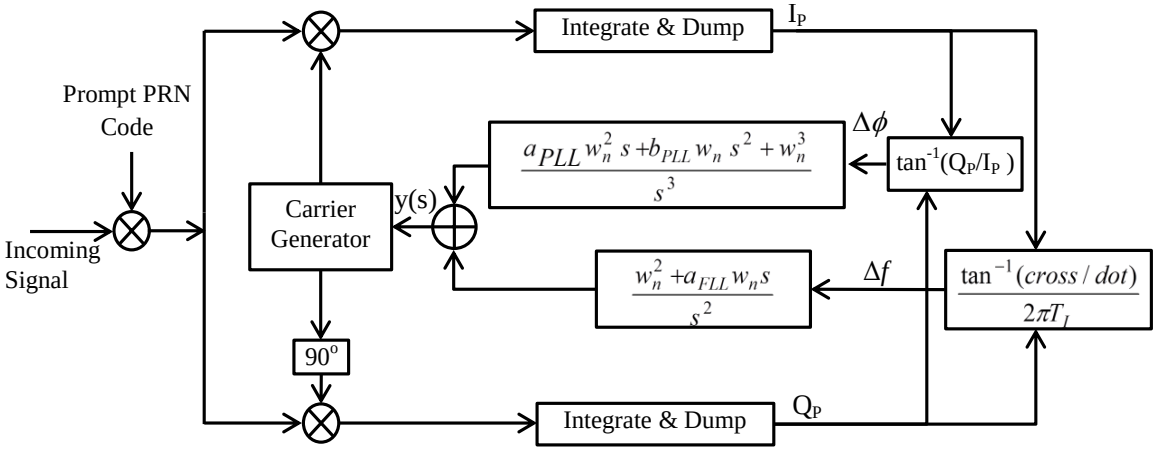

Figure 4.26: FLL-assisted PLL tracking loop design.

4.9.2 Reducing the Carrier Phase Noise using Wavelet-denoising

In order to improve the performance of the tracking loops, a wavelet denoising method is used to improve the carrier phase measurements [83]. It was observed that this technique can provide robust tracking by reducing the noise in estimating the tracking loop parameters but overall is not helpful in recovering the loss of lock during scintillation. The wavelet denoising method uses a wavelet transform for denoising the carrier phase measurements. Wavelet denoising can be accomplished in three steps. Signal decomposition through the discrete wavelet transform (DWT), denoising using soft or hard thresholding or by scales

selection and finally signal reconstruction through the inverse discrete wavelet transform (IDWT).

The wavelet transform can be defined as the multiplication of a signal $x(t)$ by the scaled and shifted versions of a function $\psi(t)$ known as a mother wavelet summed over the complete time interval [84]. Mathematically, it can be expressed as

$$\omega(s,\tau) = \frac{1}{\sqrt{s}} \int_{-\infty}^{\infty} x(t)\ \psi^* \left(\frac{t-\tau}{s} \right) dt \tag{4.66}$$

In the case of a discrete time signal, the discrete wavelet transform can be implemented using the Mallat algorithm [85] or discretizing the mother wavelet and then performing the wavelet tranform through the FFT [84]. In the DWT, the mother wavelet [11] can be discretized as

$$\psi_{m,n}(t) = s_0^{-m/2} \psi \left(\frac{t - n\tau_0}{s_0^m} \right) \tag{4.67}$$

where m and n are the integer values used to sample the $\psi_{m,n}(t)$. For denoising the carrier phase measurementss, we used the Morlet wavelet as a low pass filter to remove the high frequency noise from the phase measurements. Once denoising is done, the original signal can be reconstructed using the IDWT. A complete explanation concerning the wavelet transform and the Morlet wavelets is given in Chapter 6. The block diagrams of the PLL and the FLL-assisted PLL tracking loops, using the wavelet denoising are shown in Fig. 4.27 and Fig. 4.28 respectively. It should be noted that the wavelet denoising was implemented through post processing where the tracked signal was passed through the wavelet blocks for denoising. The main advantage that can be achieved through the wavelet denoising is that it can further reduce the noise in the carrier phase measurements without changing the tracking loop design. A further investigation is needed to implement this in real time which requires the change in the tracking loop design.

4.9.3 Performance Comparison

To compare the performance of the PLL and the FLL-assisted PLL tracking loops, simulated GPS signals were generated by using the Spirent GSS800 multi-GNSS constellation

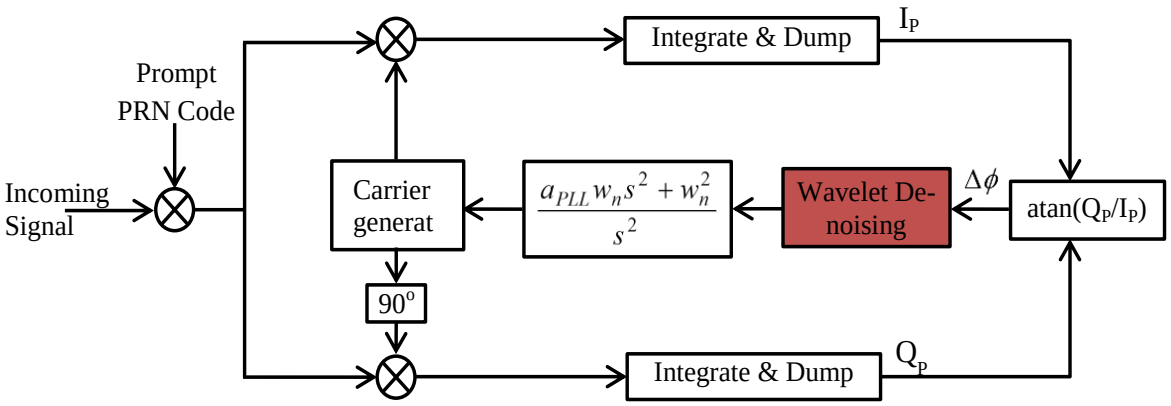

Figure 4.27: PLL tracking loop using wavelet denoising.

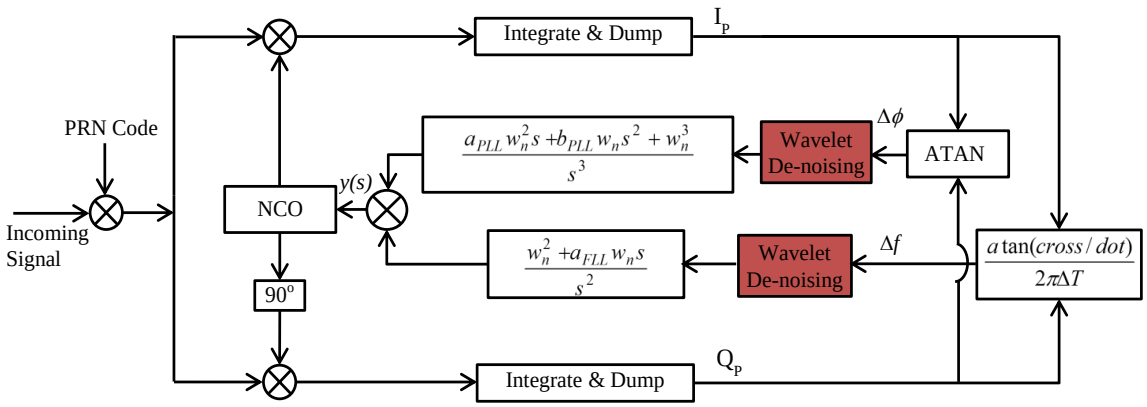

Figure 4.28: FLL-assisted PLL tracking loop using wavelet denoising [83].

simulator. Before the signal generation, the time series of the phase and log-amplitude of varying S_4 and σ_ϕ were simulated using the SPLN (St. Petersburg-Leeds-Newcastle) trans-ionospheric propagation simulator [86] capable of modeling all the scintillation effects. The SPLN simulator uses the following parameters as an input for simulating the scintillation effects: the background electron density profile, the outer scale, the variance of the electron density and the aspect ratios (transverse and longitudinal) of the irregularities, the spectral index of the irregularity anisotropic spatial spectrum, the elevation and azimuth angles and altitude of the satellite, the dip angle of the geomagnetic field and the carrier frequency of the signal. The scintillation parameters were then used in the Spirent simulator for GPS signal generation. The signals at the receiving side were collected using the USRP2 N210 front end device and saved in the binary file format for

post processing. A software development toolkit GNU radio was used to collect the data from the USRP2 running in the Linux environment. The IF frequency and the sampling rate of the USRP2 can be controlled using the GNU radio.The experimental test bed for simulating the scintillated GPS signal is shown in Fig. 4.29.

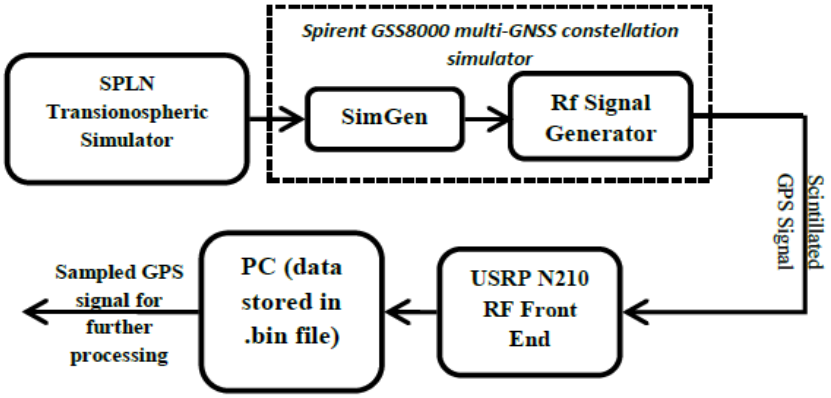

Figure 4.29: Experimental test bed for simulating the scintillated GPS signals using the Spirent and SPLN simulators.

For this particular case study, a 15 minute long GPS $L1$ C/A coded signals were generated in which the amplitude scintillation was less than 0.2 whereas phase scintillation was found to be as high as 0.6 rad. The signals were downconverted at an IF of 2 MHz and sampled at 8 MHz. Tracking was then performed on the collected signal using the PLL and FLL-assisted PLL tracking loop designs by implementing them in Matlab R2011a. For a standalone PLL, a 2nd order PLL design is used whereas, for an FLL-assisted PLL, a 3rd order PLL with a 2nd order FLL is used. The carrier tracking loop parameters used for the PLL and the FLL-assisted PLL are shown in Table 4.1 and Table 4.2 respectively. The code tracking loop parameters for both the designs are shown in Table 4.3.

Table 4.1: Tracking loop parameters for PLL design.

IF frequency	f_{IF} = 2 MHz
Sampling frequency	8 MHz
Damping ratio (ζ)	ζ = 0.7
Noise bandwidth (B_n)	B_n = 10 - 15 MHz (adjustable)
Predection Integration Time (T_I)	T_I = 1 ms
Discriminator	atan(Q_p/I_p)
PLL order	2^{nd}

Table 4.2: Tracking loop parameters for the FLL-assisted PLL design.

IF frequency	f_{IF} = 2 MHz
Sampling frequency	8 MHz
Damping ratio (ζ)	ζ = 0.7
PLL Noise bandwidth ($B_{n,PLL}$)	$B_{n,PLL}$ = 10 - 15 MHz (adjustable)
FLL Noise bandwidth ($B_{n,FLL}$)	$B_{n,FLL}$ = 2 MHz (adjustable)
Predection Integration Time (T_I)	T_I = 1 ms
PLL discriminator	atan(Q_p/I_p)
FLL discriminator	$\frac{1}{2\pi T_I}\tan^{-1}\left(\frac{cross}{dot}\right)$
PLL order	3^{rd}
FLL order	2^{nd}

Table 4.3: Code tracking loop parameters for the PLL and FLL-assisted PLL.

Correlator spacing	0.5 chips
Noise bandwidth ($B_{n,DLL}$)	$B_{n,DLL}$ = 2 MHz
Predection Integration Time (T_I)	T_I = 1 ms
Discriminator	$\frac{\sqrt{I_E^2+Q_E^2}-\sqrt{I_L^2+Q_L^2}}{\sqrt{I_E^2+Q_E^2}+\sqrt{I_L^2+Q_L^2}}$

The data was tracked successfully with no loss of lock until the 9th minute. However, during the 9th and 10th minute, a loss of lock occured for about a few milliseconds for both the PLL and FLL-assisted PLL, as can be seen in Fig. 4.30 showing the phase discriminator error of the two aforementioned tracking loops. It can be seen that both the PLL and the FLL-assisted PLL suffered loss of lock but the FLL-assisted PLL tended to recover more quickly than the PLL due to following the phase of the incoming signal more precisely than the PLL after the loss of lock. This was also discussed by [82] concluding that the FLL-assisted PLL is more robust for signal tracking during scintillation. The PLL, on the other hand, did not follow the phase as precisely as the FLL-assisted PLL and resulted in the loss of 4 to 5 data points after cycle slip recovery. The in-phase component of the navigation data was then extracted using both the PLL and FLL-assisted PLL and the results are shown in Fig. 4.31. In both cases, the navigation data was recovered successfully. The wavelet denoising was then applied to the PLL and FLL-assisted PLL carrier phase measurements and the results are shown in Fig. 4.32. The difference between

the results of the tracking using the wavelet denoising and the actual tracking loops is the reduction of the noise in the carrier phase error which can help in improving the C/N_o of the received signal as can be seen in Fig. 4.33 showing the C/N_o derived using (3.21) for the four tracking loops. In this case study, only a limited data set was used but, in the future, this study will be extended by generating more data sets for different scintillation conditions and then checking the tracking loop performances.

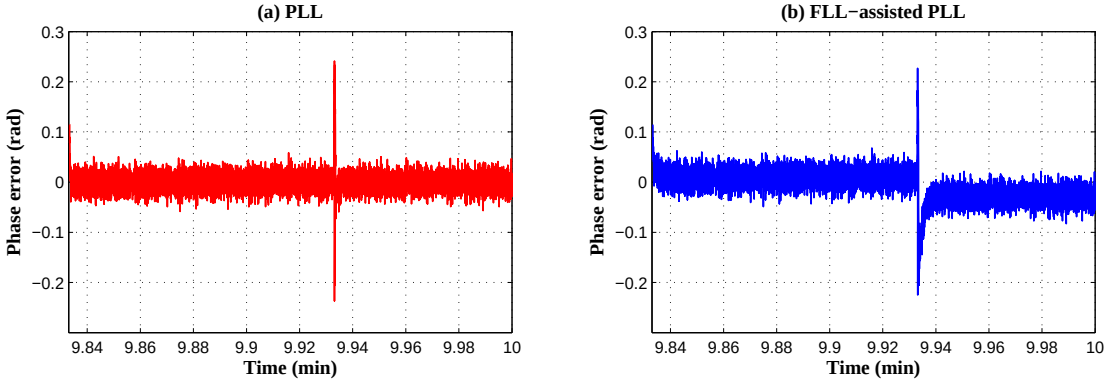

Figure 4.30: Phase error of the PLL and FLL-assisted PLL tracking loops.

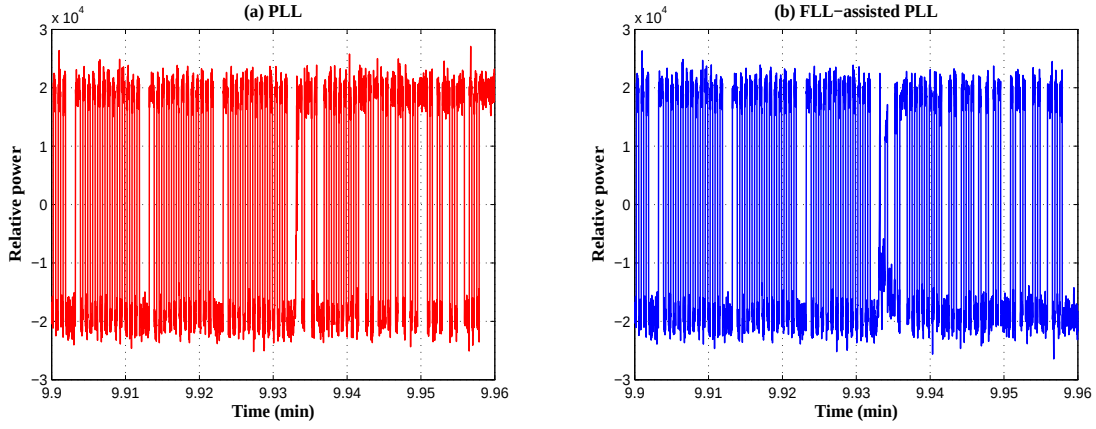

Figure 4.31: In-phase component of the navigation data for the PLL and FLL-assisted PLL tracking loops.

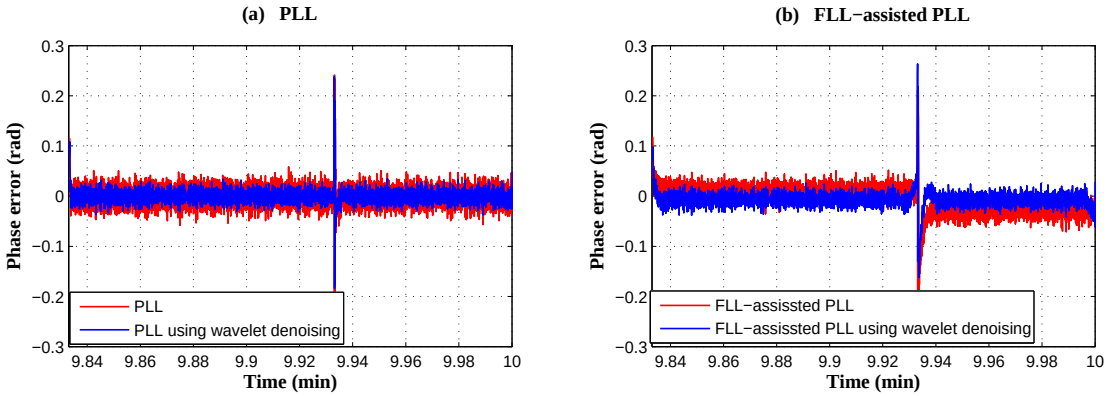

Figure 4.32: Phase error comparison of the PLL and FLL-assisted PLL tracking loops using wavelet denoising.

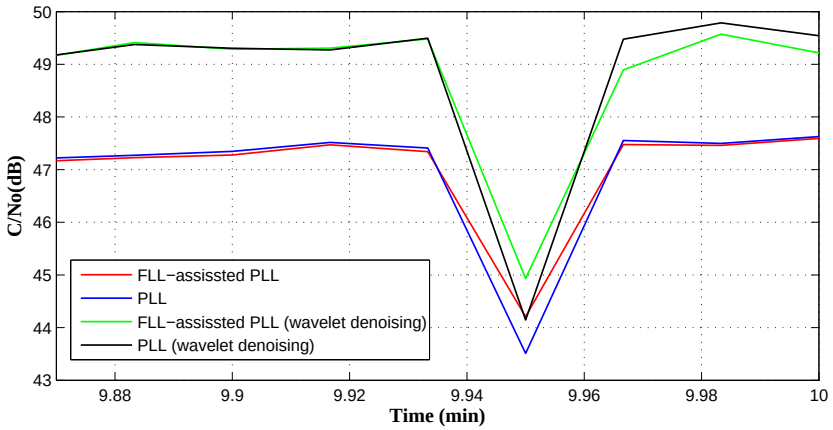

Figure 4.33: C/N_o of the PLL, FLL-assisted PLL, PLL (wavelet denoising) and FLL-assisted PLL (wavelet denoising).

4.10 Chapter Summary

In satellite-based navigation systems, the reliability of the receiver plays an important role in providing the navigation services. Acquistion and tracking are the two main parts responsible for signal acquisition, tracking and extracting the navigation data from the received signals and are both affected by amplitude and phase scintillation. At the acquisition part, the scintillation, particularly of the amplitude, results in deep and frequent power fades which results in poor detection probability. In this chapter, a new acquisition method, i. e., the RBA method is presented which can be used for faster signal acquisition

with improved detection perfromance. Apart from this, scintillation effects on the tracking loops and tracking thresholds for tracking loop loss of lock are also discussed. A case study is also presented in which the performance of the different tracking loops such as the PLL, FLL-assissted PLL, PLL using wavelet denoising and FLL-assissted PLL using wavelet denoising is also carried out and assessed.

Chapter 5

TEC-based Scintillation Indices

5.1 Introduction

The rapid variations of the small scale irregular structures in the ionosphere plasma density not only affects the GNSS signals but also affects satellite communication over a wide range of frequencies and therefore has drawn the interest of researchers from many fields to tackle this problem. The effect is more severe near the auroral zone [87, 88] and equatorial regions [62, 89, 90] during a geomagnetic storm. The occurence of these small scale structures, also known as the ionospheric electron density irregularites, normally follows, on average, the solar cycle being greater at higher levels of geomagnetic activity [91, 92]. These irregularities can range from a few metres to several kilometers in length and can last for long period of times [91]. At low latitudes, the ionospheric irregularities are associated with the equatorial spread F bubbles [93, 94] which cause amplitude and phase fluctuations on signals pass through them [95]. These bubbles are formed shortly after sunset when the low density ionosphere moves towards the upper high density ionosphere and create holes known as bubbles [96]. By contrast, the irregularities at high latitudes are associated with the polar cap patches and auroral arcs which are regions having plasma densities 5 to 10 times larger than the low density F region within the polar cap [92, 97].

In order to explain the propagation of GPS/GNSS signals through an irregular electron density medium in the ionosphere, the theory of wave propagation in a random scattered medium is used by many researchers and different mathematical derivations are used to

relate the wave propagation in a random medium with the wave propagation in the irregular electron density region in the ionosphere [93, 98, 99]. However, for transionospheric signals, it is commonly and conveniently described by using a phase screen model as used in [99, 100] which assumes that the ionospheric irregularities are concentrated within a thin layer (phase screen) at a particular height (often considered as 350 km). From [60, 61], if we consider the phase screen as discrete rod like structures aligned with the Earth's magnetic field lines, then the phase deviations produced by k such structures can be given as

$$\Phi(x) = \sum_{i=1}^{k} \Phi_{oi}\, exp\left[\frac{-(x-x_{0i})^2}{l_i^2}\right] \tag{5.1}$$

where Φ_{oi} is the maximum phase variations, l_i is the scale size of the irregularities and x is the horizontal position along the Earth's magnetic field lines. Then the maximum phase perturbations are associated with the maximum TEC variations [61] and can be given as

$$\Phi_{oi} = 2\pi \times 40.3 \frac{\Delta TEC_{max}}{cf} \tag{5.2}$$

Another approach based on the power law phase screen model was used by [62], according to which the power spectra of the received signal intensity ($\Phi_I(q)$) and phase deviations ($\Phi_P(q)$) can be given as

$$\Phi_I(q) = \Phi_\phi(q) \sin^2\left(\frac{q^2 r_F^2}{8\pi}\right) \tag{5.3}$$

$$\Phi_P(q) = \Phi_\phi(q) \cos^2\left(\frac{q^2 r_F^2}{8\pi}\right) \tag{5.4}$$

where q is the horizontal wave number of the phase fluctuations, $q_0 = 2\pi/l_0$ is an outer scale wavenumber, l_0 is the outer scale size of the irregularities, $r_F = \sqrt{2\lambda r}$ is the Fresnel radius and r is the distance between the phase screen and the ground observer which is

usually taken as about 350 km. The parameter $\Phi_\phi(q)$ is the spectrum of the phase screen given as

$$\Phi_\phi(q) = \frac{C_s}{(q^2 + q_0^2)^{-p/2}} \tag{5.5}$$

where C_s is the strength of the phase fluctuations and is proportional to the rms of the electron density fluctuations in the ionosphere. According to [93], phase perturbations in the received signal are both refractive and diffractive in nature, however only the phase deviations produced by the diffraction effect are responsible for phase scintillation and this happens when the transionospheric signals pass through the scintillation producing ionospheric irregularities. The phase perturbations at the receiver due to diffraction effect are typically produced by these irregularities near the first Fresnel radius ($r_F/\sqrt{2}$) at small wave numbers and occur when different phases exciting the phase screen interfere with each other [93]. From (5.5), which relates the strength of the phase fluctuations to the electron density variations also termed as the TEC variations (rate of change of TEC), if the change in TEC is known then it can be used to find the phase perturbations as discussed by many researchers [34, 91, 101, 102]. From section 3.6, if we denote ϕ as the phase, then the TEC can be found from the carrier phase measurements using

$$\phi = -\frac{q^2}{2c\varepsilon m_e f(2\pi)^2} \int_{rx}^{sat} N_e ds_0 \tag{5.6}$$

where q is the charge of an electron, c is the speed of light, ε is the permitivity of free space and f is the carrier frequency of the signal. The term $\int_{rx}^{sat} N_e ds_0$ is the TEC between the satellite and the receiver path. After substituting constant values, (5.6) can be simplified to

$$\phi = -2\pi \frac{40.3}{cf} TEC \qquad \text{(radians)} \tag{5.7}$$

From [62], the strength of the phase fluctuations, $\delta\phi$, can be found if the change in TEC, i.e., δTEC over a certain time interval is used in (5.7). The index used to define the phase perturbations in the received signal is the phase scintillation index denoted by σ_ϕ and can be defined as the standard deviation of $\delta\phi$ over a certain time interval.

The study of TEC variations and their association to scintillation goes back several decades [91, 98, 101, 103] but the TEC derived scintillation index was first proposed by [102]. The index proposed by [102] was denoted by I_{RoT} and derived from the dual frequency GPS observations using RINEX data from the International GPS Geodynamics Service (IGS). [102] used the rate of change of TEC (RoT) at a 1 min interval using the difference between the GPS $L1$ and $L2$ carrier phase observations for quantifying the I_{RoT} values. The RoT calculated by [102] was given by

$$RoT = S.\ [\ (\ \phi_1(t_i) - \phi_1(t_{i-1})\ ).\lambda_1\ -\ (\ \phi_2(t_i) - \phi_2(t_{i-1})\ ).\lambda_2\ ] \tag{5.8}$$

where S is a constant, t_i and t_{i-1} represents the two consecutive epochs and subscripts 1 and 2 are the phase observations from the GPS $L1$ and $L2$ signals. After removing the low frequency TEC fluctuaions from (5.8) by using a HPF, a new scintillation index, I_{RoT}, in (5.9) was calculated by using the 15 min data blocks to show the percentage occurence of phase scintillation.

$$I_{RoT} = 10.rms(RoT) \tag{5.9}$$

It was suggested by [34] that the RoT used for computing I_{RoT} in (5.9) is not sufficient to represent the phase deviations due to small scale irregularities and therefore used the standard deviation of RoT using 5 min time intervals given by

$$ROTI = \sqrt{\langle RoT^2\rangle - \langle RoT\rangle^2} \tag{5.10}$$

The work on TEC was then further followed by [104] in which the author proposed an hourly index $F_p(hr)$ using low latitude data. The $F_p(hr)$ index was computed by taking the mean of an index $f_p(n,hr,i)$ which is the index of the individual satellites using four 15 min intervals given as

$$f_P(n,hr,i) = median\left|\frac{\Delta TEC}{1\ min}\right| \tag{5.11}$$

where n is the satellite number, hr is the hour and $i = 1$ to 4 is the 15 min time section within an hour. The $F_p(hr)$ hourly index was then calculated by taking the mean value of the f_p index of all the satellites in an hour given as

$$F_p(hr) = \frac{\sum_n^{nsat} \left(\sum_i^k \frac{f_p(n,hr,i)}{k} \right)}{nsat(hr)} \tag{5.12}$$

where $nsat$ is the total number of satellites visible in a particular hour in which the mean was taken. The correlation of TEC variations and the occurence of scintillation was then further investigated by [88, 94, 105, 106]. In this regard, [106] suggested that the TEC variations are the best fit for re-defining the new indices for ionospheric perturbations and therefore proposed a new disturbance ionospheric index (DIX) using the temporal and spatial variations of TEC. The DIX proposed by [106] was given as

$$DIX = SF.\sqrt{\frac{1}{N_p.\alpha^2} \sum_{k,l} \left\{ \frac{1}{4} \left(\frac{\Delta\Phi_k}{M_k \Delta t} + \frac{\Delta\Phi_l}{M_l \Delta t} \right)^2 + \eta \left(\frac{\Delta\Phi_k}{M_k \Delta t} - \frac{\Delta\Phi_l}{M_l \Delta t} \right)^2 \right\}} \tag{5.13}$$

where $\Delta\Phi$ is the differential phase, M is the elevation mapping function, N_p is the number of IPP pairs, SF is the scaling factor, η is the tuning factor and k,l are the adjacent epochs. In [106], the DIX was used as an alternate index to represent the phase scintillation activity which was then compared with the conventional phase scintillation index, σ_ϕ, for performance evaluation. The investigation on TEC-based scintillation indices was then furthered by [107] who proposed a new analogous phase scintillation index, $\sigma_{\phi a}$, derived using the time and spatial variations of TEC to represent the phase scintillation activity at high latitudes. It was suggested by [107], that the $\sigma_{\phi a}$ index can be used as an alternative to the conventional phase scintillation index, σ_ϕ, as there was found to exist a strong correlation between the two indices. The index was also successfully used in estimating the tracking error variance of a GPS receiver and hence it was suggested that this index can be used to mitigate the effects of scintillation in GPS receivers and particularly useful due to its low computational cost and easy implementation. In this chapter, the derivation and a comprehensive explanation of the TEC-based analogous phase scintillation index, $\sigma_{\phi a}$,

will be given and it will be validated by using the GPS data from a high latitude region, i.e., Trondheim, Norway (63.41^o N, 10.41^o E) and its performance will then be compared with the conventional phase scintillation index, σ_ϕ, to indicate whether or not it can be used as an alternate to represent the phase scintillation activity.

5.2 TEC measurements from GPS

Pseudorange (ρ) and carrier phase (ϕ) are the two observables in a GPS receiver which can be used to determine the TEC present along a satellite and receiver path. From [108], the pseudorange using single frequency GPS observations can be given as

$$\rho = D + c(b - B + e + E + T + I + v_\rho) \tag{5.14}$$

where D is the true range, c is the speed of light in a vacuum, b is the receiver clock bias, B is the satellite clock bias, e and E are the time delays within the receiver and satellite, T is the tropospheric delay, I is the ionospheric range delay and v_ρ is the noise. The ambiguities in the pseudorange estimation can be removed by taking the difference between the pseudorange observations from the $L1$ and $L2$ carrier frequencies using

$$\rho_1 - \rho_2 = \Delta\rho = c(\Delta e + \Delta E + \Delta I + \Delta v_\rho) \tag{5.15}$$

where the subscripts 1 and 2 represents the pseudoranges of the $L1$ and $L2$ frequencies respectively and the terms with Δ sign are: $\Delta e = e_1 - e_2$, $\Delta E = E_1 - E_2$, $\Delta I = I_1 - I_2$, $\Delta v_p = v_{p1} - v_{p2}$. Re-arranging (5.15) will give

$$\Delta I = \frac{\Delta\rho}{c} - \Delta e - \Delta E - \Delta v_\rho \tag{5.16}$$

Equation (5.6) can also be used to find the delay incurred by the ionosphere into the signals passing through it. If we use group delay measurements, then the negative sign

in (5.6) will replaced by the positive sign and the term ϕ can be replaced by the term I representing range delay and can be given as

$$I = \frac{q^2}{2c\varepsilon_0 m_e f^2 (2\pi)^2} \text{TEC} \tag{5.17}$$

where $TEC = \int_{rx}^{sat} N_e ds_0$ is the total electron content along a slant path between the satellite and receiver and f is the carrier frequency of the received signal. If the range delay is estimated using the $L1$ and the $L2$ carrier frequencies, then the difference between the two can be given as

$$\Delta I = I_1 - I_2 = \frac{q^2}{2c\varepsilon_0 m_e f_1^2 (2\pi)^2} TEC - \frac{q^2}{2c\varepsilon_0 m_e f_2^2 (2\pi)^2} TEC \tag{5.18}$$

$$\Delta I = \frac{q^2}{8\pi^2 c\varepsilon_0 m_e} \left(\frac{f_2^2 - f_1^2}{f_1^2 f_2^2} \right) TEC \tag{5.19}$$

where f_1 is the $L1$ frequency and f_2 is the $L2$ frequency. After combining (5.16) and (5.19), the TEC using the dual frequency GPS observations can be found as

$$TEC = \frac{8\pi^2 \varepsilon_0 m_e}{q^2} \left(\frac{f_1^2 f_2^2}{f_2^2 - f_1^2} \right) [\Delta\rho - c(\Delta e - \Delta E - \Delta v_\rho)] \tag{5.20}$$

Equation (5.20) can be used to measure the TEC using the pseudorange observations. Analogously, it can also be measured using the carrier phase measurements. From [108], the carrier phase of the received signal can be found as

$$\lambda\phi = D + c(b - B + e + E + T - I + v_\phi) + m\lambda \tag{5.21}$$

where λ is the wavelength, $m\lambda$ is the phase ambiguity and v_ϕ is the phase noise. The difference between the carrier phases of the $L1$ and $L2$ signals can be given as

$$\Delta\lambda\phi = \lambda_1\phi_1 - \lambda_2\phi_2 = c(\Delta e + \Delta E + \Delta v_\phi - \Delta I) + \Delta m\lambda \tag{5.22}$$

where $\Delta v_\phi = v_{\phi 1} - v_{\phi 2}$ and $\Delta m\lambda = \Delta m_1\lambda_1 - \Delta m_1\lambda_1$. Re-arranging (5.22) will give

$$\Delta I = -\frac{\Delta\lambda\phi}{c} + \frac{\Delta m\lambda}{c} + \Delta e + \Delta E + \Delta v_\phi \tag{5.23}$$

Comparing (5.18) and (5.23), the TEC using the carrier phase measurements an be given as

$$TEC = \frac{8\pi^2\varepsilon_0 m_e}{q^2}\left(\frac{f_1^2 f_2^2}{f_2^2 - f_1^2}\right)[\, c(\Delta e + \Delta E + \Delta v_\phi) + \Delta m\lambda - \Delta\lambda\phi\,] \tag{5.24}$$

Equation (5.20) and (5.24) can be used to find the TEC using either the pseudorange or carrier phase observations in a receiver. It should be noted that the TEC calculated using (5.20) and (5.24) will be along a slant path.

5.3 Analogous Phase Scintillation Index

The TEC estimated from the dual frequency GPS observations using (5.20) and (5.24) are based on the slant path and therefore the TEC estimated from these equations can also be termed as slant TEC (STEC). In order to convert the TEC measurements made along the slant path to vertical TEC (VTEC), an elevation mapping function $M(E)$ [106] is used given as

$$M = 1/M(E) = \left(1 - \left(\frac{R_e \cos^2 E}{R_e + h_{IPP}}\right)\right)^{1/2} \tag{5.25}$$

where R_e is the radius of the earth (6378.1 km) and h_{IPP} is the height of the ionospheric pierce point generally taken as 350 km [109]. The relationship between the TEC measued along the slant path and the vertical TEC can be given as

$$VTEC = M \times TEC \tag{5.26}$$

Upon taking the time derivative of VTEC:

$$\frac{\Delta VTEC}{\Delta t} = M\frac{\Delta TEC}{\Delta t} + TEC\frac{\Delta M}{\Delta t} \tag{5.27}$$

From [107], if we assume that the IPP is moving along a horizontal direction x, the TEC differential can be given as

$$\Delta TEC = \frac{\partial TEC}{\partial x}\Delta x + \frac{\partial TEC}{\partial t}\Delta t \tag{5.28}$$

Upon taking the time derivative, (5.28) will be transformed to

$$\frac{\Delta TEC}{\Delta t} = \frac{\partial TEC}{\partial x}.\frac{\Delta x}{\Delta t} + \frac{\partial TEC}{\partial t} \tag{5.29}$$

Assuming $v_{pp} = \Delta x/\Delta t$ as the velocity of the IPP, (5.29) will be reduced to

$$\frac{\Delta TEC}{\Delta t} = \frac{\partial TEC}{\partial x}.v_{pp} + \frac{\partial TEC}{\partial t} \tag{5.30}$$

Using (5.30) in (5.27)

$$\frac{\Delta VTEC}{\Delta t} = M\left[\frac{\partial TEC}{\partial x}v_{pp} + \frac{\partial TEC}{\partial t}dt\right] + TEC\frac{\Delta M}{\Delta t} \tag{5.31}$$

The term $TEC(\Delta M/\Delta t)$ in (5.31) represents the very low frequency TEC fluctuations and can be neglected [107]. The remaining part of (5.31) not only represents the high frequency TEC fluctuations due to scintillation producing ionospheric irregularities but also contain the low frequency TEC fluctuations due to slowly varying background ionosphere, satellite-receiver clock errors, Doppler shift etc. In order to remove the low frequency TEC fluctuations, (5.31) was high pass filtered [107]. The high pass filter used here was the 2nd order Butterworth filter with a cut-off frequency of 0.1 Hz. The HPF version of (5.31) [107] can be represented as

$$VTEC_{HPF} = M(E)\left[\frac{\partial TEC}{\partial x}v_{pp} + \frac{\partial TEC}{\partial t}dt\right]_{HPF} \tag{5.32}$$

It was mentioned by [34] that the change in TEC due to small scale irregularities is often very small and fluctuates around a very small value. Therefore, to identify the effect

of scintillation producing ionospheric irregularities, the standard deviation of (5.32) was taken:

$$\sigma_{VTEC_{HPF}} = \left[\frac{1}{n-1} \sum_{i=1}^{n} \left(VTEC_{HPF} - \overline{VTEC}_{HPF} \right)^2 \right]^{\frac{1}{2}} \tag{5.33}$$

It should be noted that (5.33) will still be effected by the noise at low elevation angles. In order to reduce this noise, (5.33) was multiplied by the elevation weighting function $\varpi\left(\chi\left(M\right), v_p\right)$ to derive the final equation for the analogous phase scintillation index $\sigma_{\phi a}$ [107] given as

$$\sigma_{\phi a} = \left[\varpi\left(\chi\left(M\right), v_p\right) \times \sigma_{VTEC_{HPF}} \right] \tag{5.34}$$

From [107], the elevation weighting function, $\varpi\left(\chi\left(M\right), v_p\right)$, is given as

$$\varpi\left(\chi\left(M\right), v_p\right) = \frac{2\pi S\ 40.3}{cf} \times \left[\chi\left(M\right), v_{pp}\right] \tag{5.35}$$

where S is constant whose value is taken as 0.003 from [107], v_{pp} is the IPP velocity (see Appendix C for explanation) and $\chi(M)$ is the elevation mapping given as

$$\chi\left(M\right) = \frac{1}{\left(M_i(E) M_{i+1}(E) \right)^2} \tag{5.36}$$

where $M_i(E)$ and $M_{i+1}(E)$ represents the elevation angle from the current and future states respectively.

5.4 Methodology

In order to validate the proposed TEC-based analogous phase index ($\sigma_{\phi a}$) and to compare its performance with the standard phase scintillation index, σ_{ϕ}, we used the data from a GPS receiver station installed in Trondheim, Norway (63.41^o N, 10.4^o E) shown in Fig. 5.1. This receiver station is one of the many receiver stations (shown in Fig. 5.1) installed at high latitudes for recording the scintillation activity as part of the EPSRC (Engineering and Physical Science Research Council) Grant EP/H004637/1. The GPS receiver used to

record the data was a NovAtel GISTM-based GSV 4004B dual frequency GPS receiver which can log data for both the L1 (1575.42 MHz) and L2 (1227.6 MHz) GPS signals.

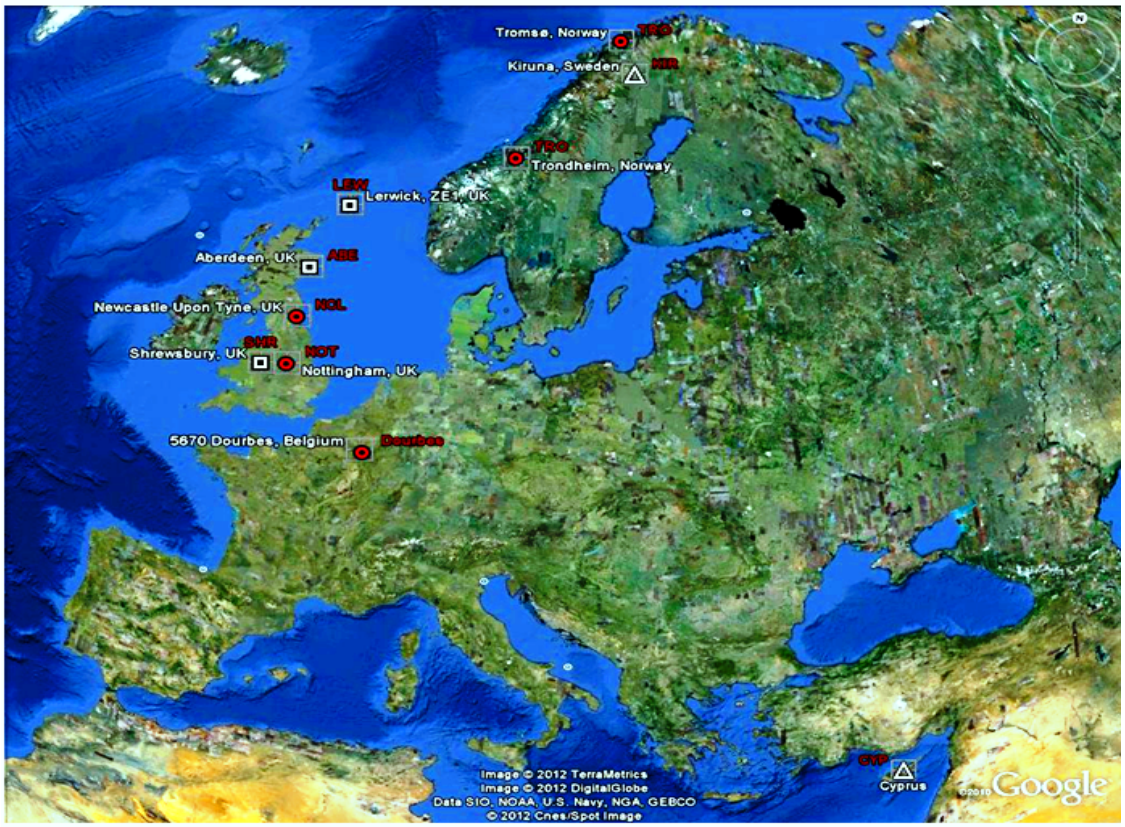

Figure 5.1: Locations of GPS receiver stations installed at various high latitude regions.

Two types of data were logged for analysis. One was the RAWSINB files containing the raw phase and amplitude at 50 Hz and the TEC measurements at 1 Hz used in deriving the $\sigma_{\phi a}$. The other was the ISMR files containing the scintillation indices (σ_{ϕ} and S_4) at a 1 min rate. The experimental used for recording the data at one of the receiver station, i. e., Newcastle Upon Tyne is shown in section 4.2. The same experimental setup was used to record the data at Trondheim. In order to validate the $\sigma_{\phi a}$ as an alternate to represent the phase scintillation intensity for high latitudes and also to compare its performance with the phase scintillation index σ_{ϕ}, the recorded data was parsed based on different geomagnetic conditions. The geomagnetic conditions were defined based on the planetary index Kp. In the results and discussion section, $Kp < 4$ is considered as the absence of a geomagnetic storm, $Kp = 4$ and 5 are considered as a geomagnetic disturbance corresponding to a minor storm and $Kp \geq 6$ is considered as strong storm conditions.

The Kp data used in this analaysis is taken from the World Data Center (WDC) for Geomagnetism, Japan. Since Kp is a global index that can only be used to observe the global geomagnetic activity, in order to confirm the effect of a storm locally at Trondheim, the H component of the magnetic field from the Tromso Geophysical Observatory, UiT - the Arctic University of Norway, Norway was used.

5.5 Results and Discussion

A comparison of the the standard phase scintillation index (σ_ϕ) and the analogous phase index ($\sigma_{\phi a}$) for two different days are shown in Fig. 5.3 and Fig. 5.5. The reason for selecting two different days for the comparison was to judge the performance of the two indices during a strong geomagentic storm ($Kp > 5$) and also when there was no storm or a minor geomagnetic storm ($Kp \leq 5$). Fig. 5.3 shows the performance of the two indices when Kp was less than or equals to 5 whereas Fig. 5.5 shows the comparison when Kp was greater than 5.

For the $Kp < 5$ case, the Kp and the H and Z components of the earth's magnetic field are plotted in Fig. 5.2 on 26 April, 2012. It can be seen that between 00:00 to 00:09 UT, the Kp value varies between 1 to 5 with a minor geomagnetic storm commencing from 00:03 UT and continuing to about 06:00 UT. This led to a disturbance in the earth's magnetic field regionally at Dombass between 00:02 to 00:05 UT as can be seen in the lower panel of Fig. 5.2. The comparison between the σ_ϕ and $\sigma_{\phi a}$ indices of some of the visible PRN's during this time are shown in Fig. 5.3. Although, there was a minor geomagnetic storm for sometime between 00:00 to 09:00 UT, no scintillation activity was observed on any visible PRN during this time. The scintillation occurence pattern, on the other hand, of both the σ_ϕ and $\sigma_{\phi a}$ indices was found to be roughly same for all the PRN's although at certain times they differ in terms of the intensity of scintillation as in the case of PRN's 3, 4, 6, 14, 20, 23 and 32 when the $\sigma_{\phi a}$ is giving over estimated scintillation values compared to the σ_ϕ index. It was also mentioned by [107] that there exists a strong correlation between the $\sigma_{\phi a}$ and σ_ϕ indices for strong geomagnetic storm conditions but that was found to be poor for weak scintillation conditions, i.e., $Kp < 5$.

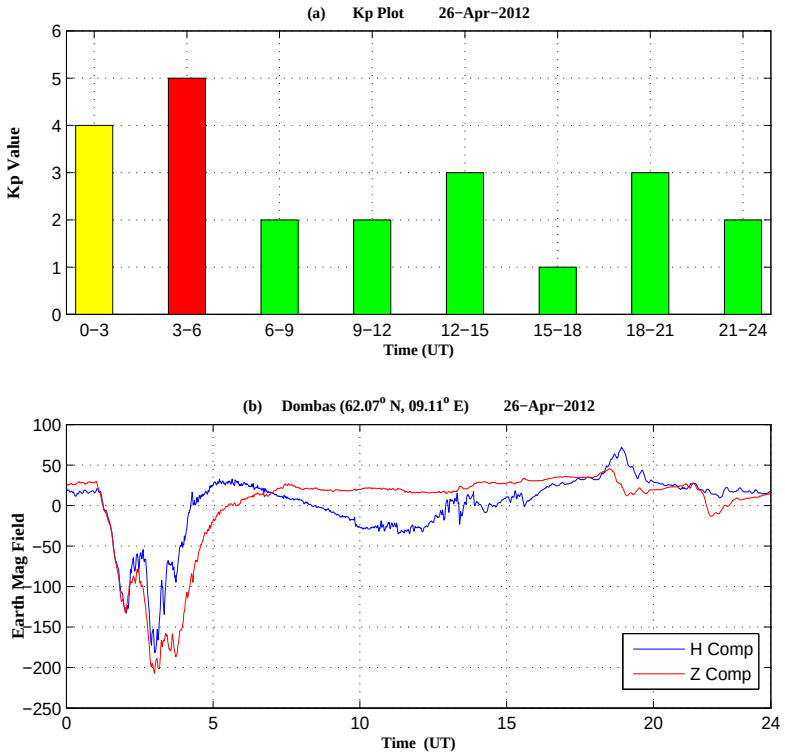

Figure 5.2: Kp plot and the H and Z components of the earth's magnetic field at Dombass, Norway on 26 April 2012.

The σ_ϕ and $\sigma_{\phi a}$ indices were then further compared on 24 April, 2012 during strong geomagnetic storm conditions when Kp was greater than 5 as can be seen in Fig. 5.4. The strong disturbance in the earth's magnetic field in the lower panel of Fig. 5.4 further confirmed that there was a strong geomagnetic storm on 24 April, 2012 started at 00:00 UT and continued to about 04:00 UT. A similar scintillation occurence pattern was also found between the two indices for the PRN's visible between 00:00 to 06:00 UT as shown in Fig. 5.5. Although, an elevation cut-off of 20^o was used in estimating the two indices, it was observed in Fig. 5.5 that when the elevation angle was between 20^o and 30^o, σ_ϕ was giving high scintillation values compared to the $\sigma_{\phi a}$ values which indicates that there is still a noise factor involved in estimating the σ_ϕ values at low elevation angles. This noise factor could be due to the non-optimal filtering or high multipath which was not fully removed and was leading to high scintillation values which cannot be taken as the true scintillation values. distinguishing between the actual scintillation and the noise at low elevation angles.

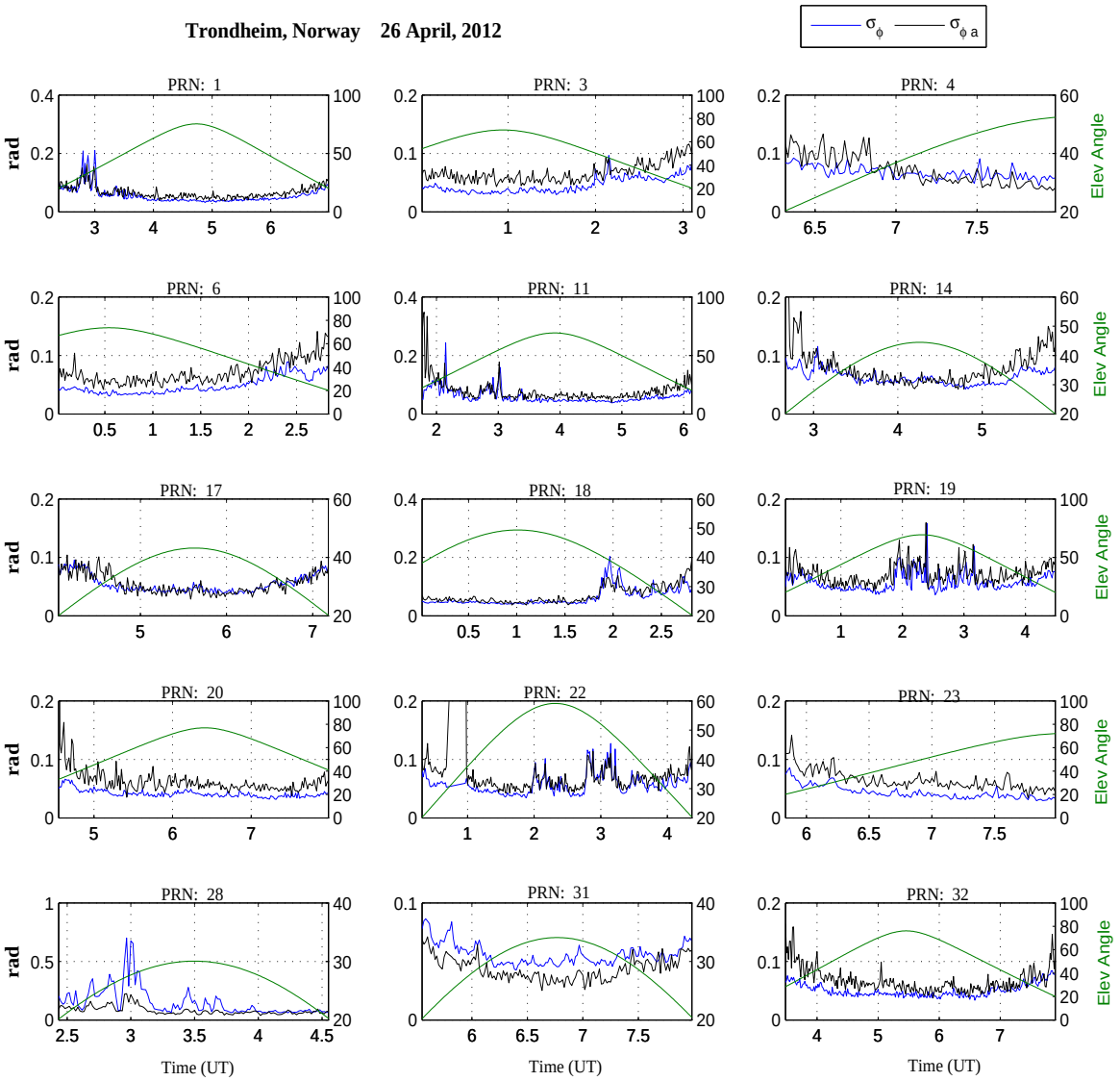

Figure 5.3: Comparison of $\sigma_{\phi a}$ and σ_{ϕ} on 26 April, 2012 for the visible satellites between 00 : 00 and 09 : 00 UT during a severe geomagnetic storm.

It was also reported by [110], that the σ_ϕ index is incapable of distinguishing between the actual scintillation and the noise which is worse at low elevation angles (due to multipath) during weak to strong scintillation conditions.

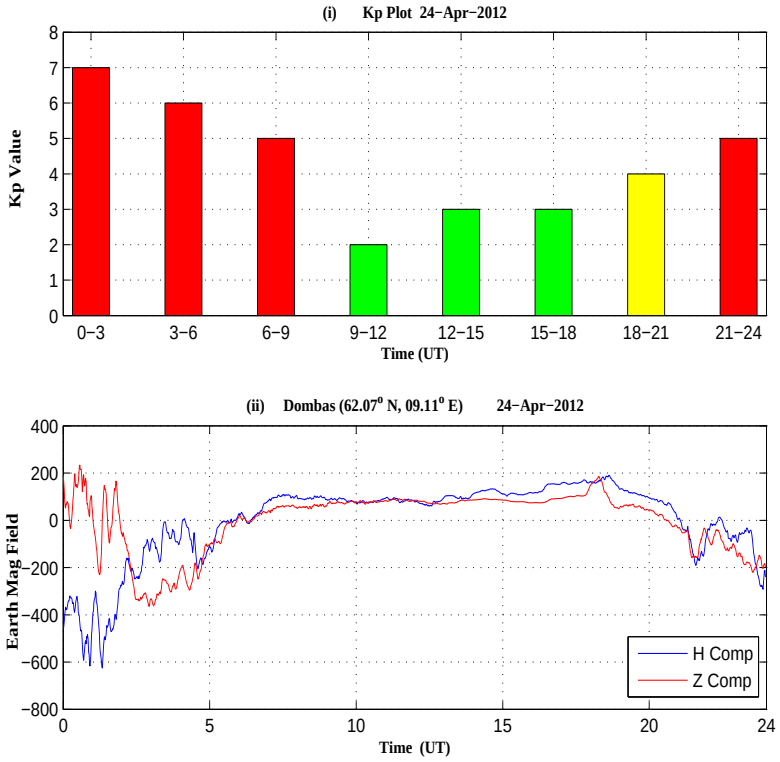

Figure 5.4: Kp plot and the H and Z components of the earth's magnetic field at Dombass, Norway on 24 April 2012.

The similarity of the scintillation occurence pattern between the two indices is then extended by counting the number of occurences of scintillation values greater than 0.2 from October 2011 to September 2012 as shown in Fig. 5.6. This is done for all the satellites that were visible from 00:00 to 23:59 MLT. In Fig. 5.6, high scintillation values can be seen pre-midnight and post midnight due to auroral activity. A strong correlation was found between $\sigma_{\phi a}$ and σ_ϕ pre-mignight and post-night. However, between 13:00 to 17:00 MLT the number of event counts in the case of $\sigma_{\phi a}$ was much higher than that of σ_ϕ. Although several researchers have shown the occurence of scintillation in the post noon period [111], it was considered that, in this case, this was due to a strong geomagnetic storm on 7th March, 9th March, 4th April and 15th July 2012 when large variations in the

earth's H and Z components were observed along with Kp values of greater than 5 and hence was resulting in high scintillation values for $\sigma_{\phi a}$. The number of occurences of the scintillation events for the σ_{ϕ} index, on the other hand, were low during the pre and post noon preiods and this may be due to missing data and frequent loss of lock in the NovAtel receiver PLL during those days which resulted in loss of scintillation values.

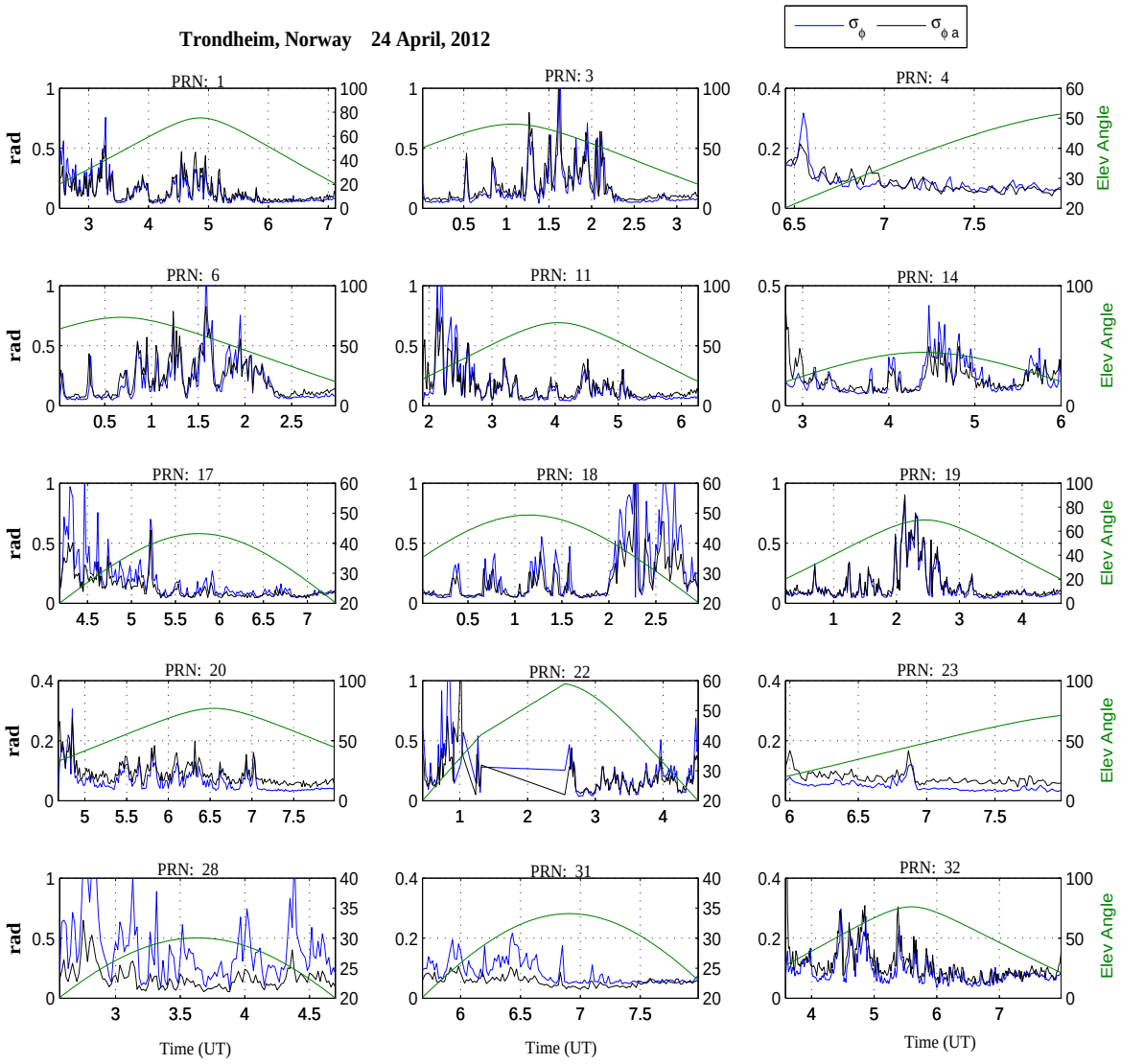

Figure 5.5: Comparison of $\sigma_{\phi a}$ and σ_{ϕ} on 24 April, 2012 for the visible satellites between 00 : 00 and 06 : 00 UT.

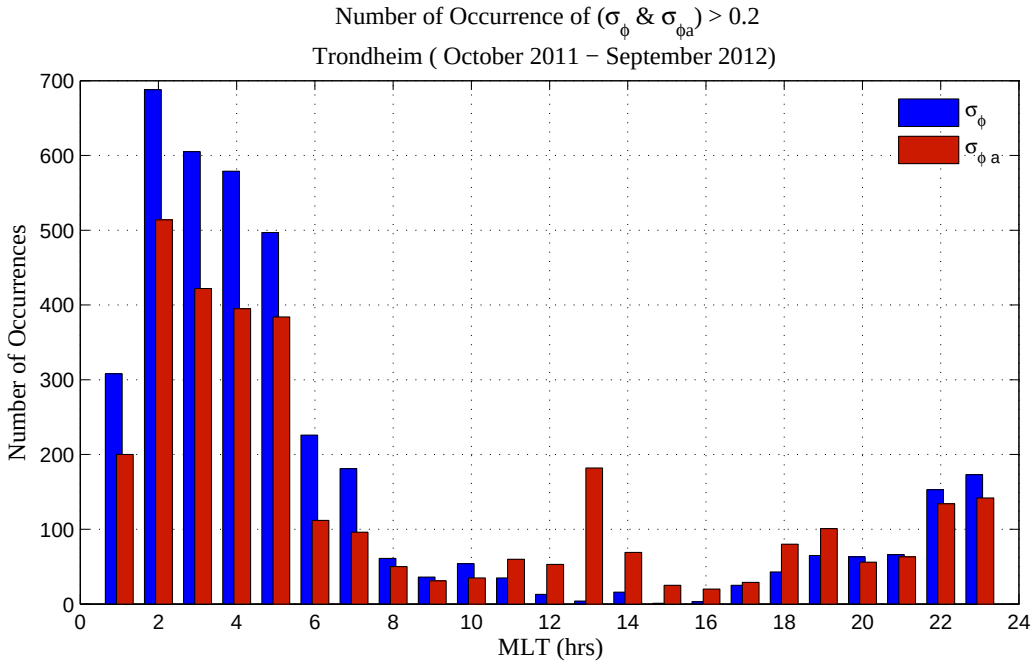

Figure 5.6: Number of occurences of scintillation values for $\sigma_{\phi a}$ and σ_{ϕ} from Spetember 2011 to October 2012 at Trondheim, Norway [107].

To further validate the $\sigma_{\phi a}$ as a good alternative to the standard phase scintillation index, σ_{ϕ}, for high latitude regions, a comparison is made between the two indices in Fig. 5.7 by plotting all the scintillation values from October 2011 to September 2012 by parsing the scintillation values of the two indices based on three geomagnetic conditions; no geomagnetic storm ($Kp < 4$), geomagnetic disturbance ($Kp = 4$), and a strong geomagnetic storm ($Kp \geq 5$).

The scintillation pattern shows a good correlation between the two indices in all three geomagnetic conditions. The corresponding correlation factors between the $\sigma_{\phi a}$ and σ_{ϕ} indices are shown in the lower panel of Fig. 5.7. In the case of $Kp \geq 5$, 78.19 % correlation was found between $\sigma_{\phi a}$ and σ_{ϕ} compared to 59.09 % for the case of $Kp = 4$. By contrast, only 11.26 % correlation was found between $\sigma_{\phi a}$ and σ_{ϕ} for the $Kp < 4$ case. The low correlation between $\sigma_{\phi a}$ and σ_{ϕ} for $Kp < 4$ was due to the unexpected high scintillation values both for $\sigma_{\phi a}$ and σ_{ϕ} which may have been due to non-optimal filtering both for $\sigma_{\phi a}$ and σ_{ϕ} as the indices are derived from two different data sources with different sampling rates.

At high latitudes, the intenstiy of scintillation depends on the increasing Kp value. The higher is the Kp the greater will be the scintillation [95]. To validate this fact using $\sigma_{\phi a}$, the average values of $\sigma_{\phi a}$ with respect to increasing Kp values are shown in the upper panel of Fig. 5.8 for a period of 12 months from October 2011 to September 2012. The increasing values of $\sigma_{\phi a}$ with increasing Kp values validates the dependency of $\sigma_{\phi a}$ on the geomagnetic activity at high latitudes and is also well correlated with the σ_{ϕ} values and the spectral index, p, which is shown in the lower panel of Fig. 5.8. The increasing value of the spectral index, p, can be used to indicate the increasing levels of scintillation.

The seasonal variations of the $\sigma_{\phi a}$ with σ_{ϕ} with respect to increasing Kp values are shown in Fig. 5.9. For this comparison, the one year data (October 2011 to September 2012) was parsed into the following four seasons; autumn (1st October to 21st December), winter (22nd December to 21sr March), spring (22nd March to 21st June), and summer (22nd June to 30th September). The seasonal variations of the spectral index, p, are also shown in Fig. 5.10. The seasonal variations of the $\sigma_{\phi a}$ values in Fig. 5.9 shows their dependence on the Kp values more during spring and autumn than during winter and summer. On the other hand, the spectral index, p, in Fig. 5.10 is also showing a similar kind of behaviour as the $\sigma_{\phi a}$ index during spring and autumn. The seasonal variation dependence of the $\sigma_{\phi a}$ index on the Kp value and its comparison with the σ_{ϕ} index and the p index shows that $\sigma_{\phi a}$ index is a good alternative for representing the phase scintillation activity at high latitudes.

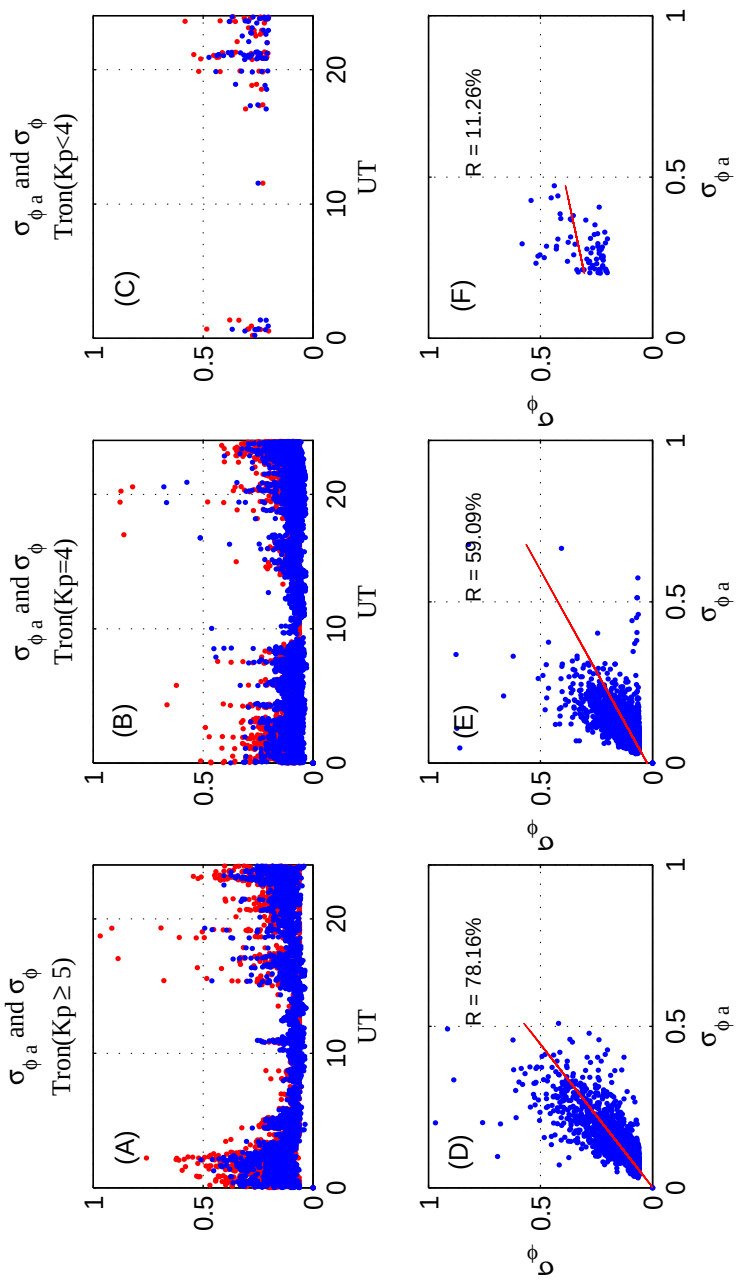

Figure 5.7: Correlation between $\sigma_{\phi a}$ and σ_{ϕ} on three different geomagnetic conditions; no geomagnetic storm ($Kp < 4$), geomagnetic disturbance ($Kp = 4$), and strong geomagnetic storm ($Kp \geq 5$) during September 2011 to October 2012 at Trondheim, Norway [107].

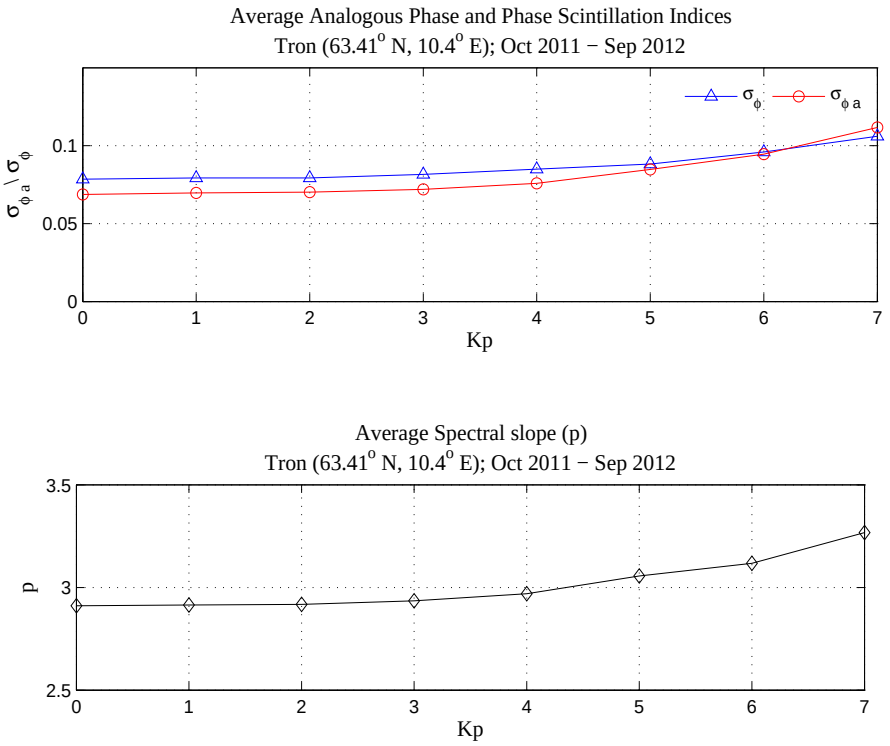

Figure 5.8: Average value of $\sigma_{\phi a}$ and σ_{ϕ} against Kp and the comparison with the spectral index p for a whole year (Sept 2011 to Oct 2012) [107].

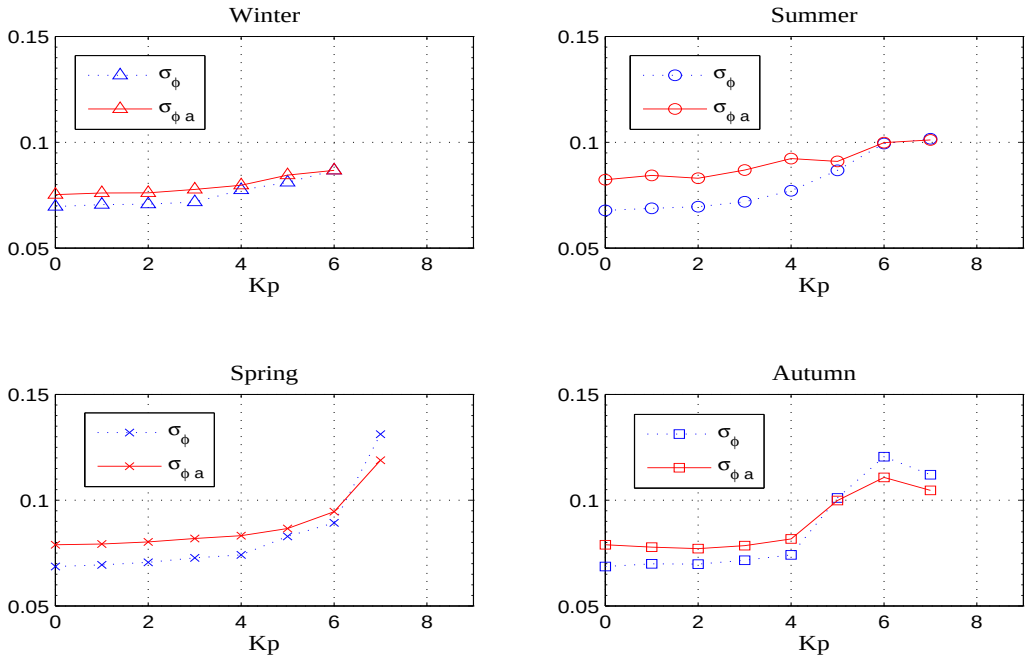

Figure 5.9: Seasonal dependence of $\sigma_{\phi a}$ and σ_{ϕ} as a function of Kp [107].

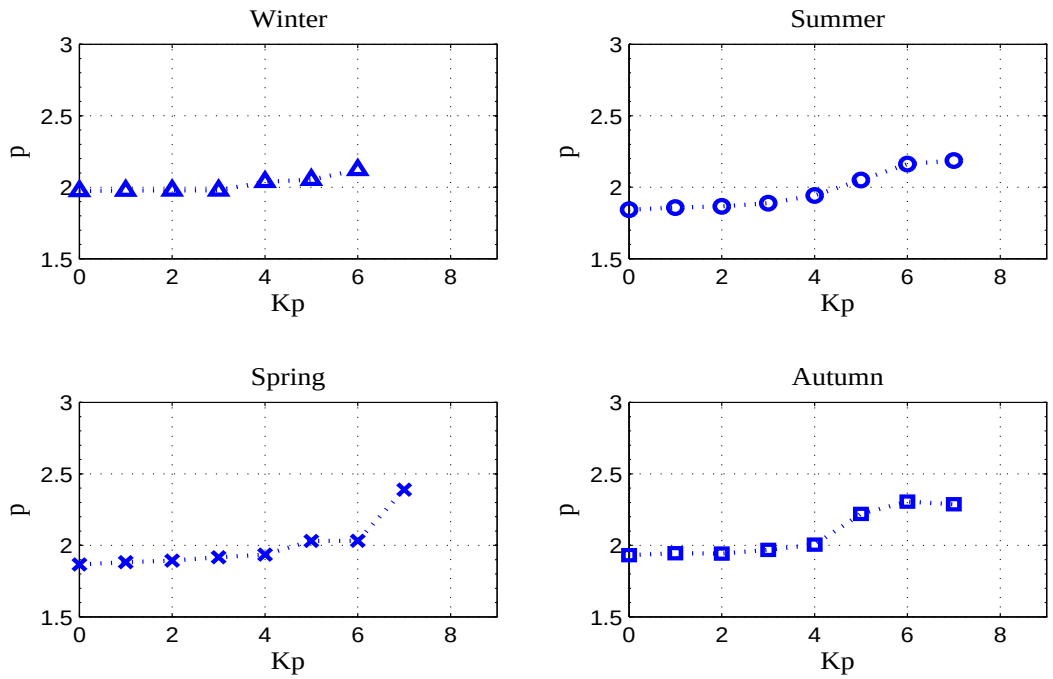

Figure 5.10: Seasonal dependence of the spectral index p as a function of Kp [107].

5.6 Chapter Summary

Most scintillation monitoring receivers (e.g., GISTM receivers) use 50 Hz amplitude and phase observations for quantifying the amplitude and phase scintillation values respectively. These methods are not only computationally intensive but also affect the hardware processing speed and increases the computational cost and therefore are not feasible to implement in the generic GNSS/GPS receivers. In order to overcome this problem, the new analogous phase index was derived as an alternate index to represent the phase scintillation values which was validated by using the data from a receiver station installed at Trondheim, Norway. The main advantage of the analogous phase index is its low implementation cost as it uses dual frequency-based TEC 1 Hz observations. This makes it suitable to implement in the generic geodetic receivers due to the much less processing speed involved compared to the GISTM receivers. This can help in modelling the regional/global ionospheric scintillation and its effects on the GNSS/GPS receivers.

Chapter 6

An Improved TEC-based Phase Scintillation Index

6.1 Introduction

The estimation of amplitude (S_4) and phase (σ_ϕ) scintillation indices involves a detrending process which requires filtering of the raw signal intensity and phase before estimation of the S_4 and σ_ϕ indices [112, 113]. In estimating the S_4 index, the detrending is done by low pass filtering (LPF) the signal intensity whereas in determining the σ_ϕ index, the phase is detrended by using a high pass filter (HPF). In scintillation monitoring receivers, usually fixed cut-off frequencies are used for filtering the raw GPS observations (intensity and phase) which are not entirely appropriate for filtering the signals affected by the scintillation and sometimes may result in the estimation of spurious values specially during geomagnetic storm conditions [114]. Several researchers [110, 115] have tried different cut-off frequencies in detrending the raw intensity and phase observations but this either resulted in under estimation, over estimation or mis-interpretation of the scintillation values as mentioned by [110, 114, 115]. In this regard, several other methods have also been tried to solve the filtering problem and also by designing new scintillation indices such as those discussed in [114, 116, 117] based on wavelet tranform based filtering. However, there are certain problems that still need to be addressed such as the upper limit of the cut-off frequency, sampling rate, computational complexity and, in this respect, we will consider

the wavelet method which can lead to the estimation of appropriate scintillation values involving minimum error.

In this chapter, a new TEC-based phase scintillation index is presented [118] which is an improved version of the analogous phase index, $\sigma_{\phi a}$, and derived using the time and spatial variations of TEC at 1 Hz. The designed index is denoted by $\sigma^{\mathrm{w}}_{\phi a}$ performance of which is validated by comparing it with the previously proposed $\sigma_{\phi a}$ and σ_{ϕ} indices using the data from a European high latitude region, i.e., Trondheim, Norway. The estimation of both the $\sigma_{\phi a}$ and σ_{ϕ} indices involve filtering the raw signal using digital HPF's with a fixed cut-off frequency of 0.1 Hz. In deriving the $\sigma^{\mathrm{w}}_{\phi a}$, rather than using the time-invariant digital HPF's, a wavelet transform is used. Since the $\sigma^{\mathrm{w}}_{\phi a}$ uses the time and spatial variations of TEC in quantifying the scintillation values, the low frequency TEC fluctuations need to be removed to use only the high frequency TEC fluctuations which can then be used to represent the phase deviations due to the scintillation producing ionospheric irregularities. In order to remove the low frequency TEC fluctuations, a wavelet-based filtering approach is used here. The reason for using the wavelet transform for estimating the $\sigma^{\mathrm{w}}_{\phi a}$ is due to the fact that it not only preserves the local features of the signal which helps in reconstructing the original signal without any loss of useful information but can also be used for time-frequency representation of a signal which can help in distinguishing the scintillation and non-scintillation events before quantifying the scintillation values. In this chapter, the wavelet-based time-frequency representation of a signal is also used to define the cut-off frequency limits for filtering the data in case 1 Hz sampling rate is used for quantifying the scintillation values. Another feature of the designed $\sigma^{\mathrm{w}}_{\phi a}$ index is its low computational cost compared to the previously used wavelet-based methods [110, 114, 115] which makes it suitable for use in the tracking error variance estimation.

The wavelet transform was first used in the present context by[116] for generating the scalograms of the amplitude time series to distinguish the background noise and scintillation. This study was focused on amplitude scintillation only which was then further progressed by [114], who proposed a new technique for deriving the amplitude and phase scintillation indices using raw GPS obervations at 50 Hz. In the [114] method, the raw signal intensity and phase were filtered using a continuous wavelet transform rather than

using the high pass filters. However, in the [114] method, the main problem was the use of high sample rate data (50 Hz) which makes this process very complex and time consuming and cannot be considered appropriate to use in the estimation of tracking error variance. Also, the analysis was limited and done only for weak scintillation conditions. In deriving $\sigma_{\phi a}$, the use of low sample rate data (1 Hz) makes it computationally intensive for estimating the phase scintillation values and its performance is also validated under both the weak and strong geomagnetic conditions by using a long data set.

6.2 Problem of Filtering the Scintillated GPS Signals

The $\sigma_{\phi a}$ is shown to be a good index for quantifying the phase scintillation values at high latitudes [107]. However, filtering the non-stationary raw TEC observations using time-invariant digital HPF's can directly affect the $\sigma_{\phi a}$ performance which can result in overestimated scintillation values. The problem of filtering in processing the raw GPS signals affected by the scintillation has been discussed by many researchers [110, 114, 115] and it is generally found that the GPS signals received at high latitudes are sensitive to the way the filtering is accomplished in computing the scintillation indices [110, 115].

In the derivation of amplitude and phase scintillation indices (S_4, σ_ϕ), a default cut-off frequency of 0.1 Hz is used for filtering. This frequency was first used by [119] where the data from auroral and equatorial latitudes were used to study the effects of structured plasmas in the ionosphere on radio wave propagation as part of a study program known as the DNA wideband satellite experiment. In this experiment, the received data was filtered using a 6th order Butterworth filter. The cut-off frequency of 0.1 Hz was then subsequently used by [112, 113] for monitoring the ionospheric scintillation using NovAtel GISTM receivers. In [112], only the raw phase observations were used for filtering but it was also suggested that using the same frequency for filtering the raw signal intensity may not be a good choice and therefore a different cut-off frequency should be used although no further information was given on this. The same cut-off frequency (0.1 Hz) was then used in scintillation receivers [113] for estimating the scintillation indices (S_4, σ_ϕ) without any performance evaluation testing. [110] was the first worker to carefully consider the

filtering problem in computing the amplitude and phase scintillation indices. He concluded that the fixed filtering windows, based on fixed cut-off frequencies, is responsible for erroneous data detrending which may result in over estimation of the phase scintillation values compared to the amplitude scintillation. He also found that the high latitude data is more likely to be affected by the filtering problem compared to low latitudes. In general, the actual cut-off frequency in filtering the raw intensity and phase should be based on the Fresnel frequency (F_f) [114]:

$$F_f = \frac{V_r}{\sqrt{2\lambda r}} \tag{6.1}$$

where V_r is the drift velocity of the irregularities and r is the distance between these irregularites in the ionosphere and the receiver. Due to difficulty in estimating the V_r and r at every given location, typical scintillation receivers uses 0.1 Hz as a default cut-off value in detrending the raw intensity and phase but due to much higher electron density irregularity drift at high latitudes compared to the low latitudes, this value may not be the optimum choice for filtering. [110, 115] have also discussed this in detail by presenting some case studies from high latitudes and also proposed a new phase scintillation index, S_ϕ. The performance of S_ϕ was evaluated using cut-off freqeuncies greater than 0.1 Hz and it was found to be a better indicator of the phase scintillation values compared to the σ_ϕ for high latitude regions. The problem of filtering the raw GPS signals was also addressed by [114, 116, 117, 120] who used a totally different appraoch which obviates the use of time-invariant digital filters. The approach used by [114, 116, 117, 120] for quantifying the scintillation values were based on detrending the raw signal intensity and phase using the wavelet transform and it was found to be a better approach than the conventional filtering approaches. In this regard, [114] proposed a new phase scintillation index σ_{CHAIN} for high latitudes in which the wavelet-based filtering was used for detrending the raw phase observations at 50 Hz.

The various scintillation indices ($S_4, \sigma_\phi, \sigma_{CHAIN}, S_\phi$) proposed above are all computationally intensive due to the use of high sample rate data (e.g. 50 Hz) and the use of the wavelet transform may not be a good choice as it significantly increases the computational cost. For example, if 1 hour of data is to be processed using the wavelet tranform at 50

Hz, then it would require processing 180,000 samples which is not an optimal choice if the scintillation indices are to be used in tracking error variance calculation for using in tracking loop parameters estimation. Further, these indices were tested using a very small data set without considering any changing scintillation conditions which further puts a questions mark whether they can be used to replace the standard indices for quantifying the scintillation values. The $\sigma_{\phi a}^{\mathrm{w}}$ index uses low sample rate data (1 Hz) and uses TEC variations rather than raw phase observations for quantifying the scintillation values which makes it quite suitable to be used as an alternate source of quantifying the phase scintillation values. The performance of the $\sigma_{\phi a}^{\mathrm{w}}$ index is validated by using an year long data set from a high latitude region considering different geomagnetic conditions. Another important thing which is covered in this chapter are the wavelet scalograms generated by using the wavelet statistical energy. The wavelet scalograms are a useful tool for identifying the strength of the TEC variations due to time varying electron density irregularities. The filtering of the signal using the wavelet transform is actually based on these scalograms which are used to separate out the scintillation and the non-scintillation based on high and low frequency TEC fluctuations even before deriving the $\sigma_{\phi a}^{\mathrm{w}}$ index.

6.3 History of Wavelet Transform

The history of the wavelet transform goes back to 1909, when Alfred Haar worked on the orthogonal systems of functions as part of his PhD work which led to the development of the Haar basis function. This was then used by [121] for image compression. However, the work that originally led to the development of the wavelet transform was initiated in the 1970's by J Morlet, an engineer in the French oil company Elf Acquitaine, who used the technique of scaling and shifting of the window functions as an alternate to the short time Fourier transform (STFT) [122]. Morlet, while studying acoustic echoes, found that a fixed window size in the STFT is not appropriate for studying the signal properties in both time and frequency and therefore used varying widths for the window size. In order to give a mathematical basis to his work, Morlet later teamed up with Alex Grossmann [123] to provide a mathematical proof that a signal can be decomposed into wavelet

coefficients by using a waveform of a limited time duration known as a wavelet and can be reconstructed again into its orginial shape from the decomposed wavelet coefficients. The wavelet transform was then used by Mallat and Meyer in 1986 to develop a multi-resolution analysis using wavelets by defining the scaling function for the wavelets. This set the basis for other researchers to design their own wavelets. This idea was then picked up by Ingrid Daubechies [124] to form an important family of wavelets known as *db* wavelets named after herself.

6.4 Wavelet Transform

From [123], the wavelet transform can be defined as the multiplication of a signal $x(t)$ by the scaled and shifted versions of a mother wavelet, $\psi(t)$, summed over a given time interval. A wavelet can be defined as a waveform of a limited duration having an average value of zero. Mathematically, the wavelet transform can be given as

$$c(a,b) = \frac{1}{\sqrt{a}} \int_{-\infty}^{\infty} x(t)\ \psi^* \left(\frac{t-b}{a} \right) dt \tag{6.2}$$

where

- $c(a,b)$ are the wavelet coefficients
- a is the scaling/dilation parameter which determines the time and frequency resolution
- b is the position/translation parameter used to move the wavelet along time t.
- $\psi^*(.)$ is the complex conjugate.

In (6.2), scaling means stretching or compressing the wavelet whereas positioning means multiplying the wavelet, $\psi(.)$, with a signal $x(t)$ at different times by moving along the time axis t. The wavelet transform produces a time-scale view of a signal which can also be represented as a time-frequency view by converting the scale parameters, a, to their corresponding frequency values. The scale parameter, a, is usually defined as the inverse of the frequency. An example of the time-scale view of a wavelet function is shown in

Fig. 6.1 where the wavelets shown in red are represented as a function of the translation parameter b and the scale parameter a.

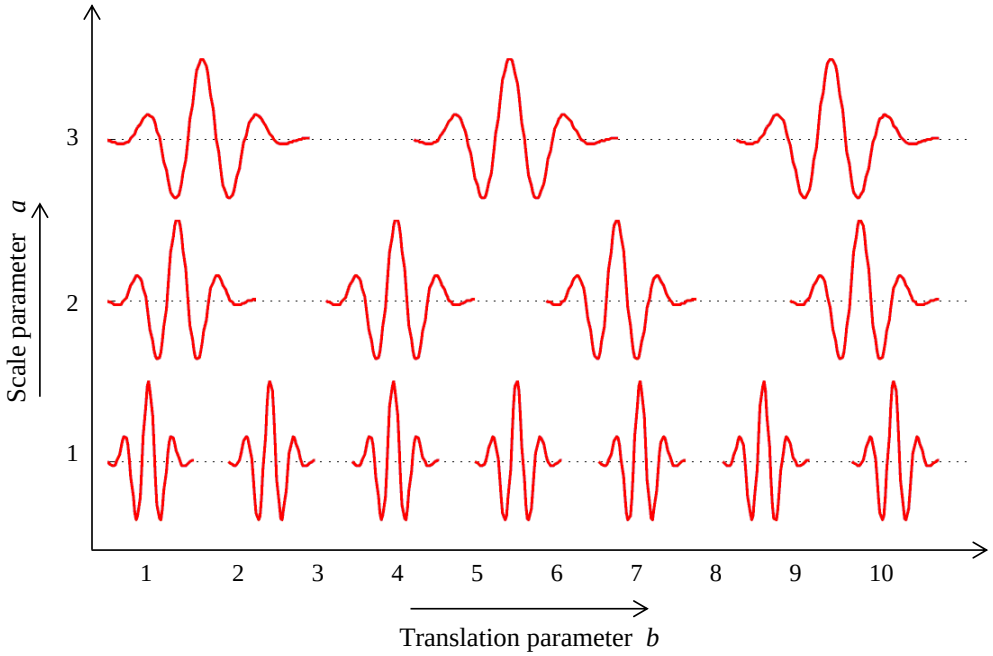

Figure 6.1: Time-scale view of a wavelet as a function of the position/translation parameter b and scale parameter a.

In Fig. 6.1, a high scale implies a more stretched out wavelet which can be used to achieve fine frequency resolution. Similary, a low scale value implies a more compressed wavelet which leads to a better time resolution. Fig. 6.2 shows the time-frequency view of the wavelet transform and the STFT. The only difference between the two is that the wavelet is using variable window sizes rather than fixed window sizes as in the case of STFT. With the STFT, once a window size is chosen, it remains fixed througout the analysis. However, this approach may not be useful for the signals which require a more flexible approach for analyzing both the time as well as the frequency information due to a discontinuity, noise or fast amplitude or frequency variations.

In Fig. 6.2, it can be seen that, for the wavelet transform, the long time regions provide more precise low frequency information whereas the short time regions provide information related to the high frequencies. On the other hand, the STFT only provides constant frequency information. The wavelet transform results in wavelet coefficients

which can then be used to reconstruct the original signal using the inverse wavelet transform (IWT) given below

$$x(t) = \frac{a}{C_\delta} \int_{-\infty}^{\infty} \int_{-\infty}^{\infty} \frac{1}{\sqrt{a}} c(a,b) \psi \left(\frac{t-b}{a} \right) \frac{dadb}{a^2} \tag{6.3}$$

where C_δ is the admissibility constant. For the IWT to hold, the C_δ must obey the following condition

$$C_\delta = \int_{-\infty}^{\infty} \frac{|\hat{\psi}(\omega)|^2}{|\omega|} \, d\omega < \infty \tag{6.4}$$

where $\psi(\omega)$ is the Fourier transform of the wavelet function. There are several wavelet functions which are used for computing the wavelet transform. The most well-known wavelets used are Morlet, Paul, Haar, Meyer and Daubechies. In our analysis we used the Morlet wavelet as our mother wavelet for computing the wavelet transform whose complete description is given below.

6.5 Morlet Wavelet

The Morlet wavelet is composed of an exponential function which is multiplied by a Gaussian window [125]. The main advantage of using the Morlet wavelet is its non-orthogonality and fine time-frequency resolution which are very helpful in observing the high and low frequency variations in the time series of a signal. This property can

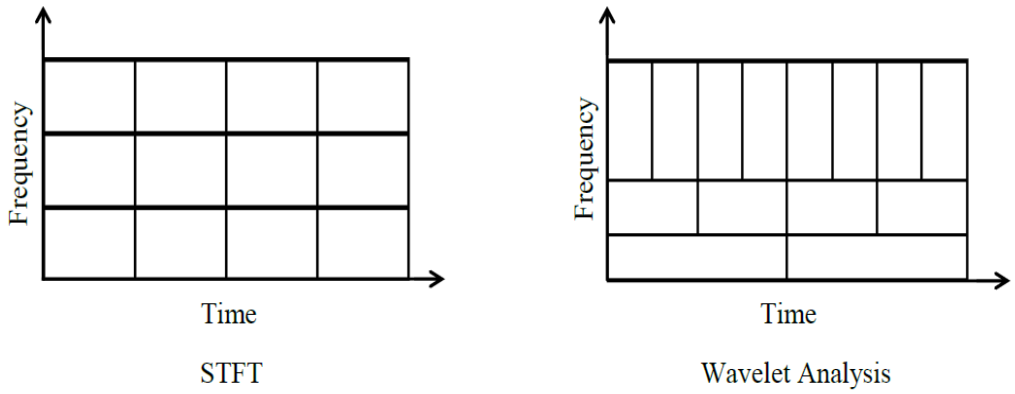

Figure 6.2: Time-frequency view of the STFT and the wavelet transform.

help in distinguishing between the scintillated and non-scintillated signals [114, 118]. This property of the Morlet wavelet is very userful in our case as the $\sigma^{w}_{\phi a}$ uses the high frequency TEC fluctuations for quantifying the phase scintillation values. The Morlet wavelet, in our case, can be used to distinguish the high frequency TEC fluctuations from the low frequency ones which represent noise in the signal and need to be removed. The mathematical form of the Morlet wavelet can be given as

$$\psi(t) = \pi^{-0.25} exp\left(i\omega_0 t - \frac{1}{2}t^2\right) \tag{6.5}$$

where w_0 is the non-dimensional frequency which is taken as 6 Hz from [84]. The real and complex part of the Morlet wavelet are shown in Fig. 6.3. In frequency domain, the Fourier transform of the scaled Morlet wavelet taken from [84] can be given as

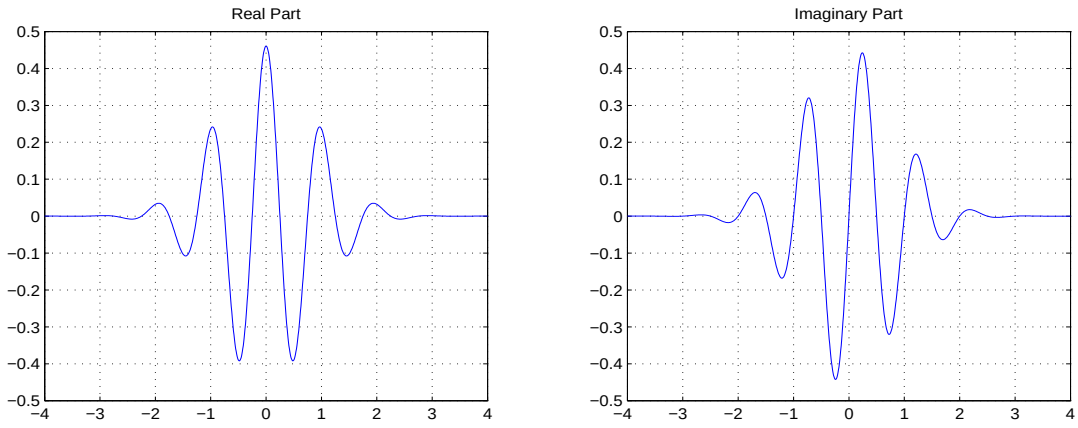

Figure 6.3: Real and imaginary parts of the Morlet wavelet.

$$\psi(a\omega) = \pi^{-0.25}\, H(\omega).exp\left(-\frac{(a\omega - \omega_0)^2}{2}\right) \tag{6.6}$$

where ω is the angular frequency and $H(\omega)$ is the Heaviside step function. $H(\omega) = 1$ if $\omega > 0$ and is zero otherwise. Using the frequency domain form of the wavelet in (6.6), the wavelet transform can also be implemented using the FFT algorithm. A complete description of how to impmlement the wavelet transform using the FFT algorithm is explained in the next section.

6.6 Wavelet Transform as a Filtering Technique

Equation (6.1) is the wavelet transform for continuous time signals, in case of the discrete time sequence $x[n]$ having N samples, the wavelet transform can be given as

$$c_b[a] = \sum_{n=0}^{N-1} x[n]\psi^* \left[\frac{(n-b)}{a}\right] \tag{6.7}$$

Equation (6.7) can also be represented as a convolution sum if we define

$$\psi_a[n] = \frac{1}{\sqrt{a}}\psi^* \left[\frac{-n}{a}\right] \tag{6.8}$$

Then (6.7) can be re-written as

$$c_b[a] = \sum_{n=0}^{N-1} x[n]\psi_a[b-n] \tag{6.9}$$

Equation (6.9) defines the wavelet transform as a convolution sum between two signals. Since it is computationally intensive to compute the wavelet transform as a convolution sum, a more efficient way, using the discrete Fourier transform (DFT) can be employed instead. If we define $X(k)$ as the DFT of the signal $x[n]$ and $\psi(k)$ as the DFT of the wavelet function $\psi[n]$ having N samples, then the wavelet transform using the DFT can be given as

$$C_b(a) = \frac{1}{N}\sqrt{\frac{2\pi a}{\delta t}} \sum_{k=0}^{N-1} X\left(\frac{2\pi k}{N\delta t}\right) \psi^*\left(a.\frac{2\pi k}{N\delta t}\right) e^{j2\pi kb/N} \tag{6.10}$$

where δt is the sampling interval and the term $\sqrt{2\pi a/\delta t}$ is the normalization factor which is used for the wavelet function, $\psi[n]$, to have unit energy at every given scale a. The selection of scales is the most important factor for proper time-frequency representation of a signal using wavelet transform. Although arbitrary values for the scales can be used for estimating the wavelet coefficients, $C_b(a)$, here the method as described in [84] was adopted, according to which the scale parameter a can be written as a fractional power of 2:

$$a_j = a_0 2^{j\delta j}, \qquad j = 0, 1, \ldots, J \tag{6.11}$$

$$J = 2(\delta j^{-1} log_2(N\delta t/s_0)) \tag{6.12}$$

where a_0 is the smallest scale, J is the largest scale, δt is the sampling time and δj is the scale increment parameter having a maximum value of 0.5 in the case of the Morlet wavelet. For this wavelet, the scale equivalent frequencies can be calculated as

$$frequency = \frac{\omega_0 + \sqrt{2+\omega_0^2}}{4\pi \times a} \tag{6.13}$$

The filtering of the signal using the wavelet transform can be done by reconstruction of the signal using the inverse wavelet transform in the discrete time domain. The scale parameter a sets the basis for using the wavelet transform either as a highpass, lowpass or bandpass filter. Since the wavelet transform results in complex values, the IWT can be obtained by taking the sum over all scales of the real values of the wavelet cofficients $C_b(a)$. Mathematically, the filtering using the IWT can be given as

$$x_n = \left(\frac{\delta j \delta t^{0.5}}{C_\delta \psi_0(0)}\right) \sum_{j=j_1}^{j_2} \frac{\Re(C_b(a_j))}{(a_j)^{0.5}} \tag{6.14}$$

where x_n is the reconstructed original signal, $\psi_0(0)$ is a constant with a value of $\pi^{0.25}$ [84] and is used for removing the energy scaling, C_δ is a reconstrcution constant with a value of 0.776 and j_1 and j_1 are the lower and upper boundary limits for the selected scales for signal reconstruction.

6.7 Improved Analogous Phase Scintillation Index

From (5.34), the mathematical form of the analogous phase index $\sigma_{\phi a}$ can be given as

$$\sigma_{\phi a} = [\varpi(\chi(M), v_p) \times \sigma_{VTEC_{HPF}}] \tag{6.15}$$

The term $\sigma_{VTEC_{HPF}}$ in (6.15) is the standard deviation of the high pass filtered VTEC output which from [107] can be given as

$$\sigma_{VTEC_{HPF}} = \left[\frac{1}{n-1} \sum_{i=1}^{n} \left(VTEC_{HPF} - \overline{VTEC}_{HPF} \right)^2 \right]^{\frac{1}{2}} \tag{6.16}$$

The term $VTEC_{HPF}$ represents both the high frequency TEC fluctuations due to scintillation producing ionospheric irregularities however due to improper filtering also contain the noise and the diffraction effect which is not fully removed as discussed in chapter 5 in the results section. The non-filtered high and low frequency TEC fluctuations which are based on the time and spatial variations of vertical TEC can be written as

$$VTEC' = M \left[\frac{\partial TEC}{\partial x} v_{pp} + \frac{\partial TEC}{\partial t} dt \right] + TEC \frac{\Delta M}{\Delta t} \tag{6.17}$$

The term $TEC\frac{\Delta M}{\Delta t}$ represents the very low frequency TEC fluctuations, is almost negligible, and can neglected as it is varying with a frequency 3×10^{-4} Hz. The term $M \left[\frac{\partial TEC}{\partial x} v_{pp} + \frac{\partial TEC}{\partial t} dt \right]$ in (6.17) not only contains the high frequency TEC fluctuations due to small scale irregularites but also contains the low frequency TEC fluctuations which need to be removed as they are refractive in nature due to the slowly varying background ionosphere, Doppler shift due to satellite and receiver motion etc. After using wavelet-based filtering [118], (6.17) can be represented as

$$VTEC'_{wav} = \left[M \left[\frac{\partial TEC}{\partial x} v_{pp} + \frac{\partial TEC}{\partial t} dt \right] \right]_{wav} \tag{6.18}$$

where the subscript *wav* represents the fact that the term in (6.18) is wavelet filtered. The final equation for the analogous phase index after wavelet filtering [118] can be given as

$$\sigma_{\phi a}^{\mathrm{w}} = \left[\varpi \left(\chi \left(M \right), v_p \right) \times \sigma_{VTEC'_{wav}} \right] \tag{6.19}$$

where $\sigma_{VTEC'_{wav}}$ is the normalized standard deviation of $VTEC'_{wav}$ over a 1 min interval. In (6.18), the main to consider when estimating the $\sigma_{VTEC'_{wav}}$, is how the high frequency TEC variations due to the diffraction effect are filtered out from the low frequency TEC variations due to refractive effect. This can be accomplished by using the suitable scales

for filtering out the low frequency TEC fluctuations in the estimation of $\sigma_{VTEC'_{wav}}$ which is done through (6.14) by generating the wavelet scalograms to represent the high and low frequency TEC fluctuations. The wavelet scalogram represents the percentage of wavelet statistical energy ($E(a,b) = |C_b(a)|^2$) for each wavelet coefficient over all scales. However, if the scales are wrongly chosen, it will cause the wrong interpretation of the wavelet statistical energy used to generate the wavelet scalograms for identifying the scintillation and non-scintillation events and, therefore will affect the filtering process. In the next section, the scalograms of scintillation and non-scintillation events are generated to distinguish between the background noise and TEC fluctuations due to scintillation producing ionospheric irregularities and also to set the limits for filtering using the wavelet transform.

6.8 Wavelet Scalograms for Identifying the Scintillation Signatures

The data used for the scalogram generation was collected using the NovAtel GISTM GSV4004B dual frequency GPS receivers installed at Trondheim, Norway ($63.41^o\,N, 10.4^o\,E$). The complete experimental setup at one of the receiver station, i. e., Newcastle Upon Tyne is shown in section 4.2. A similar kind of setup was used to log the raw TEC observations at 1 Hz at Trondheim. Ignoring the second term, the first term in (6.17) can be written as:-

$$x[n] = M\left[\frac{\partial TEC}{\partial x}v_{pp} + \frac{\partial TEC}{\partial t}dt\right] \tag{6.20}$$

In order to compute the wavelet transform of $x[n]$, the Morlet wavelet was used as a mother wavelet as given in (6.5) and the frequency domain approach was used for easier and computationally efficient implementation of the wavelet transform. The scales are calculated based on the fractional power of 2 as defined in section 6.6. Since the data that we are using has a sample rate of 1 Hz, the following values for the scale parameters were set; $\delta t = 1$, $s_o = 2$, $\delta j = 0.125$ and J was calculated using (6.12) and depends on the δt, s_o and N (total number of data samples).

The scalograms of the TEC fluctuations of different PRN's generated based on different geomagnetic conditions ($Kp \leq 5$, $Kp \geq 6$) are shown in Fig. 6.4 and Fig. 6.5 for 26 and 24 April, 2012 respectively. The reason for choosing the different geomagnetic conditions for scalogram generation was to show the wavelet statistical energy associated with the high and low frequency TEC fluctuations when there was no geomagnetic storm/minor storm ($Kp \leq 5$) and when there was a strong storm ($Kp \geq 6$).

For $Kp \leq 5$ case, the Kp plot for 26 April, 2012 is shown in Fig. 5.2 where it can be seen that there was a minor geomagnetic storm (red bar) in the early hours of the day from 03:00 to 06:00 UT followed by a geomagnetic disturbance from 00:00 to 03:00 UT (shown by the yellow bar). The regional geomagnetic disturbance in the H component of the earth's magnetic field is also shown in Fig. 5.2. The scalograms of the PRN's on 26 April 2012 that were visible between 00:00 and 09:00 are shown in Fig. 6.4. For these scalograms, the scales were converted to their equivalent frequencies using (6.13). As mentioned earlier, for the Morlet wavelets the scales are inversely propotional to frequencies, so in Fig. 6.4, high scales imply small frequencies whereas small scales imply high frequencies. The colour bar on the right hand side shows the wavelet power associated with the high and low frequency TEC variations. In Fig. 6.4, it can be seen that most of the high power TEC variations are associated with the large-scales/low frequencies ($frequencies < 0.15$ Hz) which can be due to the slowly varying background ionosphere, Doppler shift due to satellite/receiver motion, and satellite/receiver clock offsets. These need to be eliminated as they do not represent the presence of true scintillation signatures. Some medium power TEC fluctuations can also be seen for PRN 7, 12, 19 and 28 between 02:00 to 06:00 for small-scales/high frequencies ($frequencies > 0.17$ Hz) as there was a minor geomagnetic storm during this time. However, these TEC variations lasted only for a fraction of a time (few minutes) and therefore did not have a significant effect when further analyzed after estimating the scintillation values as no high scintillation activity was observed during this time.

A further analysis during the strong geomagnetic storm conditions was also carried out in Fig. 6.5 to determine the presence of scintillation signatures due to small scale ionospheric irregularities by generating the scalograms of the PRN's on 24 April, 2012

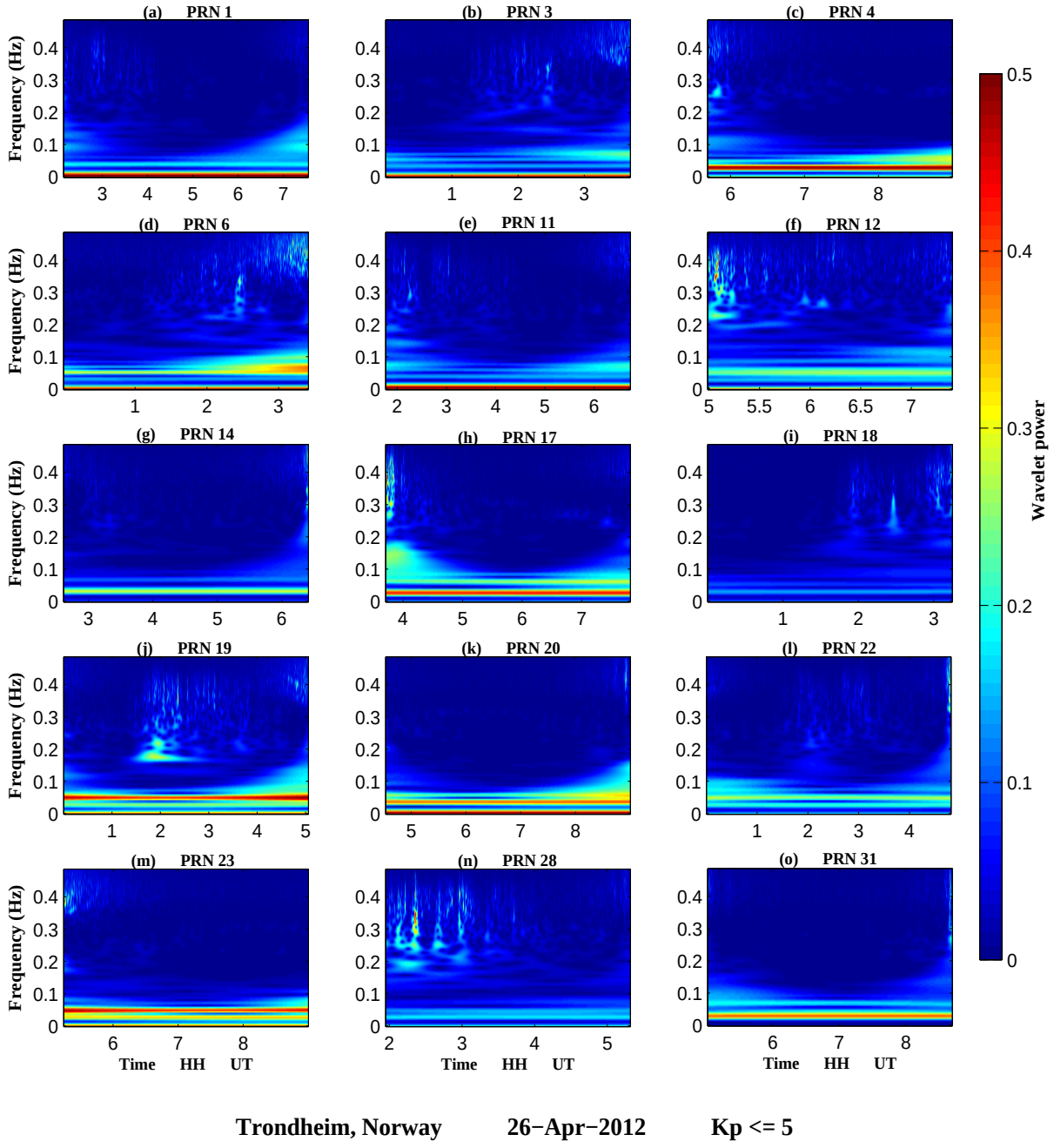

Figure 6.4: Wavelet scalograms of the selected PRN's on 26, April 2012 when $Kp \leq 5$.

when Kp was greater than 5 from 00:00 to 06:00 UT (see Fig. 5.4). In Fig. 6.5, it can be seen that almost all the PRN's faced medium to high TEC variations for small-scales/ high frequencies ($frequencies > 0.17$ Hz) depicting the presence of strong scintillation signatures. Some high power TEC variations were also seen for large-scales/ low frequencies ($frequencies < 0.15$ Hz). However most are probably due to the slowly changing background ionosphere, satellite/receiver motion and other noise effects and need to be eliminated. After carefully observing the scalograms of scintillation and non-scintillation events between August 2011 and September 2012 at Trondheim, Norway, the large scale wavelet coefficients associated with the low frequencies ($frequencies <$ 0.15 Hz) were eliminated for filtering the low frequency TEC fluctuaions and for signal reconstruction, only the small scale wavelet coefficients associated with the high frequency TEC variations ($frequencies > 0.16$ Hz) were used.

The scale boundaries were then used in (6.14) for accomplishing the fitlering process using the wavelet transform and the signal was finally reconstructed and used in (6.19) for deriving the $\sigma_{\phi a}^{\mathrm{w}}$ values. A complete flow chart for the $\sigma_{\phi a}^{\mathrm{w}}$ determination process [118] is shown in Fig. 6.6. The process starts by logging the raw binary TEC data at 1 Hz which was then converted to ASCII. Once the data was in readable form, it was examined for cycle slip detection. If the cycle slip was fixable, the program fixed it, otherwise it skipped the cycle slip data. After calculating the VTEC and the time derivative of VTEC, filtering was then performed by estimating the wavelet coefficients, skipping the large scale wavelet coefficients ($scales > 6s$, $frequencies < 0.16$ Hz) and the IWT. The final phase of the derivation involves determining the standard deviation of the filtered VTEC over 60 s which is multiplied by the elevation weighting function.

6.9 Results and Discussion

Aftre estimating the $\sigma_{\phi a}^{\mathrm{w}}$ using the above defined criteria, its performance was then compared with the σ_{ϕ} and $\sigma_{\phi a}$ indices on 26 and 24 April as shown in Fig. 6.7 and Fig. 6.8 respectively for the PRN's who's scalograms are shown in Fig. 6.4 and Fig. 6.5.

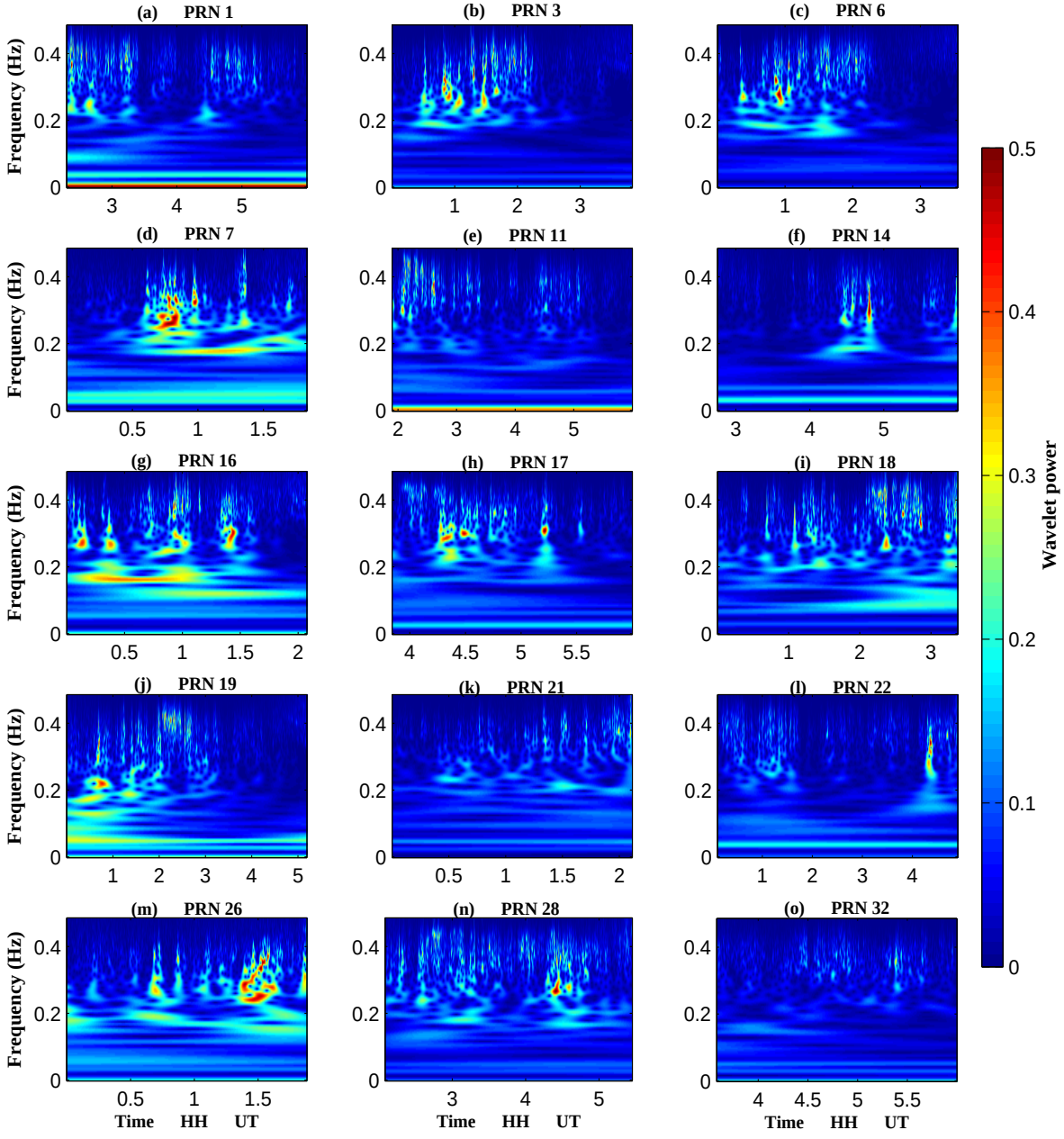

Figure 6.5: Wavelet scalograms of the selected PRN's on 24, April 2012 when $Kp > 5$.

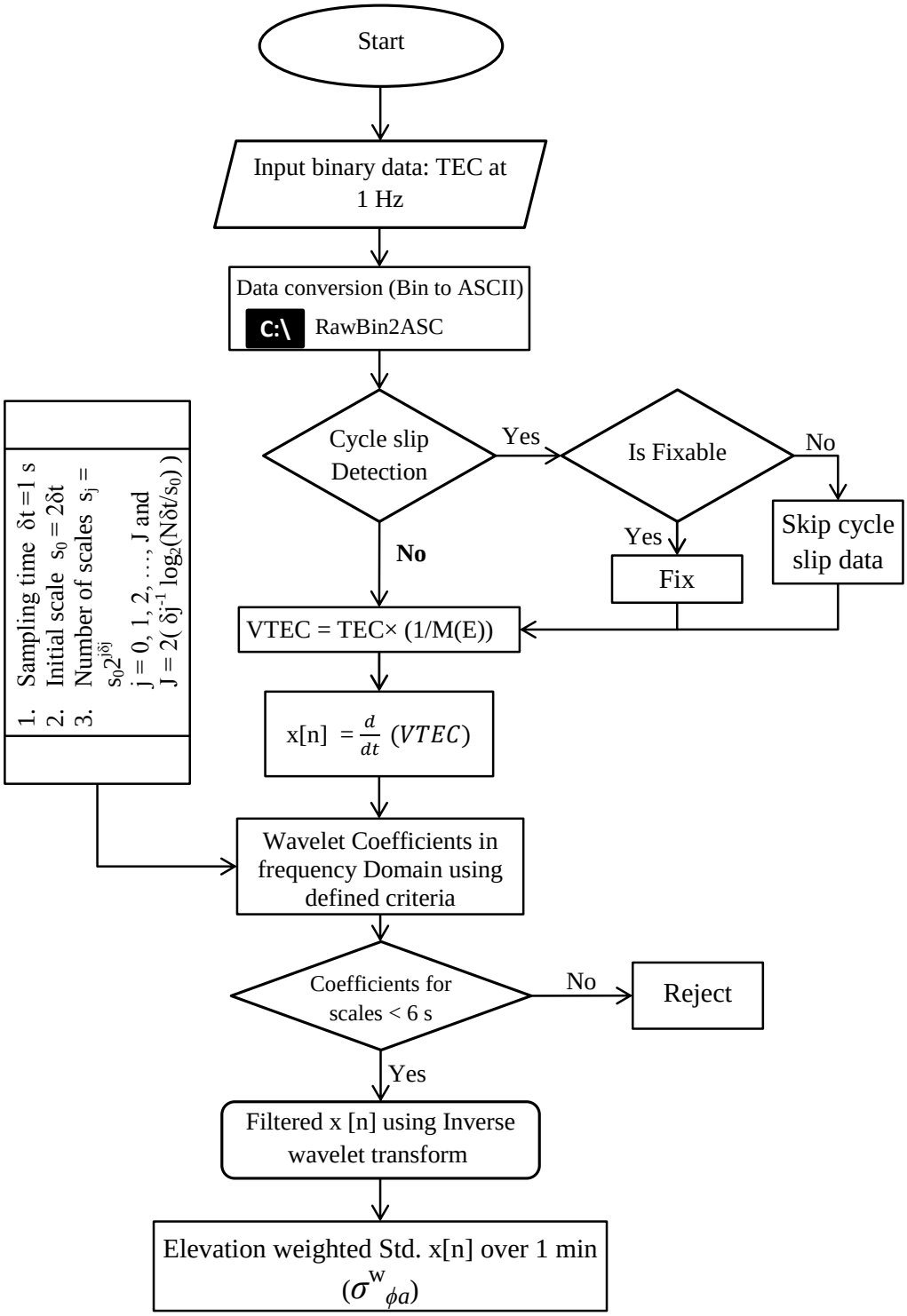

Figure 6.6: Flow chart for $\sigma^{w}_{\phi a}$ using raw TEC 1 Hz data [118].

In Fig. 6.7, on 26 April 2012 for $Kp \leq 5$ case , no strong scintillation was observed for any PRN apart from PRN 28 where the σ_ϕ values were higher compared to both the $\sigma^{w}_{\phi a}$ and $\sigma_{\phi a}$ values. Further investigation revealed that the elevation angle of this PRN was below 30^o all the time which may have led to high scintillation values in the case of σ_ϕ and could most probably be the result of improper filtering which failed to distinguish between the noise and the scintillation in the estimation process. On the other hand, in the case of $\sigma_{\phi a}$, the scintillation values for PRN's 3, 4, 6, 23 and 32 are higher than both the $\sigma^{w}_{\phi a}$ and σ_ϕ values. Although, the over estimation factor of $\sigma_{\phi a}$ is small here this is further highlighted in Fig. 6.10 for a complete one year period which gives more detailed results about this over estimation factor. It was also mentioned by [107] that for weak geomagnetic conditions, the $\sigma_{\phi a}$ may give some over estimated scintillation values which may not be truely representative of the scintillation activity.

In Fig. 6.8, for $Kp > 5$ case on 24 April, 2012, strong scintillation activity was observed for most of the PRN's that were visible during 00:00 to 00:06 UT during the course of a geomagnetic storm. The Kp plot of the day is shown in Fig. 5.4. One interesting thing to note here is that there existed a good correlation between the three indices for all PRN's except in the case of σ_ϕ, very high scintillation values were seen for low elevation satellites. It was also mentioned by [110] that the σ_ϕ cannot distinguish between the actual scintillation and the background noise at low elevation angles during weak to moderate scintillation conditions. It should be noted that, apart from the elevation angle effect, these values could also be the result of improper filtering or wrong data processing in estimating the scintillation values using σ_ϕ.

The performance of the three indices was then compared by calculating the number of occurences of scintillation values greater than 0.3 in Fig. 6.9 with respect to the magnetic local time (MLT) for a whole one year from October 2011 to September 2012 at Trondheim, Norway. The scintillation activity is strongly associated with the MLT due to coupling between the solar wind, the magnetosphere and the ionosphere as mentioned by [126]. In Fig. 6.9, during the post-midnight period, σ_ϕ index has the highest number of occurences of scintillation values greater than 0.3. The post-midnight is the period when the scintillation activity is usually at its peak due to the auroral phenomena. By contrast, for

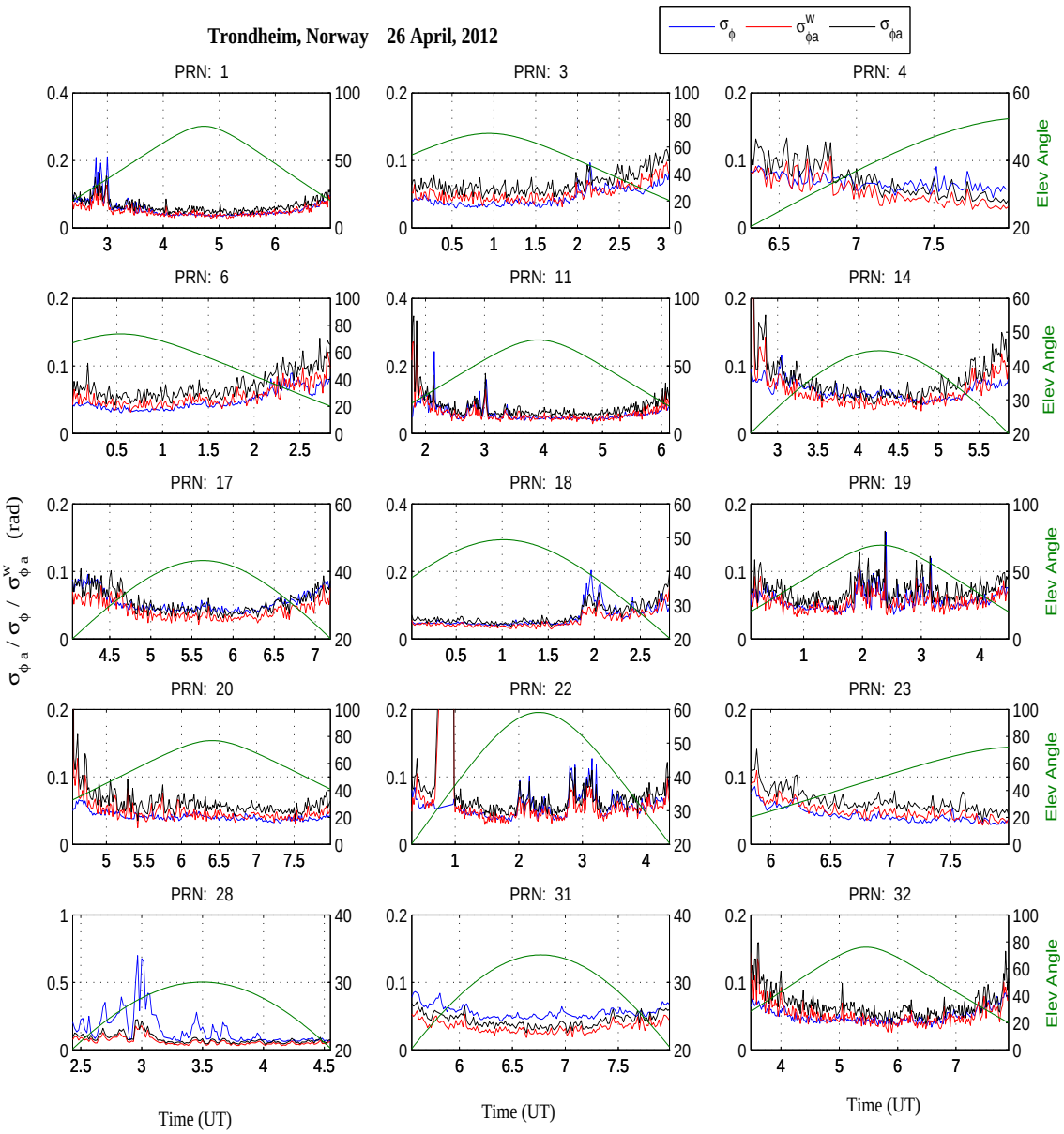

Figure 6.7: $\sigma^{\mathrm{w}}_{\phi a}$, σ_{ϕ} and $\sigma_{\phi a}$ comparison on 26 April, 2012.

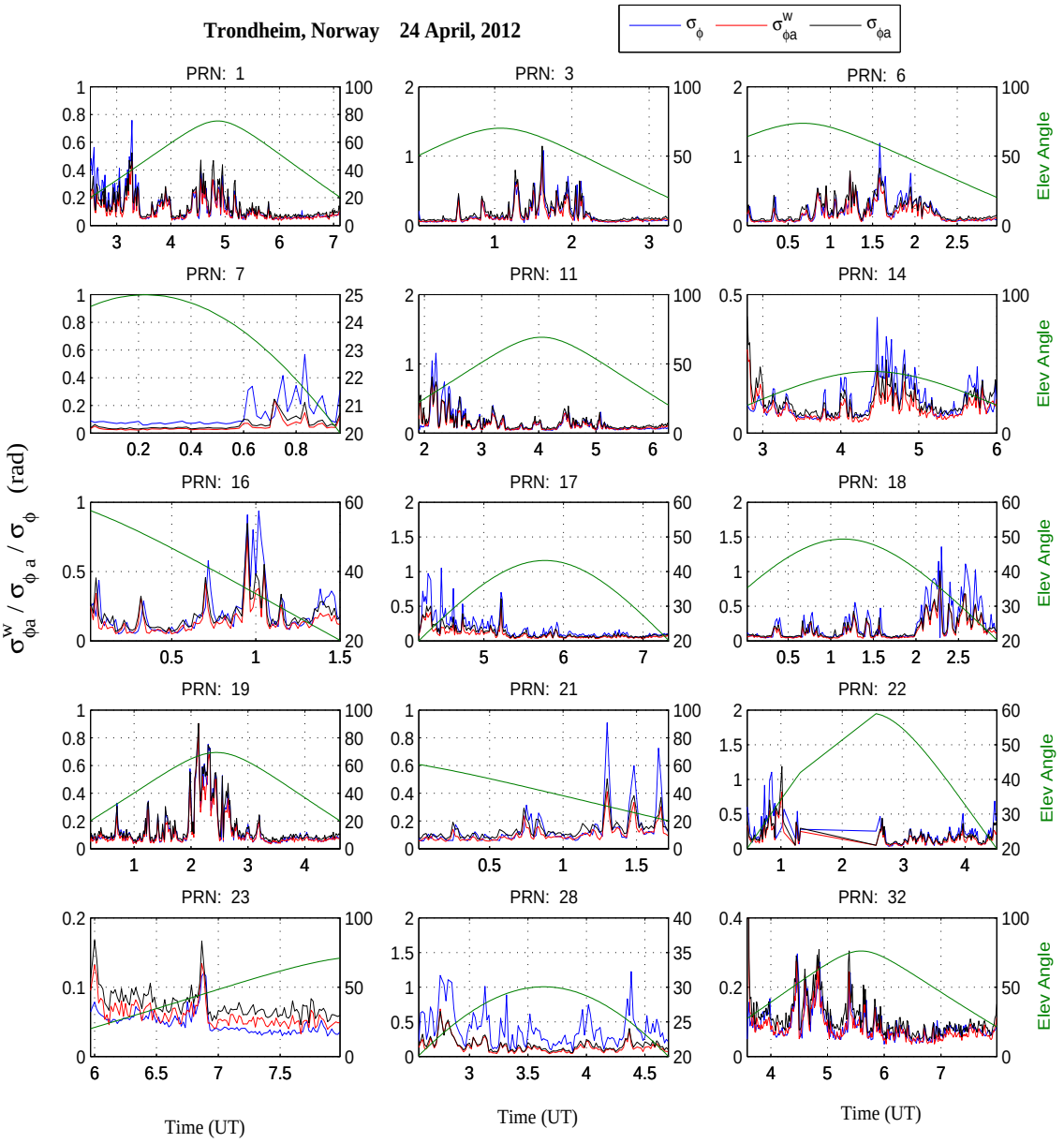

Figure 6.8: $\sigma^{\mathrm{w}}_{\phi a}$, σ_{ϕ} and $\sigma_{\phi a}$ comparison on 24 April, 2012 [118].

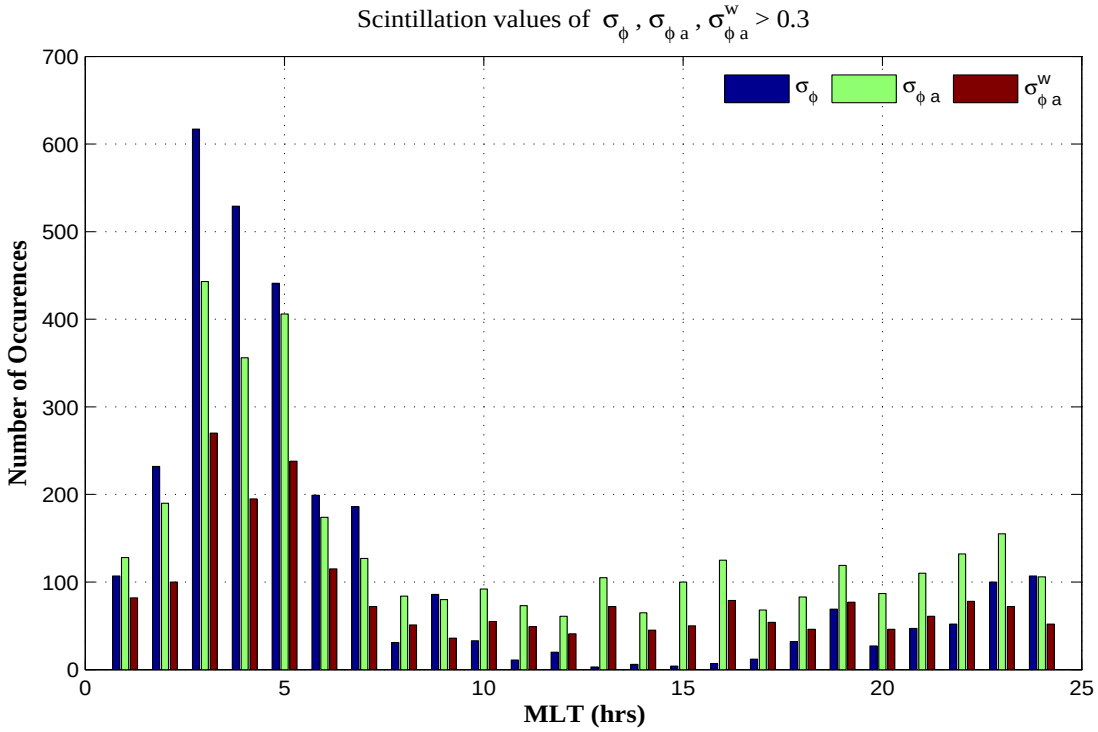

Figure 6.9: Number of occurences of scintillation values of $\sigma^{w}_{\phi a}$, σ_{ϕ} and $\sigma_{\phi a}$ for a whole one year from October 2011 to September 2012.

the pre-midnight period, the $\sigma_{\phi a}$ has the highest number of scintillation occurence values greater than 0.3 compared to both the $\sigma^{w}_{\phi a}$ and σ_{ϕ}. It can be further seen in Fig. 6.9 that after 10:00 MLT, the $\sigma_{\phi a}$ index has reported high scintillation activity compared to both the $\sigma^{w}_{\phi a}$ and σ_{ϕ} indices. Further investigation showed that the $\sigma_{\phi a}$ index was well correlated with the $\sigma^{w}_{\phi a}$ and σ_{ϕ} indices when there was a strong scintillation activity. However some high scintillation values were also observed during this time for $\sigma_{\phi a}$ whose pattern was not matching those of both the $\sigma^{w}_{\phi a}$ and σ_{ϕ}. For the case of the σ_{ϕ} index, it was observed that between 11:00 and 17:00 MLT, the number of scintillation events greater than 0.3 was very low. It was found that on 7, 8, 9, 15 March, 4 April, 3 and 3 September 2012, the post noon value of Kp was greater than 5 and the reason for σ_{ϕ} being very low on these days was due to the frequent loss of lock in the GPS receiver which resulted in low scintillation values. This is because during the re-acquisition time the NovAtel GISTM receiver usually rejects 240 to 300 s of phase data to avoid spurious values in the estimation of the σ_{ϕ} index but this also results in loss of useful information due to unavailability of information

during this time and therefore during this time the scintillation values were either small or unavailable for the σ_ϕ index.

In Fig. 6.10, scintillation values and the correlation between the $\sigma^{w}_{\phi a}$ and $\sigma_{\phi a}$ and also between $\sigma^{w}_{\phi a}$ and σ_ϕ are plotted for two different geomagnetic conditions ($Kp < 5$; $Kp \geq 5$) by using the data from a GPS receiver installed at Trondheim, Norway for a whole 1 year from October 2011 to September 2012. The correlation between the indices is calculated by using the definition of Pearson's correlation coefficient which is denoted by R.

For the $Kp < 5$ case, the scintillation values for $\sigma^{w}_{\phi a}$ and $\sigma_{\phi a}$ are shown in Fig. 6.10 (a) whereas Fig. 6.10 (b) contain the scintillation values for $\sigma^{w}_{\phi a}$ and σ_ϕ. The right hand side panels adjacent to Fig. 6.10 (a) and (b) contain the corresponding correlation plots. Although, the correlation coefficient of 0.83 was found between the $\sigma^{w}_{\phi a}$ and $\sigma_{\phi a}$ indices (Fig. 6.10(a)), the number of counts of scintillation events in the case of $\sigma_{\phi a}$ was far more than either of these. On the other hand, when $\sigma^{w}_{\phi a}$ was compared and correlated with σ_ϕ in Fig. 6.10 (b), an R value of 0.69 was found between the two indices. The reason for this poor correlation could be due to the fact that these indices were derived from different data sources and the filtering effect can be different for both cases. At certain times, the behaviour of both the indices was found to be different which was due to some unexpected high scintillation values in the case of σ_ϕ but, nevertheless, overall a similar scintillation occurence pattern was found. It was also mentioned by [110] that, σ_ϕ is not a good indicator to distinguish between the actual scintillation and the background noise for weak to moderate scintillation conditions as, during these conditions, improper filtering along with other factors lead to spurious scintillation values which can be considered as outliers.

For the $Kp \geq 5$ case, Fig. 6.10 (c) shows the scintillation values for $\sigma^{w}_{\phi a}$ and $\sigma_{\phi a}$ whereas Fig. 6.10 (d) contain the scintillation values for $\sigma^{w}_{\phi a}$ and σ_ϕ. The right hand side panels opposite to each subplot contain the corresponding correlation subplots. A very good correlation was found between the $\sigma^{w}_{\phi a}$ and $\sigma_{\phi a}$ and also between the $\sigma^{w}_{\phi a}$ and σ_ϕ with R values of 0.91 and 0.76 respectively. The scintillation pattern between the indices

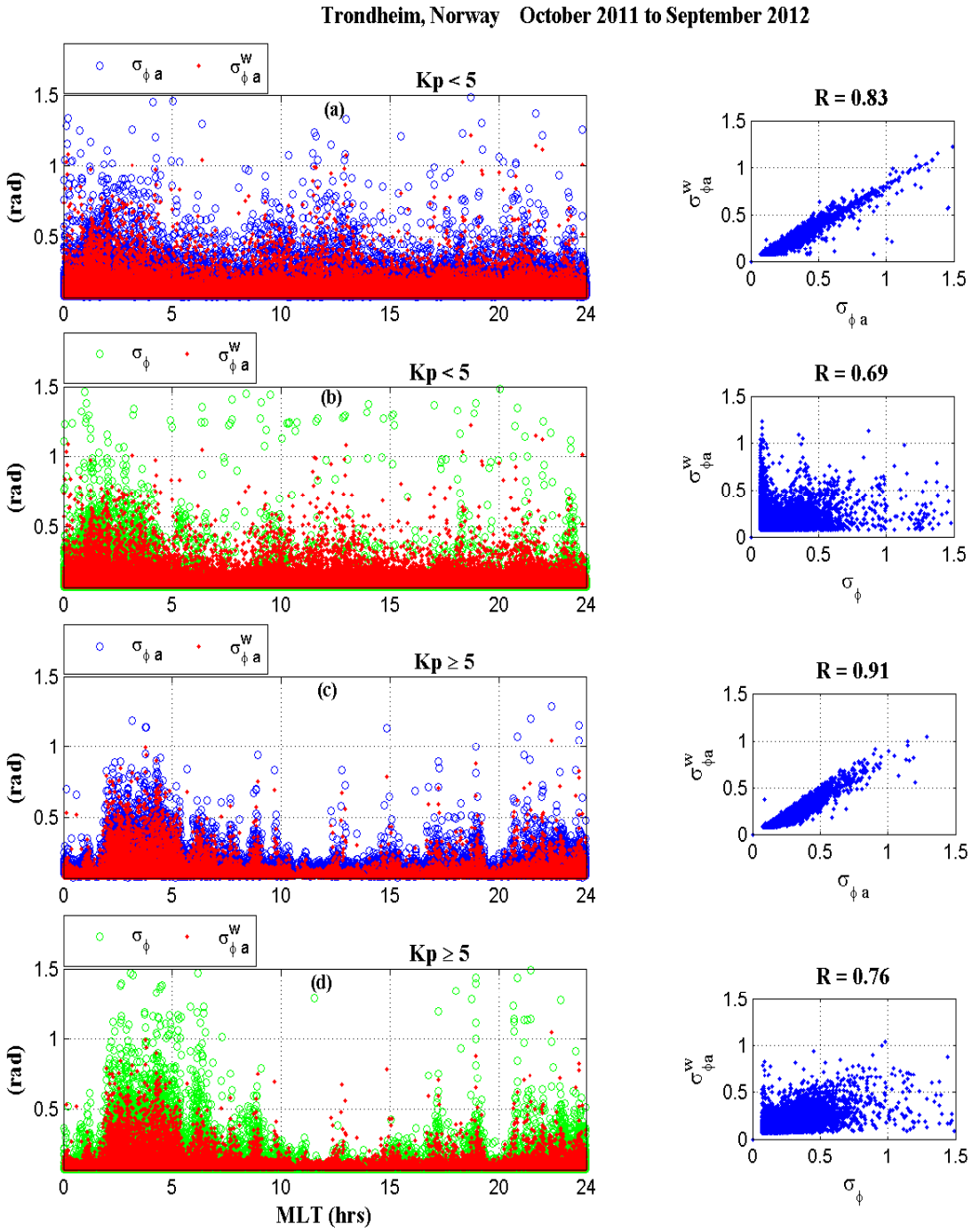

Figure 6.10: Scintillation activity and correlation coefficient R for $Kp < 5$ and $Kp \geq 5$ between $\sigma^{w}_{\phi a}$ and σ_{ϕ} and between $\sigma^{w}_{\phi a}$ and $\sigma_{\phi a}$

was also found to be very similar and no unexpected change in the scintillation pattern was observed for the $Kp \geq 5$ case.

The existence of a good correlation and the similarity of the scintillation occurence pattern of $\sigma_{\phi a}^{w}$ with those of the $\sigma_{\phi a}$ and σ_{ϕ} indices shows that it can serve as a good alternative for representing the phase scintillation activity at European high latitudes. The performance comparison of $\sigma_{\phi a}^{w}$ index with the other two indices shows that it has not only reduced the over estimation factor involved in the estimation of the $\sigma_{\phi a}$ and σ_{ϕ} indices for both the weak and strong scintillation conditions but has also shown a very good correlation with the σ_{ϕ} values during the weak geomagnetic activity which the $\sigma_{\phi a}$ failed to do.

6.10 Seasonal Variations and Statistical Significance of the $\sigma_{\phi a}^{w}$ Index

In the previous section, the performance of the $\sigma_{\phi a}^{w}$ index was compared with $\sigma_{\phi a}$ and σ_{ϕ} indices based on two different geomagnetic conditions, i. e., $Kp \geq 5$ and $Kp < 5$. The discussion is further proceeded here by comparing the seasonal variations of the $\sigma_{\phi a}^{w}$ index with those of $\sigma_{\phi a}$ and σ_{ϕ} indices for the two geomagnetic conditions which is then validated by using the statistical significance test to confirm the presence of a linear correlation between the three indices.

Fig. 6.11 and Fig. 6.12 shows the seasonal variation comparison of the scintillation values between the $\sigma_{\phi a}^{w}$ and $\sigma_{\phi a}$ and between $\sigma_{\phi a}^{w}$ and σ_{ϕ} respectively for the $Kp \geq 5$ and $Kp < 5$ cases by using the data from Trondheim receiver station for a whole 1 year from October 2011 to September 2012. For this comparison, the seasons are defined as follows: autumn (21 September to 20 December), winter (21 December to 20 March), spring ((21 March to 20 June), and summer (21 June to 20 September). The Pearson's correlation coefficient value in each case is also determined and is shown in the respective subfigure. In order to eliminate the effect of the noise at low elevation angles, an elevation angle cutoff of 20^{o} was used in estimating the scintillation values for the above indices.

For the $Kp \geq 5$ case, Fig. 6.11(a) shows the comparison between the $\sigma_{\phi a}^{w}$ and $\sigma_{\phi a}$ indices whereas Fig. 6.11(b) shows the comparison between the $\sigma_{\phi a}^{w}$ and σ_{ϕ} indices for

the four seasons. A very good correlation was found between the $\sigma_{\phi a}^{w}$ and $\sigma_{\phi a}$ with an average correlation value of 0.92 whereas it was 0.78 between the $\sigma_{\phi a}^{w}$ and σ_{ϕ} indices. The scintillation occurence pattern between the $\sigma_{\phi a}^{w}$ and σ_{ϕ} indices was almost similar due to the fact that both of these indices were derived from the same sources and $\sigma_{\phi a}^{w}$ claims to be a better indicator of the scintillaiton activity during both the weak and strong geomagnetic conditions. The scintillation occurence pattern of $\sigma_{\phi a}^{w}$ and σ_{ϕ} indices was also quite similar apart from some high values in the case of σ_{ϕ} in all the four seasons which could most likely be the result of inappropriate filtering or failure to distinguish between the noise and scintillation during the estimation process.

For the $Kp < 5$ case, Fig. 6.12(a) shows the scintillation values comparison between the $\sigma_{\phi a}^{w}$ and $\sigma_{\phi a}$ indices whereas Fig. 6.12(b) shows the comparison between the $\sigma_{\phi a}^{w}$ and σ_{ϕ} indices for the four previously defined seasons. In this case, the correlation coefficient values of $\sigma_{\phi a}^{w}$ with that of $\sigma_{\phi a}$ and σ_{ϕ} indices in all four seasons were found to be less than the $Kp \geq 5$ case. Further investigation revealed that the over estimation factor in the case of $\sigma_{\phi a}$ was quite high at certain times especially during the winter and spring seasons although there was no geomagnetic disturbance or storm during those times. This resulted in low correlation coefficient values between the $\sigma_{\phi a}^{w}$ and $\sigma_{\phi a}$. On the other hand, when comparing the $\sigma_{\phi a}^{w}$ index with the σ_{ϕ} index in Fig. 6.12(b), some high scintillation values were observed in the case of σ_{ϕ} having an inconsistent pattern especially during the autumn, spring and summer seasons when Kp was less than 5 and there was no geomagnetic disturbance regionally during those times when σ_{ϕ} was reporting scintillation values as high as 1.5. These values of σ_{ϕ} cannot be considered as the true representative of the scintillation activity.

The statistical significance of the correlation between the $\sigma_{\phi a}^{w}$ and $\sigma_{\phi a}$ and also between $\sigma_{\phi a}^{w}$ and σ_{ϕ} indices is then carried out to check the significance of the correlation existed between the indices in all the four seasons for the $Kp \geq 5$ and $Kp < 5$ cases. The significance test was accomplished using the population correlation coefficient, i. e., p-value by setting a significance level of $\alpha = 0.01$. The p-value defines the probability of getting a correlation as large as the observed value by a random chance.The results of the statistical significance test are shown in Fig. 6.13 for both the $Kp \geq 5$ and $Kp < 5$ cases.

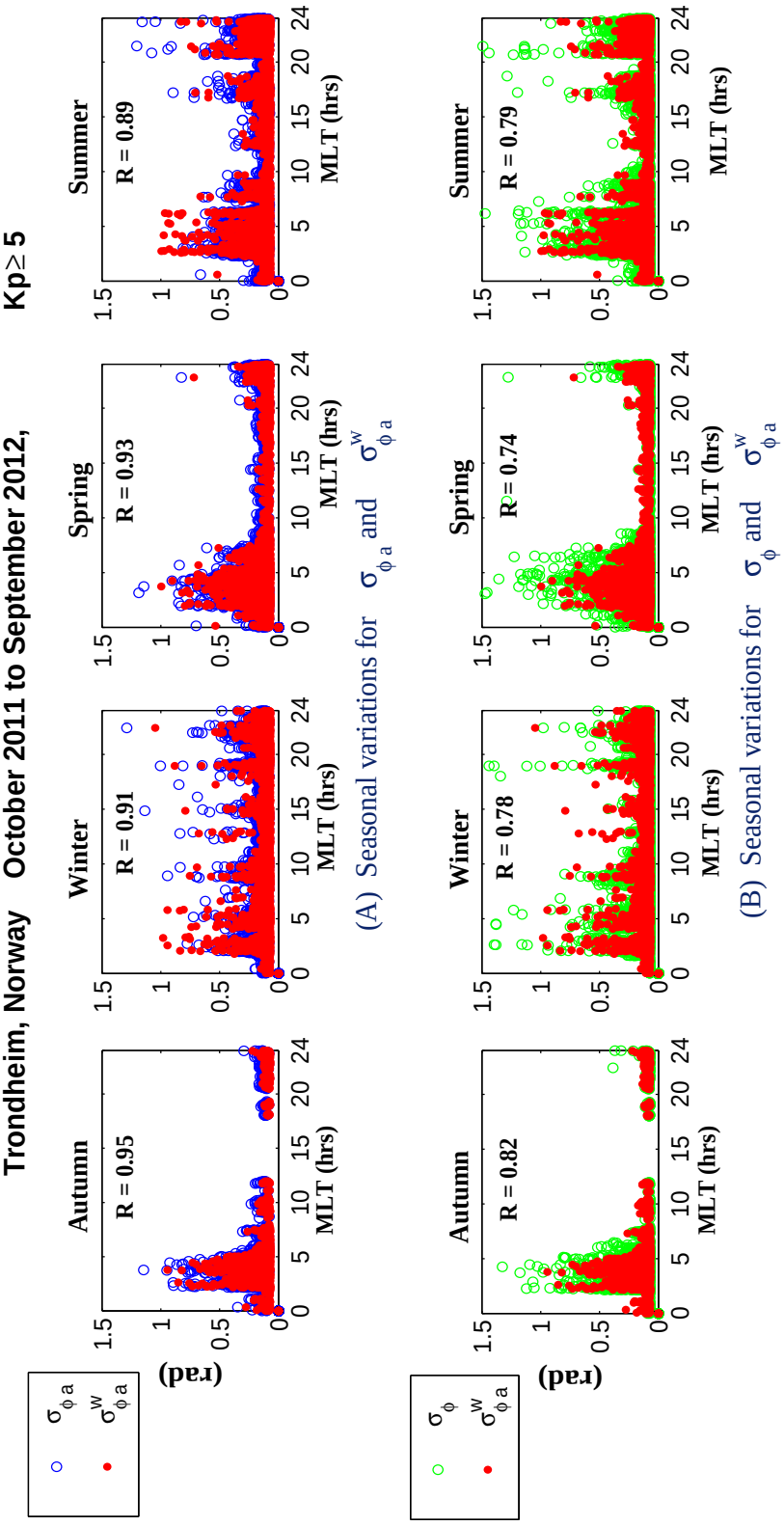

Figure 6.11: Seasonal variations of the scintillation occurence patterns of $\sigma^{w}_{\phi a}$, $\sigma_{\phi a}$ and σ_{ϕ} for $Kp \geq 5$ for a whole year from October 2011 to September 2012 [118].

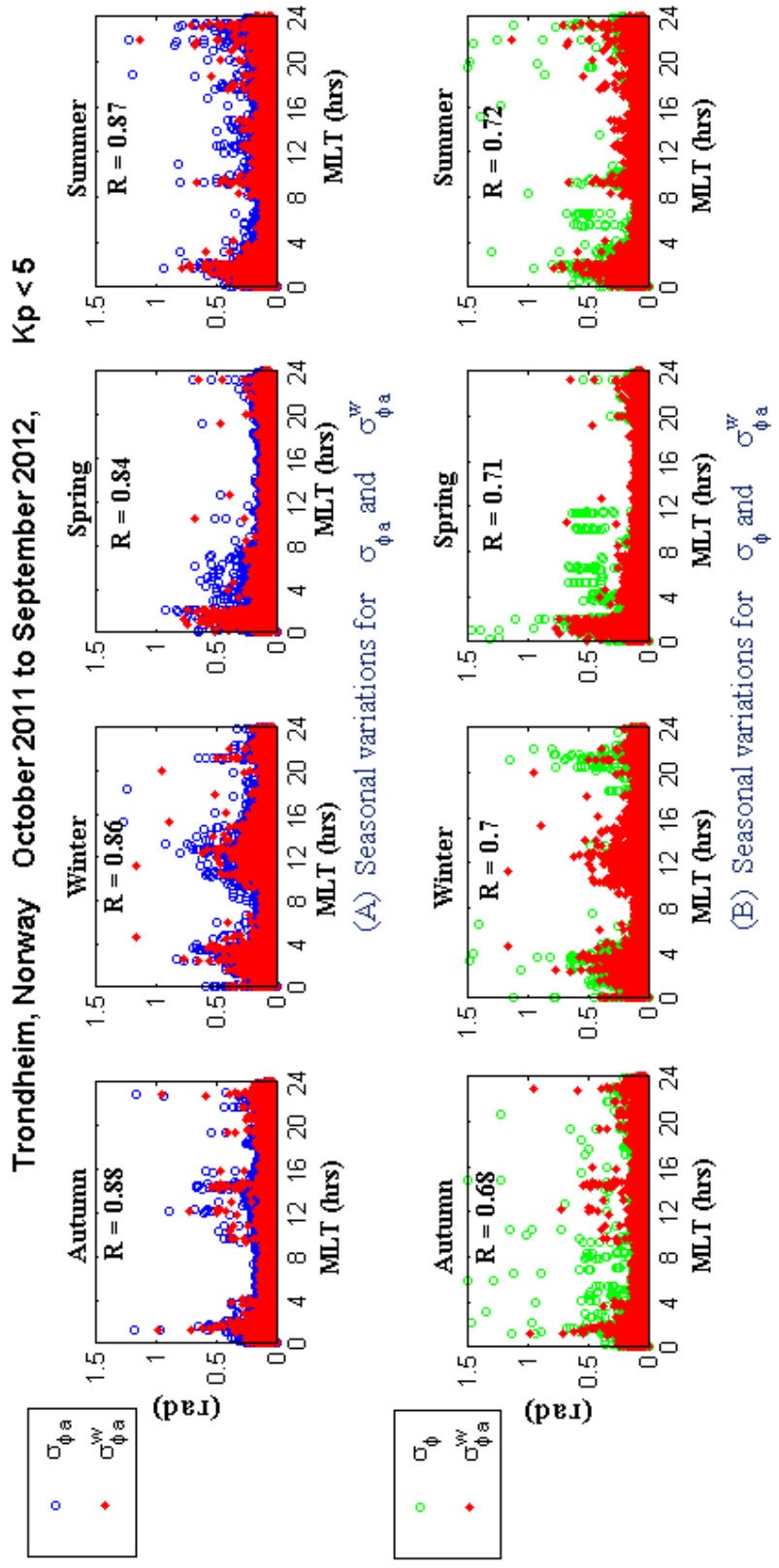

Figure 6.12: Seasonal variations of the scintillation occurence patterns of $\sigma^{w}_{\phi a}$, $\sigma_{\phi a}$ and σ_{ϕ} for $Kp < 5$ for a whole year from October 2011 to September 2012 [118].

(i) $\sigma_{\phi a}{}^{w}$ and $\sigma_{\phi a}$

Autumn		Winter		Spring		Summer	
R	0.95	R	0.91	R	0.93	R	0.89
N	292,052	N	241,128	N	269,782	N	316,129
Significance level	p< 0.01	Significance level	p< 0.01	Significance level	p< 0.01	Significance level	p< 0.01

(ii) $\sigma_{\phi a}{}^{w}$ and σ_{ϕ}

Autumn		Winter		Spring		Summer	
R	0.82	R	0.78	R	0.74	R	0.79
N	292,052	N	241,128	N	269,782	N	316,129
Significance level	p< 0.01	Significance level	p< 0.01	Significance level	p< 0.01	Significance level	p< 0.01

(a) Significance of the correlation coefficient R using 1 % significance level for $Kp \geq 5$ case

(i) $\sigma_{\phi a}{}^{w}$ and $\sigma_{\phi a}$

Autumn		Winter		Spring		Summer	
R	0.88	R	0.86	R	0.84	R	0.87
N	9,142	N	22,758	N	19,659	N	24,111
Significance level	p< 0.01	Significance level	p< 0.01	Significance level	p< 0.01	Significance level	p< 0.01

(ii) $\sigma_{\phi a}{}^{w}$ and σ_{ϕ}

Autumn		Winter		Spring		Summer	
R	0.68	R	0.7	R	0.71	R	0.72
N	9,142	N	22,758	N	19,659	N	24,111
Significance level	p< 0.01	Significance level	p< 0.01	Significance level	p< 0.01	Significance level	p< 0.01

(b) Significance of the correlation coefficient R using 1 % significance level for $Kp < 5$ case

Figure 6.13: Statistical significance of the Pearson's correlation coefficient (R) between the $\sigma_{\phi a}^{w}$ and σ_{ϕ} and between the $\sigma_{\phi a}^{w}$ and $\sigma_{\phi a}$ using 1 % significance level [118].

In all the four seasons, in both cases, the p-value was found to be less than 0.01 which shows that the correlation of the $\sigma_{\phi a}^{w}$ index with both the $\sigma_{\phi a}$ and σ_{ϕ} indices is highly significant at the 0.01 level.

The work on designing scintillation indices which can be used as true representatives of the scintillation activity has been done by many researchers and in this regard some new scintillation indices [114, 116, 117, 120] have also been proposed using the wavelet transform method. However, the analysis presented in the previous work was very limited and without considering any varying geomagnetic conditions which could verify that the

methods used by them are a better estimate of scintillation values and can used under all conditions. Based on a large scale analysis and results presented here based on varying geomagnetic conditions and seasonal variations, it is shown that $\sigma_{\phi a}^{\mathrm{w}}$ can be used as a better alternative of representing the phase scintillation activity. So far the performance of the $\sigma_{\phi a}^{\mathrm{w}}$ index is validated using the data from a single statios from European high latitudes. However, in future, the study will be extended by using the data from several stations from both the European and Canadian high latitude regions.

6.11 Chapter Summary

At present, most scintillation estimation approaches uses 50 Hz raw phase observations using GISTM receivers which are quite computationally time consuming and are also expensive to purchase. In this regard, a new TEC-based analogous phase index ($\sigma_{\phi a}$) was designed which can be implemented using generic dual frequency GPS receivers without employing any additional hardware or software. However, the main problem in estimating the scintillation values using the $\sigma_{\phi a}$ index was the improper filtering and its poor correlation with the standard phase scintillation index, σ_{ϕ}, during the weak geomagnetic conditions. In this chapter, a new improved form of the $\sigma_{\phi a}$ index is presented using the wavelet transform based filtering approach. The new index, $\sigma_{\phi a}^{\mathrm{w}}$, proved to be a good alternative to both the $\sigma_{\phi a}$ and σ_{ϕ} indices for representing the phase scintillation activity under both weak and strong geomagnetic conditions. The performance of the designed index was validated by using the GPS data from a European high latitude but, in the future, it will be tested using additional data from both the low and high latitudes.

Chapter 7

On Determining the Tracking Phase Jitter from TEC observations

7.1 Introduction

The phase jitter acts as a dominant source of phase error that affects the receiver performance during both the scintillation and non-scintillation conditions. If the phase jitter (standard deviation of the phase perturbations) exceeds the tracking threshold, the receiver loses lock. The PLL arctangent discriminator that was used in the GPS tracking loop designs in the previous chapters has a pull-in range of 180^o. From [9], one method of setting up the receiver tracking thresholds for the loss of lock is that the 3-sigma phase jitter must not exceed 1/4 of the pull-in range of the PLL discriminator given as

$$3\sigma_{PLL} = 3\sigma_j + \theta_e \leq 45^o \tag{7.1}$$

where σ_j is the phase jitter from all sources and θ_e is the dynamic stress error. From [9], the σ_j can be given as

$$\sigma_{PLL} = \sqrt{\sigma_{tPLL}^2 + \sigma_V^2 + \sigma_A^2} \tag{7.2}$$

where σ_{tPLL} is the tracking jitter due to thermal noise given in (7.3) and in [9] σ_{tPLL} is considered as the only source of tracking error in the absence of scintillation. σ_V is the

vibration induced oscillator jitter and σ_A is the Allan variance induced oscillator jitter. Upon using these values in (7.1) and simplifying, the 1-sigma phase jitter can by (7.4).

$$\sigma_{tPLL} = \sqrt{\frac{B_n}{C/N_o}\left[1+\frac{1}{2T_I C/N_o}\right]}, \qquad \text{radians} \tag{7.3}$$

$$\sigma_{PLL} = \sqrt{\sigma_{tPLL}^2 + \sigma_V^2 + \sigma_A^2} + \frac{\theta_e}{3} \leq 15^o \tag{7.4}$$

Equation (7.4) shows that, if 1-sigma phase jiiter exceeds 15^o [9], the receiver will most likely lose lock. In estimating the phase jitter using (7.1), the ionospheric scintillation effects were not considered but are the major source of carrier phase tracking errors responsible for tracking loop loss of lock. In this chapter, the wavelet-based phase scintillation index, $\sigma_{\phi a}^{\mathrm{w}}$, will be used to estimate the phase jitter which can then be used for setting up the tracking threshold to update the tracking loop parameters in a GPS receiver during scintillation conditions. Another advantage of using the $\sigma_{\phi a}^{\mathrm{w}}$ index as an alternate method of estimating the tracking phase errors is due to its simplistic computational approach which can also be used in geodetic receivers if a combination of both the hardware and software is employed in the receiver design which will obviate the use of expensive components as in the case of the scintillation monitoring receivers.

7.2 Carrier Tracking Phase Errors in the Presence of Scintillation

The ionospheric scintillation is the main cause of error in GPS tracking loop carrier phase measurements and therefore in order to set up equations for estimating the tracking thresholds for the carrier tracking loop, the ionospheric scintillation effects needs to be considered. From [80], the tracking error variance in the presence of ionospheric scintillation is

$$\sigma_{\phi e}^2 = \sigma_{\phi s}^2 + \sigma_{\phi T}^2 + \sigma_{\phi osc}^2 \tag{7.5}$$

where $\sigma^2_{\phi s}$ is the error variance due to phase scintillation, $\sigma^2_{\phi T}$ is the thermal noise error variance including the amplitude scintillation effects and $\sigma^2_{\phi osc}$ is the variance due to oscillator noise and usually taken as 0.1. From (4.45) and (4.59), the $\sigma^2_{\phi s}$ and $\sigma^2_{\phi T}$ in the presence of scintillation can be given as

$$\sigma^2_{\phi s} = \frac{\pi T}{k f_n^{p-1} \sin\left(\frac{(2k+1-p)\pi}{2k}\right)}, \quad 1 < p < 2k \tag{7.6}$$

$$\sigma^2_{\phi T} = \frac{\bar{B}_n}{C/N_o}\left[\frac{1}{1-S_4^2} + \frac{1}{2T_I C/N_o(1-3S_4^2+2S_4^2)}\right], \qquad \text{radians}^2 \tag{7.7}$$

where T is the spectral strength at 1 Hz, p is the slope of the phase PSD, k is the loop order, f_n is the loop natural frequency and $\bar{B}_n$ is the loop design bandwidth. Using (7.6) and (7.7) in (7.5), the overall tracking error variance is

$$\sigma^2_{\phi e} = \frac{\pi T}{k f_n^{p-1} \sin\left(\frac{(2k+1-p)\pi}{2k}\right)} + \frac{\bar{B}_n}{C/N_o}\left[\frac{1}{1-S_4^2} + \frac{1}{2T_I C/N_o(1-3S_4^2+2S_4^2)}\right] + \sigma^2_{\phi osc} \tag{7.8}$$

The formula in (7.8) is only valid for S_4 less than 0.7 as dicussed in section 4.7. To find the phase jitter, the spectral parameters p and T needs to be estimated which are not readily available from the ordinary geodetic and conventional scintillation receivers and involve a complex process such as determining the PSDs from the time series of high sample rate phase data which may not be available. A simple method to determine the spectal parameters (p, T) was proposed by [127] and further validated in [128] which we also used in this chapter for estimating the spectral parameters (p, T) which were then used in Conker formula [80] for estimating the phase jitter. Using [127] method, the spectral parameters can be estimated by using the known values of the scintillation indices (S_4, σ_ϕ).

From [127], the relationship between p, T, and the phase scintillation index, σ_ϕ, can be given as

$$\sigma_\phi^2 = 2T\left(\frac{f_u^r - f_c^r}{r}\right) \tag{7.9}$$

where $r = 1 - p$, f_u is the upper cutoff frequency of the detrended data (generally taken as half the sampling frequency) and f_c is the lower cutoff frequency (usually taken as the HPF cutoff used for detrending the phase measurements). From [127], the variance of the normalized amplitude scintillation index, σ_χ^2 can be given as

$$\sigma_\chi^2 = 2T\left[\left(\frac{f_F - f_c}{f_F^p}\right) + \left(\frac{f_u^r - f_F^r}{r}\right)\right] \tag{7.10}$$

where f_F is the Fresnel frequency and $S_4 \approx 2\sigma_\chi$. From the phase and log amplitude spectra graph given in [127], the area between the phase and log amplitude PSDs can be given as

$$\sigma_\phi^2 - \sigma_\chi^2 = 2T\left[\left(\frac{f_F^r - f_c^r}{r}\right) - \left(\frac{f_F - f_c}{f_F^p}\right)\right] \tag{7.11}$$

Using T from (7.9) in (7.11):

$$\sigma_\phi^2 - \sigma_\chi^2 = \left(\frac{r\sigma_\phi^2}{f_u^r - f_c^r}\right)\left[\left(\frac{f_F^r - f_c^r}{r}\right) - \left(\frac{f_F - f_c}{f_F^p}\right)\right] \tag{7.12}$$

Equation (7.12) can be used to find p $(r = 1 - p)$. Once p is known, T can be found using (7.9). In order to find the p and T, the σ_ϕ and S_4 indices needs to be estimated first. Once p and T are known, they can then be used in (7.8) to find the tracking error variance. Another more simplistic approach to find the tracking error variance was given by [129] which does not require the knowledge of the spectral parameters (p, T). The approach used by [129] was derived using the raw TEC 1 Hz data from high latitudes which replaced the term $\sigma_{\phi s}^2$ in (7.5) with the standard deviation of the HPF vertical ROT over a 1 min

interval multiplied by the scaling factor, r'. The tracking error variance using [129] method is given as

$$\sigma_{\phi e}^2 = r' \times \sigma_{VTEC'_{HPF}}^2 + \frac{\bar{B}_n}{C/N_o}\left[\frac{1}{1-S_4^2} + \frac{1}{2T_I C/N_o(1-3S_4^2+2S_4^4)}\right] + \sigma_{\phi osc}^2 \tag{7.13}$$

where $\sigma_{VTEC'_{HPF}}$ is the normalized standard deviation of the HPF vertical ROT and r' is the scaling factor which can be obtained from the straight line fitting of $\sigma_{VTEC'_{HPF}}^2$ as defined in [130]. This method of estimating the tracking error variance was also validated by using the data from high latitudes. In this chapter, instead of using [129] method in (7.13) or using Conker method, the $\sigma_{\phi a}^{\mathrm{w}}$ is used for estimating the phase jitter by employing both the Conker formula and [129] method.

In the first case, the $\sigma_{\phi a}^{\mathrm{w}}$ was first used to calculate the spectral parameters (p, T) using (7.9) and (7.12) by replacing the σ_ϕ index with the $\sigma_{\phi a}^{\mathrm{w}}$ index. These spectral parameters were then used in (7.8) for estimating the phase jitter ($\sigma_{\phi e}$). It should be noted when using $\sigma_{\phi a}^{\mathrm{w}}$ in (7.9) and (7.12), the parameter values (f_u Hz, f_c, f_o, f_F), which will be defined in the next section, will be changed because, the $\sigma_{\phi a}^{\mathrm{w}}$ and σ_ϕ indices are derived from different data sources which involve a different filtering process and a different sampling rate which are very important quantities when using (7.9) and (7.12) as using wrong values for these parameters will lead to false phase jitter values.

On the other hand, when estimating the phase jitter ($\sigma_{\phi e}$) using [129] method, the $\sigma_{VTEC'_{HPF}}^2$ in (7.13) was replaced by $\sigma_{VTEC'_{wav}}^2$ where $\sigma_{VTEC'_{wav}}$ is the standard deviation of the wavelet filtered vertical ROT over a 1 min interval given in (6.19). Using $\sigma_{VTEC'_{wav}}^2$ in (7.13), the new equation for estimating the tracking phase jitter can be given as

$$\sigma_\phi^2 = r' \times \sigma_{VTEC'_{wav}}^2 + \frac{\bar{B}_n}{C/N_o}\left[\frac{1}{1-S_4^2} + \frac{1}{2T_I C/N_o(1-3S_4^2+2S_4^4)}\right] + \sigma_{\phi osc}^2 \tag{7.14}$$

Here, the phase jitter estimated using (7.8), in which the spectral parameters were estimated using the σ_ϕ index, is named the Conker Model, whereas the tracking jitter estimated using (7.13) employing the [129] method is termed the Tiwari Model. For

the case of the new phase jitter estimation process discussed above, the phase jitters are named as Ahmed Model 1 and Ahmed Model 2. In Ahmed Model 1, (7.14) was used for estimating the phase jitter which uses the [129] method. In Ahmed Model 2, the phase jitter was estimated using the Conker formula given by (7.8) but, the spectral parameters were calculated by replacing the σ_ϕ index with the $\sigma_{\phi a}^{\mathrm{w}}$ index in (7.9) and (7.12). In the next section, these two methods are used to estimate the phase jitter and the performance is then compared with the previously proposed Conker model and Tiwari model phase jitters.

7.3 Results and Discussion

In this section, the results of the tracking phase jitters estimated using the Conker model, Tiwari method, Ahmed mode 1 and Ahmed model 2 are presented. For this analysis, the data from the receiver station installed at Trondheim, Norway (63.41^o N, 10.4^o E) was used to log the σ_ϕ and S_4 indices at the 50 Hz rate. The same was also used to record the 1 Hz raw TEC data which was used to calculate the $\sigma^2_{VTEC'_{HPF}}$, $\sigma^2_{VTEC'_{wav}}$ and $\sigma_{\phi a}^{\mathrm{w}}$ used in the Tiwari model, Ahmed model 1 and Ahmed model 2 respectively.

For the Conker model phase jitter, the following parameter values were used: $f_u = 25$ Hz, $f_c = 0.1$ Hz and $f_F = 2.5$ Hz. Similarly, in the case of the Ahmed model 2, the following parameter values were used: $f_u = 0.5$ Hz, $f_c = 0.17$ Hz, $f_F = 1$ Hz. For performance testing, a third order tracking loop ($k = 3$) is considered as an example with a noise bandwidth, B_n, of 10 Hz and $T_I = 20$ ms. The natural frequency, f_n, of the third order tracking loop can be found as

$$f_n = \frac{1.2B_n}{2\pi} \tag{7.15}$$

In the case of the Tiwari method [129] and Ahmed model 1, the scaling factor, r', is taken as 0.05 although it may vary depending on the application [130]. The above methods were then used to estimate the phase jitters of the PRN's on 24 April, 2012, that were visible during the time of a strong geomagnetic storm which occured in the early hours of the day as shown in Fig. 5.4. The Kp value on this day was recorded as high as 7 during the coarse of the storm.

In Fig. 7.1, the phase jitter calculated using the Ahmed Model 1 is compared with the Conker model (Fig. 7.1a) and Tiwari model phase jitters (Fig. 7.1b). In Fig. 7.1(a), the solid red line represents the phase jitter using the Ahmed mode 1 whereas the solid black line represents the phase jitter using the Conker model. Similarly, in Fig. 7.1(b), the solid red line is the phase jitter using Ahmed model 1 and the blue line represents the phase jitter using the Tiwari model. It can be seen that the Ahmed model 1 phase jitter (solid red line in Fig. 7.1(a) and (b)) has a very similar pattern to both the Conker and Tiwari model phase jitters. The Ahmed model 1 showed a good correlation with the Tiwari model (Fig. 7.1b). However, in the case of the Conker model (Fig. 7.1a), it was found that although there existed a good correlation between the two, the Conker model seems to underestimate the phase jitter values especially in the case of PRN's 3, 6, 18 and 19 between 01:00 and 03:00 UT when there was strong scintillation present as can be seen in Fig. 6.8 showing the scintillation activity of these PRN's on 24 April 2012. For example, in the case of PRN's 3, 6 and 19, Fig. 6.8 shows that the scintillation values reached as high as 1.2 during 01:00 and 03:00 but, the phase jitter values estimated using the Conker model are mostly within the range of 8^o to 9^o which falls in the same range as those phase jitter values for which the scintillation was less than 0.3 , i. e., before 01:00 and after 03:00 UT. On the other hand, when the phase jitter values estimated using the Ahmed model 2 were compared with the Conker and Tiwari model in Fig. 7.2, a similar pattern was also found but both the Conker and Tiwari models seem to overestimate the phase jitter values at low elevation angles and this over estimationfactor was higher in the case of the Tiwari model. Here, comparing the phase jitters of the Ahmed model 2 and Conker model during the presence of the strong scintillation (01:00 to 03:00 UT) further validates the fact that the Conker model gives somewhat underestimated values during times of strong scintillation.

The comparison of the phase jitters made in Fig. 7.1 and Fig. 7.2 was for a single day. To further extend this analysis and to validate the phase jitter performance estimated using the Ahmed models 1 and 2, a statistical study was carried out by estimating the phase jitters for all the scintillation events from October 2011 to September 2012 on the days and times when Kp was greater than or equal to 5. A comparison was then made between the

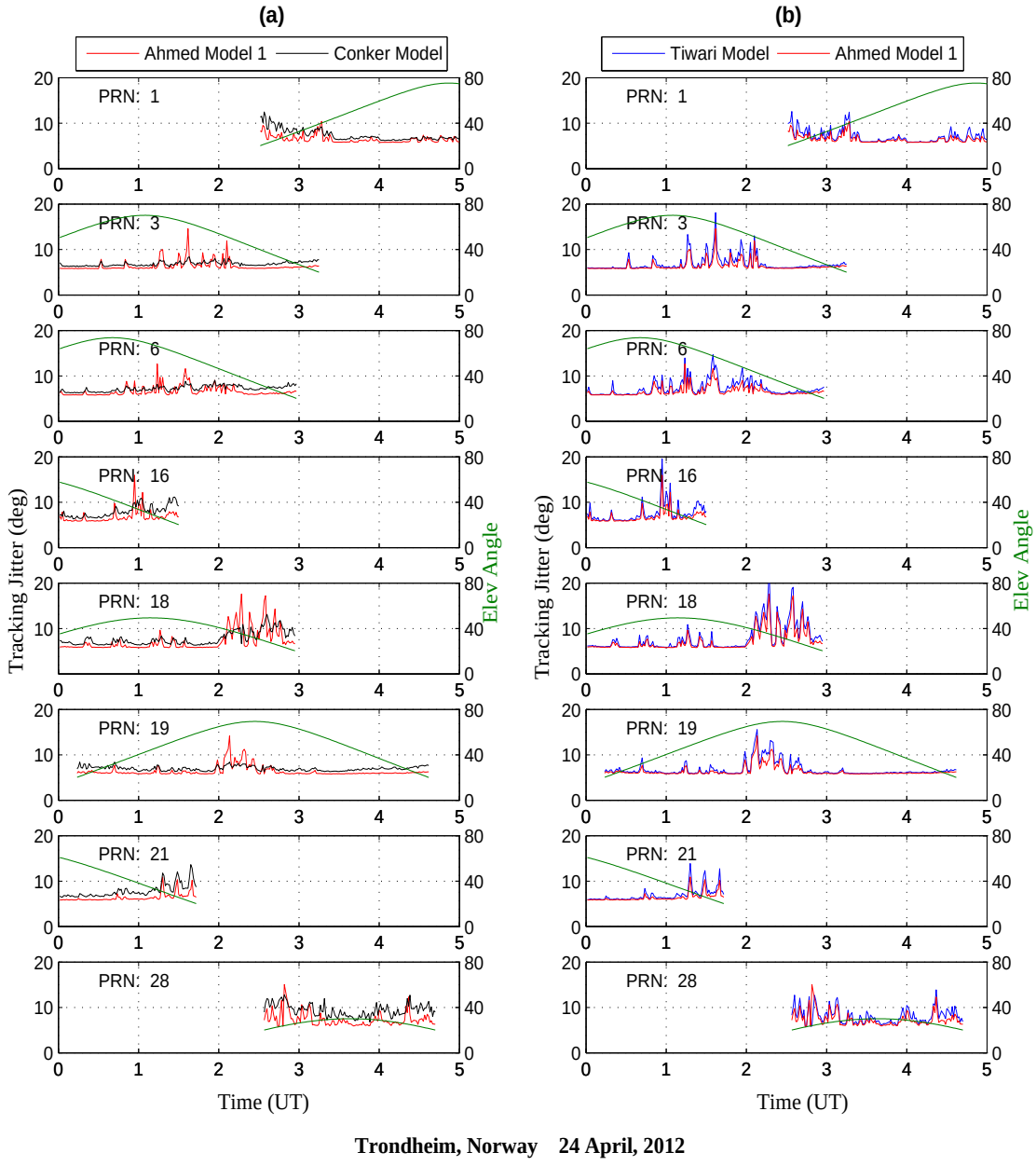

Figure 7.1: Phase jitter of a third order tracking loop using the Ahmed model 1, Conker and Tiwari models.

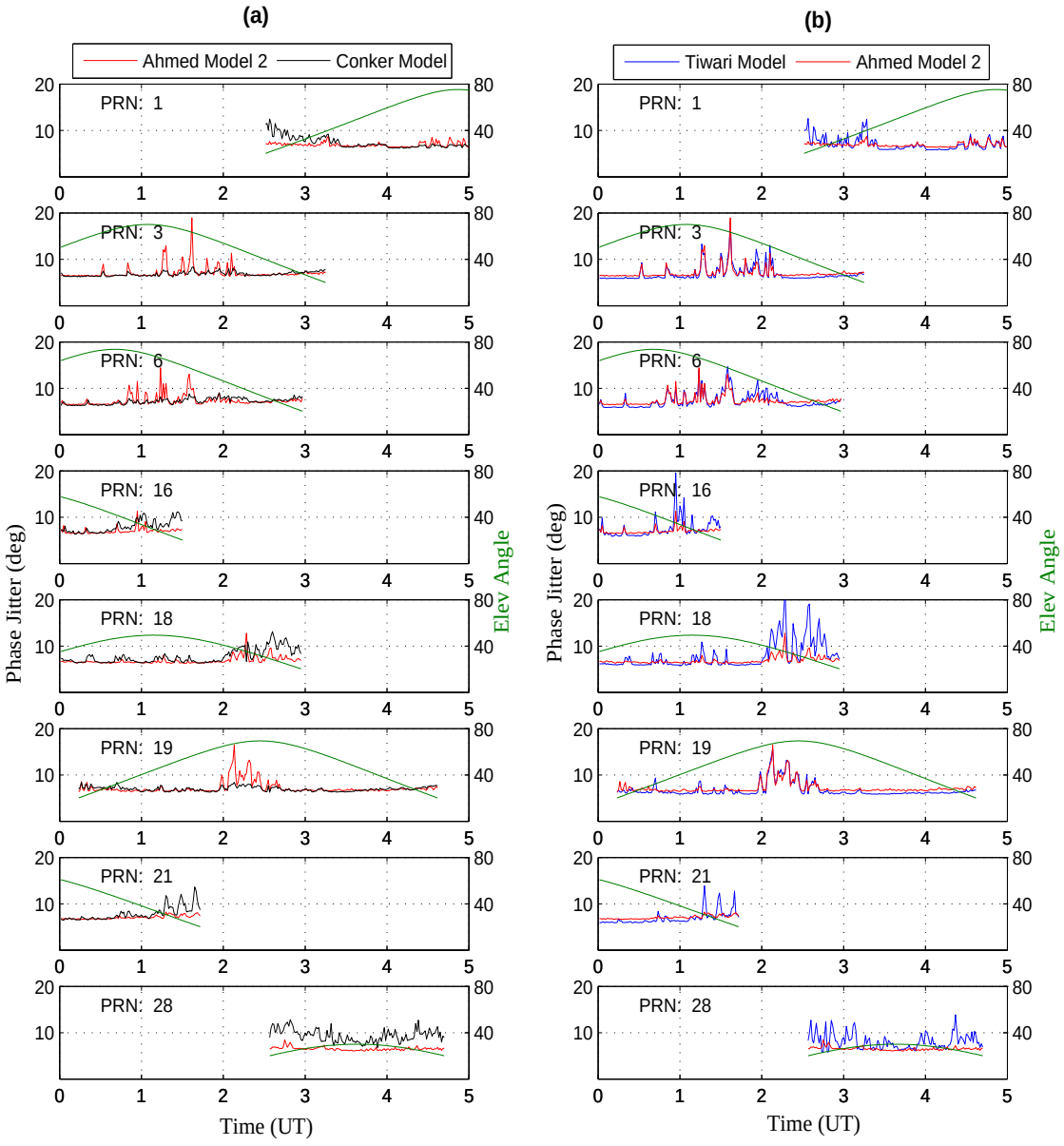

Figure 7.2: Phase jitter of a third order tracking loop using the Ahmed model 2, Conker and Tiwari models.

phase jitters estimated from the Ahmed models 1 and 2 and those from the Tiwari model and Conker model as shown in Fig. 7.3 and Fig. 7.4. The scintillation activity is also shown in the bottom panel in each figure.

In Fig. 7.3(a), it can be seen that Ahmed model 1 and Conker model have a very similar pattern which is correlating well with the Conker model. However, a few high phase jitter values can be seen in the case of Ahmed model 1 between 00:00 and 04:00 UT but, looking at the scintillation plot in Fig. 7.3(c), it can be seen that these phase jitter values were in a well defined period of high σ_ϕ values depicting that these are due to the presence of strong scintillation and therefore can be used to set tracking thresholds for the tracking loops with a minimum probability of resulting in a false alarm. Another important thing found here was that from 05:00 to 16:00, when the scintillation activity was at the lowest level, on average, the phase jitter values in the case of Conker model were 1^o to 2^o higher than the Ahmed model 1. Similarly, when the Ahmed model 1 was compared with the Tiwari model in Fig. 7.3(b), both were following a similar pattern apart from the fact that the phase jitter values in the the case of Tiwari model were quite overestimated during both the scintillation and non-scintillation conditions. This was also discussed by [129] where it was mentioned that the phase jitter estimated using the Tiwari model may be higher which sometimes can lead to a false alarm in setting up tracking loop thresholds.

Then also in Fig. 7.4, the phase jitter calculated using the Ahmed model 2 was compared with the Conker and Tiwari models. Here, the Ahmed model 2 occurence pattern was correlating well with the Conker model (Fig. 7.4a) but this was found to be not as good when compared with the Tiwari model (Fig. 7.4b). This is due to the overestimation factor involved using the Tiwari model. From the phase scintillation graph in (Fig. 7.4c), it can be deduced that the Ahmed model 2 and Conker model are depicting more accurate phase jitter values.

Based on the analysis presented above, it cannot be said for sure which model (Ahmed models 1 or 2) depicts more accurate phase jitter values. This also applies to the Conker and Tiwari models as well. However, both the Ahmed models 1 and 2 tend to give values which reflect true picture of the presence of the scintillation. This should be further investigated by implementing the two methods in a real time GPS application such as in GPS/GNSS

receivers for setting up the tracking loop thresholds for defining the tracking loop loss of lock states during scintillation conditions and this is considered a future goal for this research work.

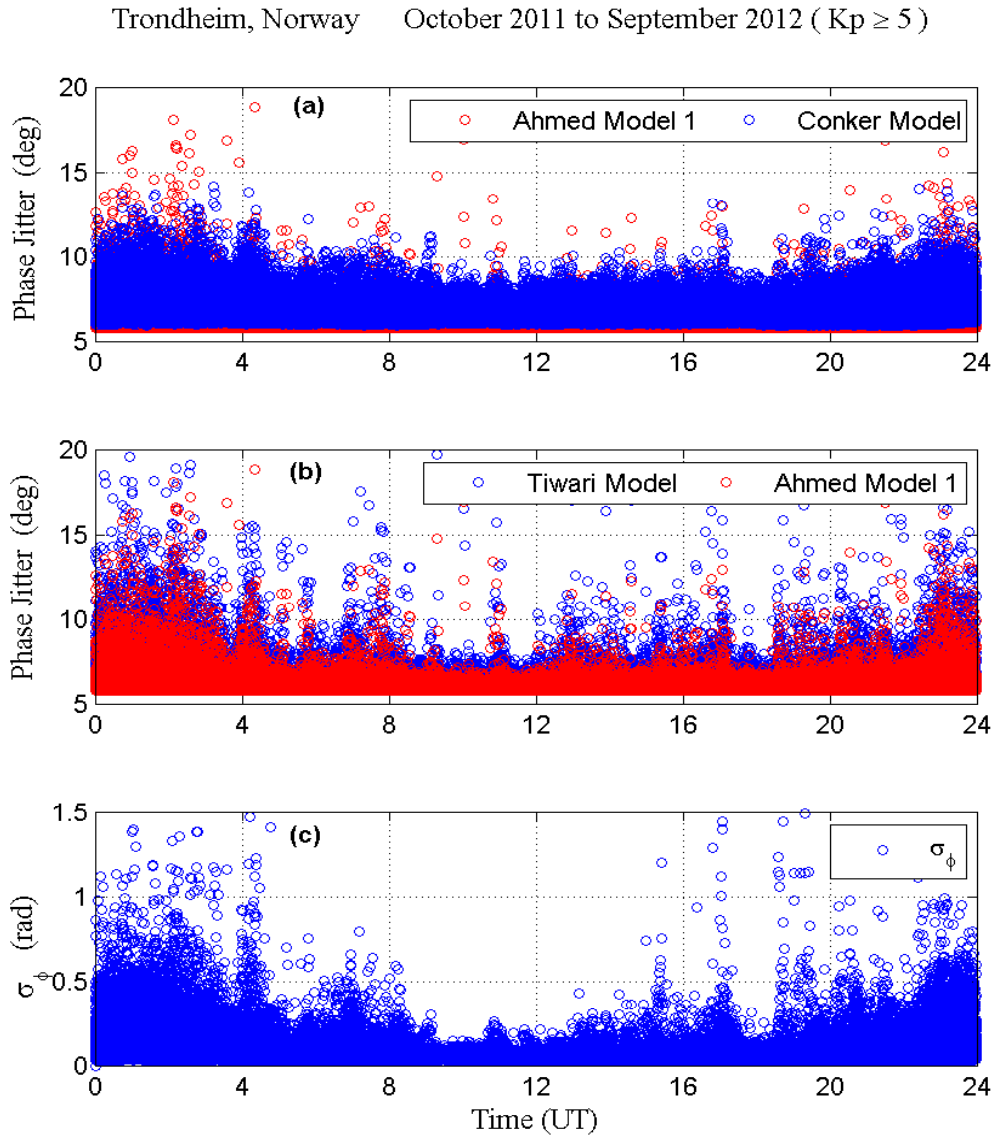

Figure 7.3: Phase jitter comparison between the Ahmed model 1 and Conker model and also between the Ahmed model 1 and Tiwari model for all the scintillation events from October 2011 to September 2012 for $Kp \geq 5$.

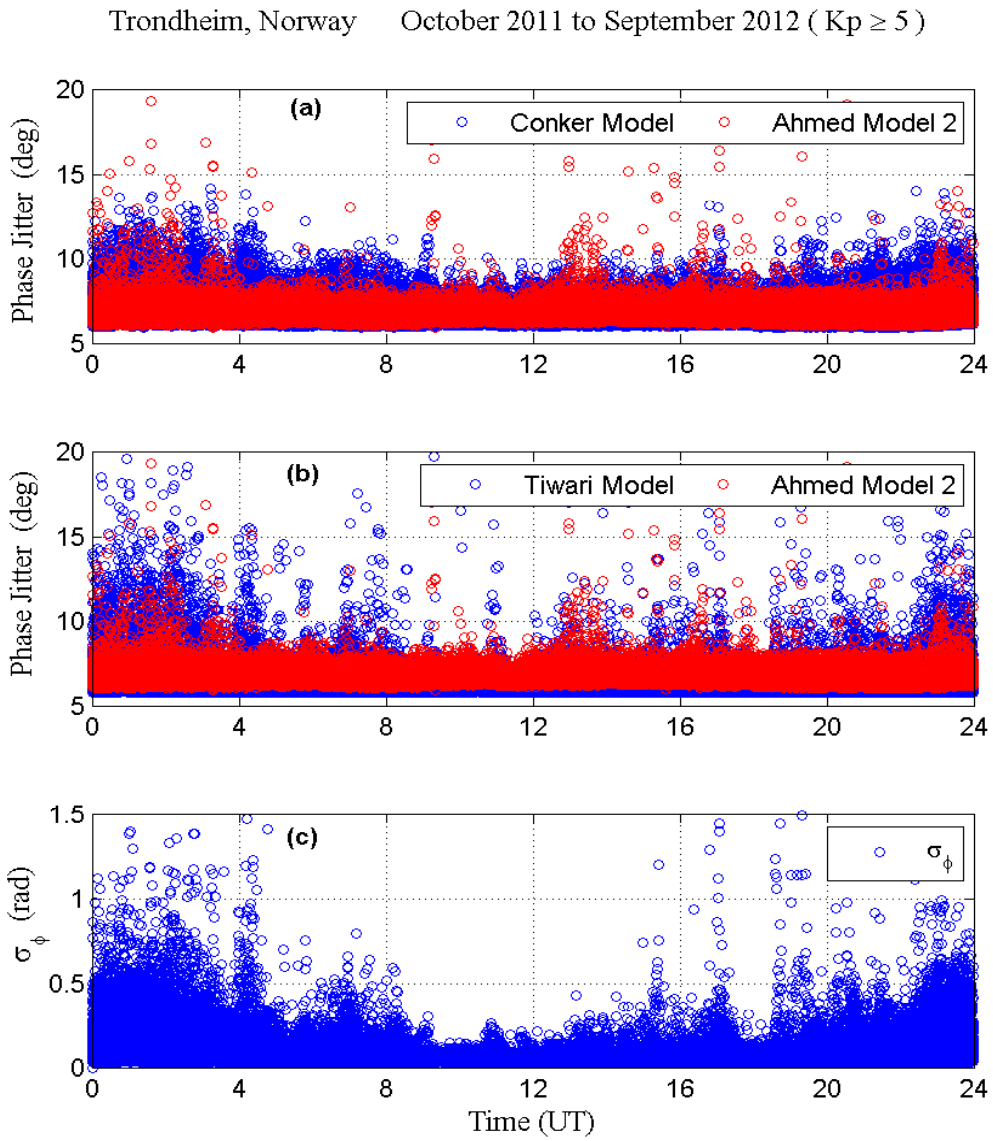

Figure 7.4: Phase jitter comparison between the Ahmed model 2 and Conker model and also between the Ahmed model 2 and Tiwari model for all the scintillation events from October 2011 to September 2012 for $Kp \geq 5$.

7.4 Chapter Summary

Determining the tracking phase jitter plays a very important role in mitigating the effects of scintillation on GPS/GNSS receivers. The phase jitter is usually used to define the tracking thresholds for the tracking loops beyond which loss of lock is most likely to occur during both scintillation and non-scintillation conditions. In this chapter two different models, namely Ahmed model 1 and Ahmed model 2, were used to calculate the phase jitter. In Ahmed model 1, the Conker formula was used but the tracking jitter due to phase scintillation was replaced with the standard deviation of the wavelet filtered vertical ROT over a 1 min interval multiplied with the scaling factor. In Ahmed model 2, the standard Conker formula was used but the spectral parameters (p, T) were estimated using the $\sigma_{\phi a}^{\mathrm{w}}$ index by a method explained in section 7.1. The phase jitter, estimated using the Ahmed model 1 and Ahmed model 2 was then compared with both the Conker and Tiwari model phase jitters. Based on the results presented in this chaper, it can be deduced that both the Ahmed models 1 and 2 can be quite useful in yielding accurate values of the phase jitter, closer to the actual values and therefore could be successfully used in GPS/GNSS receivers for defining the tracking loop thresholds during the scintillation conditions.

Chapter 8

Conclusions and Future Recommendations

8.1 Conclusion

The research work presented in this thesis can be divided into three main parts; (i) studying the effects of scintillation on GPS receivers specifically at the acquisition and tracking stages, (ii) designing a computationally intensive improved TEC-based analogous phase scintillation index for high latitudes which can also be implemented using low cost geodetic receivers and (iii) using the TEC-based observations and the improved TEC-based phase scintillation index for estimating the tracking phase jitter. Although, a general summary is given at the end of each chapter, the major conclusions that have been drawn from the thesis work are summarized here.

The first part of the thesis starts with the literature review in which the effects of scintillation on the satellite-based navigation are discussed. In this regard, scintillation effects on the GPS receiver acquisition process are analyzed in terms of the probability of detection (P_d) due to the fact that the amplitude scintillation results in the reduction of the P_d at acquisition stage. Several acquisition methodologies were implemented for analyzing the detection performance such as the parallel FFT-based circular correlation method, ZP method and a newly designed RBA method. The detection probability and the number of computations involved in each method was computed and compared and it was found that in

order to achieve a better detection performance with a reduced number of computations, the RBA method proved to be better than both the FFT-based and ZP methods. The discussion of scintillation effects on GPS receivers was then further enhanced by explaining the loss of lock in the GPS tracking loop during the scintillation conditions. This was done by estimating the tracking error variance of second and third order tracking loops. This was then used to define the tracking thresholds for the tracking loop designs of 2nd and 3rd orders beyond which the receiver loses lock. However, it was found that there were several parmeters that needed to be considered in order to define the tracking thresholds. These parameters are the spectral strength, T, at 1 Hz, the slope p of the PSD plotted on log-log axis, loop order, C/No, noise bandwidth and the amplitude scintillation, given by S4. Here, it was also found that during the scintillation conditions (both weak and strong), the second order tracking loop provides more robust tracking than the third order loop as it was less likely to loose lock than the third order loop and gave 25 to 30 % better performance. A case study was also carried out using the simulated GPS signals by implementing several tracking loop designs in Matlab R2011. The first tracking loop was the conventional 2nd order PLL, the second was the FLL-assisted PLL employing a 3rd order PLL with a 2nd order FLL, the third was the 2nd order PLL using the wavelet denoising and the fourth was the FLL-assisted PLL using the wavelet denoising. Here, the wavelet denoising was introduced by modifying the PLL and FLL-assisted PLL tracking loop designs to observe whether the modified designs using wavelet denoising could improve the receiver performance or not during scintillation conditions. The results of the comparison between these tracking loop designs showed that, although the wavelet denoising may help in decreasing the errors in the estimation of the carrier phase, overall the wavelet denoising is not useful in recovering from the loss of lock state during scintillation. It was also found that the FLL-assisted PLL was better than the conventional PLL and that its performance can be further improved by using the wavelet denoising method.

The second part of the thesis was focused on developing the new indices which could be used to better represent the phase scintillation activity at high latitudes. A relationship between the TEC variations produced due to ionospheric irregularities and their association to scintillation was discussed. The rate of change of TEC (ROT) has

been used by many researchers to link with the scintillation activity. In this regard, several TEC-based scintillation indices are proposed and in this part of the thesis, a fair amount of literature review was done to highlight the advantages of using the TEC-based scintillation indices and also the drawbacks of the previously proposed indices for deriving the scintillation values. A new TEC-based phase scintillation index, known as the analogous phase scintillation index, was also presented and its performance was compared with the standard phase scintillation index by using the data from a European high latitude region. It was found that the designed index correlates well with the standard index during the strong geomagnetic conditions but, for weak geomagnetic conditions, the correlation was found to be poor. The reason behind this poor correlation maybe due to the fact that the two indices were derived from different data sources for which the filtering effect using the time invariant digital filters could be different.

A complete analysis of the results using the large amount of data from a high latitude region showed that both the analogous phase index and the standard phase scintillation index were giving overestimated values either during the strong geomagnetic or weak geomagnetic conditions. It was also found that most of these overestimated values were due to the improper filtering effects which were more visible at low elevation angles (due to high multipath) as the indices were unable to distinguish between the noise and the actual scintillation. To address this issue, a totally new wavelet transform based filtering approach was used to design a new index known as the wavelet-based analogous phase scintillation index which removed the discrepancies involved in the estimation of the analogous phase index. This new index showed a very good correlation with both the analogous phase index and the standard phase scintillation index during both the weak and strong geomagnetic conditions. The index was validated by testing its performance with data from a European high latitude and it was found that it can be used as a good alternative to the previously proposed indices for representing the phase scintillation activity.

The third and last part has covered the practical aspects of the work presented in this thesis. This involves estimating the tracking phase jitter using the raw TEC observations and the wavelet-based analogous phase index through two different phase jitter estimation methods. These were then compared with the previous phase jitter estimation methods

which employs the analogous phase index and the standard phase scintillation index. Apart from the comparison, the main focus of estimating the tracking jitter here was to show that the new methods presented can be used in updating the tracking loop parameters during the scintillation conditions which could help in mitigating the effects of scintillation on GPS receivers but such applications comes under the future development of this research work.

8.2 Future Work

The work presented in this thesis has shown promising results which in future can be used to mitigate the effects of scintillation on GNSS/GPS receivers both at the acquisition and tracking levels. There are several issues that still needs attention and are recommended for future research:

- The designed RBA acquisition method is implemented and validated using the simulated GPS signals for varying C/N_o values in which there was no scintillation. The work is already proceeding to use the RBA method in the software-based GPS receivers designed at Newcastle University for acquiring the real GPS signals. In future, the designed software-based receiver will be used to acquire the signals affected by strong amplitude scintillation to check the performance of the RBA method along with other acquisition methods.

- The work on the TEC-based phase scintillation indices showed very good results and confirmed that these indices can be used to represent the phase scintillation activity but the performance of these indices was only validated using the data from a single high latitude region from Europe. In future, the data from both the European and Canadian high latitudes will be used to validate the wavelet-based phase scintillation index as an alternate method for representing the phase scintillation activity.

- Based on the new phase jitter estimation methods, which uses the TEC-based observations and the wavelet-based analogous phase index, it is suggested that these new methods can be used efficiently in GPS/GNSS receivers for updating the tracking loop parameters for scintillation mitigation due to low computational

cost. In this regard, the work is almost in a completion phase as the analogous phase index has already been implemented in the real GPS receivers for monitoring the scintillation activity. Regarding using the phase jitter estimation methods in GPS/GNSS receivers, the work is already in progress.

In addition to the above mentioned research areas, future work should also include the testing of the above methods in the low latitude regions as the scintillation statistics are different there from those at high latitudes.

Bibliography

[1] "GLONASS," [Online: accessed April-2015]. [Online]. Available: http://www.nis-glonass.ru/en/glonass/

[2] "Global Positioning System: Performance Standards & Specifications ," 2008, [Online; accessed April-2015]. [Online]. Available: http://www.gps.gov/systems/gps/

[3] J. B. Y. Tsui, *Fundamentals of Global Positioning System Receivers: A Software Approach*. John Wiley & Sons, Inc., 2005, vol. 2.

[4] M. S. Grewal, L. R. Weill, and A. P. Andrews, *Global Positioning Systems, Inertial Navigation and Integration*. John Wiley & Sons, Inc., 2007.

[5] A. El-Rabbany, "Introduction to GPS," in *Introduction to GPS: The Global Positioning System*. Artech House, Inc., 2002.

[6] B. W. Parkinson and J. J. Spilker, "GPS Navigation Data," in *Global Positioning System: Theory and Applications*. Washington, DC: American Institute of Aeronautics and Astronautics, Inc., 1996, pp. 121–176.

[7] B. W. Parkinson and J. J. Spilker, "GPS Receivers," in *Global Positioning System: Theory and Applications*. Washington, DC: American Institute of Aeronautics and Astronautics, Inc., 1996, pp. 329–408.

[8] J. B. Y. Tsui, "Acquisition of GPS C/A Code Signals," in *Fundamentals of Global Positioning System Receivers: A Software Approach*. John Wiley & Sons, Inc., 2005.

[9] E. D. Kaplan and C. Hegarty, "Satellite Signal Acquisition, Tracking, and Data Demodulation," in *Understanding GPS: Principles and Applications*. Artech House, Inc., 2006.

[10] K. Borre, D. M. Akos, N. Bertelsen, P. Rinder, and S. H. Jensen, "Carrier and Code Tracking," in *A software defined GPS and Galileo Receiver*. Birkhauser Boston, 2007.

[11] S. Jin, *Global Navigation Satellite Systems: Signal, Theory and Applications*. InTech., 2012.

[12] B. W. Parkinson and J. J. Spilker, "Fundamentals of Signal Tracking Theory," in *Global Positioning System: Theory and Applications*. Washington, DC: American Institute of Aeronautics and Astronautics, Inc., 1996, pp. 245–325.

[13] J. B. Y. Tsui, "Basic GPS Concept," in *Fundamentals of Global Positioning System Receivers: A Software Approach*. John Wiley & Sons, Inc., 2005.

[14] B. W. Parkinson and J. J. Spilker, "GPS error analysis," in *Global Positioning System: Theory and Applications*. Washington, DC: American Institute of Aeronautics and Astronautics, Inc., 1996, pp. 469–484.

[15] B. W. Parkinson and J. J. Spilker, "Ionospheric Effects on GPS," in *Global Positioning System: Theory and Applications*. Washington, DC: American Institute of Aeronautics and Astronautics, Inc., 1996, pp. 485–516.

[16] B. W. Parkinson and J. J. Spilker, "Tropospheric Effects on GPS," in *Global Positioning System: Theory and Applications*. Washington, DC: American Institute of Aeronautics and Astronautics, Inc., 1996, pp. 517–546.

[17] E. D. Kaplan and C. Hegarty, "Differential GPS," in *Understanding GPS: Principles and Applications*. Artech House, Inc., 2006.

[18] J. B. Y. Tsui, "Satellite Constellation," in *Fundamentals of Global Positioning System Receivers: A Software Approach*. John Wiley & Sons, Inc., 2005.

[19] M. C. Kelley, "Introductory and Background Material," in *The Earth's Ionosphere*. Academic Press., 2009.

[20] E. Kudeki, "Applications of Radiowave Propagation," 2010, [Online: accessed April-2015]. [Online]. Available: https://courses.engr.illinois.edu/ece458/458sp10.pdf

[21] A. Ghasemi, A. Abedi, and F. Ghasemi, "Radio Wave Propagation in Ionosphere," in *Propagation Engineering in Wireless Communications*. Springer-Verlag New York, 2012.

[22] C. Levis, J. T. Johnson, and F. L. Teixeira, "Characteristics of the Ionosphere," in *Radiowave Propagation: Physics and Applications*. John Wiley & Sons, Inc., 2010.

[23] C. Levis, J. T. Johnson, and F. L. Teixeira, " Ionospheric Propagation," in *Radiowave Propagation: Physics and Applications*. John Wiley & Sons, Inc., 2010.

[24] P. J. Citrone, "The Effect of the electron-Density Gradients on Propagation of Radio Waves in the Mid-latitude Trough," *Masters Thesis*, 1991.

[25] "Introduction to HF Radio Propagation," 2012, [Online: accessed March-2015]. [Online]. Available: http://www.ips.gov.au/Educational/5/2/2

[26] A. W. Wernik, L. Alfonsi, and M. Materassi, "Scintillation modeling using in-situ data," *Radio Science*, vol. 42, no. 1, 2007, rS1002. [Online]. Available: http://dx.doi.org/10.1029/2006RS003512

[27] "Basic Ionosonde Theory," [Online; accessed April-2015]. [Online]. Available: http://www.g0lfp.com/ionograms/index.php

[28] D. Allain and C. Mitchell, "Ionospheric delay corrections for single-frequency GPS receivers over Europe using tomographic mapping," *GPS Solutions*, vol. 13, no. 2, pp. 141–151, 2009. [Online]. Available: http://dx.doi.org/10.1007/s10291-008-0107-y

[29] J. Klobuchar, "Ionospheric Time-Delay Algorithm for Single-Frequency GPS Users," *Aerospace and Electronic Systems, IEEE Transactions on*, vol. AES-23, no. 3, pp. 325–331, May 1987.

[30] S. Radicella, "The nequick model genesis, uses and evolution," *Annals of Geophysics*, vol. 52, no. 3-4, 2009. [Online]. Available: http://www.annalsofgeophysics.eu/index.php/annals/article/view/4597

[31] D. Bilitza, L.-A. McKinnell, B. Reinisch, and T. Fuller-Rowell, "The international reference ionosphere today and in the future," *Journal of Geodesy*, vol. 85, no. 12, pp. 909–920, 2011. [Online]. Available: http://dx.doi.org/10.1007/s00190-010-0427-x

[32] R. W. Schunk, L. Scherliess, J. J. Sojka, D. C. Thompson, D. N. Anderson, M. Codrescu, C. Minter, T. J. Fuller-Rowell, R. A. Heelis, M. Hairston, and B. M. Howe, "Global Assimilation of Ionospheric Measurements (GAIM)," *Radio Science*, vol. 39, no. 1, 2004, rS1S02. [Online]. Available: http://dx.doi.org/10.1029/2002RS002794

[33] C. N. Mitchell, "Combining radio occultation measurements with other instruments to map the ionospheric electron concentration," in *First CHAMP Mission Results for Gravity, Magnetic and Atmospheric Studies*, C. Reigber, H. Luhr, and P. Schwintzer, Eds. Springer Berlin Heidelberg, 2003, pp. 491–499. [Online]. Available: http://dx.doi.org/10.1007/978-3-540-38366-6-67

[34] X. Pi, A. J. Mannucci, U. J. Lindqwister, and C. M. Ho, "Monitoring of global ionospheric irregularities using the Worldwide GPS Network," *Geophysical Research Letters*, vol. 24, no. 18, pp. 2283–2286, 1997. [Online]. Available: http://dx.doi.org/10.1029/97GL02273

[35] K. C. Yeh and C.-H. Liu, "Radio wave scintillations in the ionosphere," *Proceedings of the IEEE*, vol. 70, no. 4, pp. 324–360, April 1982.

[36] K. G. Budden, *The Propagation of Radio Waves*. Cambridge University Press, 1985, cambridge Books Online. [Online]. Available: http://dx.doi.org/10.1017/CBO9780511564321

[37] M. Alizadeh, H. Schuh, S. Todorova, and M. Schmidt, "Global Ionosphere Maps of VTEC from GNSS, satellite altimetry, and formosat-3/COSMIC data," *Journal of Geodesy*, vol. 85, no. 12, pp. 975–987, 2011. [Online]. Available: http://dx.doi.org/10.1007/s00190-011-0449-z

[38] J. Bohm and H. Schuh, "Ionospheric Effects on Microwave Signals," in *Atmospheric Effects in Space Geodesy*. Springer Berlin Heidelbergr, 2013.

[39] J. C. Hinks, T. E. Humphreys, B. O. Hanlon, M. L. Psiaki, and J. Paul M. Kintner, "Evaluating GPS Receiver Robustness to Ionospheric Scintillation," in *Proceedings of the 21st International Technical Meeting of the Satellite Division of The Institute of Navigation*, Savannah International Convention Center, Savannah, GA, 2008, pp. 309 – 320.

[40] A. J. Van Dierendonck, J. Klobuchar, and Q. Hua, "Ionospheric Scintillation Monitoring Using Commercial Single Frequency C/A Code Receivers," in *Proceedings of the 6th International Technical Meeting of the Satellite Division of The Institute*

of Navigation, Salt Palace Convention Center, Salt Lake City, UT, 1993, pp. 1333 – 1342.

[41] C. S. Carrano, K. M. Groves, W. J. McNeil, and P. H. Doherty, "Scintillation Characteristics across the GPS Frequency Band," in *Proceedings of the 2012 International Technical Meeting of the Satellite Division of The Institute of Navigation*, Nashville, TN, 2012, pp. 1139 – 1147.

[42] S. Basu and S. Basu, "Equatorial scintillations—a review," *Journal of Atmospheric and Terrestrial Physics*, vol. 43, no. 5–6, pp. 473 – 489, 1981, equatorial Aeronomy - I. [Online]. Available: http://www.sciencedirect.com/science/article/pii/0021916981901100

[43] R. A. Steenburgh, C. G. Smithtro, and K. M. Groves, "Ionospheric scintillation effects on single frequency GPS," *Space Weather*, vol. 6, no. 4, pp. n/a–n/a, 2008, s04D02. [Online]. Available: http://dx.doi.org/10.1029/2007SW000340

[44] J. Seo, T. Walter, T.-Y. Chiou, and P. Enge, "Characteristics of deep GPS signal fading due to ionospheric scintillation for aviation receiver design," *Radio Science*, vol. 44, no. 1, 2009, rS0A16. [Online]. Available: http://dx.doi.org/10.1029/2008RS004077

[45] L. Kersley, S. E. Pryse, and N. S. Wheadon, "Amplitude and phase scintillation at high latitudes over northern Europe," *Radio Science*, vol. 23, no. 3, pp. 320–330, 1988. [Online]. Available: http://dx.doi.org/10.1029/RS023i003p00320

[46] "Effect of Ionospheric Scintillations on GNSS: A White Paper," 2010. [Online]. Available: http://waas.stanford.edu/papers/IWG/sbas_iono_scintillations_white_paper.pdf

[47] S. Musman, J.-M. Jahn, J. LaBelle, and W. E. Swartz, "Imaging spread-F structures using GPS observations at Alcântara, Brazil," *Geophysical Research Letters*, vol. 24, no. 13, pp. 1703–1706, 1997. [Online]. Available: http://dx.doi.org/10.1029/97GL00834

[48] E. J. Weber, S. Basu, T. W. Bullett, C. Valladares, G. Bishop, K. Groves, H. Kuenzler, P. Ning, P. J. Sultan, R. E. Sheehan, and J. Araya, "Equatorial plasma depletion precursor signatures and onset observed at 11^o south of the magnetic equator," *Journal of Geophysical Research: Space Physics*, vol. 101, no. A12, pp. 26 829–26 838, 1996. [Online]. Available: http://dx.doi.org/10.1029/96JA00440

[49] R. G. Caton, M. J. Kendra, and W. J. McNeil, "GPS SCINTILLATION ANALYSIS," AIR FORCE RESEARCH LABORATORY, Tech. Rep., 1998.

[50] S. Datta-Barua, P. Doherty, S. Delay, T. Dehel, and J. Klobuchar, "Ionospheric Scintillation Effects on Single and Dual Frequency GPS Positioning ," in *Proceedings of the 16th International Technical Meeting of the Satellite Division of The Institute of Navigation*, Oregon Convention Center, Portland, OR, 2003, pp. 336 – 346.

[51] J. Seo, T. Walter, E. Marks, T.-Y. Chiou, and P. Enge, "Ionospheric Scintillation Effects on GPS Receivers during Solar Minimum and Maximum," in *International Beacon Satellite Symposium*, Boston, MA, 2007.

[52] C. Carrano and K. Groves, "Temporal Decorrelation of GPS Satellite Signals due to Multiple Scattering from Ionospheric Irregularities," in *Proceedings of the 23rd International Technical Meeting of The Satellite Division of the Institute of Navigation*, Oregon Convention Center, Portland, Oregon, 2012, pp. 361 – 374.

[53] "GLOBAL POSITIONING SYSTEM STANDARD POSITIONING SERVICE PERFORMANCE STANDARD," 2008. [Online]. Available: http://www.gps.gov/technical/ps/2008-SPS-performance-standard.pdf

[54] S. Basu, E. MacKenzie, and S. Basu, "Ionospheric constraints on VHF/UHF communications links during solar maximum and minimum periods," *Radio Science*, vol. 23, no. 3, pp. 363–378, 1988. [Online]. Available: http://dx.doi.org/10.1029/RS023i003p00363

[55] S. Priyadarshi, "A Review of Ionospheric Scintillation Models," *Surveys in Geophysics*, vol. 36, no. 2, pp. 295–324, 2015. [Online]. Available: http://dx.doi.org/10.1007/s10712-015-9319-1

[56] E. Kaplan and C. Hegarty, *Understanding GPS: Principles and Applications*. Artech House, Inc., 2006.

[57] C. Hegarty, M. B. El-Arini, T. Kim, and S. Ericson, "Scintillation modeling for GPS-Wide Area Augmentation System receivers," *Radio Science*, vol. 36, no. 5, pp. 1221–1231, 2001. [Online]. Available: http://dx.doi.org/10.1029/1999RS002425

[58] J. A. Secan, R. M. Bussey, E. J. Fremouw, and S. Basu, "High-latitude upgrade to the Wideband ionospheric scintillation model," *Radio Science*, vol. 32, no. 4, pp. 1567–1574, 1997. [Online]. Available: http://dx.doi.org/10.1029/97RS00453

[59] Y. Beniguel, "Global Ionospheric Propagation Model (GIM): A propagation model for scintillations of transmitted signals," *Radio Science*, vol. 37, no. 3, pp. 1–13, 2002. [Online]. Available: http://dx.doi.org/10.1029/2000RS002393

[60] J. Titheridge, "The diffraction of satellite signals by isolated ionospheric irregularities ," *Journal of Atmospheric and Terrestrial Physics*, vol. 33, no. 1, pp. 47 – 69, 1971. [Online]. Available: http://www.sciencedirect.com/science/article/pii/0021916971901814

[61] M. F. Knight, "Ionospheric Scintillation Effects on Global Positioning Systems Receivers," *PhD Thesis*, 2000.

[62] T. L. Beach and P. M. Kintner, "Simultaneous Global Positioning System observations of equatorial scintillations and total electron content fluctuations," *Journal of Geophysical Research: Space Physics*, vol. 104, no. A10, pp. 22 553–22 565, 1999. [Online]. Available: http://dx.doi.org/10.1029/1999JA900220

[63] D. M. Lin and T. J. B.Y., "Comparison of Acquisition Methods for Software GPS Receiver," in *Proceedings of the 13th International Technical Meeting of the Satellite Division of The Institute of Navigation*, Salt Palace Convention Center, Salt Lake City, UT, 2000, pp. 2385 – 2390.

[64] D. M. Lin and T. J. B.Y., "Acquisition Schemes for Software GPS Receiver ," in *Proceedings of the 11th International Technical Meeting of the Satellite Division of The Institute of Navigation*, Nashville, TN, 1998, pp. 317 – 325.

[65] D. M. Akos, P. Normark, J.-T. Lee, K. G. Gromov, J. B. Tsui, and J. Schamus, "Low power global navigation satellite system (GNSS) signal detection and processing," in *Proceedings of the 13th International Technical Meeting of the Satellite Division of The Institute of Navigation*, Salt Palace Convention Center, Salt Lake City, UT, 2000, pp. 784 – 791.

[66] M. Lu, S. Liguo, and W. Zhugang, "Performance Analysis of a Second Order FLL-Assisted Third Order PLL for Tracking Doppler Rates," *WSEAS TRANSACTIONS on COMMUNICATIONS*, vol. 13, pp. 26–43, 2014. [Online]. Available: http://www.wseas.org/multimedia/journals/communications/2014/b085704-251.pdf

[67] L. Zhang and Y. T. Morton, "Tracking GPS signals under ionosphere scintillation conditions," in *Proceedings of the 22nd International Technical Meeting of the Satellite Division of The Institute of Navigation*, Long Beach Convention Center, Long Beach, CA, 2009, pp. 227 – 234.

[68] P. W. Ward, "Performance comparisons between FLL, PLL and a novel FLL-Assisted-PLL carrier tracking loop under RF interference conditions," in *Proceedings of the 11th International Technical Meeting of the Satellite Division of The Institute of Navigation*, Nashville, TN, 1998, pp. 783 – 795.

[69] A. Ahmed, R. Tiwari, H. Strangeways, and S. Boussakta, "Software-based receiver approach for acquiring GPS signals using block repetition method," in *Satellite Navigation Technologies and European Workshop on GNSS Signals and Signal Processing (NAVITEC), 2014 7th ESA Workshop on*, Dec 2014, pp. 1–7.

[70] D. M. Lin, J. B. Tsui, and D. Howell, "Direct P(Y)-Code Acquisition Algorithm for Software GPS Receivers," in *Proceedings of the 12th International Technical Meeting of the Satellite Division of The Institute of Navigation*, Savannah International Convention Cen, terSavannah, GA, 1999, pp. 363 – 368.

[71] "USRP2 N210 Data sheet," 2014, [Online; accessed March-2015]. [Online]. Available: https://www.ettus.com/content/files/07495EttusN200-210DSFlyerHR1.pdf

[72] H. Li, X. Cui, M. Lu, and Z. Feng, "Dual-folding based rapid search method for long PN-code acquisition," *Wireless Communications, IEEE Transactions on*, vol. 7, no. 12, pp. 5286–5296, December 2008.

[73] M. L. Skolnik, *Introduction to Radar Systems*. McGraw-Hill Inc., 1980.

[74] K. M. and A. Finn, "The effects of ionospheric scintillations on GPS," in *Proceedings of the 11th International Technical Meeting of the Satellite Division of The Institute of Navigation*, Nashville, TN, 1998, pp. 673–685.

[75] M. L. Psiaki, "Block Acquisition of Weak GPS Signals in a Software Receiver," in *Proceedings of the 14th International Technical Meeting of the Satellite Division of The Institute of Navigation*, Salt Palace Convention Center, Salt Lake City, UT, 2001, pp. 2838 – 2850.

[76] J. B. Y. Tsui, "Tracking GPS Signals," in *Fundamentals of Global Positioning System Receivers: A Software Approach*. John Wiley & Sons, Inc., 2005.

[77] S. Skone, G. Lachapelle, D. Yao, W. Yu, and R. Watson, "Investigating the Impact of Ionospheric Scintillation Using a GPS Software Receiver," in *Proceedings of the 18th International Technical Meeting of the Satellite Division of The Institute of Navigation*, Long Beach Convention Center, Long Beach, CA, 2005, pp. 1126 – 1137.

[78] F. Ghafoori, "Modelling the Impact of Equatorial Ionospheric Irregularities on GPS Receiver Performance," *PhD Thesis*, 2012.

[79] T. E. Humphreys, M. L. Psiaki, P. M. Kintner, and B. M. Ledvina, "GPS Carrier Tracking Loop Performance in the presence of Ionospheric Scintillations," in *Proceedings of the 18th International Technical Meeting of the Satellite Division of The Institute of Navigation*, Long Beach Convention Center, Long Beach, CA, 2005, pp. 156 – 167.

[80] R. S. Conker, M. B. El-Arini, C. J. Hegarty, and T. Hsiao, "Modeling the effects of ionospheric scintillation on GPS/Satellite-Based Augmentation System availability," *Radio Science*, vol. 38, no. 1, pp. 1–1–1–23, 2003, 1001. [Online]. Available: http://dx.doi.org/10.1029/2000RS002604

[81] J. Holmes and S. Raghavan, "The mean cycle slip time for first-, second-, and third-orderPLLs," in *Aerospace conference, 2009 IEEE*, March 2009, pp. 1–8.

[82] R. Xu, Z. Liu, and W. Chen, "Improved FLL-assisted PLL with in-phase pre-filtering to mitigate amplitude scintillation effects," *GPS Solutions*, vol. 19, no. 2, pp. 263–276, 2015. [Online]. Available: http://dx.doi.org/10.1007/s10291-014-0385-5

[83] A. Ahmed, R. Tiwari, H. Strangeways, and S. Boussakta, "GPS Tracking Loop Performance using Wavelet Denoising," in *Satellite Navigation Technologies and European Workshop on GNSS Signals and Signal Processing (NAVITEC), 2014 7th ESA Workshop on*, Dec 2014.

[84] C. Torrence and G. P. Compo, "A Practical Guide to Wavelet Analysis," *Bulletin of the American Meteorological Society*, vol. 79, pp. 61–78, 1998.

[85] M. Stephane, "Wavelet Bases," in *A Wavelet Tour of Signal Processing*. Academic Press, 2008. [Online]. Available: http://www.sciencedirect.com/science/article/pii/B978012374370100001X

[86] R. Tiwari, H. J. Strangeways, S. Tiwari, V. E. Gherm, N. Zernov, and S. Skone, "Validation of a transionospheric propagation scintillation simulator for strongly scintillated GPS signals using extensive high latitude data sets," in *Proceedings of the 24th International Technical Meeting of the Satellite Division of The Institute of Navigation*, Portland, OR, 2011.

[87] S. Banola, B. Pathan, D. Rao, and H. Chandra, "Spectral characteristics of scintillations producing ionospheric irregularities in the Indian region," *Earth, Planets and Space*, vol. 57, no. 1, pp. 47–59, 2005. [Online]. Available: http://dx.doi.org/10.1186/BF03351805

[88] S. Basu, K. Groves, J. Quinn, and P. Doherty, "A comparison of TEC fluctuations and scintillations at Ascension Island," *Journal of Atmospheric and Solar-Terrestrial Physics*, vol. 61, no. 16, pp. 1219 – 1226, 1999. [Online]. Available: http://www.sciencedirect.com/science/article/pii/S1364682699000528

[89] J. Aarons, "Global positioning system phase fluctuations at auroral latitudes," *Journal of Geophysical Research: Space Physics*, vol. 102, no. A8, pp. 17 219–17 231, 1997. [Online]. Available: http://dx.doi.org/10.1029/97JA01118

[90] T. L. Beach, *Global positioning system studies of equatorial scintillations (PhD Thesis)*, 1998.

[91] M. A. Cervera and R. M. Thomas, "Latitudinal and temporal variation of equatorial ionospheric irregularities determined from GPS scintillation observations," *Annales Geophysicae*, vol. 24, no. 12, pp. 3329–3341, 2006. [Online]. Available: http://www.ann-geophys.net/24/3329/2006/

[92] G. Li, B. Ning, Z. Ren, and L. Hu, "Statistics of GPS ionospheric scintillation and irregularities over polar regions at solar minimum," *GPS Solutions*, vol. 14, no. 4, pp. 331–341, 2010. [Online]. Available: http://dx.doi.org/10.1007/s10291-009-0156-x

[93] P. M. Kintner, B. M. Ledvina, and E. R. de Paula, "Gps and ionospheric scintillations," *Space Weather*, vol. 5, no. 9, 2007. [Online]. Available: http://dx.doi.org/10.1029/2006SW000260

[94] C. S. Carrano and K. M. Groves, "TEC Gradients and Fluctuations at Low, Latitudes Measured With High Data Rate GPS Receivers," in *Proceedings of the 63rd Annual Meeting of The Institute of Navigation*, ambridge, MA, 2007, pp. 156–163.

[95] A. W. Wernik and M. Grzesiak, "Scintillation caused by the ionosphere with non-Gaussian statistics of irregularities," *Radio Science*, vol. 46, no. 6, 2011. [Online]. Available: http://dx.doi.org/10.1029/2011RS004716

[96] F. W. Perkins, "Ionospheric irregularities," *Reviews of Geophysics*, vol. 13, no. 3, pp. 884–884, 1975. [Online]. Available: http://dx.doi.org/10.1029/RG013i003p00884

[97] C. Coker, G. S. Bust, R. A. Doe, and T. L. Gaussiran, "High-latitude plasma structure and scintillation," *Radio Science*, vol. 39, no. 1, 2004. [Online]. Available: http://dx.doi.org/10.1029/2002RS002833

[98] K. Davies and J. Whitehead, "A radio lens in the ionosphere," *Journal of Atmospheric and Terrestrial Physics*, vol. 39, no. 3, pp. 383 – 387, 1977. [Online]. Available: http://www.sciencedirect.com/science/article/pii/S0021916977901532

[99] C. L. Rino, "A power law phase screen model for ionospheric scintillation: 1. Weak scatter," *Radio Science*, vol. 14, no. 6, pp. 1135–1145, 1979. [Online]. Available: http://dx.doi.org/10.1029/RS014i006p01135

[100] V. H. Rumsey, "Scintillations due to a concentrated layer with a power-law turbulence spectrum," *Radio Science*, vol. 10, no. 1, pp. 107–114, 1975. [Online]. Available: http://dx.doi.org/10.1029/RS010i001p00107

[101] A. Bhattacharyya, B. T. Rastogi, R. G., and S. Basu, "GPS studies of TEC variations and equatorial scintillation," in *Ionospheric Effects Symposium*, Alexandria, VA, 1999.

[102] L. Wanninger, "Ionospheric Monitoring Using IGS Data," in *Proceedings of the 1993 IGS-Workshop*, Berne, Astronomical Institute, University of Berne, 1993, pp. 351–360.

[103] A. Bhattacharyya and R. G. Rastogi, "Structure of ionospheric irregularities from amplitude and phase scintillation observations," *Radio Science*, vol. 26, no. 2, pp. 439–449, 1991. [Online]. Available: http://dx.doi.org/10.1029/90RS01657

[104] M. Mendillo, B. Lin, and J. Aarons, "The application of GPS observations to equatorial aeronomy," *Radio Science*, vol. 35, no. 3, pp. 885–904, 2000. [Online]. Available: http://dx.doi.org/10.1029/1999RS002208

[105] I. I. Shagimuratov, A. Krankowski, I. Ephishov, Y. Cherniak, P. Wielgosz, and I. Zakharenkova, "High latitude TEC fluctuations and irregularity oval during geomagnetic storms," *Earth, Planets and Space*, vol. 64, no. 6, pp. 521–529, 2012. [Online]. Available: http://dx.doi.org/10.5047/eps.2011.10.015

[106] N. Jakowski, C. Borries, and V. Wilken, "Introducing a disturbance ionosphere index," *Radio Science*, vol. 47, no. 4, 2012. [Online]. Available: http://dx.doi.org/10.1029/2011RS004939

[107] R. Tiwari, H. Strangeways, S. Tiwari, and A. Ahmed, "Investigation of ionospheric irregularities and scintillation using TEC at high latitude," *Advances in Space Research*, vol. 52, no. 6, pp. 1111 – 1124, 2013. [Online]. Available: http://www.sciencedirect.com/science/article/pii/S0273117713003517

[108] B. Parkinson, "Gps error analysis," in *Global Positioning System: Theory and Applications*. Washington, DC: American Institute of Aeronautics and Astronautics, Inc., 1996, pp. 469–484.

[109] J. P. McClure, "The height of scintillation-producing ionospheric irregularities in temperate latitudes," *Journal of Geophysical Research*, vol. 69, no. 13, pp. 2775–2780, 1964. [Online]. Available: http://dx.doi.org/10.1029/JZ069i013p02775

[110] B. Forte, "Optimum detrending of raw GPS data for scintillation measurements at auroral latitudes," *Journal of Atmospheric and Solar-Terrestrial Physics*, vol. 67, no. 12, pp. 1100 – 1109, 2005. [Online]. Available: http://www.sciencedirect.com/science/article/pii/S136468260500091X

[111] P. Prikryl, P. T. Jayachandran, S. C. Mushini, and R. Chadwick, "Climatology of GPS phase scintillation and HF radar backscatter for the high-latitude ionosphere under solar minimum conditions," *Annales Geophysicae*, vol. 29, no. 2, pp. 377–392, 2011. [Online]. Available: http://www.ann-geophys.net/29/377/2011/

[112] A. J. Van Dierendonck and Q. Hu, "Ionospheric Scintillation Monitoring Using Commercial Single Frequency C/A Code Receivers," in *Proceedings of the 6th International Technical Meeting of the Satellite Division of The Institute of Navigation*, Salt Palace Convention Center, Salt Lake City, UT, 1993, pp. 1333 – 1342.

[113] A. J. Van Dierendonck and H. Quyen, "Measuring Ionospheric Scintillation Effects from GPS Signals ," in *Proceedings of the 57th Annual Meeting of the Satellite Division of The Institute of Navigation*, Albuquerque, NM, 2001, pp. 391–396.

[114] S. C. Mushini, P. Jayachandran, R. Langley, J. MacDougall, and D. Pokhotelov, "Improved amplitude- and phase-scintillation indices derived from wavelet detrended high-latitude GPS data," *GPS Solutions*, vol. 16, no. 3, pp. 363–373, 2012. [Online]. Available: http://dx.doi.org/10.1007/s10291-011-0238-4

[115] B. Forte, "On the relationship between the geometrical control of scintillation indices and the data detrending problems observed at high latitudes," *Annals of Geophysics*, vol. 50, no. 6, 2007. [Online]. Available: http://www.annalsofgeophysics.eu/index.php/annals/article/view/3051

[116] M. Materassi and C. N. Mitchell, "Wavelet analysis of GPS amplitude scintillation: a case study," *Radio Science*, vol. 42, no. 1, February 2007. [Online]. Available: http://opus.bath.ac.uk/5714/

[117] F. Niu, Y. Morton, J. Wang, and W. Pelgrum, "GPS Carrier Phase Detrending Methods and Performances for Ionosphere Scintillation Studies," in *Proceedings of the 2012 International Technical Meeting of the Satellite Division of The Institute of Navigation*, Marriott Newport Beach Hotel & Spa, Newport Beach, CA, 2012, pp. 1462 – 1467.

[118] A. Ahmed, R. Tiwari, H. J. Strangeways, S. Dlay, and M. G. Johnsen, "Wavelet-based Analogous Phase Scintillation Index for High Latitudes," *Space Weather*, pp. n/a–n/a, 2015. [Online]. Available: http://dx.doi.org/10.1002/2015SW001183

[119] E. J. Fremouw, R. L. Leadabrand, R. C. Livingston, M. D. Cousins, C. L. Rino, B. C. Fair, and R. A. Long, "Early results from the DNA wideband satellite experiment—Complex-signal scintillation," *Radio Science*, vol. 13, no. 1, pp. 167–187, 1978. [Online]. Available: http://dx.doi.org/10.1029/RS013i001p00167

[120] L. Zhang and Y. Morton, "GPS Carrier Phase Spectrum Estimation for Ionospheric Scintillation Studies," *Navigation*, vol. 60, no. 2, pp. 113–122, 2013. [Online]. Available: http://dx.doi.org/10.1002/navi.33

[121] R. DeVore, B. Jawerth, and B. Lucier, "Image compression through wavelet transform coding," *Information Theory, IEEE Transactions on*, vol. 38, no. 2, pp. 719–746, March 1992.

[122] I. Daubechies, "Where do wavelets come from? A personal point of view," *Proceedings of the IEEE*, vol. 84, no. 4, pp. 510–513, Apr 1996.

[123] A. Grossmann and J. Morlet, "Decomposition of Hardy Functions into Square Integrable Wavelets of Constant Shape," *SIAM Journal on Mathematical Analysis*, vol. 15, no. 4, pp. 723–736, 1984. [Online]. Available: http://dx.doi.org/10.1137/0515056

[124] I. Daubechies, "The wavelet transform, time-frequency localization and signal analysis," *Information Theory, IEEE Transactions on*, vol. 36, no. 5, pp. 961–1005, Sep 1990.

[125] R. Merry, "Wavelet Theory and Applications: A Literature Study," 2005, [Online; accessed April-2015]. [Online]. Available: http://alexandria.tue.nl/repository/books/612762.pdf

[126] P. Prikryl, P. Jayachandran, S. Mushini, and I. Richardson, "High-latitude GPS phase scintillation and cycle slips during high-speed solar wind streams and interplanetary coronal mass ejections: a superposed epoch analysis," *Earth, Planets and Space*, vol. 66, no. 1, 2014. [Online]. Available: http://dx.doi.org/10.1186/1880-5981-66-62

[127] H. J. Strangeways, "Determining scintillation effects on GPS receivers," *Radio Science*, vol. 44, no. 1, pp. n/a–n/a, 2009. [Online]. Available: http://dx.doi.org/10.1029/2008RS004076

[128] H. J. Strangeways, Y.-H. Ho, M. H. O. Aquino, Z. G. Elmas, H. A. Marques, J. F. G. Monico, and H. A. Silva, "On determining spectral parameters, tracking jitter, and GPS positioning improvement by scintillation mitigation," *Radio Science*, vol. 46, no. 6, pp. n/a–n/a, 2011. [Online]. Available: http://dx.doi.org/10.1029/2010RS004575

[129] R. Tiwari and H. J. Strangeways, "Regionally based alarm index to mitigate ionospheric scintillation effects for GNSS receivers," *Space Weather*, vol. 13, no. 1, pp. 72–85, 2015. [Online]. Available: http://dx.doi.org/10.1002/2014SW001115

[130] R. Tiwari and H. J. Strangeways, "Modeling the Effects of Ionospheric Scintillation on GPS Carrier Phase Tracking using High Rate TEC Data," in *Proceedings of the 26th International Technical Meeting of the Satellite Division of The Institute of Navigation*, Nashville, TN, 2013, pp. 2480 – 2488.

Appendix A

Thermal Noise Tracking Error Variance in the Presence of Amplitude Scintillation

From (4.57), the thermal noise tracking error variance in the presence of amplitude scintillation is given as

$$\sigma_{\phi T}^2 = \frac{B_n(\tilde{A})}{C/N_o}\left[\int_0^\infty \frac{1}{\tilde{A_N}^2} f_{\tilde{A_N}}(A_N)d\tilde{A_N} + \frac{1}{2T_I C/N_o}\int_0^\infty \frac{1}{\tilde{A_N}^4} f_{\tilde{A_N}}(A_N)d\tilde{A_N}\right] \tag{A.1}$$

where $\tilde{A_N} = \tilde{A}/A$ is the normalized amplitude, A is the unpurturbed amplitude and $\tilde{A}$ is the purturbed signal amplitude affected by the scintillation. The term $f_{\tilde{A_N}}(A_N)$ is the Nakagami-m distrbution which from (4.58) is

$$f_{\tilde{A_N}}(A_N) = \frac{2m^m \tilde{A_N}^{2m-1}}{\Gamma(m)}.\exp(-m\tilde{A_N}^2) \tag{A.2}$$

Using (A.2) in (A.1) we have:

$$\sigma_{\phi T}^2 = \frac{2B_n(\tilde{A})m^m}{C/N_o\Gamma(m)}\left[\int_0^\infty \tilde{A_N}^{2m-3}\exp(-m\tilde{A_N}^2)d\tilde{A_N} + \frac{1}{2T_I C/N_o}\int_0^\infty \tilde{A_N}^{2m-5}\exp(-m\tilde{A_N}^2)d\tilde{A_N}\right] \tag{A.3}$$

Substituting $x = \tilde{A_N^2}$ and also $dx = 2\tilde{A_N} d\tilde{A_N}$ in (A.3) inside the integral terms:

$$\sigma_{\phi T}^2 = \frac{2B_n(\tilde{A})m^m}{C/N_o\Gamma(m)}\left[\frac{1}{2}\int_0^\infty x^{m-2}\exp(-mx)dx + \frac{1}{4T_IC/N_o}\int_0^\infty x^{m-3}\exp(-mx)dx\right] \quad \text{(A.4)}$$

Again substituting $y_1 = m-1$ and $y_2 = m-2$ in (A.4):

$$\sigma_{\phi T}^2 = \frac{2B_n(\tilde{A})m^m}{C/N_o\Gamma(m)}\left[\frac{1}{2}\int_0^\infty x^{y_1-1}\exp(-mx)dx + \frac{1}{4T_IC/N_o}\int_0^\infty x^{y_2-1}\exp(-mx)dx\right] \quad \text{(A.5)}$$

From table of integrals we have

$$\int_0^\infty x^{v-1}\exp(-zx)dx = \frac{1}{z^v}\Gamma(v) \quad \text{(A.6)}$$

Using this integral property in (A.5) and solving the integrals:

$$\sigma_{\phi T}^2 = \frac{2B_n(\tilde{A})m^m}{C/N_o\Gamma(m)}\left[\frac{1}{2}.\frac{\Gamma(y_1)}{m^{y_1}} + \frac{1}{4T_IC/N_o}.\frac{\Gamma(y_2)}{m^{y_2}}\right] \quad \text{(A.7)}$$

Using the substitute values of y_1 and y_2 in (A.7):

$$\sigma_{\phi T}^2 = \frac{2B_n(\tilde{A})m^m}{C/N_o\Gamma(m)}\left[\frac{1}{2}.\frac{\Gamma(m-1)}{m^{m-1}} + \frac{1}{4T_IC/N_o}.\frac{\Gamma(m-2)}{m^{m-2}}\right] \quad \text{(A.8)}$$

Further simplifying (A.8) will give

$$\sigma_{\phi T}^2 = \frac{B_n(\tilde{A})}{C/N_o}\left[\frac{m\Gamma(m-1)}{\Gamma(m)} + \frac{m^2\Gamma(m-2)}{2T_IC/N_o\Gamma(m)}.\right] \quad \text{(A.9)}$$

Using the property, $\Gamma(m) = (m-1)\Gamma(m-1)$, (A.9) will be transformed to

$$\sigma_{\phi T}^2 = \frac{B_n(\tilde{A})}{C/N_o}\left[\frac{m}{m-1} + \frac{m^2}{2T_IC/N_o(m^2-3m+2)}.\right] \quad \text{(A.10)}$$

From [61], using $m = \frac{1}{S_4^2}$, (A.10) will become

$$\sigma_{\phi T}^2 = \frac{B_n(\tilde{A})}{C/N_o}\left[\frac{1}{(1-S_4^2)} + \frac{1}{2T_IC/N_o(1-3S_4^2+2S_4^4)}.\right] \quad \text{(A.11)}$$

The above equation is valid for $S_4 < 0.707$ only.

Appendix B

Derivation of the Noise Bandwidth for the second order loop

From (4.25), the transfer function of the second order tracking loop is

$$H(s) = \frac{2\zeta w_n s + w_n^2}{s^2 + 2\zeta w_n s + w_n^2} \tag{B.1}$$

The noise bandwidth, B_n, can be found as

$$B_n = \int_0^\infty |\, H(w)\,|^2\, df = \frac{w_n}{2\pi}\int_0^\infty \frac{1+\left(\frac{2\zeta w}{w_n}\right)^2}{\left(1-\left(\frac{w}{w_n}\right)^2\right)^2+\left(2\zeta\frac{w}{w_n}\right)^2}\quad dw \tag{B.2}$$

Simplifying (B.2) will give

$$B_n = \frac{w_n}{2\pi}\int_0^\infty \frac{1+4\zeta^2\left(\frac{w}{w_n}\right)^2}{\left(\frac{w}{w_n}\right)^4+(4\zeta^2-2)\left(\frac{w}{w_n}\right)^2+1}\quad dw \tag{B.3}$$

Substituting $x = \left(\frac{w}{w_n}\right)$ in (B.3):

$$B_n = \frac{w_n}{2\pi}\left[\int_0^\infty \frac{1}{x^4+(4\zeta^2-2)x^2+1}\,dx + \int_0^\infty \frac{4\zeta^2x^2}{x^4+(4\zeta^2-2)x^2+1}\,dx\right] \tag{B.4}$$

The two integrals above can be found using the integration from the table of integrals given as

$$\int_0^\infty \frac{x^{u-1}dx}{x^4+(B+A)x^2+BA} = \frac{\pi}{2}\frac{A^{u/2-1}-B^{u/2-1}}{B-A}csc(\frac{u\pi}{2}) \tag{B.5}$$

Comparing the (B.4) and (B.5), $u_1 = 1$ and $u_2 = 3$ are the alternate values of u in the first and second integral terms in (B.4) respectively and

$$B+A = 4\zeta^2 - 2$$

$$BA = 1$$

Simaltaneously solving the above equations will give

$$B = (\zeta + \sqrt{\zeta^2-1})^2 \tag{B.6}$$

$$A = (\zeta - \sqrt{\zeta^2-1})^2 \tag{B.7}$$

Using (B.5), the first and the second integrals terms in (B.4) can be represented as

$$B_n = \frac{w_n}{2\pi}\left[\frac{\pi}{2}\frac{A^{u_1/2-1}-B^{u_1/2-1}}{B-A}csc(\frac{u_1\pi}{2}) + 4\zeta^2.\frac{\pi}{2}.\frac{A^{u_2/2-1}-B^{u_2/2-1}}{B-A}csc(\frac{u_2\pi}{2})\right] \tag{B.8}$$

Using the values of u_1 and u_2 in (B.8)

$$B_n = \frac{w_n}{2\pi}\left[\frac{\pi}{2}\frac{A^{-1/2}-B^{-1/2}}{B-A}csc(\frac{\pi}{2}) + 4\zeta^2.\frac{\pi}{2}.\frac{A^{1/2}-B^{1/2}}{B-A}csc(\frac{3\pi}{2})\right] \tag{B.9}$$

where $csc(\frac{\pi}{2}) = 1$ and $csc(\frac{3\pi}{2}) = -1$:

$$B_n = \frac{w_n}{2\pi}\left[\frac{\pi}{2}\frac{A^{-1/2}-B^{-1/2}}{B-A} - 4\zeta^2.\frac{\pi}{2}.\frac{A^{1/2}-B^{1/2}}{B-A}\right] \tag{B.10}$$

Upon using the values of A and B in (B.10) and simplifying, (B.10) will be transformed to

$$B_n = \frac{w_n}{2\pi}\left[\frac{\pi}{2}.\frac{1}{2\zeta} - 4\zeta^2.\frac{\pi}{2}.\left(-\frac{1}{2\zeta}\right)\right] \tag{B.11}$$

Further simplification will give

$$B_n = \frac{w_n}{2\pi}\left[\frac{\pi}{4\zeta} + \pi\zeta\right] \tag{B.12}$$

Appendix C

Ionosphere Pierce Point Velocity

From [61], the ionosphere pierce point velocity, v_{pp}, can be given as

$$v''_{pp} = R_T \times v_{ECEF} \tag{C.1}$$

where R_T is the transformation/rotational matrix used to convert the satellite coordinates to local level coordinates and v_{ECEF} is the velocity of the of the IPP in Cartesian Earth Centred Earth Fixed (ECEF) coordinate system which is converted to the local coodinates by multiplying with the R_T in order to get the velocity in meters per second. The v_{ECEF} can be given as

$$(v_{ECEF})_i = \left(v_{p_x}, v_{p_y}, v_{p_z}\right) = \frac{(\overrightarrow{r}_{IPP})_{i+1} - (\overrightarrow{r}_{IPP})_i}{t_{i+1} - t_i} \tag{C.2}$$

where $(\overrightarrow{r}_{IPP}) = (x_{IPP}, y_{IPP}, z_{IPP})$ in (C.2) is the position of the IPP in ECEF coordinates at two consecutive epochs i and $i+1$. The rotational matrix, R_T, [61] can be given as

$$R_T = \begin{bmatrix} -\sin(\lambda_{IPP}) & \cos(\lambda_{IPP}) & 0 \\ -\sin(\phi_{IPP})\cos(\lambda_{IPP}) & -\sin(\phi_{IPP})\sin(\lambda_{IPP}) & \cos(\phi_{IPP}) \\ \cos(\phi_{IPP})\cos(\lambda_{IPP}) & \cos(\phi_{IPP})\sin(\lambda_{IPP}) & \sin(\phi_{IPP}) \end{bmatrix} \tag{C.3}$$

where ϕ_{IPP} is the latitude and λ_{IPP} is the longitude of the IPP and can be given as

$$\phi_{IPP} = \phi_R + \Psi\cos(a) \tag{C.4}$$

$$\lambda_{IPP} = \lambda_R + \frac{\Psi\sin(a)}{\cos(\phi_{IPP})} \tag{C.5}$$

where ϕ_R and λ_R are the receiver latitude and longitude respectively and can be obtained by converting the ECEF coordinates to geodetic coordinates, a is the azimuth angle and Ψ is the earth's centered angle given as

$$\Psi = 90 - e - \sin -1\left(\frac{\cos(e)R_e}{R_e + h_{IPP}}\right) \tag{C.6}$$

where e is the elevation angle, $R_e = 6378$ km is the radius of the earth and h_{IPP} is the IPP height generally taken as 350 km. Using the R_T and v_{ECEF} in (C.1), the final form of the v_{pp} is

$$v''_{pp} = \begin{bmatrix} v_{p_x} & v_{p_y} & v_{p_z} \end{bmatrix} \begin{bmatrix} -\sin(\lambda_{IPP}) & \cos(\lambda_{IPP}) & 0 \\ -\sin(\phi_{IPP})\cos(\lambda_{IPP}) & -\sin(\phi_{IPP})\sin(\lambda_{IPP}) & \cos(\phi_{IPP}) \\ \cos(\phi_{IPP})\cos(\lambda_{IPP}) & \cos(\phi_{IPP})\sin(\lambda_{IPP}) & \sin(\phi_{IPP}) \end{bmatrix} \tag{C.7}$$

Equation (C.1) will give the velocity component of the v_{pp} in easting, northing and up directions whose absoltue value can be taken to find the veolcity of the IPP as

$$v_{pp} = |v''_{pp}| \qquad \text{m/s} \tag{C.8}$$